Dissertation

Amir Morteza Azim Zadeh

The genetic model of the Hohentauern/Sunk sparry magnesite deposit (Eastern Alps/Austria)

Dissertation

PhD Thesis submitted to obtain the degree of:
Doktor der montanistischen Wissenschaften

Amir Morteza Azim Zadeh BSc. & MSc.

Supervisor:
O. Univ.-Prof. Dr. phil. Fritz Ebner

Department of Applied Geosciences and Geophysics
Geology and Economic Geology

University of Leoben, Austria
2009

Referees: O. Univ.-Prof. Dr. phil. Fritz Ebner

Ao. Univ.-Prof. Dr. Ronald J. Bakker

I declare in lieu of oath, that I wrote this thesis and performed the associated research myself, using only literature cited in this volume.

Amir M. Azimzadeh

Leoben, May 2009

„…und dicht neben meinem Wissen lagerte mein schwarzes Unwissen.“

Also sprach Zarathustra
Friedrich Wilhelm Nietzsche

Contents:

Abstract

The Carboniferous of the Veitsch nappe in the Graywacke Zone (Eastern Alps/Austria) is the type region of the "Veitsch type" sparry magnesite. The numerous deposits/occurrences of sparry magnesite and talc are known as the "Veitsch nappe magnesite-talc district" in the Metallogenic Map of Austria. The Hohentauern/Sunk deposit, at the structural base of the Veitsch nappe, is one of the best exposed magnesite deposits in this district. The stratiform magnesite displays distinct metasomatic textures at the contact to the carbonate host rocks with distinct sedimentary and diagentic features. Dolomitization and redolomitization processes lasted from the diagenetic stage until late orogenic stages. Sparry magnesite of the Hohentauern/Sunk deposit is characterized by pinolites, rosettes and banded (zebra) textures. The magnesite contains irregularly distributed mikroinclusions of fine grained dolomite and evaporite minerals (sylvinite). On the other hand magnesite formation is followed by several generations of late dolomite. The sparry magnesite of the deposit has lower MgO and higher CaO contents in comparison to stoechiometric magnesite crystals. The elevated CaO/MgO ratio derives from relics of the dolomite microinclusions and various types of late dolomite formed by redolomitization of the magnesite. The concentrations of some trace elements (Sr, Ba, Ti, Fe, Mn, Cr, Ni, Co) illustrate a marine/evaporitic and a Mg^{2+}-metasomatic origin of the magnesite mineralization. In the Hohentauern/Sunk deposit the sparry magnesite displays REE patterns with low LREE/HREE, depletion of LREE and a negative Ce anomaly. The stable isotopes ($\delta^{18}O$ and $\delta^{13}C$) data of the sparry magnesite overlap with those typical for magnesite formed by metasomatic dolomite replacement. Strongly scattered $^{87}Sr/^{86}Sr$ ratios are affected by several processes. Therefore they give no significant hint for the magnesite formation. However Nd-Sr isotopes show that the mineralizing fluid percolated through crustal rocks. Fluid inclusion studies on the sparry magnesite indicate a high salinity of the Mg-rich fluid which transformed the dolomite protolites. Sm-Nd geochronology of the sparry magnesite shows a range of Late Carboniferous to Early Permian. All geological, petrographical and geochemical features of the Hohentauern/Sunk deposit support a diagenetic dolomitization of carbonate host rocks followed by an epigenetic formation of the magnesite deposit, via metasomatic replacement of a dolomitic protolith by Mg-rich solutions. The age of mineralization, however, is still the subject of intensive discussion.

Zusammenfassung

Die Veitscher Decke (Vise-Oberkarbon) in der Grauwackenzone (Ostalpen/Österreich) ist die Typuslokalität des "Veitsch-Typ" Spatmagnesites. Die zahlreichen Lagerstätten/Vorkommen von Spatmagnesit und Talk dieser Zone werden in der Metallogenetischen Karte von Österreich als "Magnesit-/Talkbezirk Veitscher Decke" zusammengefaßt. Die Spatmagnesitlagerstätte von Hohentauern/Sunk liegt an der strukturellen Basis der Veitscher Decke. Sie ist eine der bekanntesten und am besten aufgeschlossenen Lagerstätten dieses Bezirks. Der lagenförmige Magnesit zeigt verschiedene metasomatische Strukturen am Kontakt zu den karbonatischen Wirtsgesteinen mit unterschiedlichen sedimentären und diagenetischen Texturen. Dolomitisations- und Redolomitisationsprozesse dauerten von diagenetischen bis zu spätorogenetischen Phasen an. Die Spatmagnesitlagerstätte Hohentauern/Sunk zeichnet sich durch Pinolit, Rosetten und gebänderte (Zebra) Texturen aus. Der Magnesit enthält irregulär verteilt submikroskopische Dolomitrelikte und evaporitische Mineralien (Sylvin). Der Magnesitbildung folgten mehrere Generationen von Dolomit. Der Großteil der Spatmagnesite hat im Vergleich zur idealen Magnesitzusammensetzung niedrigere MgO- und höhere CaO Gehalte. Das erhöhte CaO/MgO-Verhältnis ergibt sich aus submikroskopischen Dolomitrelikten und verschiedenen Arten von spätigem Dolomit der Magnesitredolomitisation. Die Konzentrationen einiger Spurenelemente (Sr, Ba, Ti, Fe, Mn, Cr, Ni, Co) zeigen eine Meerwasser/evaporitische Herkunft der magnesitbildenden Lösungen bei der Mg^{2+}-Metasomatose. In der Lagerstätte Hohentauern/Sunk zeigt der Spatmagnesit geringe LSEE/SSEE-Verhältnisse, eine LSEE-Abreicherung und eine negative Ce-Anomalie. Die $\delta^{18}O$- und $\delta^{13}C$-Werte sind ident mit den für Spatmagnesit aus der Grauwackenzone bekannten Werten. Sie überlappen mit Werten für Magnesit, der durch matasomatiche Verdrängung aus Dolomit gebildet wurde. Die $^{87}Sr/^{86}Sr$-Verhältnisse isolierter Magnesit-Kristalle sind variabel. Grund dafür sind die mehrphasige Mineralisationgeschichte sowie submikroskopische Dolomitrelikte bzw. Redolomitisierung entlang von Spaltrissen und Klüften. Deshalb ist das $^{87}Sr/^{86}Sr$-Verhältnis für die Magnesitbildung nur von untergeordneter Aussagekraft. Allerdings zeigen Nd-Sr-Isotope, dass die mineralisierende Lösung durch die Kruste migrierte. Die Zusammensetzung der Flüssigkeitseinschlüsse im Spatmagnesit entspricht einer hochsalinaren, Mg-reichen Lösung, die die dolomitischen Protolite umgewandelt hat. $^{147}Sm/^{144}Nd$-Daten von Pinolitmagnesiten weisen auf einen oberkarbonen-unterpermischen Zeitbereich.

Alle geologischen, petrographischen und geochemischen Daten der Spatmagnesitlagerstätte Hohentauern/Sunk zeigen eine diagenetische Dolomitisation der karbonatischen Wirtsgesteine und eine epigenetische Bildung der Magnesitlagerstätte über die metasomatische Umwandlung eines dolomitischer Protolithe durch Mg-reiche Lösungen. Das Alter der Lagerstättenbildung ist jedoch nach wie vor Gegenstand intensiver Diskussion.

Publications and conference presentations of A. M. Azim Zadeh related to this thesis

EBNER F., PROCHASKA W. & AZIM ZADEH A. M. (2003): The type region of "Veitsch type" sparry magnesite (Austria/Eastern Alps). - Int. Conf. of Mineralization in Precambrian Terranes & UNESCO/IUGS IGCP 443 Annual Meeting and Field Correlation, Abstr. Vol., 11-18, Nanjing.

EBNER F., PROCHASKA W., TROBY J. & AZIM ZADEH A. M. (2004 a): Carbonate hosted sparry magnesite of the Greywacke zone, Austria/Eastern Alps. - Acta Petrol. Sinica., 20: 791-802, Peking.

EBNER F., MALI H. & PROCHASKA W. (with a contribution of AZIM ZADEH, A. M.) (2004 b): Excursion to Magnesite, Siderite and Talc Deposits in Austria.-IGCP No. 443, Final Fieldmeeting, Guidebook, 40 pp., Leoben.

AZIM ZADEH A. M., EBNER F. & PROCHASKA W. (2004): The Sunk/Hohentauern Magnesite Deposit (Eastern Alps/Austria): Geological situation and genetic aspects. - 32nd IGC Florence, Sci. Sessions, Workshops, 1518 (oral presentation).

AZIM ZADEH A., EBNER F., PROCHASKA W. & JIANG, S.-Y. (2005): Tektonische Struktur und Geochemie der Magnesitlagerstätte Hohentauern. - Mitt. Österr. Geol. Ges., 151, 23, Wien (Poster, awarded as the best student poster presentation).

AZIM ZADEH A. M., EBNER F. & JIANG S.-Y (2007) Stable Isotope ($\delta^{18}O$ and $\delta^{13}C$) pattern of the Hohentauern/Sunk sparry magnesite deposit (Austria/Eastern Alps). The 8th Austrian Stable Isotope User Group Meeting, Isotopes in Ecology and Earth Sciences (Stable Isotope Network Austria), Vienna/Austria (poster).

EBNER F. & AZIM ZADEH A. M. (2007): Beeinflussung der Magensitlagerstätte Sunk/Hohentauern durch die Pölsstörung. - Unpubl. Report ÖAW – Kommission für Grundlagen der Mineralrohstoffforschung, 30 pp., Wien.

EBNER F. & AZIM ZADEH A. M. JIANG, S.-Y. (2008): Isotope characteristics of Veitsch type sparry magnesite. - 33rd Int. Geol. Congr. Oslo, EUR-MRB-01 , Abstract CD-Rom (poster).

AZIM ZADEH A. M., EBNER F., JIANG S.-H. & KLÖTZLI U. (2008): Mineralisationsphasen in der Spatmagnesitlagerstätte Sunk/Hohentauern-Stmk./Ostalpen. - Pangeo 2008, Kurzfassungen und Abstracts, Journal of Alpine Geology, 49: 4-5c (oral presentation).

AZIM ZADEH A. M., EBNER F. & JIANG S.-Y (2009): The Hohentauern/Sunk deposit – a key for unraveling sparry magnesite formation in the Graywacke zone/Eastern Alps, Austria. - Mitt. Österr. Geol. Ges., 155, (submitted).

Acknowledgements

I would like to thank my supervisor O. Univ.-Prof. Dr. phil. Fritz Ebner for his continuous support, his engagement, for the helpful discussions and the examination of this work.

Special thanks must go to Ass. Prof. Dipl.-Ing. Dr. mont. Heinrich Mali**,** who has kindly supported me during my work.

I am thankful to Ao. Univ.-Prof. Dr. Ronald J. Bakker and Ao. Univ.-Prof. Dr. phil. Walter Prochaska for their time and assistances.

I appreciate the great support of Prof. Dr. Shao-Yong Jiang (The State Key Laboratory for Mineral Deposits Research-Nanjing University) for trace, rare earth element, stable and radiogenic analyses, Ao. Univ. Prof. Mag. Dr. Urs Klötzli (Department of Lithospheric Research, Center for Earth Sciences-University of Vienna) for in situ Sr isotope analyses, Dr. Federica Zaccarini (Department of Applied Geological Sciences and Geophysics-University of Leoben) for EPMA analyses and O. Univ.-Prof. Mag. et Dr. rer. nat. Walter Vortisch **(**Department of Applied Geological Sciences and Geophysics-University of Leoben) for cathodoluminescence microscopy.

I very much appreciate the good collaboration and discussion with Dr. Friedhelm Henjes-Kunst (Federal Institute for Geosciences and Natural Resources, Hannover), Dr. Achim Bechtel (Eawag: Swiss Federal Institute of Aquatic Science and Technology), Prof. Dr. Erich Schroll (†), Ao. Univ.-Prof. Dr. phil. Johann G. Raith (Department of Applied Geological Sciences and Geophysics-University of Leoben), Ao. Univ.-Prof. Mag. rer. nat. Dr. mont. Thomas Meisel (Department of General, Analytical and Physical Chemistry-University of Leoben)**,** Univ.-Doz. Mag. Dr. Martin Kralik (Umweltbundesamt, Austria) and Ao. Univ.-Prof. Dr. Christoph Spötl (Faculty of Geo- and Atmospheric Sciences-University of Innsbruck), who always showed an interest in my study and were always available for discussions.

I also appreciate very much Dr. J. M. McArthur (Strontium Isotope Stratigraphy Group-Department of Earth Sciences-University College London) and Kenneth R. Ludwig (Berkeley Geochronology Center) for their support to have new software in geochronology.

Thanks also go to the technical staff of the Department of Applied Geosciences and Geophysics, particularly Siegfried Schider and Sabine Feuchter for thin and polished section preparation and Helmut Mühlhans for his assistance with the microprobe.

Furthermore I would like to thank all the helpful people in the library and secretariats, especially Mrs. Renate Reichl and Mrs. Andrea Winkler. Without their help I would not have been able to finish this work as fast as I did.

I also extend my gratitude to my colleges Konstantin Horkel, Thomas Unterweissacher, Klaus Lassnig and Claudia Kaiser for their assistance.

Thanks to the mining company ”RHI-AG” and to Dr. Roland Nilica for XRF measurements at the Research and Development Departments in RHI Technology Center Leoben and Dipl.-Ing. Karl-Heinz Krisch (Veitsch–Radex GmbH) for topographic mapping and informations going back to the last years of mine operations in the Hohentauern/Sunk deposit.

I am grateful to the UNESCO/IUGS (International Union of Geological Sciences) and IGCP (International Geoscience Programme) 443 for providing workshops and excursions.

I would also like to thank the Austrian Exchange Service (ÖAD) for their “EZA 2109” grant.

This work was partly supported by the Austrian Academy of Sciences through project “Beeinflussung der Magnesitlagerstätte Sunk/Hohentauern durch die Pölsstörung.”

Finally I thank my friend Thomas Aiglsperger for his great friendship.

List of figures

Chapter 1:

Chapter 2:

Chapter 3:

Chapter 5:

Chapter 6:

Chapter 7:

Chapter 8:

Chapter 9:

Chapter 10:

Chapter 11:

List of tables

1. Introduction

Magnesite ($MgCO_3$) is a very simple chemical compound. Mineralogically magnesite occurs in a wide variety of geological environments. However, important deposits of magnesite, obviously have formed under conditions not observed today. An early attempt at the beginning of the 20th century (Redlich 1909) to describe types of magnesite deposits was based on the deposits/occurrences then known in Austria, which was at that time the worlds leading producer. On the basis of field observations and petrographic constraints, magnesite deposits/occurrences have been grouped into three types: A) sediment-hosted deposits in older geological formations, B) deposits that have been formed within ultramafic complexes of all ages and sedimentary basins very close to ultarmafic complexes e.g. Bela Stena type, and C) deposits formed in modern sabkha and alkaline lake environments. Most of the available resources of natural magnesite are sediment-hosted (Pohl & Siegl 1986, Ebner & Wilson 2006).

Veitsch type magnesite is one of the economically important types of magnesite deposits which occurs typically in Proterozoic-Paleozoic sporadically terrigenous influenced marine clastic/carbonate shelf sediments. Sparry magnesite of Veitsch type was described for the first time from the Graywacke zone in the Eastern Alps/Austria (Redlich 1909, Ebner et al. 2004a). Despite a high economic significance, however, its origin remains controversial. "The formation of Veitsch type deposits is discussed between the extremes of a mainly synsedimentary origin from seawater and an epigenetic replacement model with a wide range of parameters concerning source, transport of Mg-ions and the formation of magnesite (Pohl 1989)".

The Hohentauern/Sunk deposit (Graywacke zone, Eastern Alps/Austria) is one of the best known sparry magnesite deposits of the Veitsch type (Ebner et al. 2004a). It is hosted in the Early Carboniferous Steilbachgraben formation within shallow water carbonate rocks metamorphosed within the greenschist metamorphic facies during the Cretaceous Alpine orogeny.

In this study, using a multi-method approach, we tried to access the way which answer some outstanding open problems of numerous questions and finally a genetic model based on field work and laboratory experiments was established. Of course, a genetic model including all relevant parameters would need a development of modern hightech analytical

methods. Especially the origin of the Mg^{2+}-solution necessary for the magnesite formation is controversial. The relationship between early dolomitization processes and magnesite formation in carbonate rocks is another important objective that could advance our present knowledge on the magnesite formation.

1.1 Aim

The main objective of this thesis is to decipher the formation of the carbonate-hosted magnesite deposit of Hohentauern/Sunk related to the present genetic theories. To achieve this aim, an interdisciplinary research approach including field work and laboratory experiments was performed. The detailed field work included geologic mapping and structural investigation. Sampling was done in July and August 2003 and July 2004. Besides field work structural analysis and stratigraphy were applied. The laboratory experiments including various methods were carried out by the application of different microscopic techniques, intensive complementary geochemical analytical work and fluid inclusion studies.

Within this unifying aim, this thesis explores numerous minor investigations. The minor aims include:

- Characterization all of the host rocks and the succession of the formation of all mineralogical carbonate phases of the deposit.
- In situ Sr-isotope analysis of carbonate minerals and comparison with solution-based Sr-analysis.
- First Sm-Nd dating of the carbonate-hosted sparry magneseite of the stratiform Hohentauern/Sunk deposit.
- Characterization of the fluid chemistry of the sparry magnesite.
- Impacts of geological processes to the quality of the magnesite.

1.2 Applied methods

The study has been carried out on representative samples well constrained in terms of their field location and geological setting. All samples have been studied in detail by different microscopical and analytical methods.

1.2.1 Field methods and sampling

The magnesite ore body and its clastic/carbonate host rocks were sampled along 15 profiles at the mining area. A traverse has been carried out along every profile within the 1/250 scale. An attempt was made to collect at least one sample per each 2.5 m. All representative types of carbonate, clastic rocks and talc were collected from profiles.

1.2.2 Analytical techniques

Representative samples were used for the petrographical, mineralogical, geochemical and fluid inclusion study. A multi analytical approach has been applied based on the following techniques:

1.2.2.1 Petrography

Petrographic descriptions of sparry magnesite and clastic/carbonate host rocks were performed at the Chair of Geology and Economic Geology at the Department of Applied Geosciences and Geophysics at the University of Leoben, using an Olympus BX 60 microscope.

1.2.2.2 Cathodoluminescence microscopy

Cathodoluminescence microscopy has been developed as a standard technique for mineralogical and petrological investigation in geosciences. A cathodoluminescence (CL) microscope combines methods from electron and regular (light optical) microscopes. It is designed to study the luminescence characteristics of solids in polished thin sections irradiated by an electron beam. Using cathodoluminescence microscopy textures and fabrics within crystals will become visible which cannot be seen under normal light conditions. Cathodoluminescence microscopy and imaging with cold cathode system (model CITL Mk3) was carried out at the Chair of Prospection and Applied Sedimentology at the Department of Applied Geosciences and Geophysics at the University of Leoben in cooperation with Dr. Vortisch.

1.2.2.3 Electron microprobe analysis (EPMA)

The Electron Microprobe Analysis (EPMA) is a micro analytical method which can produce qualitative and quantitative chemical analyses of major and minor elements on

spots ranging in size from approximately 1x1x1.5 microns to approximately 100x100x1.5 microns. The electron microprobe is used to determine the chemical composition of solid materials from minerals and glasses in rocks and meteorites, to metals and even composite materials. The utility of microprobe is that it is a non-destructive, in-situ, analytical tool that requires minimal sample preparation. The electron microprobe can analyze all elements from Boron (Z=5) to Uranium (Z=92). The modern electron microprobe is based on two components: the electron-optical system and the X-ray spectrometer. Samples for analysis, like those for imaging, are polished petrographic thin sections (27 mm wide by 46 mm long). Sample surfaces must also be cleaned so that they are free of dust, oils, polishing material, and such. Non-conductive samples must be conductively coated with a layer of carbon (for analysis) to EPMA study. All samples were analyzed with an ARL-SMQ microprobe additionally equipped with a LINK-860 EDS and a new Superprobe JEOL JXA 8200 at the chair of Mineralogy and Petrology at the Department of Applied Geosciences and Geophysics at the University of Leoben in cooperation with Dr. Zaccarini.

1.2.2.4 X-ray fluorescence spectrometry (XRF)

X-ray Fluorescence Spectrometry (XRF) has been used as a research tool for the analysis of major and minor trace elements in geological materials. The major elements were analyzed by a BRUKER SRS 3400 at the Chemistry Department of Research and Development Departments in RHI Technology Center Leoben. Hand specimens (about 1000-2000 g weight) of selected samples were crushed and pulverized in an automatic agate mortar to obtain homogeneous and representative rock powders. Samples are prepared by fusion with lithiumtetraborate ($Li_2B_4O_7$) flux. This bulk was heated and casted to tablets to be measured automatically afterwards.

1.2.2.5 Inductively coupled plasma mass spectrometry (ICP-MS)

Inductively Coupled Plasma Mass Spectrometry (ICP-MS) is a mass spectrometry method that is highly sensitive and capable for the determination of a wide range of metals and several non-metals at concentrations below one part in 10^{12}. It is based on coupling together an inductively coupled plasma as a method of producing ions (ionization) with a mass spectrometer as a method of separating and detecting the ions. ICP-MS is also capable of monitoring isotopic speciation for the ions of choice.

Trace and rare earth element analysis, stable and radiogenic isotope analysis were carried out with the following analytical equipment: HR-ICP-MS (Finnigan Element II), JY38S ICP-OES, TIMS (Finnigan Triton TI), stable isotope mass spectrometry (Finnigan MAT-252), and CF-IRMS (Finnigan Delta Plus XP) which equipped with Gas Bench II, Flash EA, and TC/EA. These instruments are capable for high precision analysis of major, trace and rare earth elements, stable O-C isotopes, and radiogenic isotopes of Rb-Sr, Sm-Nd in the State Key Laboratory of Mineral Deposit Research at the University of Nanjing, China in cooperation with Prof. Dr. Shao Yong Jiang. The data derived from hand picked crystals using a dental drill.

1.2.2.6 Atomic absorption spectroscopy (AAS)

Atomic Absorption Spectroscopy (AAS) is another common method to specify the element composition especially trace elements of minerals and rocks. The spectrometer consists of a light source, an atomization unit (flame, graphite tube etc.), a monochromator and a detector. In atomic absorption spectroscopy (Maxwell 1968, McLaughlin 1977 and Welz & Sperling 1997) a solution of the sample is sprayed into a flame-less graphite furnace, causing the compounds present in the solution to dissociate into their constituent atoms. The atom-absorption depends on the nature of free atoms to absorb photons of certain energy which thereby exchange in higher energy levels. “The absorption occurs at the same wave lengths as the atoms emit light. The heating-rate (by an electric current around 400 A and up to 3000°C) and the temperature-dispersion in the graphite furnace are decisive for the quantitative atomization of an element. Typical concentrations range in the low mg/l range. The method is based on the absorption of radiation of element-specific wavelength, which results in well-defined spectra. Each element needs a different lamp to produce its characteristic radiation. The total amount of light absorbed is measured and, by comparison with the standards, element concentrations can be calculated. The analysis ideally requires several microliter sample material. The detection limit for the graphite furnace AAS (Analyst 3030 Perkin-Elmer) is 0.1 ppm for Ca, 0.01 ppm for Na and Mg and 0.05 ppm for K (Dünkel 2002)”.

For the implementation of an atomic absorption measurements to determine the chemical composition of the whole-rock and mineral samples, the samples material are first crushed by a hammer and the grains with a size around 1-2 mm are screened out. These grains are several times cleaned with distilled water and dried. A quarter of homogenized material is

selected and put in an agate mortar. Around 0.2 g. of milled samples (using fine balance Mettler model AE 163) with 1-2 ml perchloric (70-72%) and 10 ml hydrofluoric (48%) acid are put in a crucible. Then the crucible is placed on a sandbathing heats up until the last components in solution decreased. After a brief cooling-off period, 2 ml hydrochloric acid (36-38%) with double distilled water is added in the crucible and put to the calibration markings at 50 ml. For the analysis of Mg and Ca, a 100-fold dilution was necessary (Welz & Sperling 1997).

1.2.2.7 Fluid inclusion analysis

Fluid inclusions in general can be analyzed by a variety of methods. This analysis can be divided into destructive and non-destructive techniques, such as microthermometry, crush-leach and Raman spectroscopy (Reßler 2007).

1.2.2.7.1 Ion chromatography (IC)

Ion chromatography is a process that allows the separation of ions and polar molecules based on the charge properties of the molecules. This method is applied to analyze the extracted fluid inclusions using Crush and Leach technique. “A Dionex system (DX-500) with a micro membrane suppressor was used. The improved signal to the noise ratio obtained by this method gives the Dionex system detection limits, which are an order of magnitude better than in conventional systems without autosuppression. For the analyses of the anions it is important that very low contents of iodide (in the range of 0.x ppb) can be analyzed by means of the Dionex amperometric detector. For standard runs a 25 ml sample loop was used except for I (500 ml). At these conditions detection limits were as follows (ppb): F: 5, Cl: 100, Br: 10, I: 0.1, SO_4: 10. To improve detection limits for Br larger sample loops (100 ml) were used when necessary. Chromatograms were automatically integrated although sometimes manual integration was necessary. Accuracy was tested by running standards and turned out to be at 5% for element ratios (Na/Br, Cl/Br). The cations were analyzed by a Dionex DX-120 system (Kaiser 2005).”

The “Crush and Leach” technique includes the analyses of cations and anions in an aqueous fluid obtained from all inclusions extracted from the samples by crushing (e.g. Gleeson 2003). The technique obtained the term “Crush and Leach” because of crushing the samples in an agate mortar and the following leaching process. Therefore, it is a bulk fluid analysis. The technique, as first described by Roedder (1958) and Roedder et al.

(1963), involves crushing samples under vacuum, collection of the volatiles released, leaching the exposed inclusion with a known amount of solvent, which is then analyzed (e.g. Banks & Yardley 1992). Aim of this investigation is to detect parts not bound to the lattice because they present the original composition of the fluids. The total content of the analyzed elements in the rocks is generally higher than the leached part. During analyze of carbonates by leaching with DDW only univalent cations (Na^+ and K^+) and anions (Fl^-, Cl^-, Br^-, I^-, NO_3^-, SO_4^{2-}) can be analyzed, because they show no adsorption-occurrences. Anyway the most important bivalent cations (Ca^{2+}, Mg^{2+}, Fe^{2+}) have no significance in fluid inclusions in carbonates because of the contact of the fluid with carbonatic host minerals. The objective of this technique is to get information where and how the plaeo-fluids receive their salinity. To analyze the inclusion fluids a modified technique described by Botrell et al. (1988) was used. The "Crush and Leach" technique has been used successfully to develop a genetic model of the "Veitsch type" sparry magnesite by Prochaska (2000a, b). Generally inclusions in sparry magnesite, late dolomite, limestone host rock, talc and quartz were analyzed.

The material must be first washed and cleaned with a brush and then dried. After drying, the sample was crushed to a grain size between 0.25 and 1 mm and cautiously cleaned, any impurities were removed. These grains are cleaned with double distilled water (DDW) until the water was free of electrolytes and dried for a second time at a temperature of 50°C. One gram of dried material was selected and put in an agate mortar. With 5 ml double distilled water (DDW) the sample was crushed 2 min by hand. During this process the fluid inclusions were crushed and the entrapped fluids went into solution. Later, the resulting suspension was extracted with a syringe equipped with a special filter.

1.2.2.7.2 Microthermometry

Microthermometry is the most important analytical technique for characterizing fluid inclusions. Microthermometric analysis of fluid inclusions provides an estimate of fluid trapping temperature and of fluid density and bulk composition. Microthermometric measurements were carried out on doubly polished thick sections which is removed from the glass plate, using a polarization microscope (an Olympus BX 60 with adapted 40X and100X LWD objective) equipped with a Linkam MDS 600 programmable freezing-heating stage and a Nokia445Xpro monitor digital photo camera and image analysis system. The stage is cooled with liquid nitrogen and heated with electricity. The stage has

a temperature range from –196 C to +600 C. The cooling-heating stage was calibrated by replicate measurements of synthetic fluid inclusion standards in quartz (containing H_2O and CO_2-H_2O gas inclusion), i.e. the triple point of pure CO_2 (-56.6 °C), the melting point of pure H_2O (0.0 °C) and the critical homogenization of pure H_2O (374 °C). The phase transition of fluid components observed during heating and cooling provide information about pressure, temperature and composition/salinity of the inclusion. "The phase transitions are expressed in melting and homogenization temperature of the inclusion" (Reßler 2007).

1.2.2.8 Raman Spectroscopy

Raman spectroscopy is the measurement of the wavelength and intensity of inelastically scattered light from molecules. The Raman scattered light occurs at wavelengths that are shifted from the incident light by the energies of molecular vibrations. The mechanism of Raman scattering is different from that of infrared absorption, and Raman and IR spectra provide complementary information. Typical applications are in structure determination, multicomponent qualitative analysis, and quantitative analysis. Raman spectroscopy and associated imaging techniques are generally non-destructive, and can be used to identify a wide range of materials, including minerals and gemstones (Hope et al. 2001). Raman spectroscopy is a sensitive technique which requires minimal sample preparation and can be used on massive specimens from lump ore to fine powders and liquids. In addition Raman spectroscopy can be used to identify fluids within inclusions. Most gases, e.g. CO_2, H_2S, CH_4, N_2 and fluids, e.g. H_2O, H_2S are Raman active.

Raman spectroscopic measurements were performed with a LABRAM (ISA Jobin Yvon) instrument at the Chair of Mineralogy and Petrology at the Department of Applied Geosciences and Geophysics in cooperation with Dr. Bakker. The laser beam is focused through an Olympus BX 40 microscope onto the object of interest, either mineral or fluid, using 40x or 100x magnification combined with a confocal optical arrangement, enabling a spatial resolution in the order of one cubic micrometer. The apparatus has a 100 mW frequency-doubled Nd-YAG laser with 532 nm wavelength (green), which is reduced to 38 mW at the measured object. A portion of the scattered light is collected through the microscope and focused onto a diffraction grating. The grating selects the desired region of the Raman spectrum and reflects this onto a Peltier-cooled, CCD matrix detector.

1.2.2.9 Laser-ablation MC-ICP-MS isotope analysis

Laser-ablation MC-ICP-MS (LA MC-ICP-MS) is a microanalytical technique for the determination of trace elements and isotopes in solid materials with a growing number of applications in fields such as geochemistry, materials science, forensics and environmental studies. LA MC-ICP-MS combines the micrometer-scale resolution of a laser probe with the speed, sensitivity and multi-element capability of MC-ICP-MS, and rivals other microbeam techniques such as the proton microprobe and secondary ion mass spectrometry. A laser ablation module connected to an MC-ICP-MS instrument represents just one of a number of different sample introduction systems used in MC-ICP-MS analysis (Guillong 2004). A pulsed laser beam is used to ablate a small quantity of sample material which is transported into the Ar plasma of the MC-ICP-MS instrument by a stream of Ar carrier gas. The laser beam can be thought of as a "light chisel" which interacts with the solid sample material by a physical process (ablation) that generates very fine solid particles leaving behind a minute ablation crater (in the order of tens of μm in diameter).

In most instances, sample preparation for LA ICP-MS analysis is very simple. As long as the sample fits into the sample chamber, it may not even need a perfectly flat or polished surface. Most commonly, samples are in the form of epoxy mounts (e.g. rock fragments or mineral grains), pressed powder briquettes (for bulk rock analysis) similar to those used in XRFS, or petrographic thin-sections similar to those used in electron microprobe analysis. LA experiments were conducted on ~50-μm-thick thin sections prepared for electron microprobe work. In situ Sr isotope analyses were obtained at the Geochronology Division of the Department of Lithospheric Research in cooperation with Dr. Klötzli (University of Vienna) using an MC-ICP mass spectrometer (Nu PLASMA HR MC-ICP-MS) coupled to a state of the laser-ablation system (New Wave 193SS) and an optics system.

1.3 Magnesite as mineral and ore

Magnesite ($MgCO_3$) is an important industrial mineral with a maximum magnesia, MgO content of 47.8% (CO_2 52.2%) and is the world's most important source of magnesia, because it provides magnesia (MgO) upon calcination. In carbonate terrains magnesite is often rock forming and the main mineralic constituent of largely monomineralic masses. Magnesite dose not ordinarily form good crystals but can make up a substantial portion of

some rock types. Magnesite has the same crystal structure of calcite, hence its inclusion into the calcite mineral group. Many of properties of magnesite are either identical or similar to those of calcite or dolomite (Wilson & Ebner 2005). "The physical characteristics of magnesite are (Wilson & Ebner 2005):

- Colour is white or grey, also tinted yellow or brown.
- Lustre is vitreous.
- Trancparency crystals are translucent to transparent only in individual crystals.
- Crystal system is trigonal.
- Crystal Habits are usually massive forms such as lamellar, fibrous and coarse to fine grained rocks. Crystals are extremely rare, but when found are in the form of rhombohedral or hexagonal prisms.
- Cleavage is perfect in three directions forming rhombohedrons.
- Fracture is conchoidal to uneven.
- Hardness is 4–4.5.
- Specific gravity is approximately 3.0 (average).
- Streak is white.
- Associated Minerals calcite, dolomite, aragonite, strotianite and serpentine.
- Other characterictics: effervesces easily only in hot dilute hydrochloric acid.
- Best field indicators are crystal habit, reaction to acid, occurrence and cleavage."

"Magnesite ($MgCO_3$) as mineral belongs to the group of rhombohedral carbonate minerals that include also calcite ($CaCO_3$), siderite ($FeCO_3$) and rhodochrosite ($MnCO_3$). In these minerals the cations can be substituted in the crystal lattice by each other. Minerals with cations of similar ion radii (e.g. Fe^{2+}, Mg^{2+}, Mn^{2+}) form complete solid solution series. When difference is larger (e.g. Ca^{2+}) only limited substitution is possible at the end of the $MgCO_3$-$CaCO_3$ series. Within the lattice of dolomite Ca^{2+} and Mg^{2+} alternate in a regular manner. FeO and MnO contents in magnesite are the result of cation substitution in the lattice and they can not be removed by upgrading prior to calcining. On the other hand the higher contents of CaO in magnesite ore are the result of an admixture of dolomite that

may be the relict of the unmineralised host rock or later formed dolomite in veins or as grains inside the rock. They can be removed by physical upgrading (Wilson & Ebner 2005)."

"Other chemical impurities of the magnesite ore, often limiting the technical applications, are SiO_2 due to mineralogical admixture of quartz or chalcedony, silicate minerals like talc, sepiolite, enstatite and clay and micaceous minerals: the latter group is responsible for the Al_2O_3-content. Other commercially important magnesium-bearing minerals are dolomite, $CaMg(CO_3)_2$ which supplies the aggregate industry and chemical industries; brucite, $Mg(OH)_2$ which is used in the production of both caustic and sintered magnesia; olivine, $(MgFe)_2\ SiO_4$, which serves the refractory and heat storage industries and talc, $Mg_3Si_4O_{10}(OH)_2$ which is utilised widely as a filler in paper and plastic and as an ingredient in cosmetics, and serpentine $Mg_3Si_2O_5(OH)_4$ (Wilson & Ebner 2005)".

Magnesite is used to produce magnesium metal and caustic, dead-burned and fused magnesia. Caustic magnesia is calcined below 900°C and is chemically active because of its small (1-20 μm) crystal size (Canterford 1985). Caustic magnesia, and derived tertiary products are used in chemical (fertilizer) and industrial applications, construction (cement), animal foodstuffs (cattle feed) and environmental rehabilitation (water treatment), among other uses. Dead-burned magnesia is calcined above 1200°C and is chemically unreactive due to its larger crystal size (30-120 μm). Dead-burned and fused magnesia are used mostly in high-performance refractories as a refractory lining in steel-making furnaces (Canterford 1985). Magnesium metal has a wide range of end uses, mostly in the aerospace and automotive industries. The automotive market for magnesium metal is expected to expand rapidly with current efforts to reduce the weight of vehicles to improve fuel economy and reduce harmful emissions. Raw magnesite also has been marketed as a fertilizer component to reduce magnesium deficiency in soil and to counteract acidic rainfall (Weiss & Horn 1989).

1.4 Types and origin of magnesite

"Magnesite as mineral and ore occurs in two mineralogical modifications (Wilson & Ebner 2005):

- Fine to coarse grained crystalline sparry magnesite with crystals up to size of some cm.

- Cryptocrystalline magnesite, sometimes also referred as amorphous with crystal in the range of 1-10 μm."

Classification of magnesite deposits traditionally has been based on "types" named after localities in Austria. "Magnesite as mineral occurs in various geologic environments but as ore it forms three main types of deposits (Wilson & Ebner 2005).

- Sparry (crystalline) magnesite hosted in carbonate rocks: Veitsch Type
- Cryptocrystalline magnesite hosted in ultramafic rocks: Kraubath Type
- Cryptocrystalline precipitation in young clastic freshwater sediments: Bela Stena Type"

1.4.1 Sparry magnesite deposits-Veitsch Type

The type deposit of sparry magnesite is located at Veitsch in Austria/Styria within the Veitsch Nappe of the Austroalpine Greywacke zone. The Veitsch type magnesite hosted in carbonate rocks, mainly dolomitic, represents marine, shallow water environments of Proterozoic and Paleozoic ages. Sometimes it is associated with pelite, sandstone, conglomerate and basic volcanics and often it occurs in metamorphic terrains. The sparry magnesite in the deposits is white to black, grey, blue, reddish and fine to coarse grained, with mono- and bipolar crystal growths. Often it displays decorative pictures like box and rosette texture, pinolitic texture (large elongated cm-sized light magnesite crystals in a fine grained dark matrix) or zebra banding. Veitsch type sparry magnesite forms layered and lens shaped deposits and irregular stocks. Often the layered texture and the magnesite-dolomite boundaries are angular to the sedimentary bedding that mostly can hardly be recognized. Often there are transitions of the ore body to dolomite and the host limestone (Wilson & Ebner 2005).

1.4.2 Cryptocrystalline magnesite deposits

There are two major types of cryptocrystalline ultramafic-associated magnesite deposits/occurrences which are associated with ultramafic rocks: the Kraubath Type and Bela Stena Type.

Kraubath type formed by the reaction of CO_2-rich meteoric water (infiltration type) or CO_2-rich hydrotermal crustal fluids (hydrothermal type) associated with ultramafic rocks.

In Bela Stena type cryptocrystalline magnesite precipitated from hydrothermal water or after transportation of fine clastic magnesite materials or Mg^{2+} rich solutions from ultramafic terrain to a freshwater basin (Fig. 1. 1).

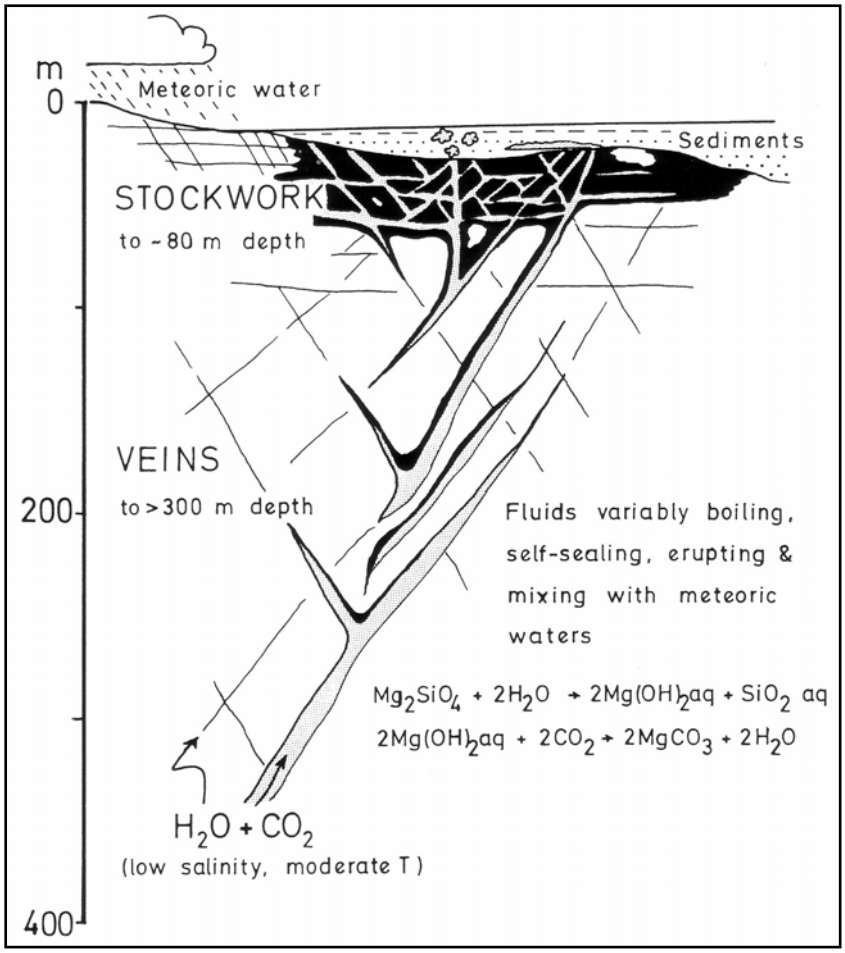

Fig. 1. 1 Types of cryptocrystalline magnesite deposits (modified after Pohl 1990).

Kraubath Type

The type deposit is situated in the ophiolitic ultramafic massif of Kraubath (Austria/Styria), which is part of the Middle Austroalpine crystalline complex of the Eastern Alps; Tollmann 1977, Frisch & Neubauer 1989, Neubauer & Frisch 1993). Important host lithologies of Kraubath type magensite are olivine rich rocks (dunite, peridotite) of ophiolite zones or other ultrabasic magmatic intrusive complexes. Kraubath type magnesite is snow white with tints to yellow, yellow or buff and occurs in cryptocrystalline texture with conchoidal fracture, sometimes cauliflower shaped and with transitions to fibrous and granular types. Massive bodies, veins, stockworks and layers within the ultramafic rocks are the main shapes of the deposit. Mineralisations in shallow niveaus (extending only

some 10 m to the depth) occur close to the recent or paleosurfaces in networks or layers or as thicker veins rarely extending some km in strike and some 100 m to the depth. In comparison to sparry magnesite deposits the potential of cryptocrystalline magnesite deposits is smaller (up to several tens of 10^6t; Wilson & Ebner 2005).

Bela Stena Type

For the first time the Bela Stena Type has been described in Serbia, fomer Yugoslavia (Ilic 1968). The magnesite is cryptocrystalline with conchoidal fracture (bone magnesite) and withe, yellow or buff. Magnesite layers (up to some m thick) and nodules occur mainly within clastic lacustrine sediments of Tertiary age in the neighborhood of ultramafic rock complexes (Wilson & Ebner 2005).

2. Gological structure of the Eastern Alps and position of sparry magnesite deposits

In a geographical sense the Alps are divided into the E-trending Eastern Alps and the arc of the Western Alps, divided by the Rhine valley south of the Bodensee (Lake Constance) and its southward extension (Fig. 2. 1). The Eastern and Western Alps display a fundamentally different geological structure, geological development and in part a distinct geomorphology (Neubauer et al. 2000). The geological make-up of the Eastern Alp, Western Carpathians and the basement units of the Pannonian Basin, together with all Tertiary volcanic phenomena of the Inner Carpathian volcanic arc, are the result of the Mesozoic-Cenozoic Alpine orogeny. Nevertheless, this area also includes numerous pre-Alpine structural elements. During the last decade the geodynamics and minerogeny of all these features has become well known (Ebner et al. 2000). The Eastern Alps are a complex fold and thrust belt formed in a collisional setting during the Alpine orogeny in late Mesozoic and Cenozoic times. The internal parts of this belt comprise the basal (Penninic) units which are overthrusted by the Austroalpine nappe system (traditionally summarized as the Lower, Middle and Upper Austroalpine systems). All these units include a ± metamorphosed pre-Alpine basement and Permomesozoic cover units (Tollmann 1977). Nevertheless, Frank (1987) and Schmid et al. (2004) provides other models in which the Austroalpine nappe system is subdivided within a Lower and Upper thrust system. Due to new insights to the metamorphic history, Alpine paleogeography and kinematic, the Middle Austroalpine is strongly reduced (Frank 1987) or even cancelled (Schmid et al. 2004).

All Veitsch-type magnesite deposits in Austria occur in the Austroalpine Paleozoic basement units. The Austroalpine units represent a continental basement-cover nappe pile, which received its essential internal nappe structure during the Cretaceous orogenic events (Ratschbacher 1986, Dallmeyer et al. 1998). They can basically be divided into the Central Eastern Alps with dominant basement exposures and the Northern Calcareous Alps with predominant Permian to Cenozoic cover sequences. The Austroalpine units subdivided into Lower, (Middle) and Upper Austroalpine nappe complexes in the Eastern Alps (Fig. 2. 2), the subdivision is easily applicable over large portions of the Austroalpine nappe pile, which is bound to the south by the Periadriatic fault zone. The SAM (southern limit of Alpine metamorphism, Hoinkes et al. 1999) situated in more southern parts of the

Austroalpine thrust system displays significant regional differences. This denomination reflects the present tectonic superposition, originally the upper sub-unit occupied the southernmost, the lower the northernmost position.

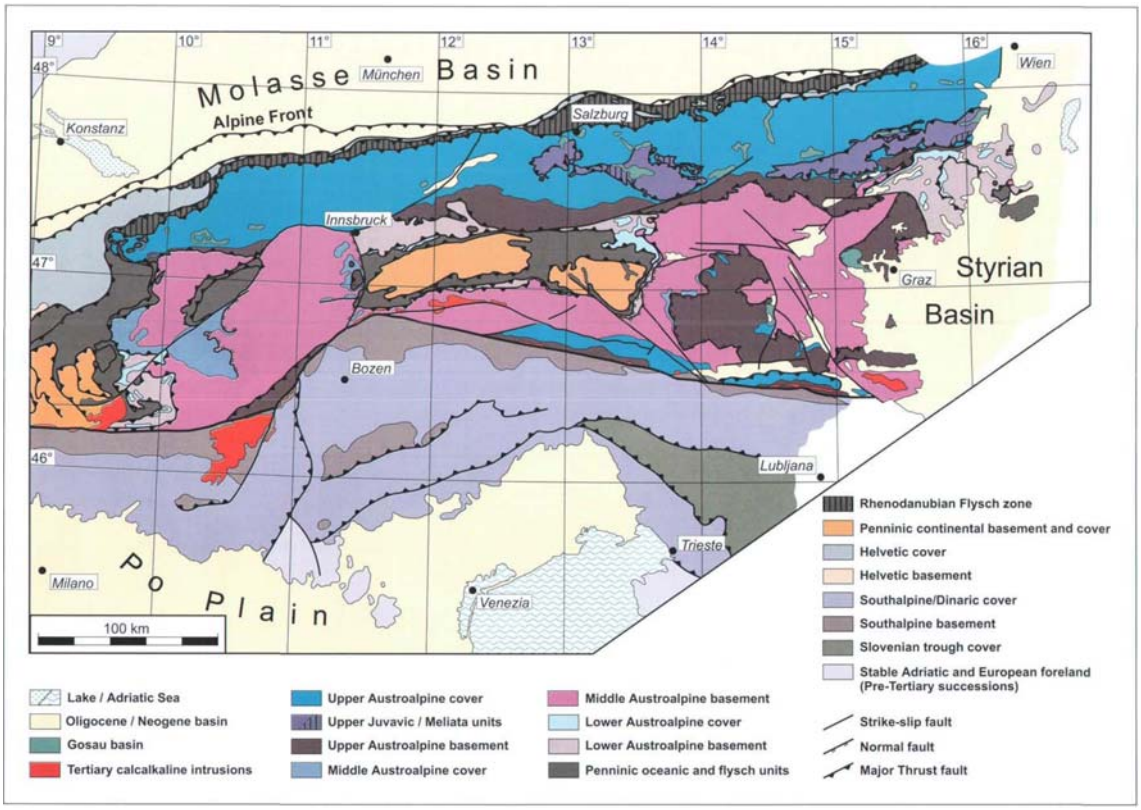

Fig. 2. 1 Simplified geological overview of the Eastern Alp (Neubauer & Höck 2000).

Cover sequences of the Austroalpine basement include a nearly continuous, conformable Late Carboniferous to early Late Cretaceous succession of continental molasse, rift, carbonate platform, shelf margin and pelagic formations. The principal initial rift phase began during the Permian and resulted in a rapid tectonic subsidence during the Triassic, when a passive continental margin was formed. The Austroalpine system was closed during Eo-Alpine (Cretaceous) nappe tectonics (Schmid et al. 2004).

Major basement units of the Upper Austroalpine are the Graywacke zone, the Paleozoic of Graz and the Gurktal thrust system (Schönlaub & Heinisch 1993). They are continuous fossiliferous Ordovician to Early/Late Carboniferous sequences affected by a late Variscan and/or Cretaceous very low to low-grade metamorphic (greenschist facies) overprint (Neubauer et al. 2000, Ebner et al. 2008b).

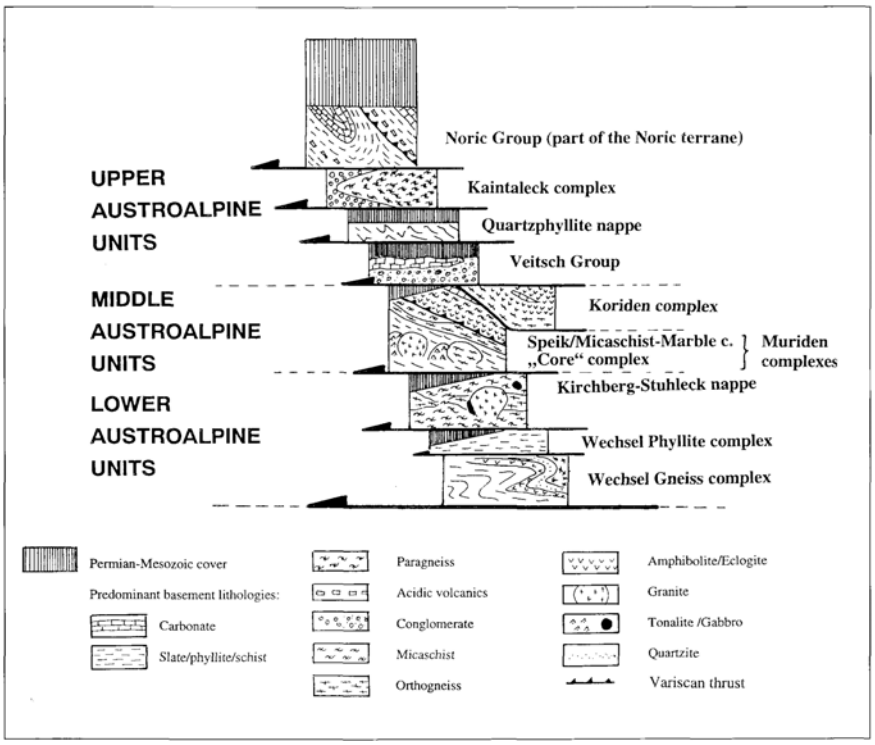

Fig. 2. 2 Tectonostratigraphy within the Austroalpine units of the Eastern Alps (Neubauer & Handler 2000).

The Graywacke zone nappe complex and the overlying Northern Calcareous Alps are located along the northern leading edge of the Austroalpine nappe complex. These Upper Austroalpine units were derived from an originally southeastern paleogeographic position (Neubauer et al. 2000). Most Austrian sparry magnesite deposits are found in Upper Austroalpine sub-units. E.g.: Western Graywacke zone: Hochfilzen; Eastern Graywacke zone/Veitsch nappe: Sunk/Hohentauern, Wald/Schoberpass, Oberdorf/Laming, Veitsch; Graz Paleozoic: Breitenau. Only the Radenthein deposit occurs in the Middle Austroalpine Crystalline complex (sensu Tollmann 1977; Fig. 2. 3)

2.1 Graywacke zone

Parts of the Graywacke zone (Noric nappe) are the Paleozoic basement of the Tyrolian parts of the Calcareous Alps. Fundamental overviews on the geology and tectonostratigraphy of the Graywacke zone were given by Schönlaub (1982), Neubauer et al. (1994), Schönlaub & Heinisch (1993) and Ebner et al. (2008). The rock series of the Graywacke zone range from the Ordovician to the Carboniferous and comprise carbonates, metapelites and metamorphosed acid to basic volcanics. The grade of metamorphism is

generally of lower greenschist facies both in the Variscan and in the Eoalpine tectono-metamorphic event (Ebner et al. 2008b).

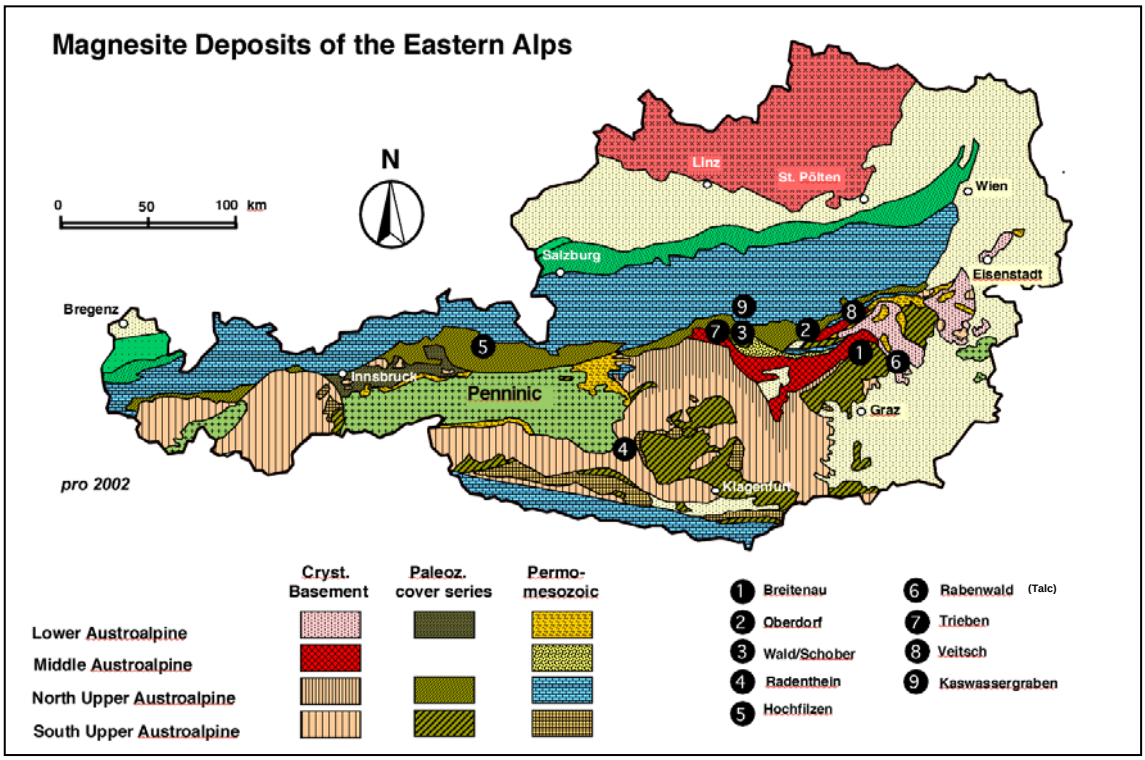

Fig. 2. 3 Position of important magnesite deposits/occurrences in the Eastern Alps of Austria (Prochaska 2000b). The No. 2, 3, 7 and 8 belong to the Veitsch nappe.

In the Eastern Graywacke zone carbonate-hosted sparry magnesite mineralizations occur exclusively in Lower Carboniferous strata of the Veitsch nappe which is affected only by low-grade Alpine metamorphism (Ratschbacher 1984, Prochaska 2000a,b and Ebner et al. 2008b). In the Eastern Graywacke zone sparry magnesite mineralizations of Veitsch type and its equivalents are located in a thin nappe comprising of Lower and Upper Carboniferous rocks between a minor Permo-Triassic cover on the Middle Austroalpine metamorphics underneath and some other Alpine nappes of Paleozoic and metamorphic rocks (Fig. 2. 4; Schönlaub 1979, Neubauer et al. 1994). Some important sparry magnesite mineralizations in the Veitsch nappe of the Eastern Graywacke zone gathered in the Metallogenetic Map of Austria as the “Magnesite-Talc district”, Veitsch nappe (Weber 1997) are St. Martin/Grimming, Lassing, Hohentauern/Sunk-Trieben, Wald/Schoberpass, Häuselberg/Leoben, Oberdorf/Laming and Veitsch. Beside the type deposit of Veitsch, the operating mines around Oberdorf, Wald/Schoberpass and the closed mine of Hohentauern/Sunk provide excellent outcrops.

2.1.1 Veitsch nappe (Veitsch Group)

The Veitsch nappe situated at the base of the Graywacke zone is one of the Alpine (Createceous) nappes/imbrication structures forming the Paleozoic basement of the Upper Austroalpine Calcartaeous Alps (Fig. 2. 4; Tollmann 1977, Neubauer et al. 1994, Schönlaub 1979). Sedimentation of the Veitsch nappe began as a post-orogenic molasse like marine formation within the late Viséan after deformation and metamorphism ("Bretonic phase") of the internal basement zones presently included in the Eastern Alps (Flügel 1977, Ebner 1992, Ebner & Prochaska 2003, Ratschbacher 1984 & 1987a, Ebner et al. 2007 & 2008).

The Veitsch nappe contains a continuous stratigraphic section that includes fossil-bearing Early and Late Carboniferous formations (Ratschbacher 1984, 1987a, Ratschbacher & Nievoll 1984, Krainer 1992, Nievoll 1983) extending into possibly Permian clastic sequences (Neubauer & Vozarova 1990). This foreland basin was linked to some other more southerly situated pelagic Austroalpine and Southalpine Carboniferous domains. The latter were affected by the Variscan orogeny during the Carboniferous orogenic phases (Ebner 1992) whereas the Veitsch zone underwent exclusively Alpine (Cretaceous) deformation and greenschist facies metamorphism (Ratschbacher 1984 & 1987a, Ebner et al. 2007 & 2008). Neubauer et al. (1994) proposed an assemblage of lithostratigrahic units of the Veitsch nappe as the Veitsch group. Detailed lithostratigraphic subdivisons into formations were only performed in the western part of the Veitsch nappe (Ratschbacher 1984, 1987a).

The Veitsch nappe hosts numerous deposits/occurrences of sparry magnesite and talc. They were outlined as the "Veitsch nappe magnesite-talc district" within the Metallogenic Map of Austria (Weber 1997, Ebner & Prochaska 2001, Ebner et al. 2003 a,b and Ebner & Wilson 2006). A set of lens-shaped magnesite bodies of various sizes can be found in a sequence of sericite schist, graywackes, conglomerates and metatuffs. Upper Tournaisian - Viséan Carbonate units are hosting the magnesite bodies and exhibit marine, shallow water environment. Timing and processes of the magnesite formation have been controversially discussed (Azim Zadeh et al. 2004). A strong argument for an "early" (pre-thrusting) formation is the fact, that magnesite is exclusively occurring in the Veitsch nappe and carbonatic levels of the other nappes are never transformed to magnesite. Another hard fact is that already formed magnesite is included within the Cretaceous nappe structures.

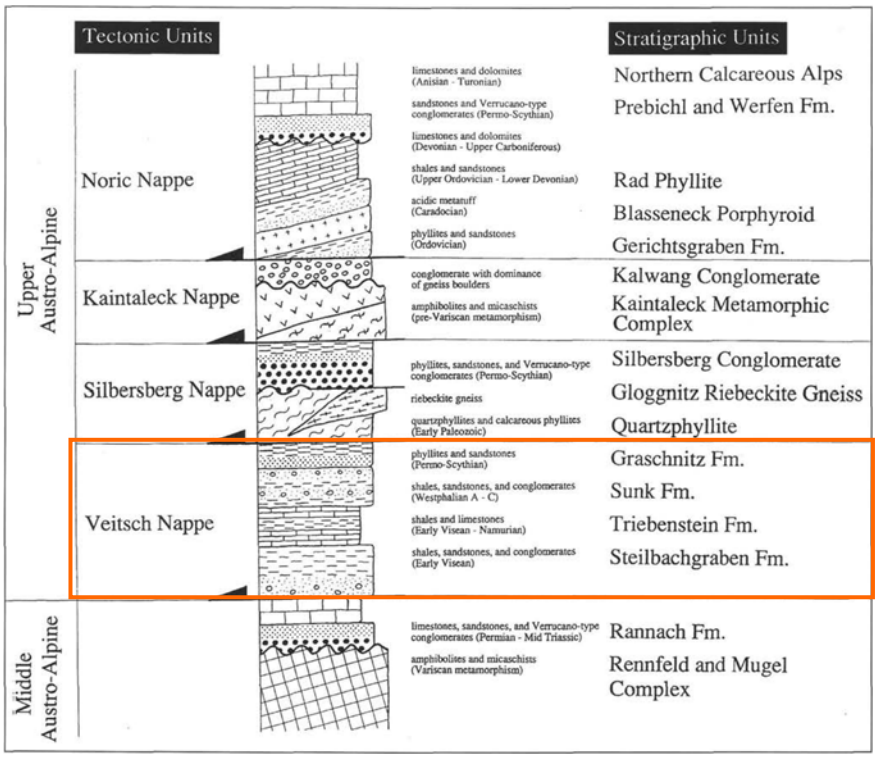

Fig. 2. 4 Tectonostratigraphy and lithostratigraphy within the Cretaceous nappe stuck of the Graywacke zone (Neubauer et al. 1994).

2.1.1.1 Distribution of sparry magnesite deposits/occurrences in the Veitsch nappe and their commercial importance

Most of the numerous Veitsch type sparry magnesite deposits/occurrences in the Eastern Alps of Austria occur in the Graywacke zone. The minerogenetic map of Austria (Weber 1997) exhibits several locations of magnesite mineralization within the Veitsch nappe. Many of them have been exploited in the past (Fig. 2. 5). Some of the magnesite mineralizations are of considerable economic importance (Ebner & Wilson 2006).

Today only the magnesite deposits of Oberdorf/Laming and Wald/Schoberpaß are in operation (Styromgnesit Company). The type deposit of Veitsch nowadays is worked for construction material. After world war II additionally some other deposits were also mined in the Veitsch nappe (year of closedown): Lassing (1964) and Hohentauern/Sunk (1991). The Hohentauern/Sunk deposit is one of the important magnesite deposits in the Veitsch nappe magnesite district of the Eastern Graywacke zone (Weber 1997, Ebner 1997). The following overview of the geotectonic and metallogenic framework of sparry type magnesite mineralization will provide a better understanding of the Hohentauern/Sunk deposit.

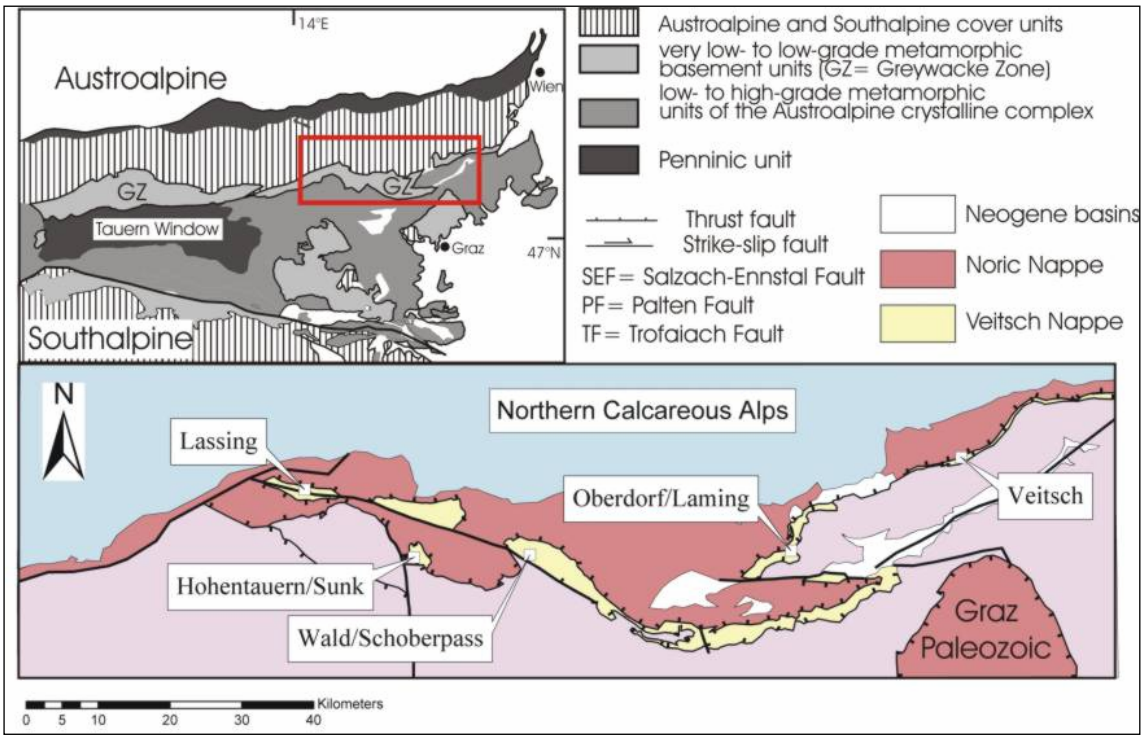

Fig. 2. 5 Geological situation of the sparry type magnesite deposits at the base of the Veitsch nappe of the Eastern Graywacke zone in the Eastern Alps (Rantitsch et al. 2004).

2.1.1.2 Geological and petrological characteristics of the Veitsch type magnesite

The type area of the sparry Veitsch type magnesite deposits which are hosted in Paleozoic carbonatic rocks is in the Province of Styria/Austria. Geological, petrological and geochemical characteristic features for Veitsch type magnesite are summarized by Redlich (1909), Weber & Schroll (1997), Ebner & Prochaska (2001) and Ebner et al. (2004a,b). Characteristically the magnesite forms layers or lenses and irregular bodies within the Late Viséan shallow marine fossiliferous (crinoids, corals, brachiopods) carbonatic host rocks. The regional metamorphic overprint of the host rocks is within the greenschist metamorphic facies of Cretaceous age (Rantitsch et al. 2004). The magnesite has light grey–yellowish grey magnesite crystals (up to cm size) and a coarse to fine grained and mostly pinolitic or banded texture. The matrix of the pinolite is black, fine grained and rich in dispersed organic (graphitic) matter. The pinolite texture is a typical texture with big light crystals, shaped as seeds of pignolians in a black matrix. In the Veitsch type magnesite, seams of dolomite are mostly surrounding the magnesite and magnesite is followed by several generations of dolomite. Large idiomorphic crystals of dolomite in the magnesite (“Rosszähne or teeth of a horse”) are frequent. Chlorite/leuchtenbergite and talc are bound to tectonized zones and marginal parts of the magnesite bodies. Temporarily this

talc was also mined. Sulfide vein mineralizations (tetraedite, chalcopyrite, pyrite) belong to a younger metallogenic event (Weber 1997).

2.2 Genetic models of sparry magnesite deposits

Prochaska (Prochaska in Ebner et al. 2004b) summarizes the individual concepts for mangesite formation in the Veitsch Nappe: "Opinions concerning the genesis of the Austroalpine sparry magnesite mineralizations are inconsistent and discussion about this topic is longstanding tradition. Different genetic models, including a synsedimentary origin or an Eoalpine metamorphic vein-type or metasomatic mineralization have been proposed in the past. There is no consensus about the genetic model and not even about the principal mechanisms for the magnesite mineralization. Starting soon after the discovery of the world's first magnesite deposits in the Eastern Alps after 1850, syngenetic models (e.g. Rumpf 1873, Leitmeier 1917) and epigenetic models (e.g. Koch 1893, Vacek 1886, Redlich 1907) were published. In the 1950's a general trend towards syngenetic and early diagenetic models can be observed (De Llarena 1953, Leitmeier & Siegl 1954). Niedermayer et al. (1989) argued for synsedimentary or early diagenetic genesis for magnesite mineralization in Permian series of the Eastern Alps and extended this model to the Alpine sparry magnesites. Pohl and Siegl presented an extensive overview on the magnesite mineralizations of the Eastern Alps in 1986. Möller (1989) edited a monograph on magnesite summarizing the recent geochemical and mineralogical facts on the "magnesite problem". Earlier workers (Redlich 1907, Petrascheck 1932, Rüger 1939, Clar 1954, Friedrich 1969 etc.) already mentioned a consanguineous origin of the Alpine sparry magnesite and siderite mineralizations. In general they argued for hydrothermal fluids of different origin, such as magmatic or metamorphic fluids of Alpine (Tertiary) age. Nevertheless these concepts never gained general acceptanc."

Accordingly "the formation of Veitsch type deposits is discussed between the extremes of a mainly synsedimentary origin from seawater (possibly in relation with an evaporitic environment) and an epigenetic replacement model with a wide range of parameters concerning source, transport and deposition of Mg (Pohl 1989)".

Syngenetic formation of the sparry magnesite was first thought to have occurred from "warm, saturated solutions of $MgCO_3$ in marine basins" (Rumpf 1873), at the time apparently meaning hydrothermal sources on the sea floor (Pohl & Siegl 1986). Apparently

the first author proposing the possibility of a purely sedimentary or diagenetic origin of magnesite was Leitmeier (1917a,b). Inspired by earlier work on dolomite (Klement 1895) he argued that either magnesite could form by syngenetic replacement of calcite by dolomite and then magnesite, or by direct precipitation of hydrous Mg-carbonate on the sea floor. This would not necessarily imply an evaporitic setting. A purely evaporitic model was advocated by Rosza (1925), in location similar to the Karabogas Bay (Caspian lake) $MgCl_2$-brines could replace limestone (Pohl & Siegl 1986).

Epigenetic, metasomatic replacement of pre-existing carbonate by Mg-solutions was first suggested by Koch (1893). He already described the crinoids replaced by magnesite and the crosscutting relation between country rock and magnesite at the Veitsch deposit. Vacek (1886) had written that the magnesite evidently was younger than its country rocks. Redlich (1907, 1911, 1913) developed a coherent metasomatic model and proposed a genetic relationship of the magnesite and the siderite/ankerite deposits of the eastern Alps. During further development of the metasomatic model, the source question, the type of solution involved and the relation to the siderite deposits were the main topics of interest. Petrascheck (1932) favoured chloridic Mg-Fe solutions derived from andesitic volcanism which is common eastwards from the eastern Alps. Angel (1939) and Angel & Trojer (1953, 1955) proposed the liberation of Mg-solution by the serpentinzation of ultramafics regional metamorphism. Also a metamorphic mobilization of the Mg-solution, but from Paleozoic carbonates rich in biogenic Mg was suggested by Mostler (1973), Haditsch & Mostler (1979) and Morteani et al. (1982). Based on the observation of overthrusting in the Western Graywacke zone, this model implies the stacking of cooler units beneath hotter ones during syn-metamorphic deformation (Pohl & Siegl 1986). Recently Prochaska (2000a,b) proposed a hydrothermal-metasomatic model with evolved evaporitic brines as magnesite forming fluids which circulated in shallow crustal niveaus during a Permoskythian rifting phase.

3. The Hohentauern/Sunk magnesite deposit

3.1 Geographic setting

The Hohentauern/Sunk magnesite deposit is located in Eastern Alps/central Austria (Fig. 3. 1) and approximately 5 km SSW of Trieben in Styria (Fig. 3. 2). Magnesite outcrops are situated on both sides of the Sunk creek about 2 km to the NW of the village Hohentauern. The major part of the deposit is situated SE of the Sunk creek. This part was mined at XIV levels in an open pit and underground operations until 1991.

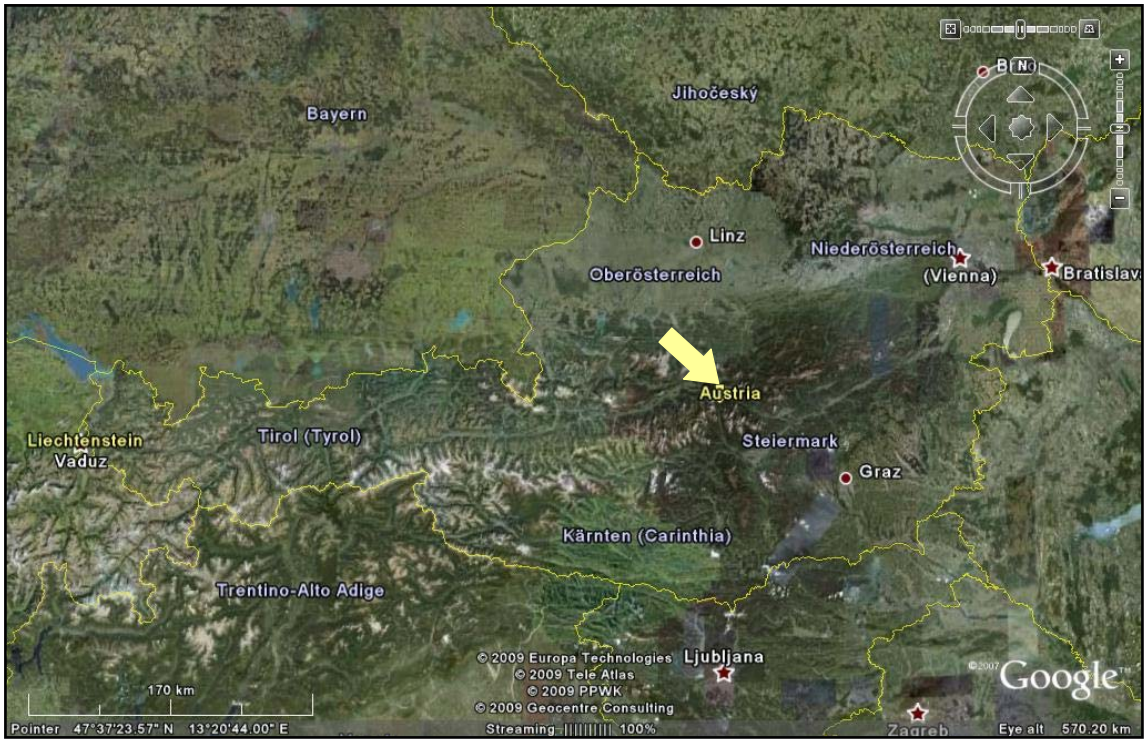

Fig. 3. 1 Geographical overview of the Eastern Alps and Austria (Google Earth, http://earth.google.com) with the position of the Hohentrauern/Sunk magnesite deposit (yellow arrow).

3.2 History of the mine

The Hohentauern/Sunk magnesite deposit had been mined by Veitscher Magnesitwerk AG from 1907 to 1991 underground and in an open pit operation, until it was finally closed in 1997. In total the production was about some 5.5 Mio t magnesite ore and a reserve of >10 Mio. t is still in the deposit. A computer model based on the data of the abandoned mine operation exhibits an initial volume of about some 10 Mio m^3 of the deposit which can be followed along >750 m to the NW (Krisch 2001, Walter 2001).

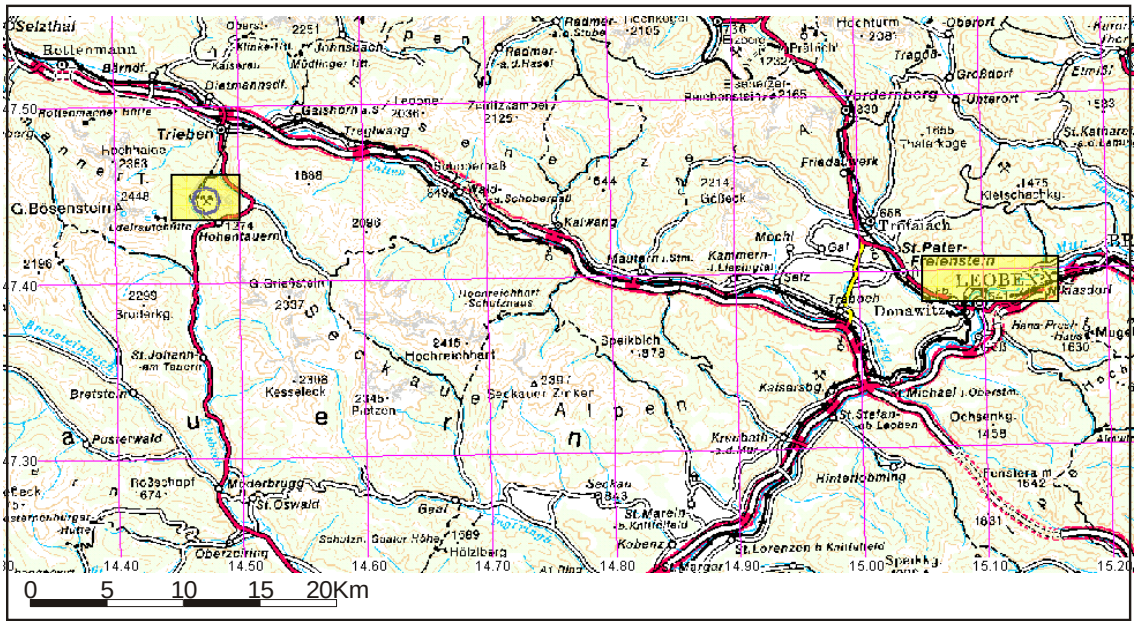

Fig. 3. 2 The magnesite deposit is located about 5 km SSW of Trieben and 2 km to the NW of village Hohentauern.

3.3 Lithostratigraphy, geologic setting and tectonic structure

3.3.1 Lithostratigraphy

The Hohentauern/Sunk magnesite deposit is situated in the Viséan Steilbachgraben Fm. at the structural base (Veitsch nappe) of the Upper Austroalpine Graywacke zone of the Eastern Alps (Styria/Austria). Detailed lithostratigraphic subdivisions of the Veitsch nappe were only done in its western part (Ratschbacher 1984, 1987a). Ratschbacher (1987a) introduced a subdivision of the Carboniferous part of the Veitsch nappe (group) into three formations. From the footwall to the top he distinguished the Steilbachgraben Fm., Triebenstein Fm. and Sunk Fm..

3.3.1.1 Steilbachgraben Fm.

The Steilbachgraben Fm. forms the stratigraphic base of the Veitsch nappe. It consists of a 230 m thick sequence of silty/sandy shales, often rich in organic materials, calcareous shale, dark limestones and dolomite. All lithologies are to be understand as their greenschist metamorphic equivalents. Corals and brachiopods are frequent in dark limestones and calcareous schists. The age of the mineralized carbonate rocks was determined biostratigraphically by corals as Upper Viséan Dibonuphyllum zones 2–3 (Felser 1977). The fossils (corals, crinoids) indicate an environment, predominantly

dominated by normal marine saline conditions. Local intercalations of basic volcanics found at sites outside the Hohentauern/Sunk deposit, derived from tholeiitic intraplate basalts (Prochaska & Ebner 1989). Lenses and layers of magnesite are situated in this sequence. The magnesite, hosted by carbonate rocks, is occurring in irregular stocks, lenses and layers. The massive to thick bedded magnesite is always enveloped by dolomite (Felser 1977, Ebner & Prochaska 2001, Ebner et al. 2003a, b).

3.3.1.2 Triebenstein Fm.

The Triebenstein Fm. is a 50–300 m thick sequence of layered, banded and massive pure limestone, also with crinoids, corals and some greenschists. This formation shows a lensoid geometry and where preserved from tectonometamorphic obliteration. Limestone layers up to a few tens of meters thick are the lateral most persistent members of the Veitsch nappe (Ratschbacher (1987a).

3.3.1.3 Sunk Fm.

The Sunk Fm. is composed of 50–150 m thick siliciclastic rocks and consists preferably of quartz conglomerates, metapelite/-psammite and seams of anthracite/graphite. The Sunk Fm. was dated by plants with Westfalian A–C (Tenchov 1980). Graphite is also enriched in the Sunk Fm., it was mined in the Hohentauern area in the Sunk deposit from 1871 until 1992 (Weber et al. 1997). For other localities which were mined for graphite in the past see Rantitsch et al. (2004).

3.3.1.4 Graschnitz Fm.

At the top, the greyish clastics of the Sunk Fm. grade into the Graschnitz Fm. (Neubauer 1983, Neubauer & Vozarova 1990) that includes light-colored, brownish to reddish sandstones, phyllites and rare quartz breccias. This situation is represented only at one locality S of Kapfenberg. A Permian age is suggested for the Graschnitz Fm. (Neubauer & Vozarova 1990). In other parts of the Veitsch nappe the stratigraphic sequence is not developed in the same way as described above. Nevertheless the sedimentary piles are also dominated by clastic and carbonate lithologies which were sometimes influenced by basic volcanics (Prochaska & Ebner 1989) and carbonaceous materials. The magnesite forms layers, lenses or stocks which are associated with the carbonate rocks.

3.3.2 Geological setting of the Hohentauern/Sunk deposit

The Hohentauern/Sunk magnesite deposit is bordered in the north by the NW-SE normal faults to the Triebenstein-Fm.. Some 100 m south of the deposit there is the Pöls fault, another late orogenic (Tertiary) dextral strike slip fault. In the south the thrust contact to the tectonic footwall, the Middle Austroalpine is hidden by morains. Previous the sequence of the deposit (in the open pit) was regarded as a more or less continuous sequence including three major magnesite niveaus (footwall–middle and hangig wall layers; Redlich 1935, Felser 1977, Kralik & Kiesl 1992). Generally this sequence together with lithological characteristics is shown by Felser 1977. As a result of bed to bed investigations and detailed tectonic analysis the sequence, structure and lithological succession of the deposit was reconstructed in the following way (Azim Zadeh in Ebner et al. 2004b, Azim Zadeh et al. 2005; Fig. 3. 3).

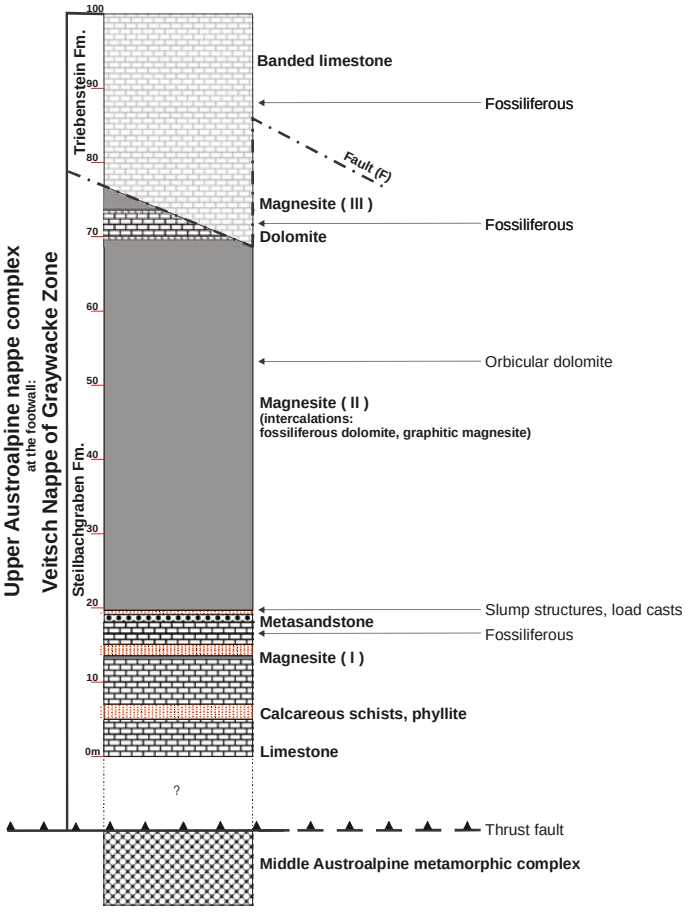

Fig. 3. 3 Stratigraphic sequence of the Hotentauern/Sunk deposit in the open pit (Azim Zadeh in Ebner et al. 2004b, Azim Zadeh et al. 2005).

At the footwall there are about 20 m thick thin bedded limestones, calcareous shists and graphitic shales with the intercalation of a thin magnesite layer (magnesite I). Another intercalation is a layer of medium graind metasandstone, with talc mineralzations in its surroundings. This is followed by 50 m thick bedded to massive sparry magnesite (magnesite II) with some minor intercalations of fossiliferous dolomite, graphitic magnesite and up to 1 m thick stratiform (Siegl & Felser 1973, Haditsch 1968) as well as crosscutting orbicular dolomite. Above magnesite II are some meters of bedded dolomite and magnesite (magnesite III) cut by fault and followed by the Triebenstein-Fm.

At the bottom of magnesite II there are load casts (Fig. 3. 4) and sedimentary flame structures (Fig. 3. 5) as well as a m-thick shaly layer with dm-thick balls and nodules of magnesite in it. This horizon is interpreted as creep horizon of carbonatic material which was mineralized after creeping. This is indicated by lithological boundaries of fine grained dolomite and magnesite which crosscut truncated creep folds (Fig. 3. 6). Sedimentary flame structures formed during creeping and further sedimentation by the sinking of the more dense dolomite or magnesite into the underlying shale which begins to rise through the dolomite or magnesite (Price & Cosgrove 2005).

Fig. 3. 4 Load casts and balls (large load features) on lower beds of magnesite.

Fig. 3. 5 Flame structures associated with load casts at the base of magnesite.

Fig. 3. 6 Load structure as a geopetal fabric at the bottom of the creep horizon in the limestone host rock.

Some layers of gypsum and anhydrite were found by underground drilling within a sequence of magnesite, calcareous schists and dark schists at two sites and along three exploration boreholes in the NW part of the deposit (Fig. 3. 7). In accordance with the generally strike (WWN-SEE) and steep dip of the host rock the layers of gypsum and anhydrite are considered as stratigraphic intercalations. This is also consistent with possibly Carboniferous $\delta^{34}S$ values (Petrascheck 1978).

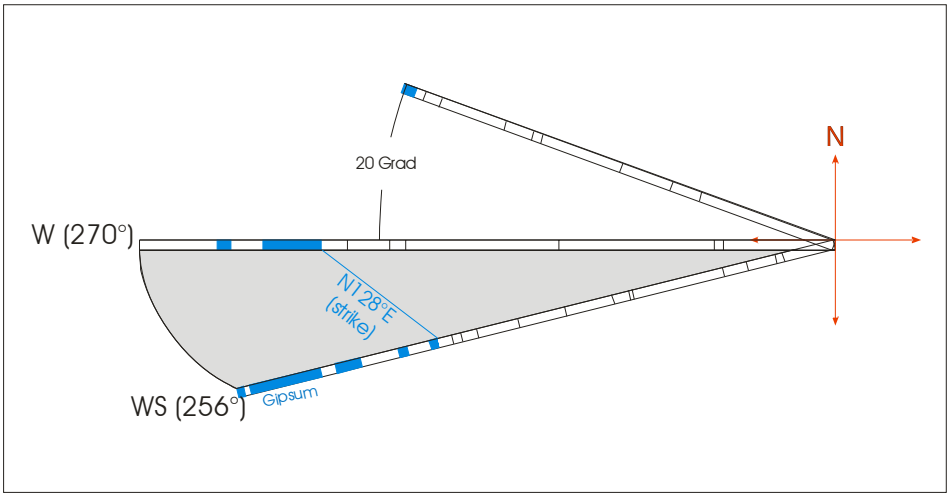

Fig. 3. 7 Three exploration boreholes drilled layers of gypsum and anhydrite intercalated parallel to the magnesite ore body and the host rocks (according to drill mine protocols 1972).

3.3.3 Tectonic structure

The Veitsch nappe shows no Variscan deformation and metamorphism. The tectonothermal overprint is exclusively Alpine (Cretaceous) and controlled by thrusting/folding, followed by the uplift of adjacent metamorphic core complexes. The grade of metamorphism is within the greenschist metamorphic facies (Ratschbacher 1978 Ratschbacher & Klima 1985, Ebner et al. 2008b). Using Raman microspectroscopy for the investigation of graphite the peak temperature was estimated approximately 330±20°C during Cretaceous thrusting and 500±50°C in a following second metamorphic event at the margins of an adjacent exhuming metamorphic dome (Rantitsch et al. 2004). Cretaceous thrusting, folding and metamorphism was followed during the Tertiary by an E-directed lateral extrusion with heavy strike slip and fault tectonics (Ratschbacher et al. 1991).

The major tectonic style at the Hohentauern/Sunk mining area, which also affected the magnesite, includes anticlinal and synclinal folding with axis plunging to the NW (Fig. 3. 8). The deposit continues with a general NW-dip to the Sunk creek where it was mined due to the plunging of the fold axis down to the 250 m level below the creek. The folding style in the study area is related to the deformation of a multilayered sequence. It is controlled by some lithological features such as rock composition, mechanical properties and thickness of each of the constituent layers. Dissimilar properties of host rocks and magnesite ore body formed a polyharmonic fold system with different wavelengths, where multilayers were folded with more than one wavelength.

A π-diagramm of the sedimentary bedding planes is shown in Fig. 3. 9. The fold axis was determined by constructing the π-circle through the two centers of concentrations of the two fold limbs. The pole to the best fit π-circle indicates a plunge of the fold axis with 24° toward NW (309/24, Fig. 3. 9). The fold shape is defined by determining the interlimb angel which is the angle between tangents to the fold surface drawn through the inflexion lines. Generally the interlimb angel in the folding system is about 20°, therefore the fold shape is defined in tight category (Fleuty 1964). The axial surface is inclined (250/40) and doesn't divide the fold domain into mirror symmetric quarter waves, hence the fold is asymmetric (Fig. 3. 9).

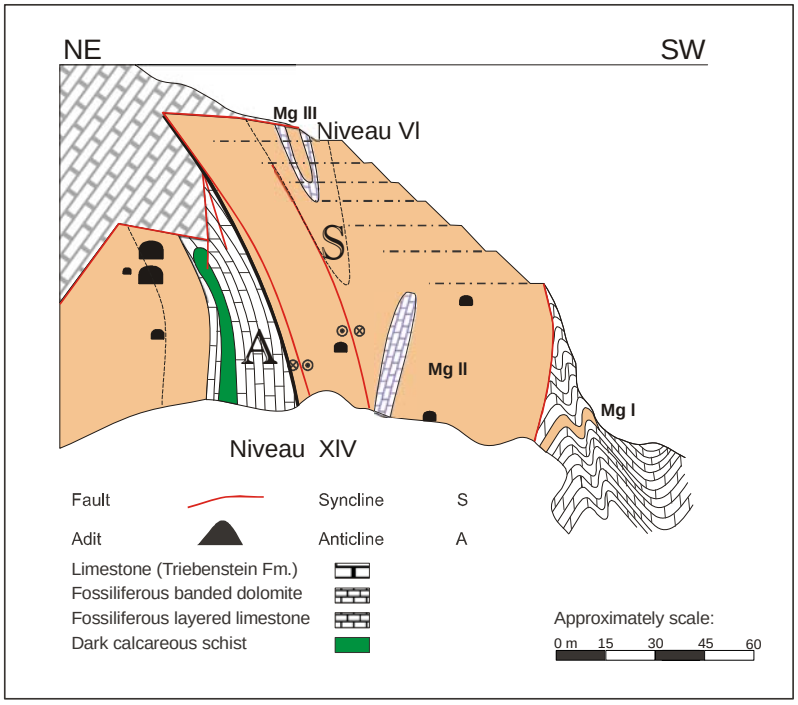

Fig. 3. 8 Anticlinal and synclinal folding system in the open pit of the deposit SE of Sunk creek.

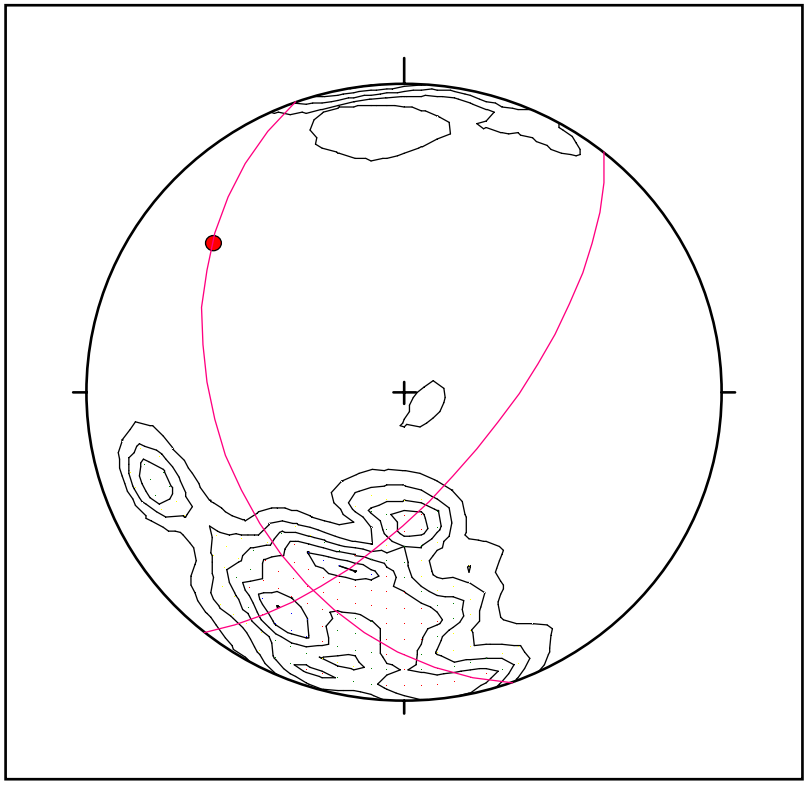

Fig. 3. 9 Contoured version of 161 poles of sedimentary bedding planes of the open pit quarry SE of Sunk creek plotted in equal area projections (Contours at: 1.00, 2.00, 3.00, 4.00, 5.00, 6.00 %; Max. value: 6.15%). The mean π-circle, fold axis and axial surface indicate an asymmetric and tight fold system with axis plunging to the NW.

Also the magnesite bodies were deformed by folding. Host rocks and magnesite of variable thickness and different competent-incompetent layer ductility are compressed at a high angle to, and/or extend in the plan of the layering. The main structures which result from such deformation are boudins (Fig. 3. 10). The three-dimensional cylindrical geometry of the host rock of magnesite boudins is shown in Fig. 3. 11.

Fig. 3. 10 Magnesite boudin in dolomite host rock, which separated by scar fold and brittle failures (Mining level VI).

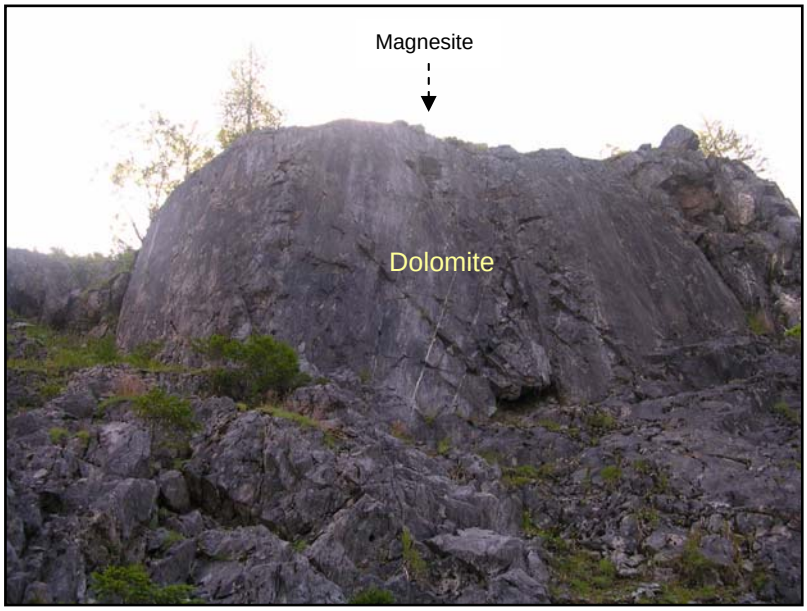

Fig. 3. 11 Three-dimensional geometry of host rock of cylindrical magnesite boudin (Fig. 3. 10) in mining level VII.

The anticlinal and synclinal fold structure is disturbed by 1) ± N-S (strike slip and parallel to Pöls fault) and 2) ± E-W (strike slip and Riedel plane of Pöls fault) trending fault systems (Fig. 3. 12).

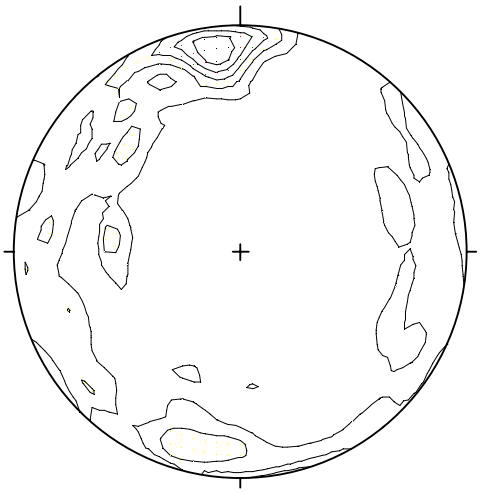

a). Equal area projection of contoured diagram.

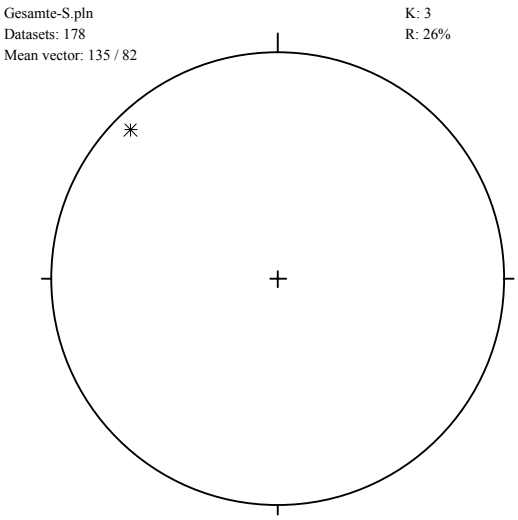

b). Lower hemisphere plot of the mean vector

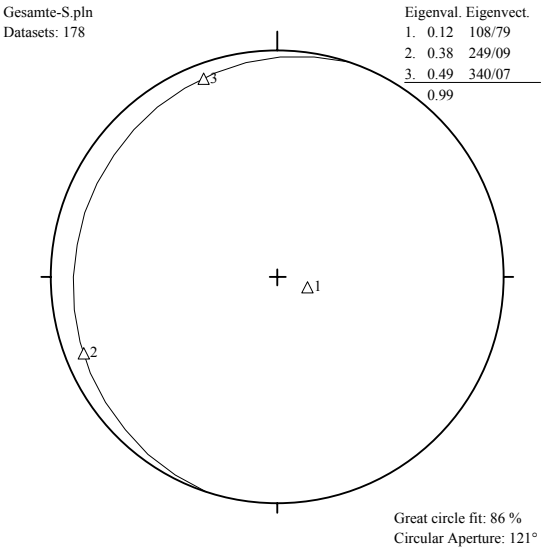

c). Equal area projection of eigenvectors, great circle through eigenvectors with median and greatest eigenvalue and smallest eigenvalue as pole ("best fit great circle").

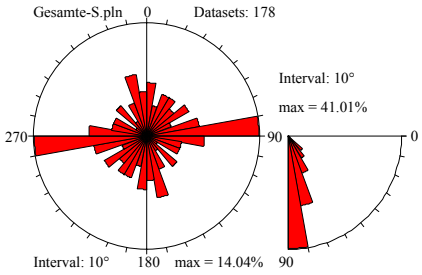

d). Rose diagram of measured fault planes.

Fig. 3. 12 Statistically analyses of the 178 datasets of measured fault planes in Hohentauern/Sunk magnesite deposit.

Equal area projections of 178 data show contoured poles of fault planes in Fig. 3. 12 a. The mean vector calculated by using R% and center method. It indicates a mean value of fault

planes in N45E trending (135/82, Fig. 3.12b). The eigenvectors and eigenvalues of fault planes are also calculated. The equal area projection of eigenvectors shown in (Fig. 3. 12c). The eigenvectors with greatest (0.49), median (0.38) and smallest (0.12) eigenvalue are 340/07, 249/09 and 108/79 respectively. These mean statistically, 49% of measured fault planes is orientated in the direction 160/83 (N70E), 38% in the direction 69/81 (N159E) and 12% in the direction 288/11 (N18E). It indicates two major orientations (± N-S and ± E-W trending) of fault planes. A rose diagram of the same data is shown in Fig. 3. 12d. The data are counted in intervals 10° of azimuth and dip, and indicate a maximum distribution (14.04%) of faults by ± E-W trending.

Fault kinematic analysis is based on measurements of faults and associated slickensides. Fault kinematic analysis normally gives the reduced stress tensor, i.e. the directions of principal stresses ($\sigma1 > \sigma2 > \sigma3$), and the stress ratio $R = (\sigma2 - \sigma3/\sigma1 - \sigma3)$ at a locality. Fault kinematic analysis hence give information of the orientation and shape of the stress ellipsoid but does not yield information about the absolute values of stress. For fault kinematic data visualization, processing, and analysis, the *TectonicsFP* by Reiter & Acs (2000) has been used. After input of the raw data, data files are corrected so that all striae lie absolutely on the respective fault planes (no misfit). To do this, fault-striae are rotated along a great circle, which is defined by the striae and the pole of the fault plane, to align on the fault plane. This operation is necessary to be carried out before further processing of the data files. Fault-striae data can be represented graphically in equal area, lower hemisphere stereonets by two different ways (Fig. 3. 13): a) The Angelier plot (Angelier & Goguel 1979) displays fault planes as great circles and an arrow pointing in the direction of relative slip of the hanging wall; b) the Hoeppener plot (Hoeppener 1955), also called tangent lineation plot, displays poles to faults with the arrows drawn in the pole point as tangents to the common great circle of the fault plane and the striae. The arrow points in the direction of slip of the hanging wall. This representation is particularly useful for large data sets. The directions of principal stresses are determined by using *P*-*T* method of Turner (1953). For every fault plane, a contraction (*P*-axis) and extension axis (*T*-axis), both lying in the plane given by the fault plane and the striae, is built with an angle τ between the fault plane and the *P*-axis. τ corresponds to the fracture angle defined above and may differ between 0° and 90°. In a first step, all data are considered and the best fit τ angle is used to construct the *P*-*T* axes. The results of fault kinematic analysis and the directions of principal stresses are represented in Fig. 3. 14. The orientation of the principal

stress axes based on calculation of the *P-T* axes are σ1: 45/25, σ2: 184/66, σ3: 314/10. These can compare to anticlinal and synclinal folding structure with axis plunging to the NW and its stress ellipsoid.

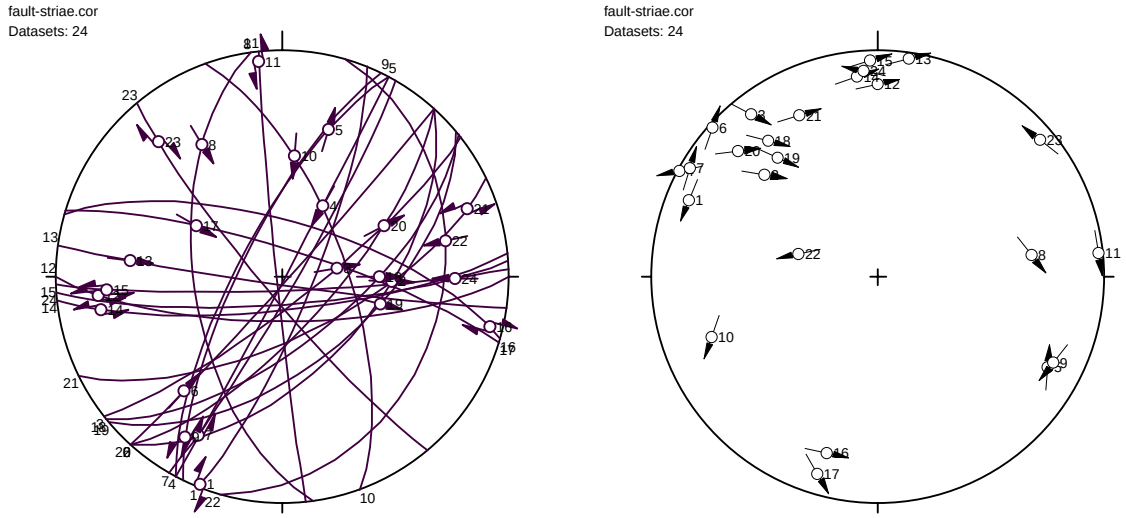

a) *b)*

Fig. 3. 13 Fault kinematic data representation: a) Angelier plot, b) Hoeppener plot.

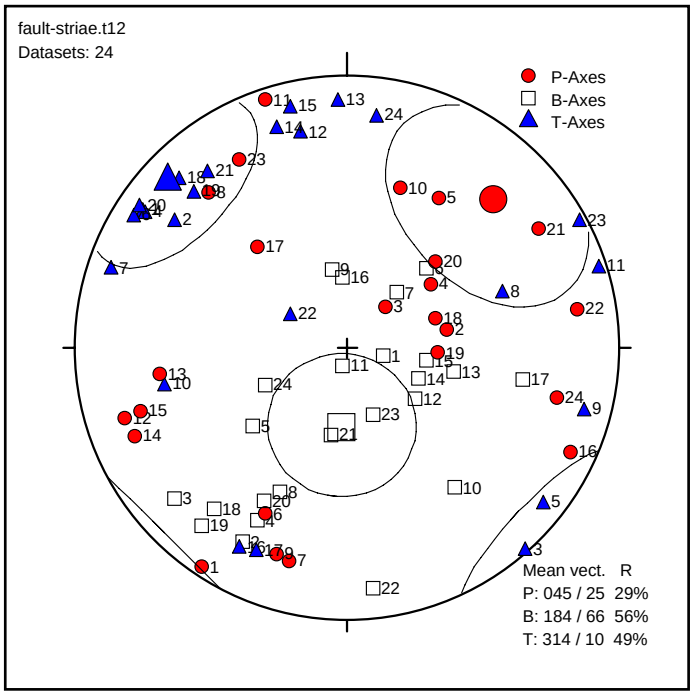

Fig. 3. 14 calculation of the P-T axes based on 24 datesets of faults and associated striae.

3.4 Petrography and texture of host rocks, magnesite and late mineralizations

The following succession of carbonate rock/mineral phases was recognized in account of field observations, petrographical and geochemical investigations (Azim Zadeh et al. 2005, 2008):

Host rocks

- Shallow marine limestone, rich in fossils (e.g. corals, crinoids).
- Early diagenetic fine grained/dense dolomite (partly with fossils) and fine banded microcrystalline limestone/dolomite.

Magnesite ore body

- Sparry magnesite of several types, the pinolite type is typical.

Late dolomite

- Sparry dolomite (coarse grained) at the contact to the magnesite (coexisting dolomite).
- Submciroscopic redolomitization of magnesite.
- Idiomorphic dolomite crystals (”Rosszähne”) in veins and partially open spaces.
- Orbicular dolomite.
- Dolomite as joint fillings.

Late non-carbonate mineralization

Talc mineralization is bound to tectonized zones and marginal parts of the magnesite bodies. Talc was formed by the interaction of a SiO_2-rich fluid with dolomite/magnesite along joints and shear zones in a very late orogenic stage. Sulfide vein mineralizations with tetrahedrite, chalcopyrite, pyrite and gold belong to a younger metallogenic event (Ebner et al. 2004b).

3.4.1 Limestone

Limestone host rock is cm- to dm- bedded, fine-grained, light to dark-gray, and banded (Fig 3. 15). Some layers are rich in fossils (e.g. corals, crinoids). Calcite is the dominant

mineral in fine laminated limestone (crystal size between 75 µm to 500 µm). Some limestones bear quartz, feldspar (Fig 3. 15d) and a fine laminated microcrystalline dolomite (Fig. 3. 16). Pyrite crystals with rims of iron oxides (limonite?) are also included (Fig. 3. 16b).

a) Outcrop of fossiliferous limestone.

b) Outcrop of laminated limestone.

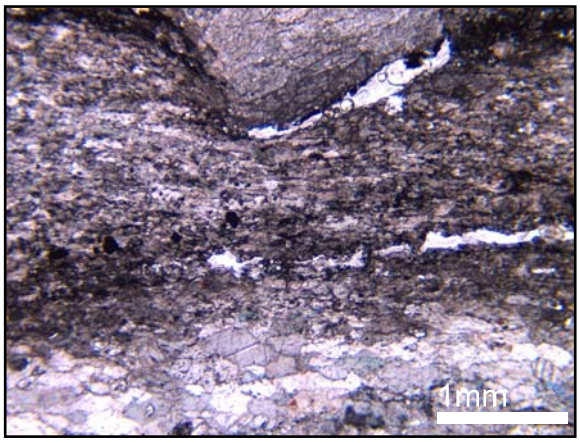

c) Photomicrograph of laminated limeston.e

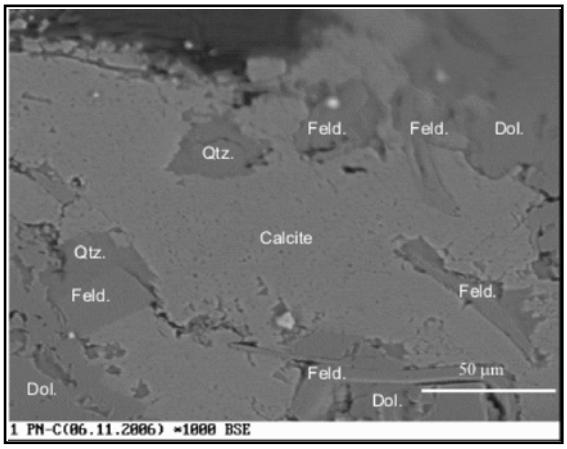

d) Backscattered electron (BSE) images of fine laminated limestone.

Fig. 3. 15 Limestone of the Steilbachgraben Fm, the host rock of the Hohentauern/Sunk magnesite deposit. Crinoids and corals are frequent in Steilbachgraben limestones.

3.4.2 Early Dolomite

Early dolomite as a host dolostone is interpreted to have formed during dolomitization of the primary Steilbachgraben limestone (see also chapter 4). Early dolomite is shown by the following types: fine banded microcrystalline limestone/dolomite to fine grained/dense dolomite (partly with fossils) and relicts of dolomite within the magnesite.

Fine laminated limestone/dolomite (Fig. 3. 16a) displays an alternation of fine to very fine grained carbonate minerals with insoluble carbonaceous material which is black colored (graphite?). Lamination is caused by the fine alternation of microcrystalline dolomite and calcite macro sparite. The calcite crystals show twinning and cleavage planes. These features are generally visible within the lower beds of the host rock, suggesting that they represent the original bedded sedimentary structure. Backscattered electron image of the same sample (Fig. 3. 16b) indicates that laminated parts form the transition between the coarser calcite crystals and very fine grained crystals of calcite and dolomite.

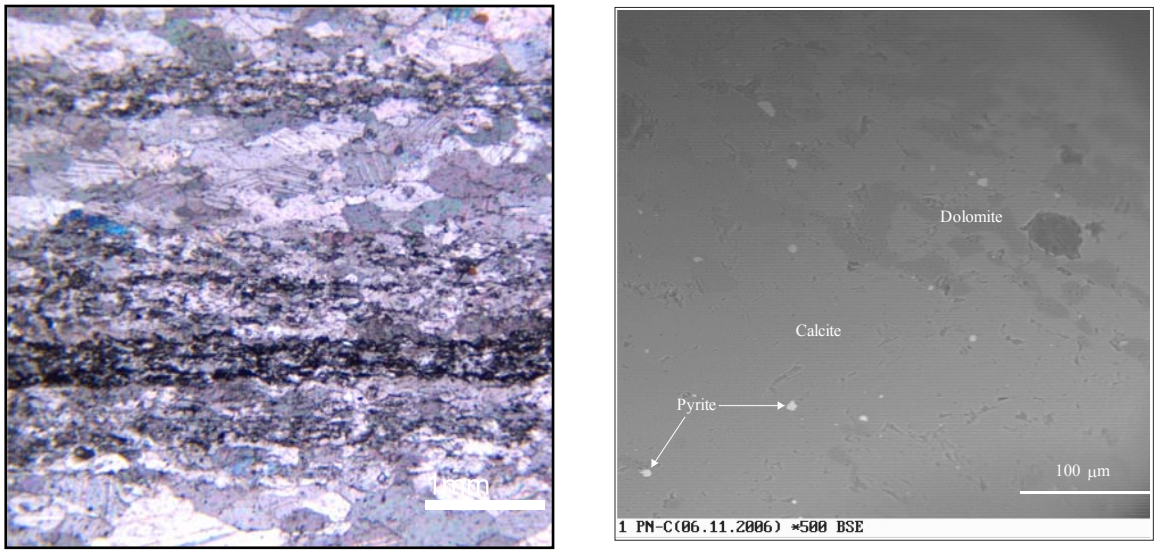

a) *b)*

Fig. 3. 16 Petrographic features of early dolomite. a) Photomicrograph of laminated limestone/dolomite exhibiting alternation of fine crystalline dolomite and coarse crystalline calcite bands. b) Backscattered electron images of very fine dolomite crystals.

Dolomite inclusions within the magnesite are relicts of the replaced early fine grained dolomite. They are distributed irregularly in magnesite. They are interpreted as relicts of the metasomatically replaced dolostone precursor during magnesite formation. Back-scattered electron images indicate these as microinclusions (<50µm) within magnesite (Fig. 3. 17). Backscattered electron images and the conventional element-mapping have revealed a variation in Ca-, Fe- and Mg-concentrations within the individual carbonate crystals (Fig. 3. 18). The element-mapping clearly indicates the distribution of the dolomite crystals (dolomite relicts). They contain high Ca and lower amounts of Mg and Fe than the magnesite crystals.

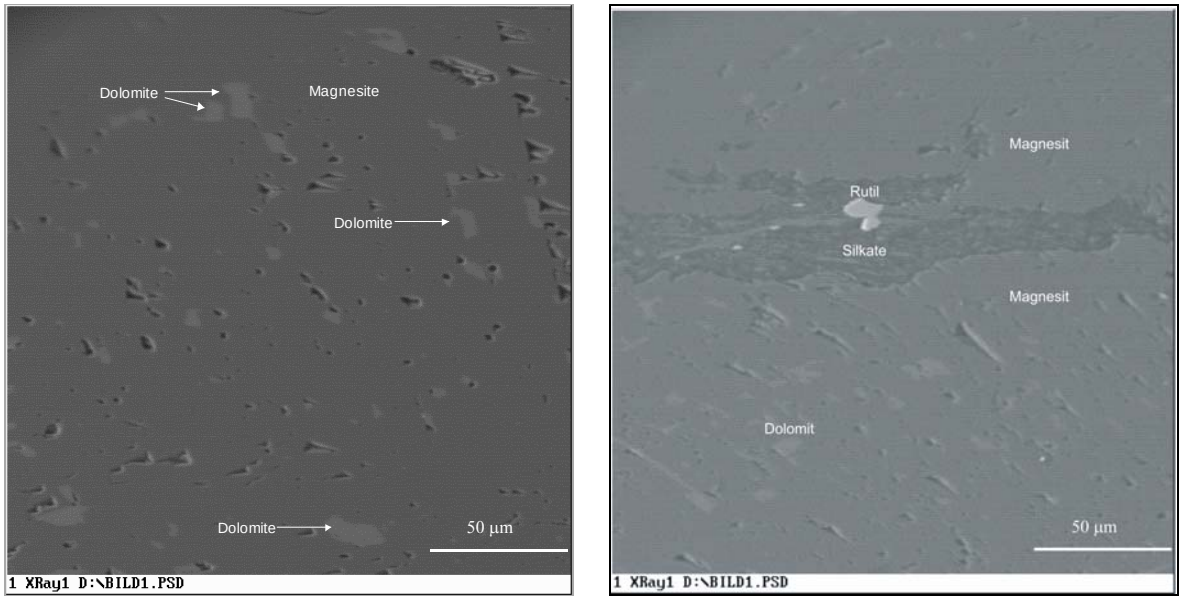

a) *b)*

Fig. 3. 17 BSE image of dolomite relicts (light part) within magnesite (grey-dark grey).

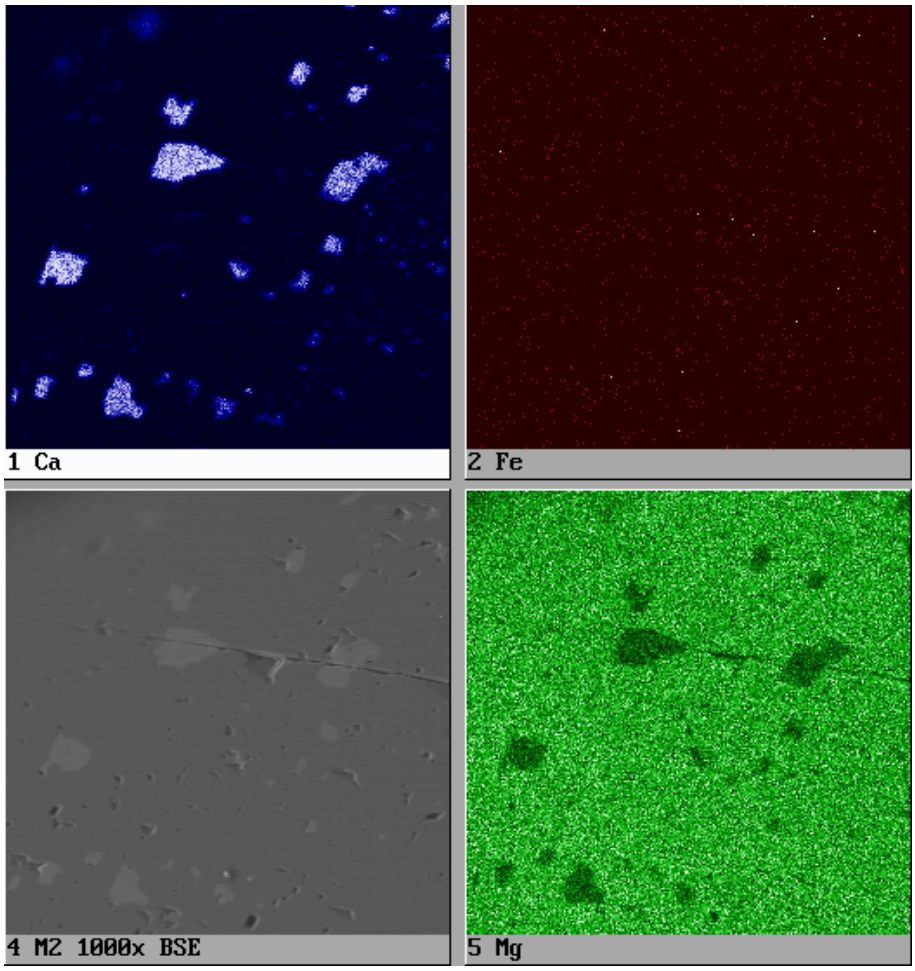

Fig. 3. 18 Element (Ca, Fe, Mg) distributions mapping of magnesite crystals. The dolomite relicts show higher Ca and lower Mg and Fe contents.

3.4.3 Magnesite

Medium to coarse grained euhedral sparry magnesite is replacing the Carboniferous dolomite, rich in biogene detritus. The differentiation of magnesite from dolomite under optical microscopic methods is not easy. Therefore petrographic description of sparry magnesite and related carbonate minerals was performed using optical microscopy in combination with Raman spectroscopy. Fig. 3. 19 shows the Raman spectrum of a magnesite crystal from Hohentauern/Sunk deposit.

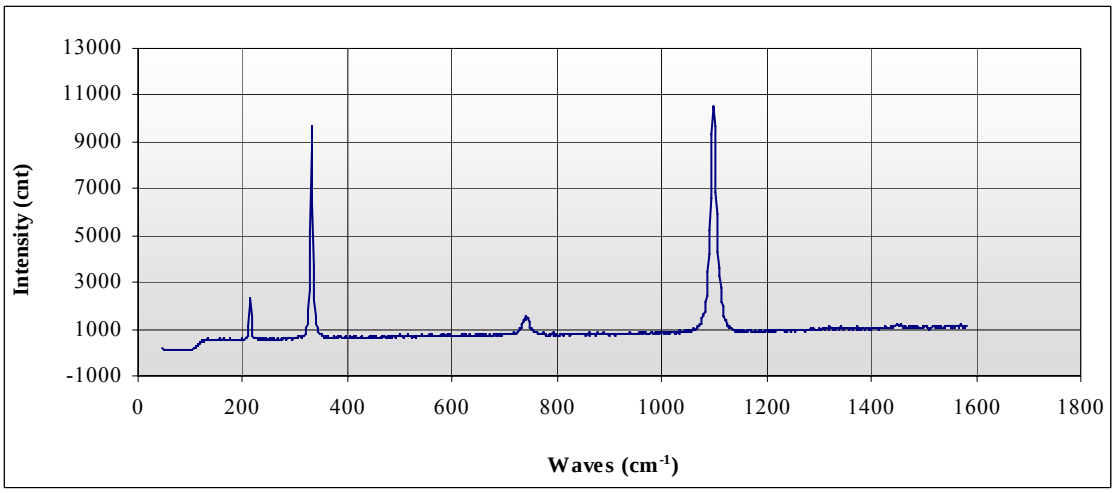

Fig. 3. 19 Magnesite spectrum of sample PE16 (Raman spectroscopy).

The texture of the magnesite is varying (Fig. 3. 20). Mostly the fabric is made up of large (up to some cm-size) light crystals of magnesite arranged in a black matrix of fine grained magnesite, carbonaceous material (graphite) and phyllosilicates (chlorite). Typically there is also the pinolitic texture. The big oval shaped, up to cm-sized light crystals in a fine and black matrix, where matrix materials separate single crystals form pinolites (Fig. 3. 20a, b). Isolated crystals or groups of crystals may also float in the fine, dark matrix and form freely grown magnesite pinolites and rosettes textures with inclusions of dark matrix in fine-grained magnesite (Fig. 3. 20c). Sometimes the crystals form a banding or a fine–medium grained granular texture (Zebra banding) in which smaller crystals may be replaced by groups and boxes of bigger crystals. These magnesite crystals contain thin laminations, composed of insoluble materials such as chlorite and graphite (Fig. 3. 20 d, e). The orientation of the magnesite crystals is neither controlled by sedimentary nor tectonic features. (Ebner & Prochaska 2001 a, cum lit.). The lenticular crystals grew perpendiculary away from stylolith sutures (Fig. 3. 20a, Fig. 3. 21a) and strata surfaces (Fig. 3. 20d, e; Fig. 3. 21b), and present a irregular banding structure.

a) Coarse grained (partially redolomitized) pinolite

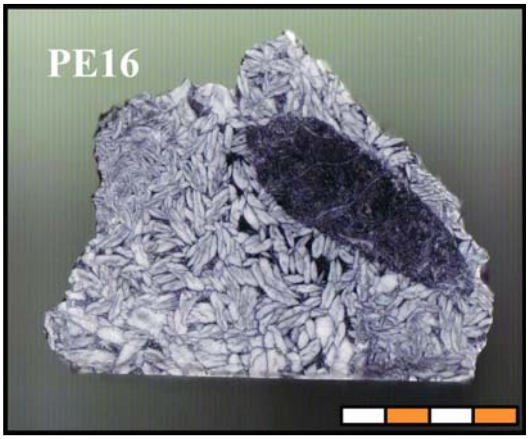

b) Middle grained pinolite

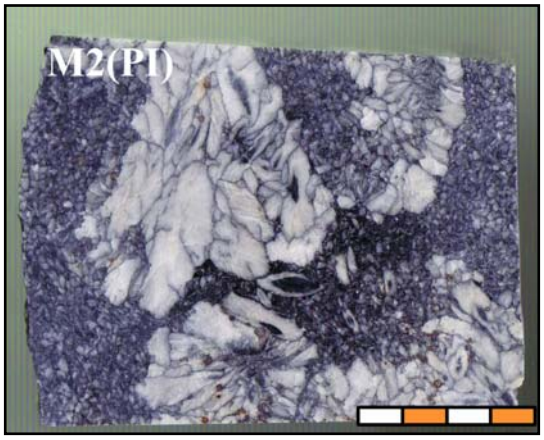

c) Rosettes textures with inclusions of dark matrix

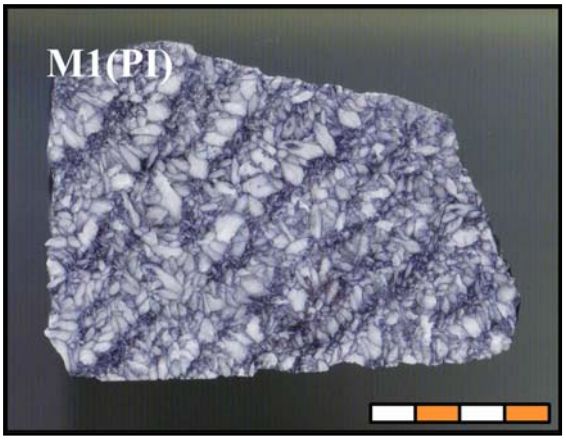

d) Zebra Banded magnesite

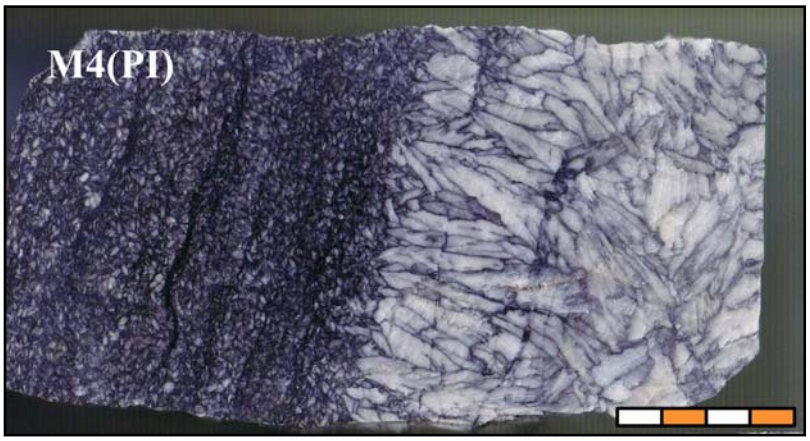

e) Banded magnesite

Fig. 3. 20 Textures of Hohentauern/Sunk deposit sparry magnesite.

The characteristic black and white banded structure (Zebra banding) is due to the change in size of the magnesite crystals and admixture of insoluble material. The white layers display big crystals of magnesite replacing dolomite without matrix impurities. The dark layers

show fine grains of magnesite crystals which are mixed with phyllosilicates (chlorite) and carbonaceous materials. Insoluble black colored materials (carbonaceous and phyllosilicates) were concentrated between two replacing magnesite crystals (Fig. 3. 21c, d) or along stylolite sutures and strata surfaces where fine grained chlorite and organic (graphitic) matter were enriched in the dolomite magnesite precursor. All studied magnesite contain irregularly distributed dolomite microinclusions (Fig. 3. 17). Coarse-grained magnesite crystals include more dolomite relicts than fine grained magnesite.

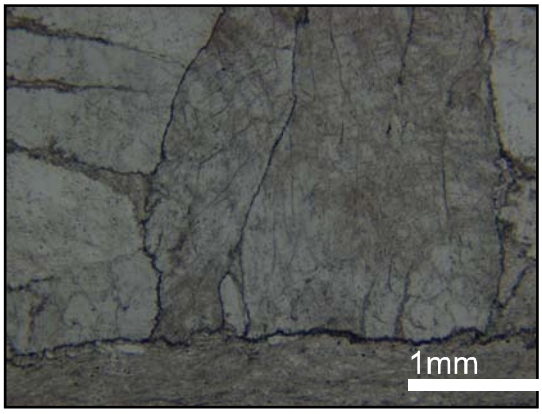

a) The lenticular crystals grew perpendiculary away from stylolith sutures.

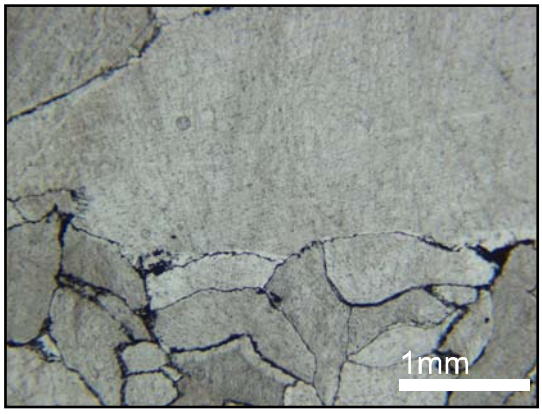

b) Irregular banding structure is due to the change in size of the magnesite crystals and admixture of insoluble material.

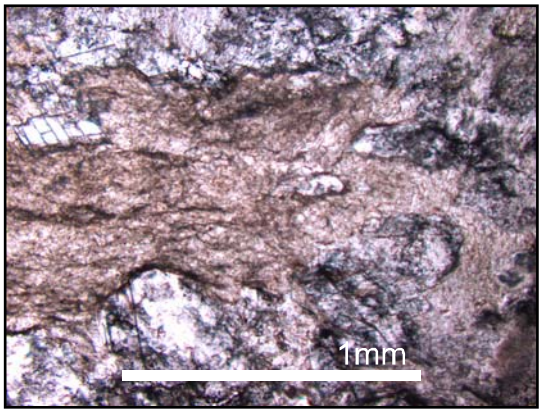

c) Insoluble materials (chlorite) were concentrated between two replacing magnesite crystals.

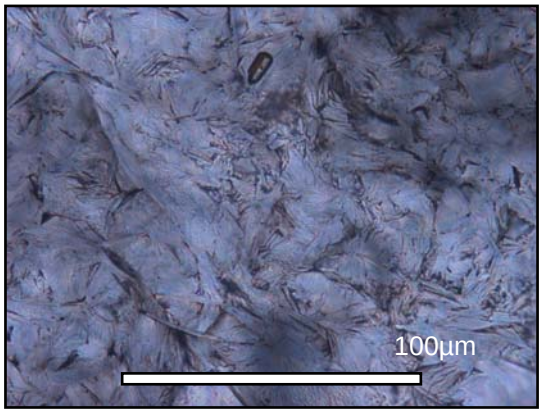

d) Phyllosilicates (chlorite) enriched between magnesite crystals.

Fig. 3. 21 Photomicrographs of pinolite magnesite.

3.4.3.1 Cathodoluminescence

Cathodoluminescence (CL) microscopy is a well-established petrographic technique in the study of carbonate rocks. It can provide a powerful tool for the recognition and differentiation of diagenetic textures not visible in normal light. Recognition of growth textures in coarse-crystalline magnesite is often impossible when standard transmitted and reflected-light microscopy, ultraviolet-fluorescence microscopy, or etching and staining techniques are used. Cathodoluminescence observations were visually categorized into the three classes moderately bright, dull and non luminescent. Comparing normal light with CL views reveals crystal zoning patterns (Fig. 3. 22). Some magnesite crystals are composed entirely of an inclusion-poor part (transparent part), normally in the core of crystals, with non luminescent appearance and an inclusion-rich dully luminescing part, normally on the rim of crystals. Petrographic study of magnesite rocks from the Eastern Alps using cathodoluminescence (Spötl 1991) indicates low Fe content zones coincide with areas of most intense luminescence and Fe-rich zones appear nonluminescent. Cathodoluminescence view of magnesite samples from Hohentauern/Sunk deposit shows a visible zoning (Fig. 3. 22b) in which Fe-poor zones appear luminesence (normally on the rim of crystals) and normally non luminescent Fe-rich zones in the core of crystals. The dolomite crystals are characterized by their bright orange cathodoluminescence color, suggesting that dolomite crystals are nonferroan or have very low iron contents only.

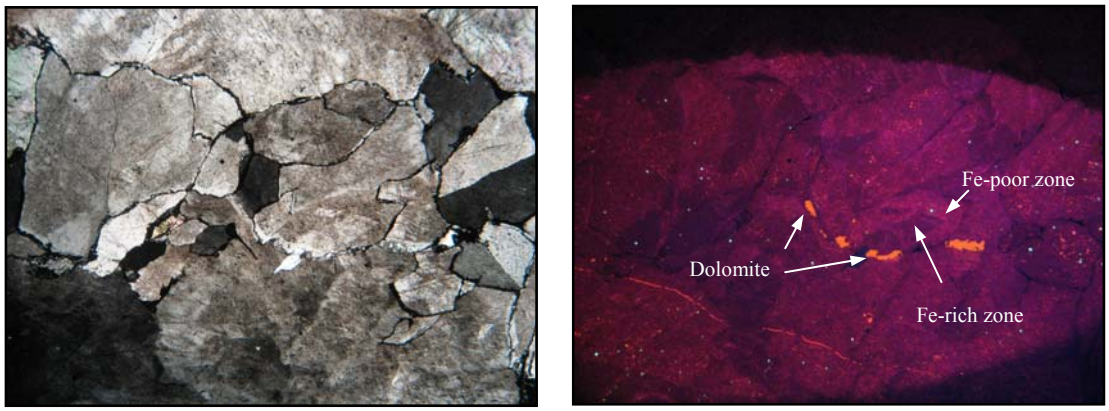

a) *b)*

Fig. 3. 22 compartion of photomicrograph (a) and CL view (b) of magnesite (sample No. M2, Rosettes textures, x2.5).

3.4.3.2 Accessory minerals within magnesite

The occurrence of other non carbonate accessory minerals [rutile (Fig. 3. 23a), pyrite, apatite, zircon, and evaporite minerals] is rare. Submicroscopic inclusions of evaporite minerals are also hosted in magnesite (Fig. 3. 23b). Qualitative analysis of evaporite minerals using wavelength dispersive mode EMPA indicates the evaporite minerals as KCl crystals (Azim Zadeh et al. 2008; Fig. 3. 24).

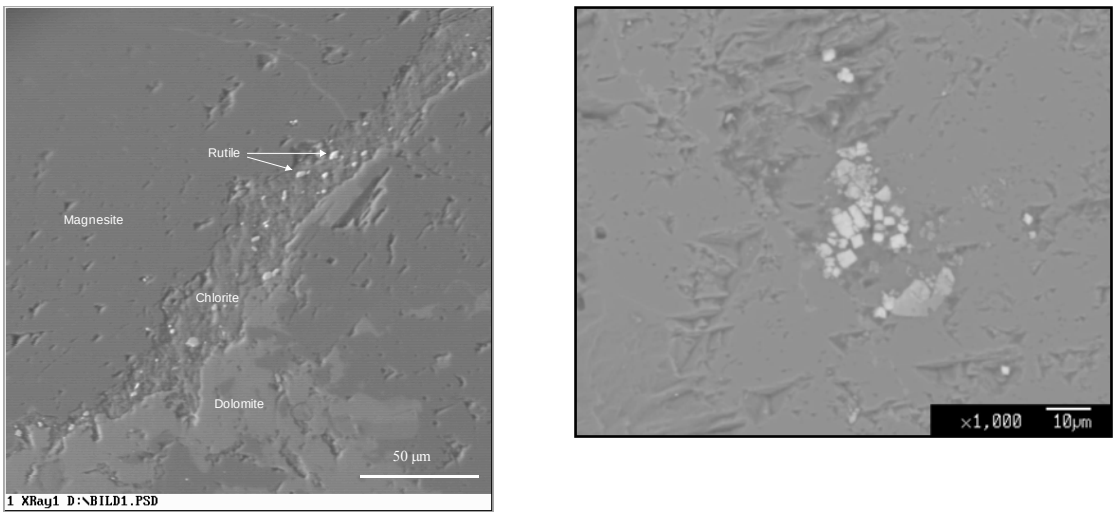

a) *b)*

Fig. 3. 23 SEM image of a) admixture of rutile grains and chlorite between two individual magnesite crystals. b) solid inclusion of KCl evaporite minerals within magnesite (sample No. PM 15-16-1a).

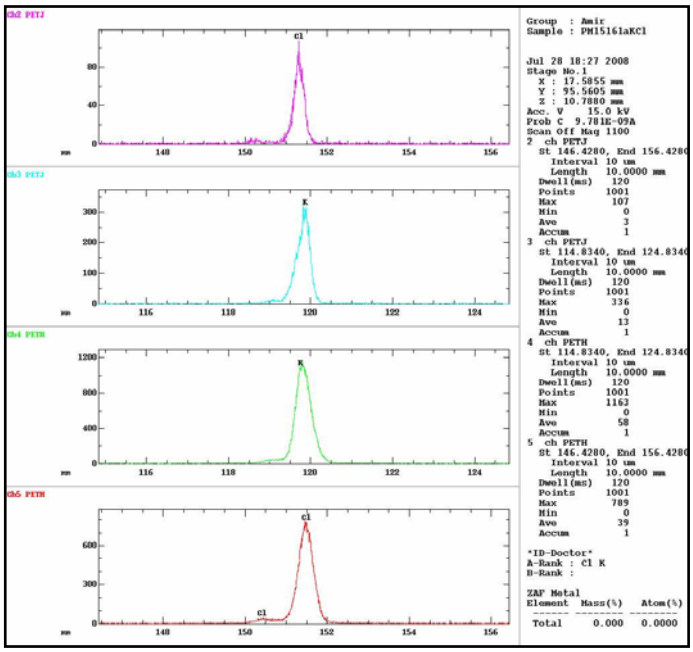

Fig. 3. 24 Qualitative analysis of evaporite minerals using wavelength dispersive mode EMPA (sample No. PM 15-16-1a).

3.4.4 Late dolomite

Magnesite formation is followed by several generations of dolomite. Five main types of late dolomite were identified by field and petrographic studies.

3.4.4.1 Sparry dolomite at the contact to the magnesite

Sparry dolomite at the contact to the magnesite is the transition from the dolomite host rock to the magnesite ore body (Fig. 3. 25). Usually the sparry dolomite occurs between the host rocks and the magnesite and varies extremely in thickness and size (up to some mm-size). Alteration phenomena of the sparry dolomite are not very distinct from the host rock. The dolomite in transition zone is coarse grained and microscopically a weak recrystallization can be observed.

Fig. 3. 25 Sparry dolomite at the contact to the magnesite.

3.4.4.2 Submicroscopic redolomitization of magnesite

Back scattered electron image of some magnesite samples showed that magnesite is replaced by dolomite. This replacement of the magnesite by euhedral dolomite crystal assemblages initiates preferentially at crystal boundaries, cleavage planes and microfractures cutting the magnesite crystals (Fig. 3. 26).

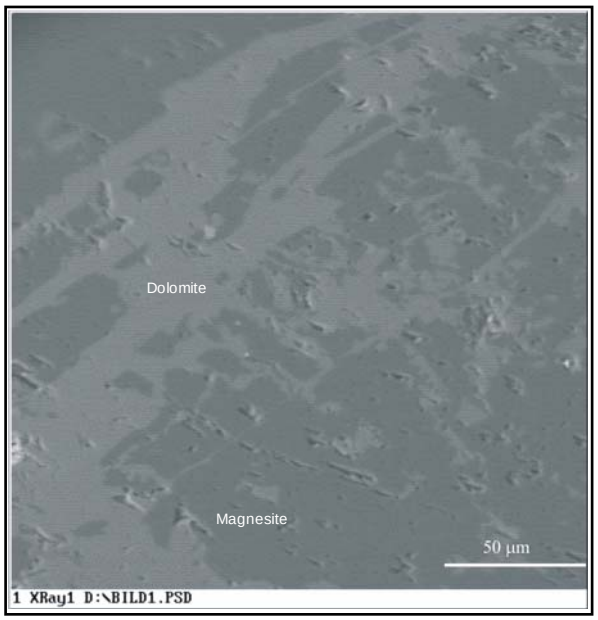

Fig. 3. 26 BSE image of magnesite crystal (grey-dark grey) which was replaced by dolomite (light grey).

3.4.4.3 Orbicular dolomite

Another remarkable intercalation in the Hohentauern/Sunk deposit is a m-thick layer of orbicular dolomite (Fig. 3. 27). It is composed of light dolomite spheres build up of concentric seams around angular fragments of dark dolomite and pinolite magnesite (Haditsch 1968, Siegl & Felser 1973). The orbicular dolomite is composed of light grey colored aggregates of dolomite spheres with a diameter up to 5 cm within a black-dark grey fine grained dolomite matrix. The cores of the spheres are angular fragments of fine grained black dolomite or pinolite magnesite fragments. These are surrounded by some mm-thick, concentric seams of light radially orientated dolomite crystals.

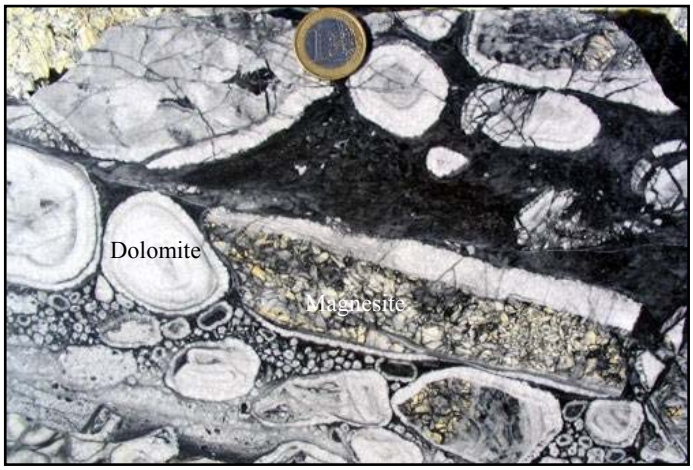

Fig. 3. 27 Orbicular dolomite composed of light dolomite spheres and pinolite magnesite as cores.

So it is clear that magnesite formation occurred before the formation the orbicular dolomite. In the past it was interpreted as a ± sedimentary ooid/onkoide like formation (Siegl & Felser 1973). But recently the crosscutting character of the orbicular dolomite was found in the field (Fig. 3. 28). Therefore it is suggested that orbicular dolomite was formed as a hydrothermal breccia after magnesite formation and lithification of the sequence.

Fig. 3. 28 Orbicular dolomite as hydrothermal breccias along fault zones formed after magnesite formation.

3.4.4.4 Rosszähne (horse tooth dolomite)

Large (up to 10 cm) idiomorphic dolomite crystals (”Rosszähne”) are frequent in the magnesite. “Rosszähne”-dolomite displays a idiotopic fabric consisting of transparent to translucent mega-sparry crystals, which contain relicts of the magnesite precursor (Fig. 3. 29). This type of Rosszähne-dolomite occurs in veins and partly open spaces. The Rosszähne dolomite also occurs as euhedral crystals overgrowths on magnesite. The Rosszähne dolomite is interpreted to have formed during replacement of earlier magnesite.

3.4.4.5 Dolomite in joints

Dolomite as joint fillings is hosted by fine-grained dolomite (Early dolomite). The mineralization consists of fine grained, sparry light brown dolomite crystals inside individual joints. The thickness of dolomite veinlets is not usually more than 1 cm (Fig. 3. 30).

Fig. 3. 29 Large idiomorphic dolomite crystals (”Rosszähne”) and relicts of magnesite which were replaced by dolomite.

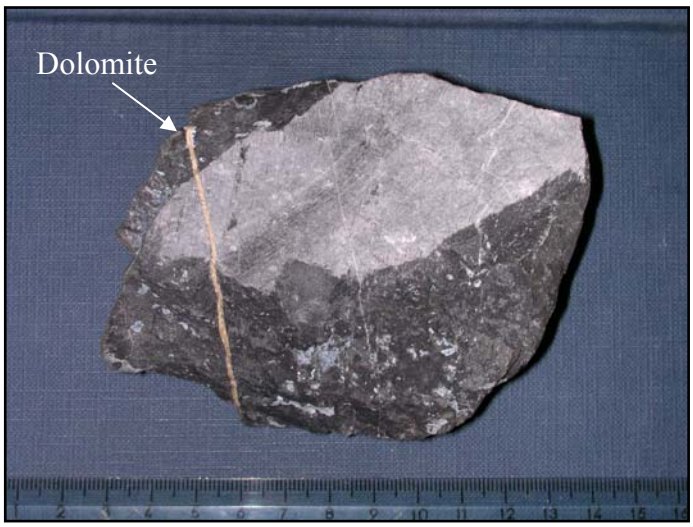

Fig. 3. 30 Dolomite as joint fillings is interpreted as the youngest dolomite generation.

3.4.5 Talc

Talc mineralization occurs in the study area as an alteration product from magnesite and dolomite by the interaction with a SiO_2–rich fluid. Talc commonly forms fine-grained, fibrous aggregates (Fig. 3. 31, Fig. 3. 32) along joints and shear zones in a very late orogenic stage. The magnesite and especially carbonaceous and clay insoluble materials are included as impurities in the talc veins.

Fig. 3. 31 Fibrous aggregates of talc along a joint.

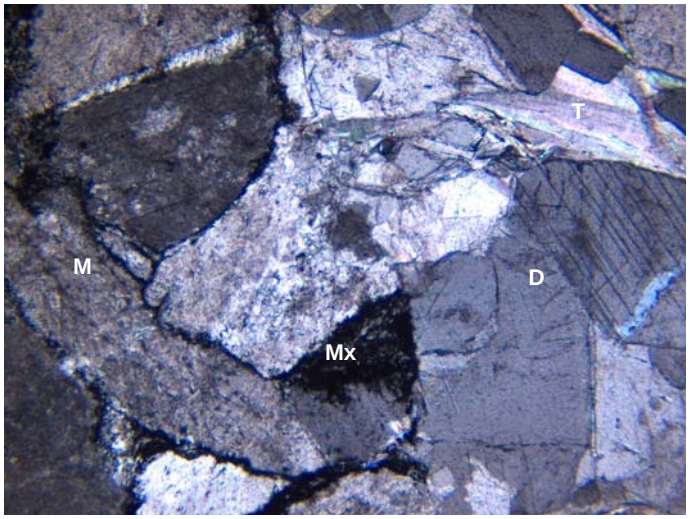

Fig. 3. 32 Talc was formed by the interaction of a SiO_2–rich fluid with dolomite/magnesite (M: magnesite, D: dolomite, T: talc, Mx: matrix).

3.5 Modelling of the deposit

In accordance to a 3-D model (Walter 2001; Fig. 3. 33), at the surface the ore-bodies generally strike in SE-NW direction. The shape of the magnesite layers of the open pit (dipping 30–40° to the NW) are changing to cylindrical and lenticular geometries towards the depth and much more shallow dipping by approaching the Middle-/Upper Austroalpine thrust plane. From the model, it became apparent that the dip changes at the mine's 50m level from about 70 to 37 degrees. This change may be attributed to the overthrust of the base of the Upper Austro-Alpine nappe which shows the same dip. The magensite bodies are more or less elongated lenses which show complex cuspate-lobate structures. Therefore

a separation of the bodies by boudinage mechanisms is assumed. It is likely that the bodies are intersected by a fault zone, which may be depicted in a generalized way as a listric surface (Walter 2001).

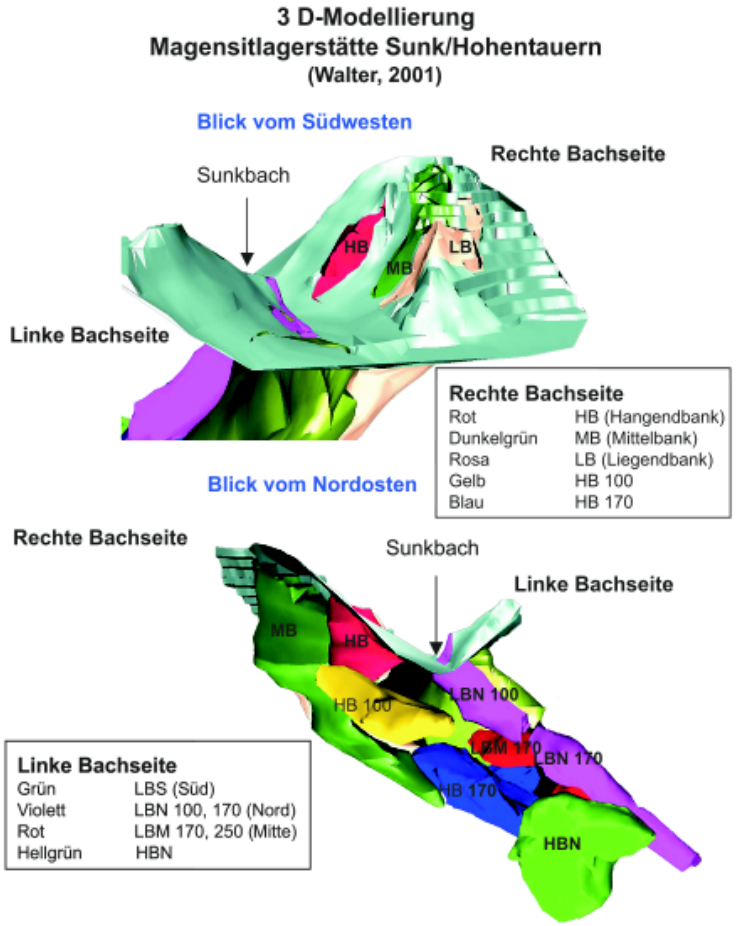

Fig. 3. 33 3D model of Hohentauern/Sunk magnesite deposit (Walter 2001).

4. Geochemistry

4.1 Major elements

In order to understand the geochemical characteristic of the magnesite ore body and carbonate host rocks, 90 samples were chemically analyzed. 51 whole-rock samples were analyzed for major elements oxides by X-ray fluorescence spectrometry (XRF) technique at RHI Technology Center Leoben (Tab. 1, Appendix A). 20 whole-rock samples and 19 separated mineral samples (Tab. 2 and 3, Appendix A) were analyzed in-house for major elements by Atom-absorption spectrometer (AAS). 8 samples of different mineral phases (magnesite, dolomite, calcite and silicate) including 123 points, were analyzed by wavelength dispersive system (WDS) at EPMA.

The average geochemistry of the mined magnesite (Ebner & Prochaska 2001) was MgO 43.3 wt. %, CaO 2.5 wt. %, SiO_2 2.0 wt. %, Fe_2O_3 2.4 wt. % (FeO 2.2 wt. %) and LOI 49.8 wt. %. The chemical composition of selected magnesite samples from open pit shows some variations. The bulk composition of magnesite (Tab. 1., Appendix A) ranges from 27.75 to 45.26 wt. % of MgO, 0.62 to 20.90 wt. % of CaO, 0.02 to 5.53 wt. % of SiO_2, 0.02 to 1.24 wt. % of Al_2O_3, 1.49 to 2.61 wt. % of Fe_2O_3 and 46.12 to 52.10 wt. % of LOI. Lower MgO and higher CaO contents in the magnesite ore body in comparison with stoichiometric magnesite mineral are due to relicts of dolomite inclusions within the magnesite crystals and different features of late redolomitization of magnesite. SiO_2 contents may have derived from Mg-chlorite, talc and sometimes quartz. Iron is an isomorphic admixture for Mg^{2+} in the crystal lattice of magnesite and the Fe_2O_3 contents are due to Fe substitution in the magnesite crystal lattice.

The CaO/MgO ratio of carbonate is a signature to measure the enrichment degree of Mg as it has close relation with mineral composition of rocks. Carbonate with calcite > 95 % and dolomite <5 % has CaO/MgO > 50 and MgO content is 1.085 %. While dolomite and calcite have equal contents, the CaO/MgO ratio of carbonate is 4.0 and MgO content is 10.85 %. The CaO/MgO ratio is close to 1.4 and the MgO content is 21.7 % when carbonate is mainly composed of dolomite (>95 %). When the main minerals of the carbonate are dolomite and magnesite, CaO/MgO ratio will greatly decrease while MgO content greatly increase. CaO/MgO ratio is 0.84 and MgO is 28.18 % when dolomite is the

major mineral (dolomite 75 %, magnesite 25 %), while CaO/MgO ratio is 0.03 and MgO content is 43.94 % when magnesite (dolomite 5 %, magnesite 95 %) is the major mineral (Cong-Xi Chen et al. 2003). Carbonate rocks in the study area can be divided into three rock types based on CaO/MgO ratio and MgO contents of carbonates (Fig. 4. 1 and 4. 2): Ca-carbonate (limestone), dolomite and magnesite.

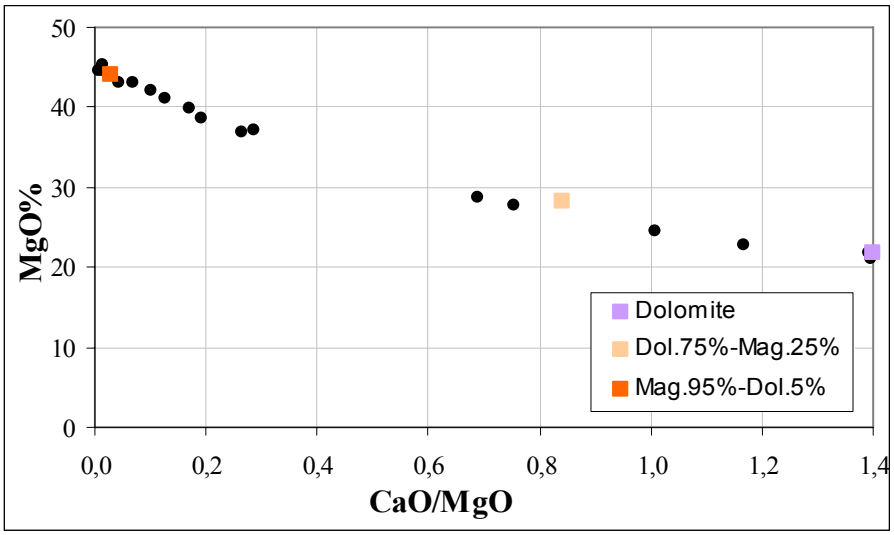

Fig. 4. 1 Different carbonate generations occurring in the Hohentauern/Sunk deposit according to mineralogical composition, which range from magnesite to dolomite.

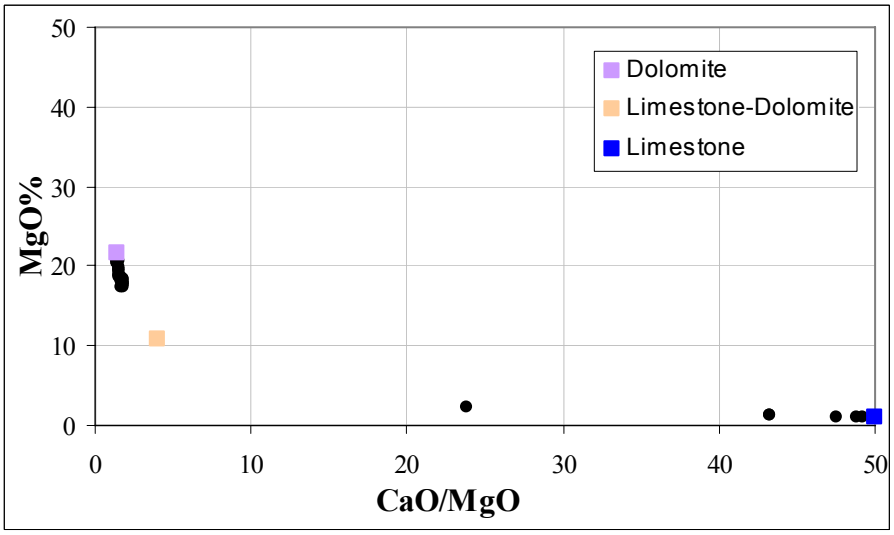

Fig. 4. 2 Different carbonate generations occurring in the Hohentauern/Sunk deposit according to mineralogical composition, which range from dolomite to limestone.

According to the stoichiometry calculation of the bulk composition, the mineral composition of limestone contains about 88.34–92.87 % of calcite and 7.13–11.66 % of

dolomite. Some of the dolomite samples display about 7.65–14.07 % of magnesite, which occurred as alteration haloes at the contact to the magnesite bodies (sparry dolomite). The mineral composition of magnesite ore ranges from 26.62 to 93.76% of magnesite and 6.24–73.38% of dolomite. Lower magnesite and higher dolomite contents in some magnesite ore samples are due to strong redolomitization of magnesite ore.

Correlation between MgO-Fe_2O_3 (Fig. 4. 3) of the bulk compositions of the magnesite ore body and carbonate host rocks (XRF analyses) shows three domains: limestone, dolomite and magnesite. Limestone contains about 0.24–0.36 wt. % of Fe_2O_3 (0.28 wt. %, mean value), Fe_2O_3 content of dolomite range from 0.49–3.31 wt. % and magnesite has 1.48–2.61 wt. % of Fe_2O_3 (1.94 wt. %, mean value). Maximum total iron value expressed as Fe_2O_3 is lower in dolomite host rocks than in magnesite (1.37 wt. % of difference value), although differences in iron content are not true in all profiles. This should be compared with data where Fe reaches a maximum in the magnesite ore body. Besides the Fe^{2+} ion preferably substituting for Mg^{2+} in the carbonate, other factors probably influence the Fe-distribution, including the availability of sulfur (pyrite), the paleogeographical situation of the sedimentary basin, and the amount and type of weathering products (Fe^{3+}) brought from adjacent land (Pohl & Siegl 1986).

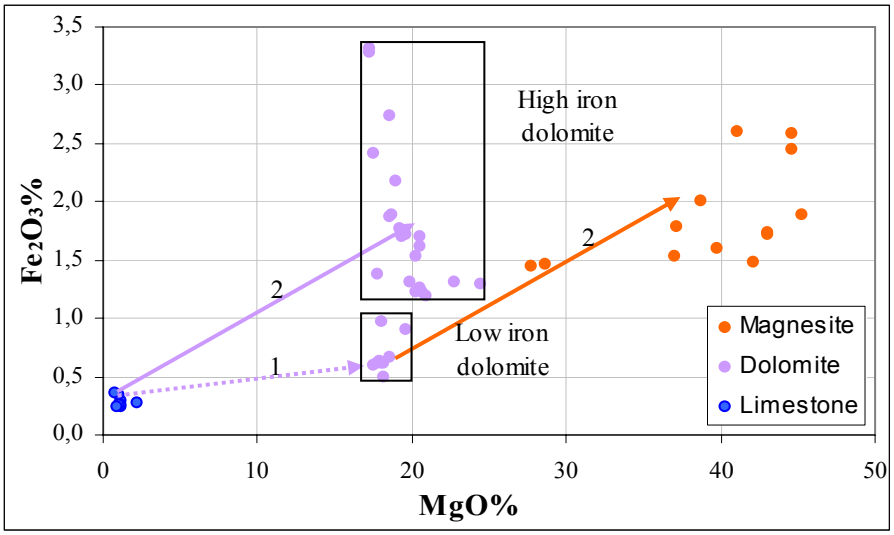

Fig. 4. 3 MgO - Fe_2O_3 variation diagram of carbonate host rocks and magnesite ore body in the Hohentauern/Sunk deposit indicates two different iron enrichment phases.

Dolomite can be divided into two subdomains with different Fe_2O_3 concentrations: low iron dolomite subdomain with 0.67 wt. % mean value of Fe_2O_3 (compared to Fe_2O_3 content

of dolomite microinclusions in magnesite with 0.66 wt. %, mean value) and high iron dolomite subdomain with 1.86 wt. % mean value of Fe_2O_3. MgO-Fe_2O_3 variation diagram reflects two different iron enrichments, suggesting that low iron dolomite occurred during early dolomitization of limestone. High iron dolomite and magnesite with the same iron content probably were formed due to late Mg-Fe bearing solutions.

XRF whole rock and AAS mineral analyses indicate a rather positive correlation between Fe_2O_3 and MnO in all carbonate samples (r=0.74, Fig. 4. 4) as well as in all magnesite samples (r=0.88, Fig. 4. 5). Mn^{2+} with ionic radius of 0.81 A° can substitute for Mg^{2+} (R=0.86 A°) and/or Fe^{2+} (R=0.92 A°) in magnesite crystals.

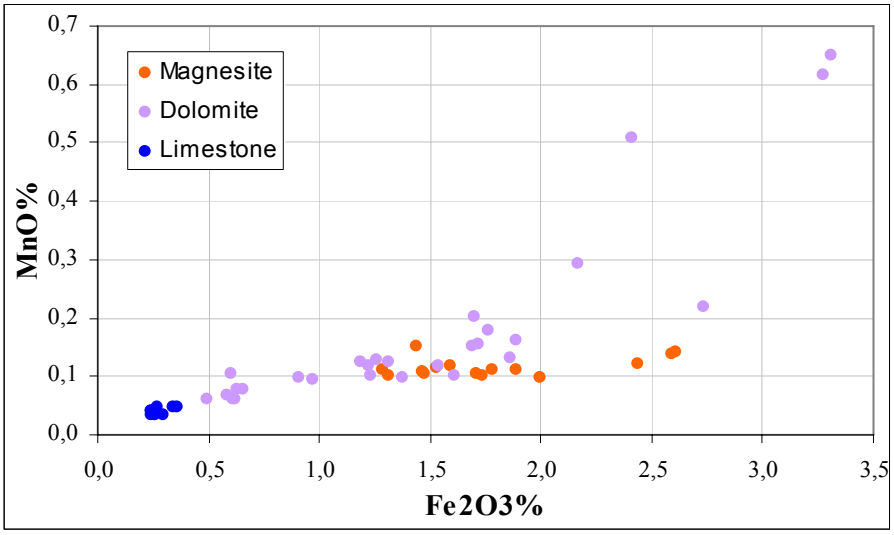

Fig. 4. 4 Fe_2O_3 – MnO variation diagram of carbonate host rocks and magnesite ore body in the Hohentauern/Sunk deposit has a positive correlation (XRF, whole rock analyses).

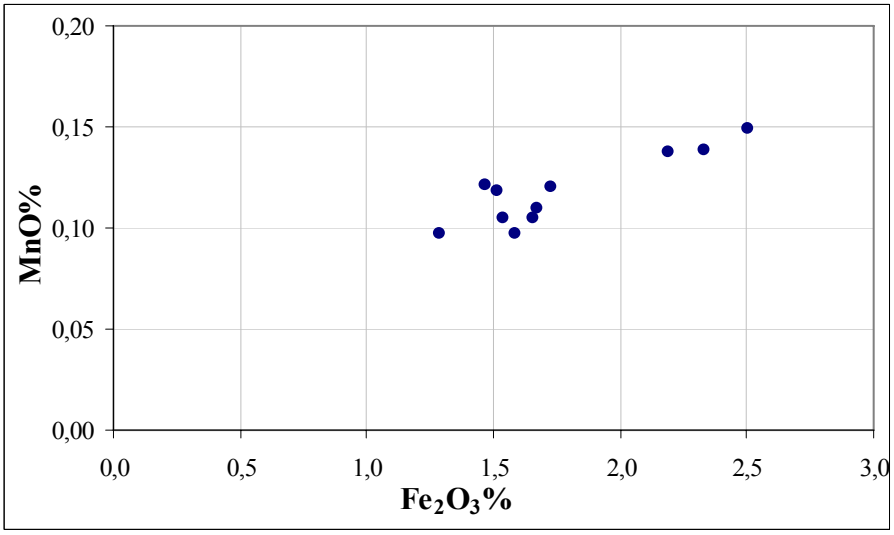

Fig. 4. 5 Fe_2O_3 – MnO variation diagram of all magnesite samples indicates a positive correlation (AAS, separated mineral analyses).

According to bulk compositions of all magnesite samples, the correlations between SiO_2, Al_2O_3, K_2O and TiO_2 are positive. Correlation coefficients are $r_{=}0.95$ for Al_2O_3- TiO_2, $r_{=}0.89$ for SiO_2- K_2O, $r_{=}0.87$ for SiO_2-TiO_2, $r_{=}0.84$ for K_2O-TiO_2, $r_{=}0.80$ for SiO_2-Al_2O_3 and $r_{=}0.66$ for Al_2O_3-K_2O. The positive correlations reflect the detrital aluminosilicate fraction of the magnesite samples.

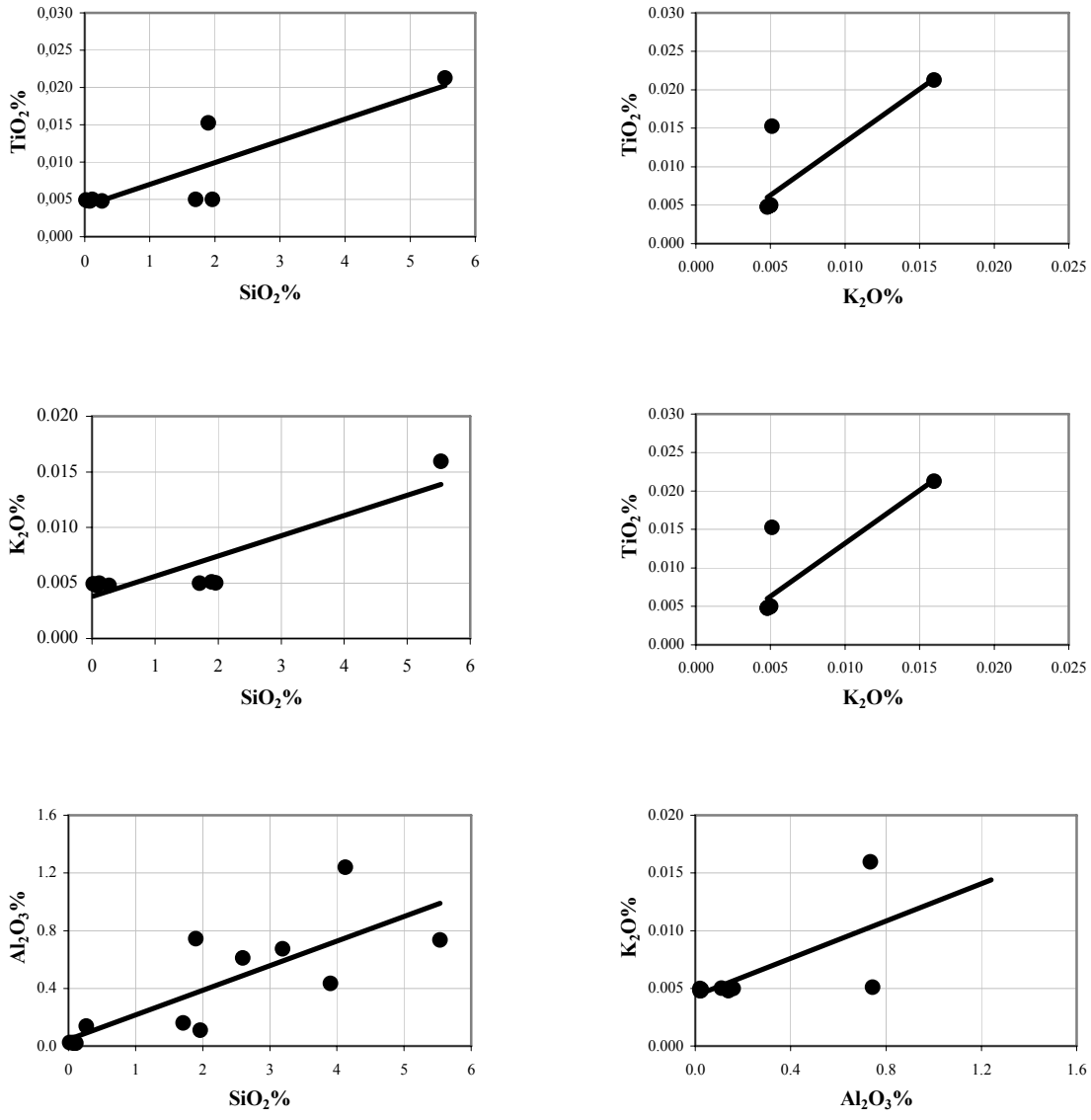

Fig. 4. 6 Selected variation diagram for all magnesite samples (XRF whole rock analyses).

SiO_2 as interstitial quartz grains or veinlet in magnesite is not frequent, but magnesite samples show an average content of SiO_2 about 2.0 % and a positive correlation between SiO_2 and Al_2O_3, suggesting that most of the SiO_2 occurred in talc and Mg rich aluminosilicates (chlorite?).

A positive correlation between SiO_2-TiO_2 and Al_2O_3–TiO_2 and petrographic composition (chapter 3, Fig. 3. 23a) indicate that rutile (TiO_2) is one of the main detrital (Ratschbacher 1987a) heavy minerals which coexists with Mg rich aluminosilicates (chlorite?).

The electron microprobe analyses of selected major elements of the Hohentauern/Sunk carbonates are listed in Tab. 4. 1.

Magnesite crystals contain 47.80 wt. % of MgO (mean value) and they are relatively rich in Fe_2O_3, up to 3.11 wt. % but their mean value is 2.23 wt. % of Fe_2O_3. Magnesit crystals have small amounts of CaO (0.46 wt. %, mean value) which indicate residual micro inclusions of dolomite in magnesite. Dolomite micro inclusions in magnesite have lower Fe_2O_3 contents (0.66 wt. %, mean value), compared to the host magnesite (2.23 wt. %, mean value) and late dolomite as submciroscopic redolomitization of magnesite along micro-joints (1.55 wt. %, mean value). Dolomite micro inclusions in magnesite show lower Fe_2O_3 content than magnesite, suggesting they are relicts of early fine-grained dolomite which metasomatically replaced by magnesite. Late dolomite shows lower Fe_2O_3 values than magnesite but higher than the dolomite relicts of the host dolostones, suggesting that replacement (redolomitization of magnesite) occurred at slightly higher oxidation conditions, inducing the precipitation of iron oxides and/or hydroxides.

	MgO%	CaO%	Fe_2O_3%	MnO%
		Magnesite (n=29)		
Mean	47.80	0.46	2.23	0.15
Median	47.38	0.28	2.18	0.15
Standard deviation	2.81	0.46	0.57	0.04
		Dolomite relicts in magnesite (n=16)		
Mean	24.97	26.16	0.66	0.09
Median	24.23	30.89	0.62	0.07
Standard deviation	3.54	8.50	0.21	0.04
		Late dolomite (n=8)		
Mean	22.25	29.81	1.55	0.11
Median	21.95	30.41	1.62	0.09
Standard deviation	2.07	3.41	0.81	0.07

Tab. 4. 1 Statistical data of magnesite and dolomite electron microprobe analyses.

4.2 Trace elements

Trace elements in magnesite and related carbonate rocks have been studied in order to use their signatures as a hint to the source rocks from which Mg^{2+} ions have been derived (Möller 1989). Different sets of trace elements of the magnesite ore body and carbonate host rocks were analyzed to depict their geochemical behavior (Tab. 4, Appendix A). To characterize the individual geochemical environment of important magnesite forming processes (Möller 1989), different groups of trace elements (Sr-Ba, Ti, Fe-Mn and Cr-Ni-Co) were studied (Fig. 4. 7).

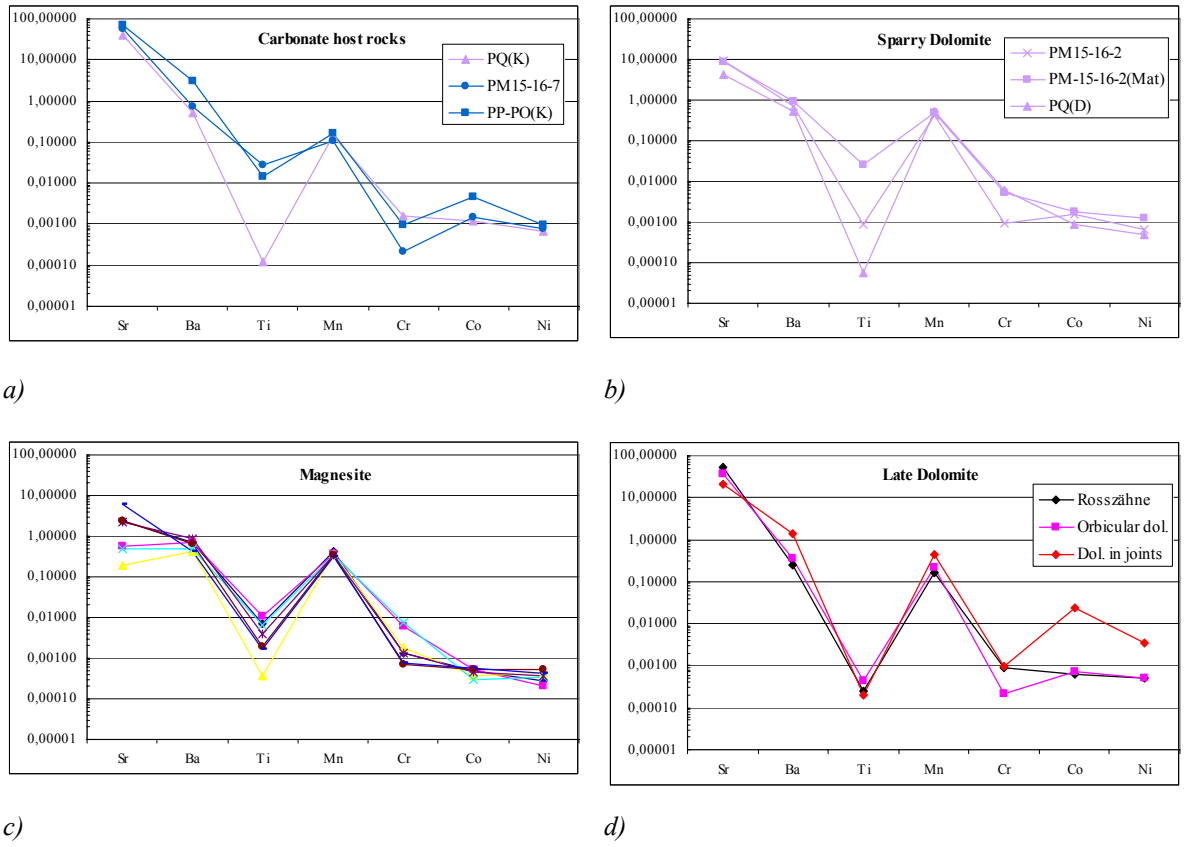

Fig. 4. 7. Chondrite normalized selected trace elements patterns of a) Carbonate host rocks, b) Sparry dolomite, c) Magnesite ore body and d) Late dolomite.

Sr and Ba

Sr^{2+} and Ba^{2+} have the same ionic charge and their ionic radii are 1.32 A° and 1.49 A°, respectively. Both of these elements belong to large ion lithophile (LIL) elements and low filed strength (LFS) elements, therefore they have similar geochemical behavior. But in all studied carbonate samples of the study area there is no meaningful correlation between Sr and Ba. The Sr and Ba contents of the investigated magnesite (Sr: 2.0-62.7 ppm, Ba: 0.4–

3.2 ppm) are generally lower than those of the limestone and dolomite host rocks (Sr: 413.0–727.0 ppm, Ba: 1.8–10.9 ppm) as well as redolomitizated magnesite (Sr: 60.9–526.2 ppm, Ba: 1.1–4.0 ppm). The carbonates of Sr and Ba crystallize in the aragonite structure, for that reason, Sr and Ba substitution in calcite-structure magnesite should be of minor relevance. The Sr and Ba ions will be constantly rejected during magnesite crystallization and recrystallization because they are to large and cannot enter the magnesite lattice (Möller 1989). Therefore low Sr and Ba concentration in magnesite samples do relate to ionic radii differences between the large Sr and Ba ions and the smaller Mg and Fe ions. The relatively high Sr concentrations in some samples probably reflect dolomite inclusions and redolomitization of magnesite. Sr contents of sparry dolomite (at the contact to the magnesite) are very much lower (45.1–99.4 ppm) than of dolomite host rock (413.0 ppm) and late dolomite (222.0–572.3 ppm) and are near the magnesite values. The concentration of Sr and Ba of all magnesite samples indicate Log C_{Sr}: 3.309 to 2.721 and Log C_{Ba}: -0.392 to 0.604. These values compared to the marine/evaporitic, lacustrine and Mg^{2+}-metasomatism magnesite for Sr concentration (Fig. 4. 8 a-b), and marine/evaporitic magnesite for Ba concentration (Fig. 4. 8 c-d).

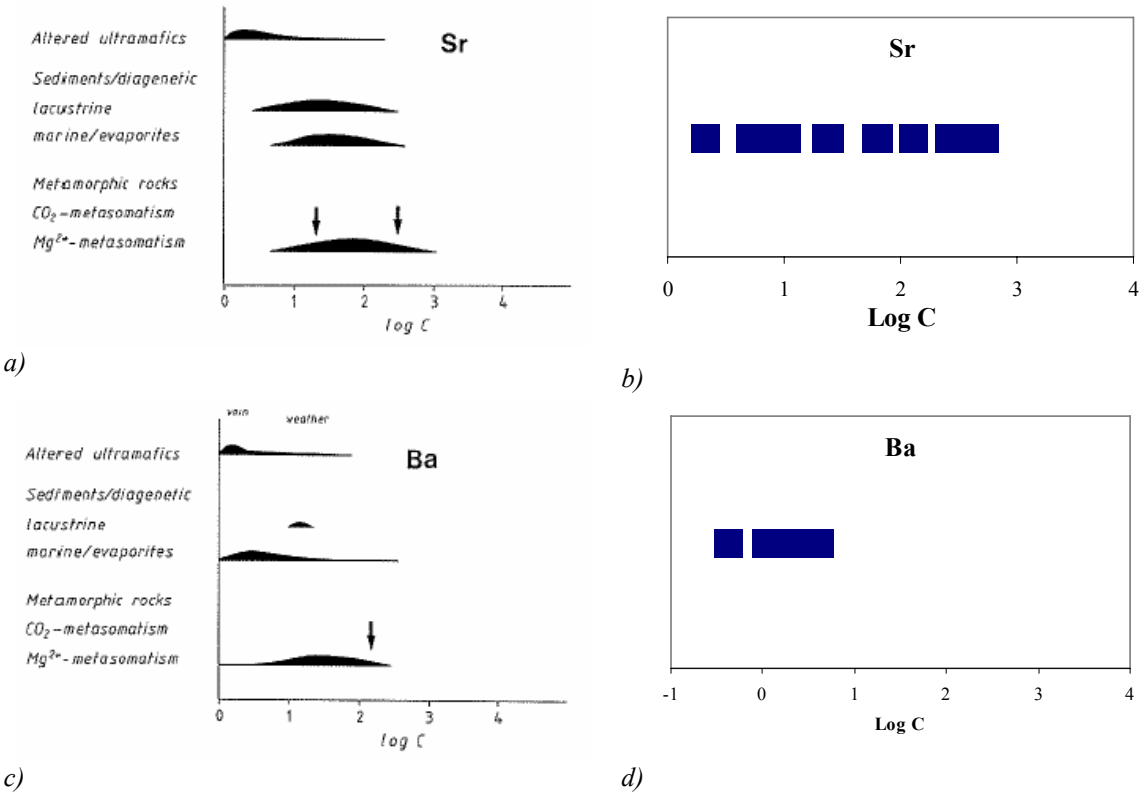

Fig. 4. 8 Distribution of Sr (ppm) and Ba (ppm), a and c in magnesite from different environments (Möller 1989); b and d in magnesite from Hohentauern/Sunk.

Ti

Ti concentration of all magnesite samples range from Log C_{Ti}: –0.755 to 0.922, it is lower than magnesite deposited from marine/evaporitic environment and Mg^{2+}-metasomatism magnesite (Fig. 4 9 a-b). Ti concentration covers partially the range of magnesite, which derived from ultrabasic rocks. Ti is present exclusively as a minor trace phase and is always in the insoluble residue (Martiny & Rojkovic 1977). Petrography and major elements geochemistry of magnesite samples from the study area show that rutil is a main detrital heavy mineral, which mixed with insoluble material. Therefore lower concentration of Ti in magnesite samples from Hohentauern/Sunk deposit in comparison with marine/evaporitic magnesite and Mg^{2+}-metasomatism magnesite can be related to analytical methods. Magnesite samples of study area were analyzed by AAS as separated mineral samples which have very low insoluble material (carbonaceous and clay minerals), while analytical results which used to describe magnesite from different environments (Möller 1989) derived from magnesite bulk samples.

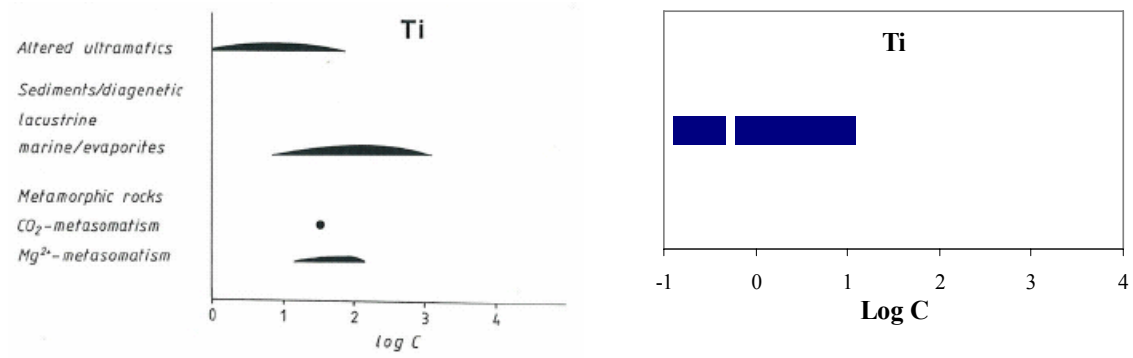

a) *b)*

Fig. 4. 9 Distribution of Ti (ppm), a in magnesite from different environments (Möller 1989); b in magnesite from Hohentauern/Sunk.

Fe and Mn

Fe and Mn have similar geochemical behavior in all magnesite samples analyzed and they show positive correlation (correlation coefficient r = 0.8848, Fig. 4. 10). Both elements are partly hosted in the magnesite. Positively correlated Mn with Fe is interpreted to indicate that Mn was incorporated into the magnesite lattice during magnesite formation.

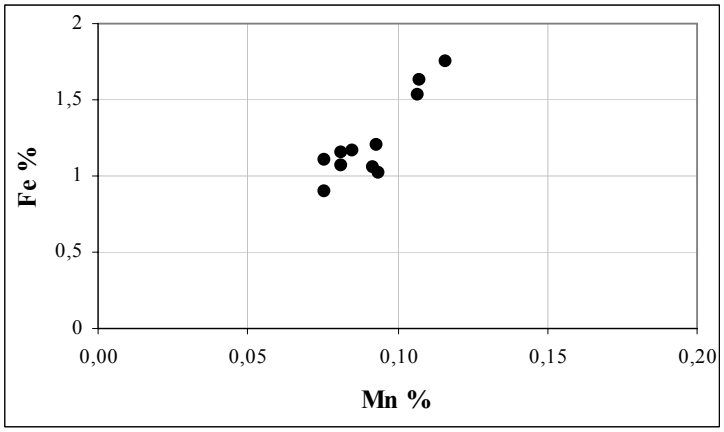

Fig. 4. 10 Fe-Mn correlation in magnesite samples analyzed by AAS.

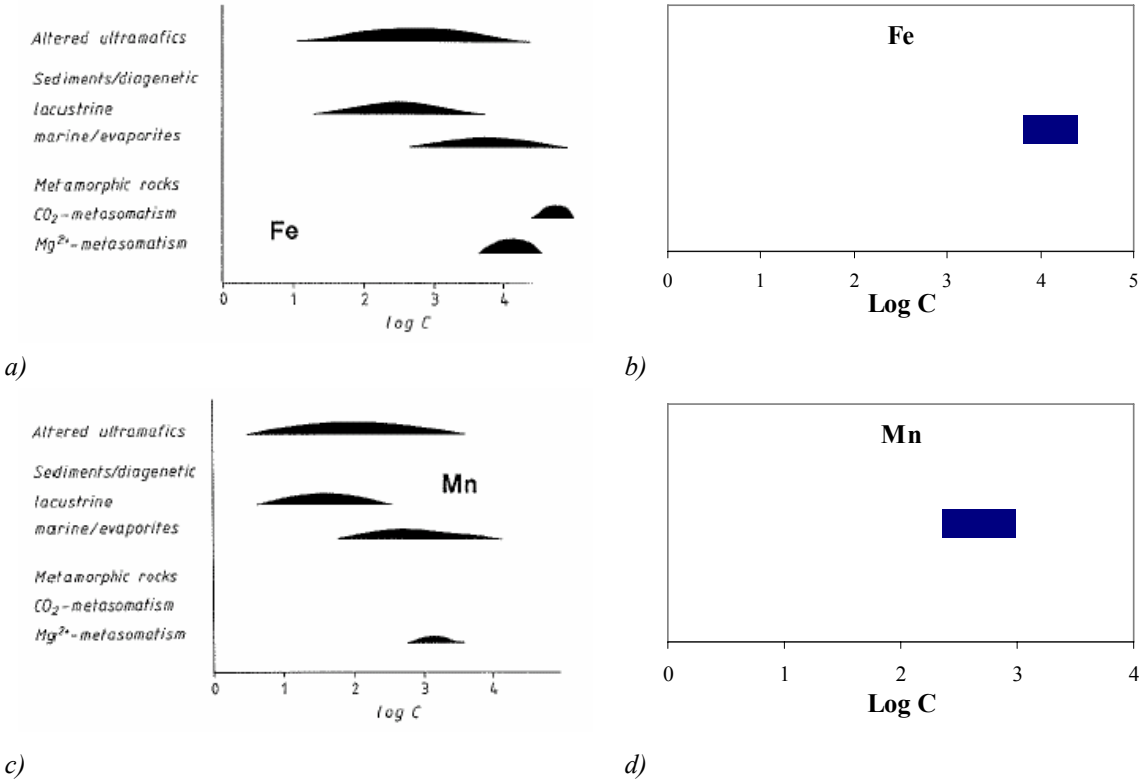

Fig. 4. 11 Distribution of Fe (ppm) and Mn (ppm), a and c in magnesite from different environments (Möller 1989); b and d in magnesite from Hohentauern/Sunk.

Fe and Mn concentrations cover ranges typical for lacustrine as well as marine/evaporitic magnesite and their concentration is high in Mg^{2+}-metasomatism magnesite (Fig. 4. 11 a-c). Fe and Mn concentrations of all magnesite samples from the Hohentauern/Sunk deposit indicate Log C_{Fe}: 3.95 to 4.24 and Log C_{Mn}: 2.88 to 3.06. These values fit to the marine/evaporitic magnesite and Mg^{2+}-metasomatism magnesite (Fig. 4. 11 b-d).

Cr, Ni, Co

Cr, Ni and Co concentrations of all magnesite samples from Hohentauern/Sunk deposit indicate Log C_{Cr}: 0.089 to 1.224, Log C_{Ni}: 0.300 to 0.946 and Log C_{Co}: -0.862 to -0.340 (Fig. 4. 12 b-d-f).

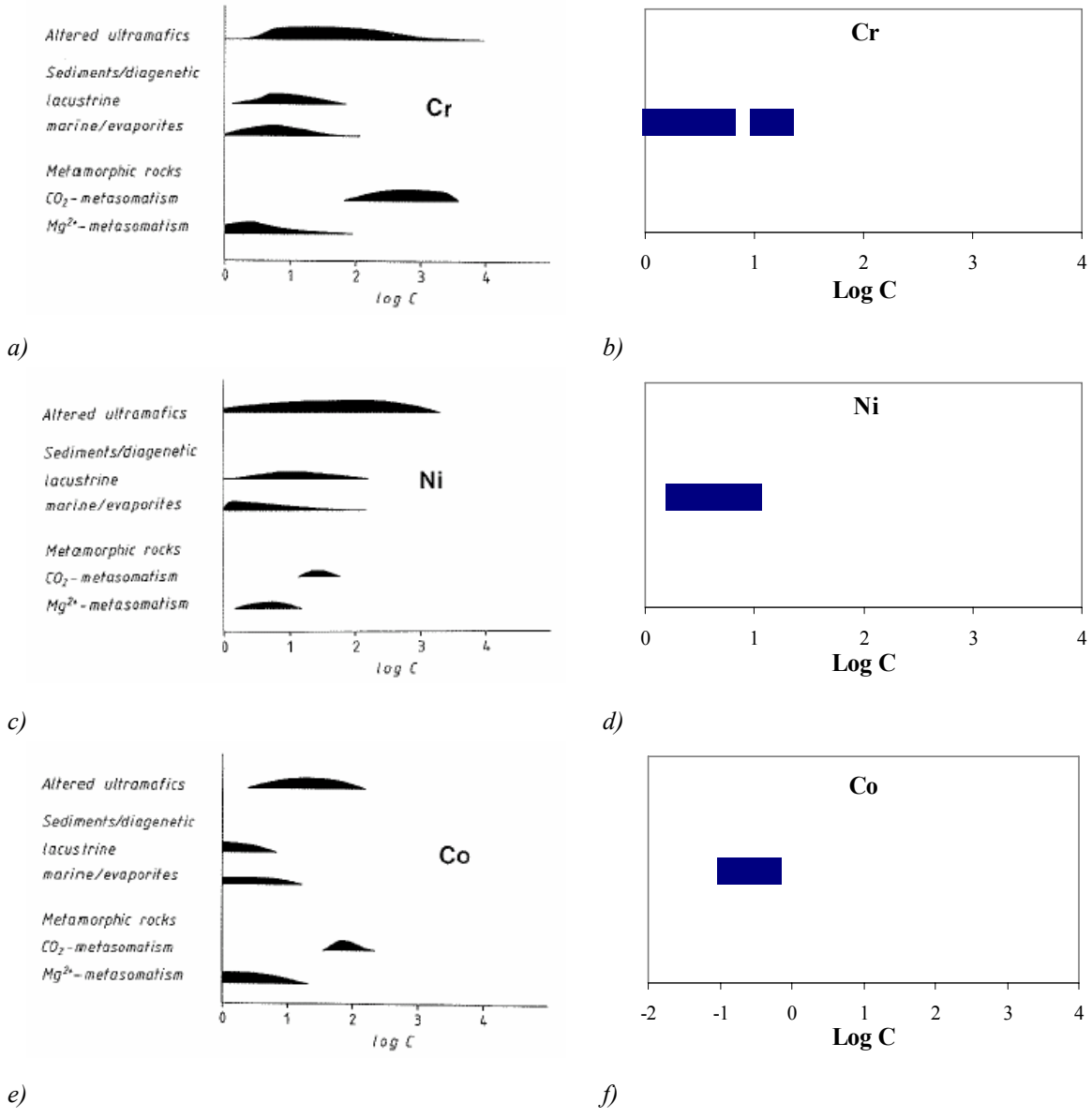

Fig. 4. 12 Distribution of Cr (ppm), Ni and Co (ppm), a, c and e in magnesite from different environments (Möller 1989); b, d and f in magnesite from Hohentauern/Sunk.

Concentration of Cr cover mainly ranges of marine/evaporitic magnesite and Mg^{2+}-metasomatism magnesite and partly of lacustrine magnesite. In the lacustrine environment Mg^{2+} is largely derived from ultramafic rocks in contrast to Mg^{2+} in marine environment (Möller 1989). Therefore concentration of Cr can indicate marine/evaporitic and Mg^{2+}-

metasomatism environment. Ni has a same concentration pattern such as Cr and reflects marine/evaporitic magnesite and Mg^{2+}-metasomatism magnesite. Co concentration of magnesite samples is very low in contrast to magnesite from different environments.

4.3 Rare earth elements (REE)

It may be possible to distinguish between the main lines of thought of magnesite formation, i.e. precipitation and metasomatism, by studying the REE distribution in magnesite (Morteani et al 1982, 1983). Among the trace elements in carbonates, the lanthanides are most useful to know about the probable sources of magnesite-forming Mg^{2+} ions (Möller 1989). Because their concentration levels are well below 1000 ppm, their trivalent ionic radii (1.17-1.0 A°) correspond well with that of Ca^{2+} (1.14 A°) in coordination number VI (Shannon 1976), and most of the chemical and physico-chemical properties change aperiodically within their series.

It is important to know that the contamination of magnesite and other carbonate rock mineral phases by detrital material (aluminosilicates) has an effect on REE distributions, which is indicated by the positive correlation between Al_2O_3 and REE contents. According to Parekh et al. (1977), roughly 1 percent of contaminating clay minerals contains amounts of REE comparable to the amount of such elements in a pure low magnesian calcite. The positive correlation between Al_2O_3 and REE contents is due basically to LREE, which are preferentially concentrated in clay minerals. In contrast, small amounts of clay minerals within the carbonate phases show little effect on REE distributions. Therefore, to avoid such contamination, only magnesite samples without or with very low amounts of deterital aluminosilicates were considered in the interpretation of the REE geochemistry. The abundance of REE in the magnesite ore body, its carbonate host rocks and late dolomite mineralization phases are shown in Tab. 5, Appendix A and chondrite normalized REE patterns (Fig. 4. 14 to 4. 18).

Carbonate host rocks and sparry dolomite

Total REE concentrations in all analyzed samples of carbonate host rocks (limestone and early dolomite) and sparry dolomite (at the contact of the magnesite ore body) are positively correlated with Al_2O_3 (r=0.89). This reflects the contamination by detrital aluminosilicates and the clay minerals (Fig. 4. 13). Limestone and early fine-grained dolomite (dolostone) as host rocks of the magnesite ore body have similar chondrite

normalized REE patterns (Fig. 4. 14). Though, the total REE contents of the fine-grained dolomite (absolute values: 2.66 ppm) are much lower than of limestone (absolute values: 17.33–29.51 ppm, mean: 23.42 ppm) and show a general decrease of REE abundances, suggesting that fine-grained dolomite has very low content of clay minerals (Fig. 4. 13) in comparison with limestones (Al_2O_3 content of fine-grained dolomite is 0.032 % and 0.570 % in limestone).

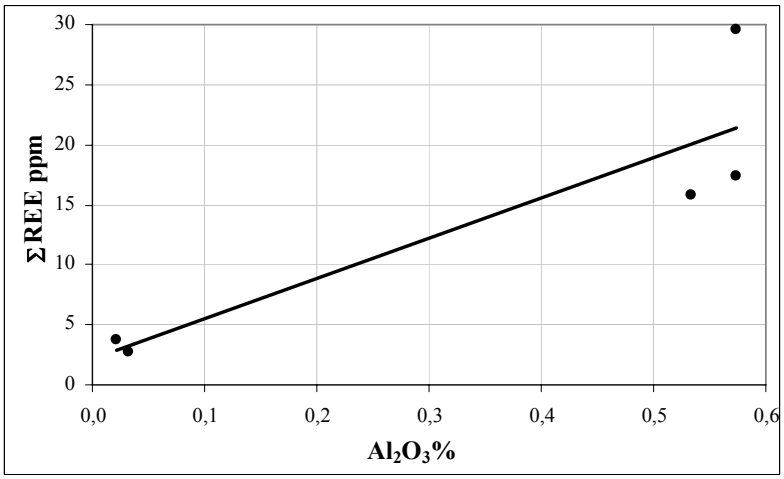

Fig. 4. 13 A positive correlation between REE contents and Al_2O_3 of carbonate host rock.

The normalized REE patterns of all carbonate host rock samples exhibit the characteristic negative Ce anomalies[1] (Fig. 4. 14). According to Möller (1989) and Bau & Möller (1992), two processes of carbonate formation can produce a negative Ce anomaly: deposition from seawater and from hydrothermal solutions equilibrated with highly oxidized sediments. This second case can be discarded because of the presence of abundant pyrite and carbonaceous material, which indicates formation under euxinic conditions. The negative Ce anomaly indicates that these rocks formed in a marine environment.

The negative Eu[2] anomalies of the limestone (Fig. 4. 13) can be explained by contamination of noncarbonate (e.g. clay minerals) components of the original sediments (Kiesl et al. 1990) and/or formation under euxinic conditions (Lugli et al. 2000). The positive Eu anomaly of the fine-grained dolomite (Fig. 4. 14) may have been effected by a feldspathic component (see chapter 3), because feldspars are the most abundant minerals with prominent positive Eu anomalies.

[1] $Ce/Ce^* = Ce/\sqrt{(La \times Nd)}$
[2] $Eu/Eu^* = Eu_N/\sqrt{(Sm_N \times Gd_N)}$

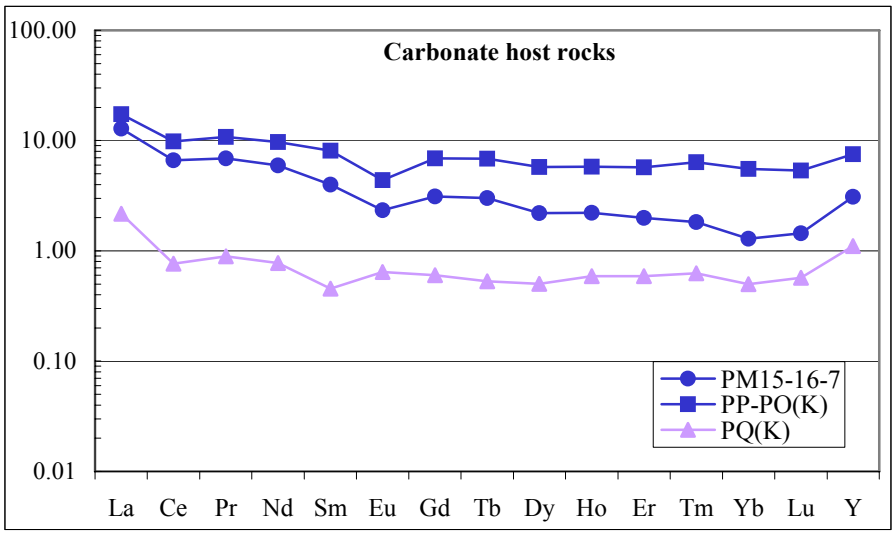

Fig. 4. 14 Chondrite normalized REE patterns of carbonate host rocks (Blau: Limestone, Purple: Dolomite).

Sparry dolomite, which formed at the contact of the magnesite ore body has chondrite normalized REE patterns similar to carbonate host rocks (Fig. 4. 15). The total REE content (absolute values: 3.72 ppm) of the sparry dolomite [bulk sample of dolomite crystals and matrix, PQ (D)] is very close to the early fine-grained dolomite (absolute values: 2.66 ppm) with similar Ce and Eu anomalies. Separated material of sparry dolomite crystals and matrix indicate the following (Fig. 14. 5):

-The chondrite normalized REE pattern of the matrix is similar to those of the limestone host rocks, which are characterized by negative Ce and Eu anomalies.
-The REE pattern of dolomite crystal grains differ markedly from matrix materials with any Eu anomaly and it is comparable to early fine-grained dolomite.

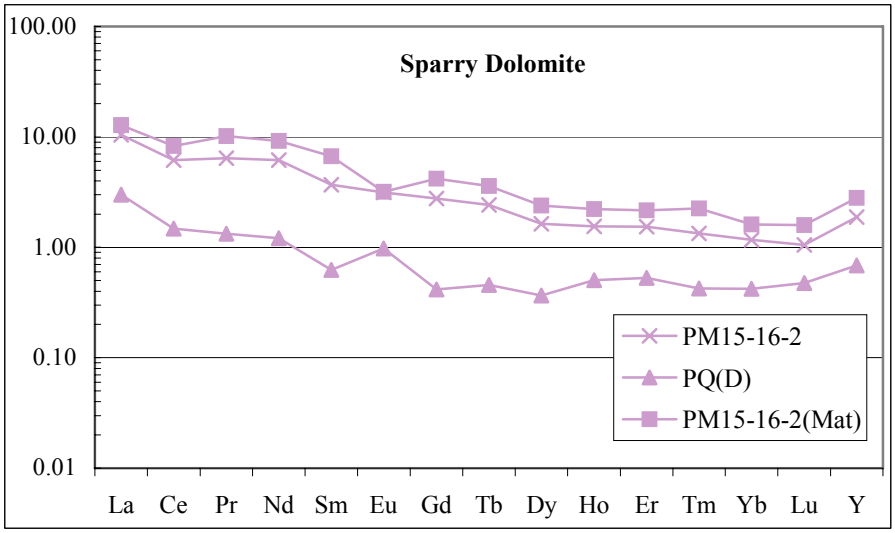

Fig. 4. 15 Chondrite normalized REE patterns of sparry dolomite.

Magnesite

The normalized REE patterns of magnesite of the ore body are shown in Fig. 4. 16 and 4. 17. The REE contents of the magnesite (absolute values: 3.18 –29.17 ppm, mean: 13.53 ppm) are lower as in the host limestone, mainly due to their low concentration of LREE, and higher as in the early fine-grained dolomite. The LREE content in the magnesite seems to indicate a higher mobility than the HREE, because the ion radii of the HREE are much more similar to the Mg^{2+} ion radius than those of the LREE. Hence the LREE will be enriched in the fluid phase and can thus be depleted in the solid phases. The LREE which concentrate in the fluid phase can later be captured during redolomitization (Fig. 4. 17 and 4. 18). Depletion of LREE in magnesite samples is reflected by low LREE/HREE ratios of magnesite. The LREE/HREE ratios of magnesit samples without redolomitization are between 0.13 and 3.02. They are lower than in magnesite affected by redolomitization (the LREE/HREE ratios are between 1.16 and 4.45) and carbonate host rocks with LREE/HREE ratios of 2.80 to 5.23. The sparry magnesite with big crystals [M4 (PI)] shows extremely low LREE contents (Fig. 4. 16). Depletion of LREE in comparison to carbonate host rocks is a result of mineralogical control (Krupenin 2002). Additional fractionation and decrease of LREE is connected to metasomatic recrystallization (Möller 1989), because more quantity of fluids has passed through such zones (Krupenin 2002).

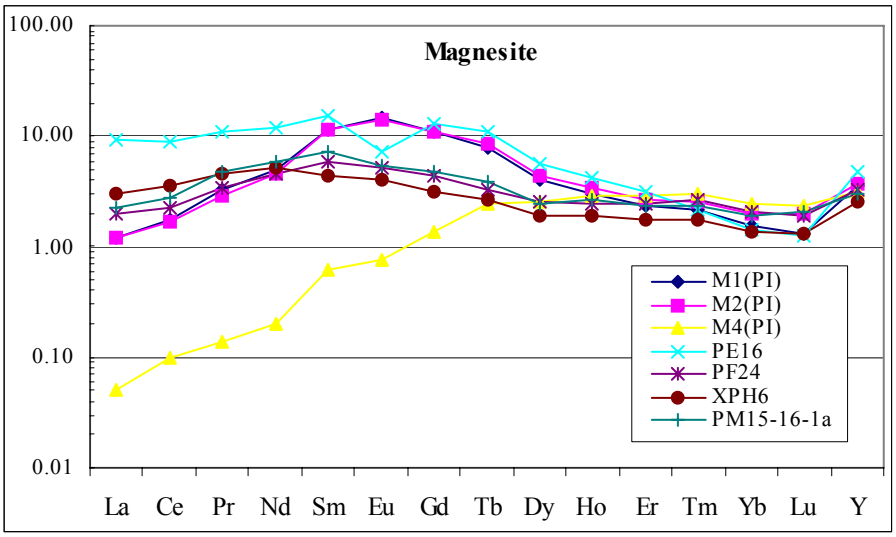

Fig. 4. 16 Chondrite normalized REE patterns of magnesite.

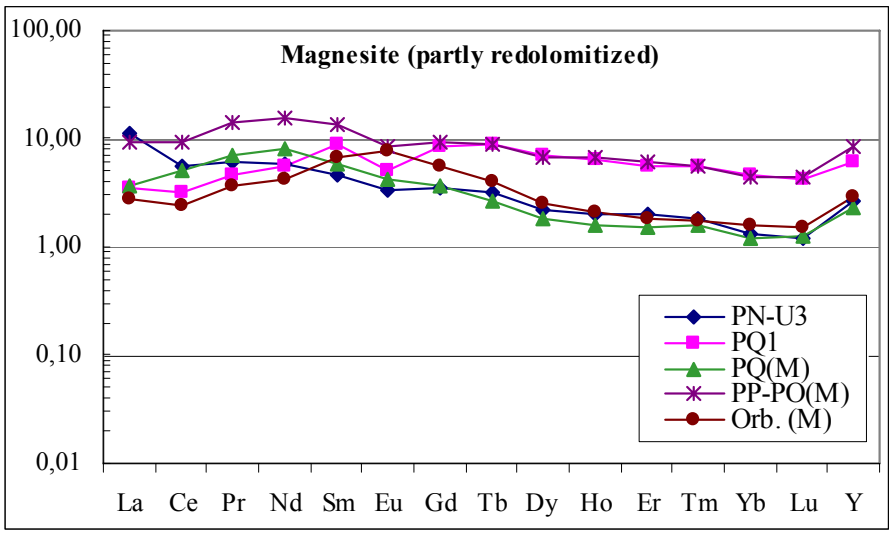

Fig. 4. 17 Chondrite normalized REE patterns of magnesite with partly redolomitized.

The normalized REE patterns of all magnesite samples are characterized by negative Ce-anomalies. They show the same type of negative Ce-anomalies (Ce/Ce* = 0.71-0.97) as the sparry dolomite (Ce/Ce* = 0.77) and carbonate host rocks (Ce/Ce* = 0.59-0.76, Fig. 4. 16 to Fig.4. 17). These negative Ce-anomalies were inherited by magnesite from its dolomitic precursors and carbonate sediments which are marked by the Ce-deficiency in seawater (Hogdahl 1968 and Morteani et al. 1982). The normalized REE patterns of magnesite samples are not clearly characterized by distinct Eu anomalies. Three samples of magnesite without redolomitization have a negative Eu anomaly (Eu/Eu* = 0.51-0.93) and four of them a positive Eu anomaly (Eu/Eu* = 1.01-1.31). In general, the negative Eu-anomalies are due to magnesite formation in a chemical reducing environment (Möller 1983), and the positive Eu-anomalies in the REE patterns of the magnesite formation can indicate that the fluid was involved in decomposition of feldspars prior to magnesite formation since feldspars are the only magmatic rock-forming minerals with excess of Eu.

Late dolomite

The late dolomite normalized REE patterns with high LREE/HREE ratios (2.96 to 3.62; Fig. 4. 18) are different to those of magnesite samples without redolomitization. They are characterized by negative Ce anomalies (0.38-0.74) and their Eu anomalies are not clearly characterized (0.62 to 1.11). Comparison between late dolomite and magnesite normalized REE patterns shows an enrichment of LREE in comparison with magnesite, suggesting that LREE was enriched in solution during magnesite formation, captured by dolomite

along redolomitization and late dolomite formation. Therefore, it seems that the dolomite with the relatively high concentration of LREE crystallized from LREE-enriched solutions which were rejected by magnesite mineral phase.

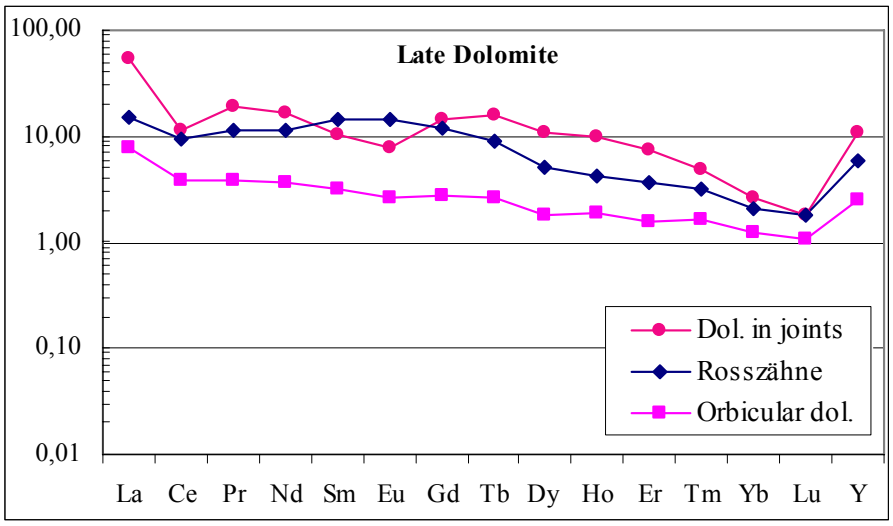

Fig. 4. 18 Chondrite normalized REE patterns of late dolomite.

4.4 Stable isotope geochemistry

Data of isotopes of O and C give fundamental information regarding carbonates, e.g. the origin of C and O in fluids, mixing of fluids, secondary processes, biogenic activity and temperature range of fluids (Schroll 2002). The O and C isotopic compositions (the variations of the $\delta^{18}O$ and $\delta^{13}C$ values) of limestones provide criteria for the evaluation of the depositional environment for samples of a wide range of geological age. Especially the C isotopes are the most significant, as tracers for the origin of C, while O isotopes store informations of the paleotemperature (Clark & Fritz 1997). The O isotopic composition of dolomite reflects the temperature of precipitation and the isotopic composition of the dolomitizing fluids and the C isotopic composition of dolomite is generally strongly influenced by that of the precursor $CaCO_3$ and gives information on the source of the C in carbonates (Tucker & Wright 1990). Stable isotope data are being increasingly used in the genetic interpretation of dolomites and when combined with trace elements and petrography they can help greatly to elucidate their origin (Tucker & Wright 1990).

The O and C isotopic compositions of magnesites correspond to the classification of magnesite deposits and could offer an important tool for distinguishing between different genetic types of magnesite (Schroll et al. 1986b, Aharon 1988, Schroll 2002). The O

isotope data reflects the isotopic signature of water in which the magnesite precipitates and the temperature in which precipitation occurs. The C isotopes are important markers in determining the source of C (Schroll 2002). The C isotopes of magnesite depend among others on the C isotopic compositions of coeval seawater and its carbonate rocks, evaporation, CO_2-C from microbial fermentation processes, anaerobic decomposition of organic matter, thermal decomposition of carbonates (± organic matter), CO_2 produced by metamorphic and magmatic processes or combination of each above (Schroll 2002).

O and C stable isotope measurements were carried out with a MC-ICP-MS in the Stable Isotope Laboratory of the University of Nanjing, China. There were analyzed 29 mineral separate samples of the different carbonate types. O and C isotope compositions of the different carbonate types (Azim Zadeh et al. 2007, Ebner et al. 2008a) are listed in Tab. 4. 2 and plotted in Fig. 4. 19.

Carbonate host rocks

Limestone from Steilbachgraben formation yields $\delta^{18}O$ values ranging from 14.49 ‰ to 14.85 ‰ SMOW (mean: 14.63 ‰; n=3) and $\delta^{13}C$ values ranging from 1.59 ‰ to 3.27 ‰ PDB (mean: 2.66 ‰; n=3). The $\delta^{18}O$ and $\delta^{13}C$ values are within the normal range for marine carbonates (Fig. 4. 19). Lower values of $\delta^{18}O$ for limestone in comparison with shallow marine sediments (30.4 to 32.5 ‰ SMOW, Veizer 1983) can be attributed to the effects of more depleted seawater (Tucker & Wright 1990) or that they have reequilibrated with solutions that were more depleted in $\delta^{18}O$ than marine waters, most likely during diagenesis (Fernandez-Nieto et al. 2003).

Early fine-grained dolomite

The $\delta^{18}O$ and $\delta^{13}C$ values of early fine-grained dolomite samples are plotted in Fig. 4. 19. Early fine-grained dolomite has $\delta^{18}O$ values of 18.95 ‰ to 19.11 ‰ SMOW (mean: 19.05 ‰; n=3). The $\delta^{18}O$ values are within the marine limestone domain but they have higher $\delta^{18}O$ values than those of limestones. Dolomite typically shows higher $\delta^{18}O$ values as compared to calcite, due to the enrichment in $\delta^{18}O$ occurring during dolomite-calcite fractionation (Clark & Fritz 1997). The $\delta^{18}O$ value of the early fine-grained dolomite is about 4 ‰ heavier than those of limestone. It can be interpreted to dolomite-calcite fractionation $\Delta\ ^{18}O_{dol\text{-}cal}$ during diagenesis (Fig. 4. 20).

Sample No.	$\delta^{13}C$ (PDB) ‰	$\delta^{18}O$ (PDB) ‰	$\delta^{18}O$ (SMOW) ‰
	Limestone		
PM15-16-7-a	3.13	-15.88	14.54
PM15-16-7-b	3.27	-15.93	14.49
PP-PO(K)	1.59	-15.58	14.85
	Fine-grained dolomite		
PQ(K)-a	1.11	-11.46	19.10
PQ(K)-b	1.10	-11.60	18.95
PQ(K)-c	1.09	-11.45	19.11
	Magnesite		
M1(PI)-a	-2.05	-19,34	10.97
M1(PI)-b	-1.95	-19.45	10.86
M1(PI)-c	-1.83	-19.44	10.87
M2(PI)	-2.23	-20.55	9.72
M4(PI)-g	-2.01	-18.03	12.32
PE16	-1.20	-20.68	9.59
PF24	-1.82	-20.67	9.60
PM15-16-1a	-0.61	-18.33	12.01
XPH6	-0.02	-20.24	10.05
XPH6(Matrix)	-1.33	-16.63	13.77
	Magnesite (partly redolomitized)		
PN-U3	-0.76	-15.87	14.55
PP-PO(M)-a	-0.71	-19.91	10.38
PP-PO(M)-b	-0.69	-19.76	10.54
PQ(M)	-0.34	-20.08	10.21
PQ1	-0.83	-14.24	16.23
Orbicular.(Mag.)	-1.12	-15.99	14.43
	Sparry dolomite		
PQ(D)	0.79	-19.43	10.88
PM15-16-2-a	0.34	-19.18	11.14
PM15-16-2-b	0.33	-18.98	11.34
PM15-16-2(Matrix)	0.26	-14.89	15.56
	Late dolomite		
Orbicular.(Dol.)	-0,54	-16,57	13.83
Orbicular.(Matrix)	-0,27	-16,34	14.06
“Rosszähne” dolomite	-1.26	-16.51	13.89
Dolomite in joints	1.74	-11.47	19.08

Tab 4. 2 Stable isotope data from different carbonate minerals of Hohentauern/Sunk magnesite deposit.

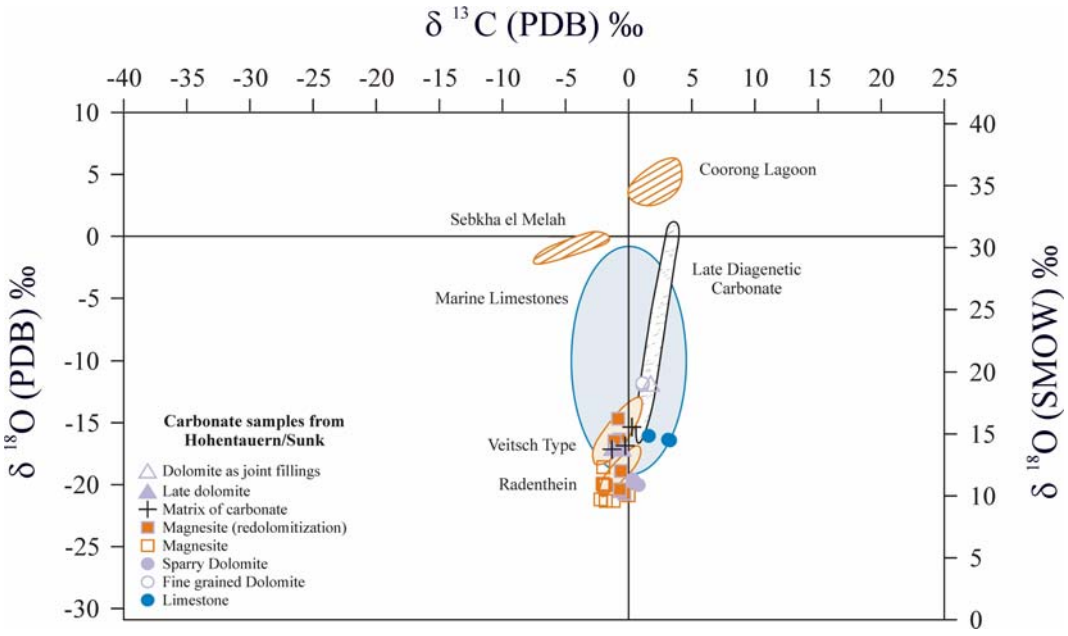

Fig. 4. 19 C versus O isotope values from different carbonate minerals of the Hohentauern/Sunk magnesite deposit documented in the diagram after Schroll 2002.

The $\delta^{13}C$ values of the early fine-grained dolomite are 1.09 ‰ to 1.11 ‰ PDB (mean: 1.10 ‰; n=3) and well situated within the field of marine $CaCO_3$. This suggests that the $\delta^{13}C$ has been inherited from the $CaCO_3$ replaced by the dolomite or derived from the dolomitizing fluids (modified seawater) which had a $\delta^{13}C$ value similar to the seawater from which the $CaCO_3$ grains were precipitated (Tucker & Wright 1990). The $\delta^{18}O$ and $\delta^{13}C$ values indicate that the early fine-grained dolomite is within the late diagenetic carbonate domain (Fig. 4. 19).

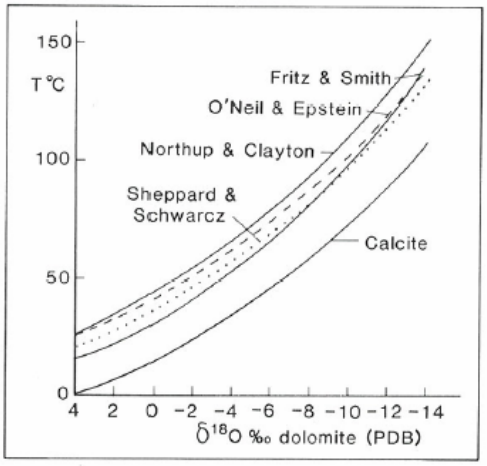

Fig. 4. 20 Dolomite – water and calcite – water fractionation equations show that dolomite will be about 3 ‰ to 6 ‰ heavier than coprecipitated calcite (Tucker & Wright 1990).

Magnesite

The $\delta^{18}O$ values of magnesite range from 9.59 ‰ to 12.32 ‰ SMOW (mean: 10.67 ‰; n=9) those of $\delta^{13}C$ from -2.23 ‰ to –0.02 ‰ PDB (mean: -1.52 ‰; n=9). They are depleted relative to the carbonate host rocks and overlap with values reported for magnesite formed by metasomatic dolomite replacement (Fig. 4. 19). The isotope data of deposits of sparry magnesite hosted by metasediments correspond with marine carbonate rocks ($\delta^{13}C$ at 0 ‰ PDB and $\delta^{18}O<20$ ‰ SMOW). There is no significant isotopic difference between sparry magnesite and their supposed precursor rocks.

The lighter $\delta^{18}O$ values of magnesite samples can be referred to as increasing of temperature (Hudson 1977). They are indicating an increase in the temperature after the deposition (Velasco et al. 1987). The shifting to lower $\delta^{18}O$ values is typical for magnesite deposits influenced by diagenetic and metamorphic processes (Schroll 2002). Mineral phases of partly redolomitized magnesite and late dolomite are enriched in $\delta^{18}O$.

The $\delta^{13}C$ values of magnesite as well as partly redolomitized magnesite and late dolomite tend toward lighter and negative contents (Fig. 4. 19). This would be expected if the sedimentary C was mixed with the lighter C from the organic material oxidized during metamorphic processes (Velasco et al. 1987). Increasing metamorphism changes the $\delta^{13}C$ into lighter C (Schroll 2002).

Sparry dolomite

Sparry dolomite has $\delta^{18}O$ values varying from 10.88 ‰ to 11.34 ‰ SMOW (mean: 11.12 ‰; n=3) and $\delta^{13}C$ values from 0.33 ‰ to 0.79 ‰ PDB (mean: 0.49 ‰; n=3). Sparry dolomite has similar $\delta^{18}O$ values and heavier $\delta^{13}C$ values than magnesite (Fig. 4. 19). Its $\delta^{13}C$ values are positive and they are close to early fine-grained dolomite. The matrix materials of sparry dolomite have $\delta^{18}O$ values of 15.56 ‰ SMOW and $\delta^{13}C$ value of 0.26 ‰ PDB. Their $\delta^{18}O$ value is similar to limestone (mean value: 14.63 SMOW ‰) and the $\delta^{13}C$ value is positive, too.

Partly redolomitized magnesite

Magnesite affected by redolomitization has heavier $\delta^{18}O$ values from 10.88 ‰ to 16.23 ‰ SMOW (mean: 12.62 ‰; n=7) and $\delta^{13}C$ values from -1.12 ‰ to -0.34 ‰ PDB (mean: -0.72 ‰; n=7) than magnesite without redolomitization (Fig. 4. 19). The variation in $\delta^{18}O$ within the two mentioned types of magnesite can be interpreted as the effects of different isotopic fractionation for magnesite and dolomite.

Late dolomite

Late dolomite has $\delta^{18}O$ values from 13.83 ‰ to 13.89 ‰ SMOW (mean: 13.86 ‰; n=2) and $\delta^{13}C$ values from -1.26 ‰ to -0.54 ‰ PDB (mean: -0.90 ‰; n=2). In comparison to sparry magnesite late dolomite is enriched in $\delta^{18}O$ and $\delta^{13}C$ (Fig. 4. 19). The similar $\delta^{18}O$ and $\delta^{13}C$ values of the partly redolomitized magnesite and late dolomite and the similar increasing path of the $\delta^{18}O$ values in Fig. 4.19 suggest that redolomitization of magnesite and formation of late dolomite occurred during the same geologic events which produced the fluids for redolomitization.

Dolomite as joint fillings is hosted by early fine-grained dolomite. It has $\delta^{18}O$ value of 19.08 ‰ SMOW and $\delta^{13}C$ value of 1.74 ‰ PDB. Its $\delta^{18}O$ and $\delta^{13}C$ values are very different compared to late dolomites. Dolomite as joint fillings has similar $\delta^{18}O$ and $\delta^{13}C$ values as early fine-grained dolomite (Fig. 4. 19), suggesting that crystallization of dolomite occurred by dissolution and remobilization of early fine-grained dolomite.

4.5 Sr isotopes characteristic

The Sr isotopes have been used to characterize environments and, particularly, to differentiate between the marine and continental environments (Clauer & Tardy 1971, Faure & Barrett 1973). Isotopic composition of Sr in carbonate rocks has become an important tool for environmental and diagenetic studies. Interpretations of the original environment and secondary changes have been fostered by investigating seawater, river water and subsurface brines (Kralik 1989). However, this technique requires some precautions. The natural disintegration of the radioactive ^{87}Rb contained in the authigenic samples gives radiogenic ^{87}Sr and hence must be taken into account (Clauer 1976). In minerals which contain very low concentrations of Rb (<1 ppm) but high concentrations of

common Sr, the $^{87}Sr/^{86}Sr$ ratio may yield an approximate measure of the isotopic composition of Sr in the mineralizing fluid. If the Rb/Sr ratio is less than 0.1, the minerals can be analyzed without any correction for the radiogenic ^{87}Sr. On the other hand, the carbonates of Sr crystallize in the aragonite structure, for that reason Sr substitution in the calcite-structure of magnesite should be minor. The Sr ions will be constantly rejected during magnesite crystallization and recrystallization because they are to large and cannot enter the magnesite lattice (Möller 1989). Therefore low Sr concentration in magnesite samples do relate to ionic radii differences between the large Sr ions and the smaller Mg and Fe ions. As expected, Sr contents are below the detection limit for magnesites (<10 ppm, Lugli et al. 2002) though the relatively high Sr concentrations in some samples probably reflect dolomite inclusions and redolomitization of magnesite.

23 samples from Hohentauern/Sunk magnesite deposit have been chosen on the basis of petrography and major element geochemistry for Sr-isotope characterization. The $^{87}Sr/^{86}Sr$ ratio of these samples have been analyzed whit two different analytical methods:

- Hand picked minerals (separated by using a dental drill) analyzed by HR-ICP-MS.
- LA-MC-ICP-MS along selected profiles of polished sections.

The $^{87}Sr/^{86}Sr$ ratio and Rb and Sr concentrations of magnesite and their adjacent dolomites and limestone are listed in Tab. 4. 3.

The Sr-concentration of the magnesite samples varies between 2.04-62.67 ppm. A positive correlation between Sr and CaO content in whole-rock and mineral samples (Fig. 4. 21, 4. 22) show that Ca is substituted by Sr. The various amounts of CaO in magnesite indicate that the magnesite contains residual inclusions of dolomite which depends on the replaced dolostone precursor or redolomitization of magnesite. In this case, the $^{87}Sr/^{86}Sr$ ratios of dolomites can have an effect on the $^{87}Sr/^{86}Sr$ ratios in magnesite which were measured by HR-ICP-MS. For evaluation of this effect, Sr contents of magnesite and dolomite relicts have been quantitatively analyzed by electron microprobe.

Sample No.	Sr (ppm)	Rb (ppm)	Rb/Sr	$^{87}Sr/^{86}Sr$
		Limestone		
PM15-16-7	609.03	0.285	0.00047	0.708256
PP-PO(K)	726.95	1.900	0.00261	0.708735
		Fine-grained dolomite		
PQ(K)	412.98	0.047	0.00011	0.709338
		Magnesite		
M1(PI)	24.61	0.126	0.00514	0.710881
M2(PI)	6.07	0.077	0.01260	0.709668
M4(PI)	2.04	0.019	0.00933	0.710026
PE16	22.80	0.025	0.00109	0.709180
PF24	5.06	0.011	0.00209	0.709591
XPH6	24.44	0.005	0.00019	0.709662
XPH6(matrix)	10.42	0.037	0.00353	0.709924
PM15-16-1a	62.67	0.020	0.00031	0.710506
		Magnesite (partly redolomitized)		
PQ1	526.19	0.055	0.00010	0.709940
PQ(M)	60.91	0.032	0.00052	0.710003
PP-PO(M)	125.46	0.019	0.00015	0.709315
Magnesite core of Orbicular.dol.	260.12	0.042	0.00016	0.708457
PN-U3	358.41	0.243	0.00068	0.709872
		Sparry dolomite		
PM15-16-2	99.42	0.088	0.00089	0.708976
PM15-16-2(matrix)	88.57	0.585	0.00660	0.709158
PQ(D)	45.13	0.018	0.00039	0.709128
		Late dolomite		
Orbicular dolomite	381.29	0.006	0.00002	0.708392
Orbicular dol.(matrix)	137.71	0.016	0.00012	0.708374
“Rosszähne” dolomite	572.26	0.045	0.00008	0.709790
Dolomite in joints	221.91	0.073	0.00033	0.710513

Tab. 4. 3 Sr isotope data and Rb and Sr concentrations of magnesite and other carbonate minerals of the deposit.

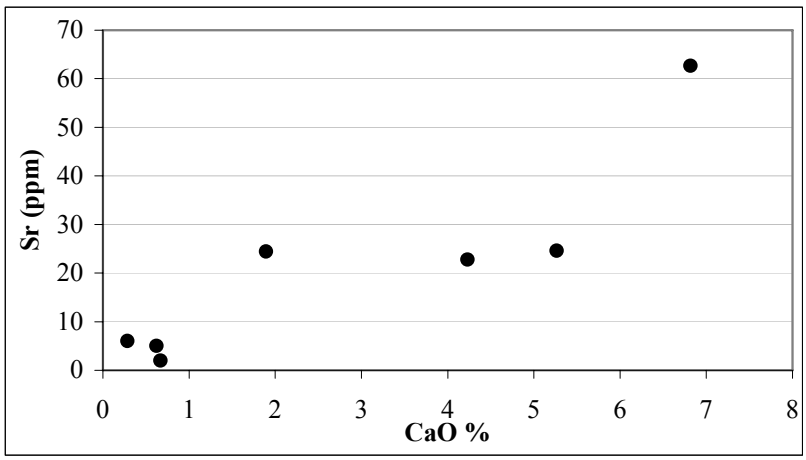

Fig. 4. 21 Positive correlation between CaO and Sr (whole-rock magnesite samples).

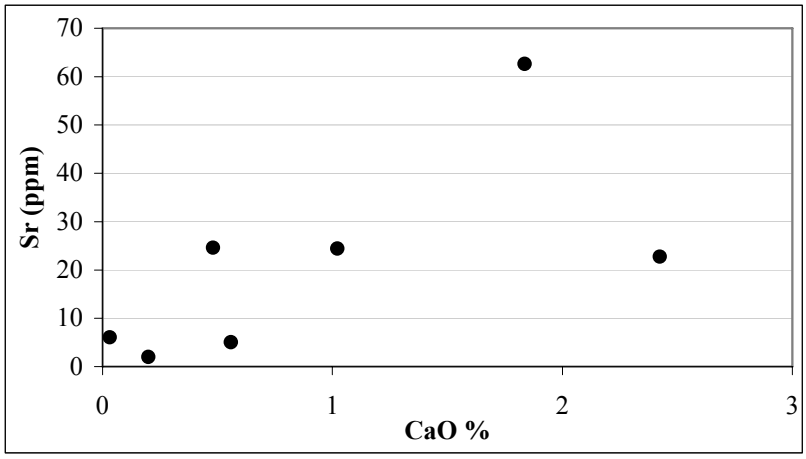

Fig. 4. 22 Positive correlation between CaO and Sr (hand picked magnesite sample).

The electron microprobe analyses of Sr in sparry magnesite and their dolomite microinclusions (Fig. 4. 23) are listed in Tab. 4. 4. The analyses show that magnesite has lower Sr contents than dolomite. The high Sr content of dolomite microinclusions can change the $^{87}Sr/^{86}Sr$ ratios of magnesite, respectively.

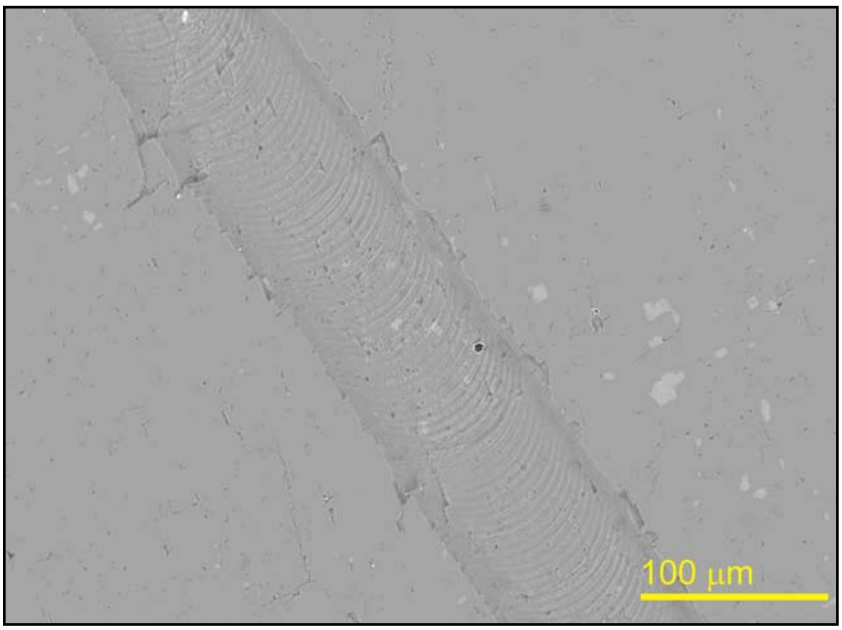

Fig. 4. 23 BSE image of magnesite crystal (dark grey) and dolomite micro inclusions (light grey). The line is a slit of laser ablation across the magnesite crystal.

		SrO%	Sr ppm
Magnesite	mg. 1	BDL*	BDL
	mg. 2	0.011	93
	mg. 3	BDL	BDL
	mg. 4	BDL	BDL
	mg. 5	BDL	BDL
	mg. 6	0.009	76
Dolomite	dol. 1	BDL	BDL
	dol. 2	BDL	BDL
	dol. 3	0.179	1517
	dol. 4	0.16	1356
	dol. 5	0.116	983
	dol. 6	0.071	602
	dol. 7	0.086	729

* Bleow Detection Limit

Tab. 4. 4 Sr contents of sparry magnesite (mg 1 – 6) and dolomite microinclusions (dol 1 – 7) within the magnesite by EMP.

The $^{87}Sr/^{86}Sr$ ratios measured in magnesite by HR-ICP-MS range from 0.70918 to 0.710881. These values are increased in comparison to Early Carboniferous seawater (Fig. 4. 24) in a similar way as also other $^{87}Sr/^{86}Sr$ ratios measured in other carbonate mineral commodities.

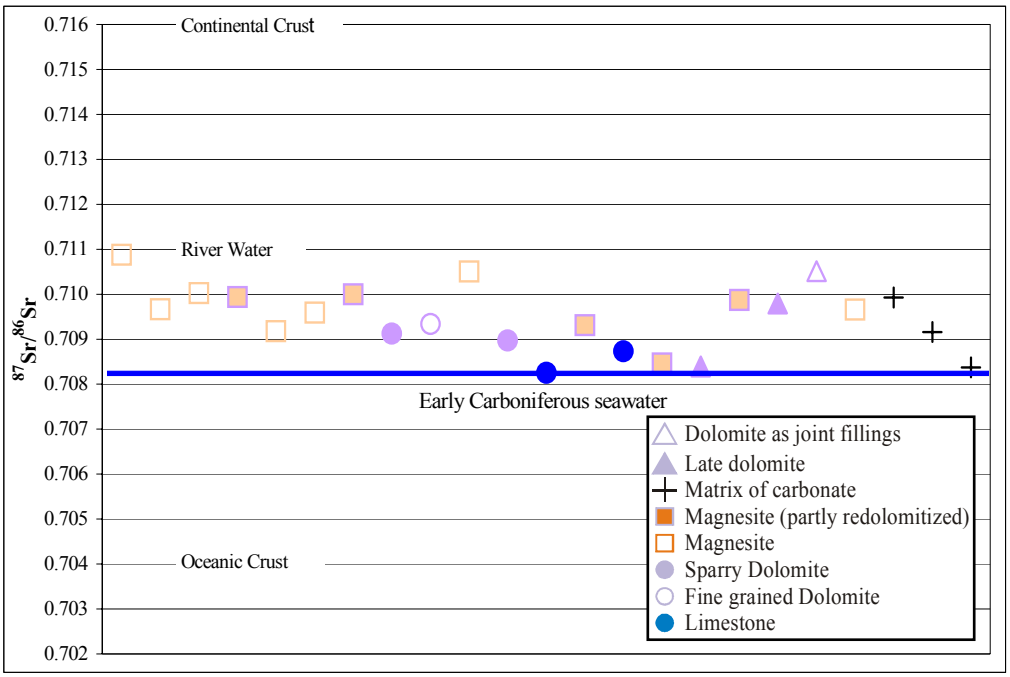

Fig. 4. 24 Distribution of $^{87}Sr/^{86}Sr$ values of carbonate rock/mineral types of the Hohentauern/Sunk deposit.

The following factors may increase the Sr-initial ratio secondarily:

A) The Rb concentration (decay of ^{87}Rb)

B) The age, depending on A, and

C) The Rb/Sr ratio, depending on A and B.

D) Weathering and

E) Recrystallization, according to the isotopic composition of the remobilizing fluids.

The influence of factors A-C can be determined analytically, that of factor D may be largely avoided by eliminating weathered samples. Factor E has to be estimated from regional studies (e.g. regional metamorphism), field-work and microscopic observation (Frimmel 1988).

The higher $^{87}Sr/^{86}Sr$ ratios of the magnesite without signs of macroscopical redolomitization (Tab. 4. 4 and Fig. 4. 24) in comparison to limestone host rocks, (variation of $^{87}Sr/^{86}Sr$ ratios between 0.70918 and 0.710881) can be explained as followed:

1) High $^{87}Sr/^{86}Sr$ ratios of dolomite microinclusions.

2) Rb substitute for K in solid inclusion of KCl evaporite minerals within magnesite and decay of ^{87}Rb to ^{87}Sr.

3) Rb concentration during leaching of Rb-bearing phases from different lithologies.

4) Incorporation of radiogenic ^{87}Sr into clay minerals (or their metamorphic equivalents) which are regarded as the relevant Rb-bearing phases in host rock (Frimmel 1988).

5) By (re-)crystalization in the presence of metamorphic fluids (Frimmel 1988, Kralik et al. 1988).

In situ Sr-isotope analysis of 13 samples of different carbonate rocks of the deposit (4 samples of magnesite ore body and 9 samples of carbonate host rocks and late dolomite) were carried out by laser ablation MC-ICP-MS. The laser system was operated in high-resolution line scans mode and a slit traversed the sample along selected profiles. 37 profiles were chosen for high-resolution Sr-isotope analysis.

For the calculation of the $^{87}Sr/^{86}Sr$ ratio from laser ablation MC-ICP-MS data, the intensity of measured atomic masses (88, 87, 86, 85, 84) versus time (ablation time) is drawn along

selected profiles. In carbonate materials, the analysis of Sr isotope variations in situ is potentially compromised by a variety of isobaric interferences (Woodhead et al. 2005) such as gas-related and sample-related interferences. The most important gas-related interference is from Kr, which is usually present as a trace impurity in the Ar and He carrier gases used in ICP-MS. The other interferences are also relevant to the measurement of Sr-isotope ratios in carbonates are ^{87}Rb on ^{87}Sr and Ca. Correction of raw data and recalculation is implemented using the "LamTool-Sr, version: 060424" software.

The values of the laser ablation analysis of magnesite samples along the profiles differ from the conventional solution-based analysis of selected crystals. The $^{87}Sr/^{86}Sr$ ratios measured by LA-MC-ICP-MS along selected profiles indicate strong heterogeneity between matrix materials, individual crystals and even inside the crystals (Fig. 4. 25). The scatter of Sr-isotopes is not clearly known, it can be depended on different mineral phases, especially dolomite relicts (Fig. 4. 23) or redolomitization, compositional heterogeneity between individual crystals and distributions of fluid inclusions. A segment of a 250 μm traversed slit on a magnesite sample, which has a low compositional heterogeneity was selected according to petrographical properties. Recalculation of Sr-isotope in this section indicated an average $^{87}Sr/^{86}Sr$ ratio of 0.70815 which is similar to limestone host rocks. However the scatter of Sr-isotopes along the profile displays a variable change in the $^{87}Sr/^{86}Sr$ ratios.

4.6 Nd – Sr isotopes chemistry

Combined Nd–Sr isotopic studies potentially provide a powerful tracer for contamination of mineralization fluids in different rock types. The correlation between εNd and $^{87}Sr/^{86}Sr$ ratios has been used to define a thoroughfare for the Mg-rich solutions. The epsilon notation is an alternative way of expressing isotope ratios which allow greater flexibility in the way in which isotopic data are presented.

Nd and Sr isotope ratios of all magnesite samples were recalculated for an assumed age of 285 Ma. The Nd and Sr isotopic compositions are shown in the εNd versus $^{87}Sr/^{86}Sr$ diagram (Fig. 4. 26). Typical continental crustal rocks have lower Sm/Nd and therefore lower $^{143}Nd/^{144}Nd$ ratios (negative εNd values) than those derived from upper mantle. The magnesite samples with Sr isotopic ratios of 0.709167 to 0.710821 and εNd of –5.6087 to –5.1793 concentrate in continental crust domain, suggesting that continental crust

contamination played a major role in the genesis of the magnesite mineralization. Therefore the percolating Mg rich fluids passed crustal rocks.

a:

b:

c:

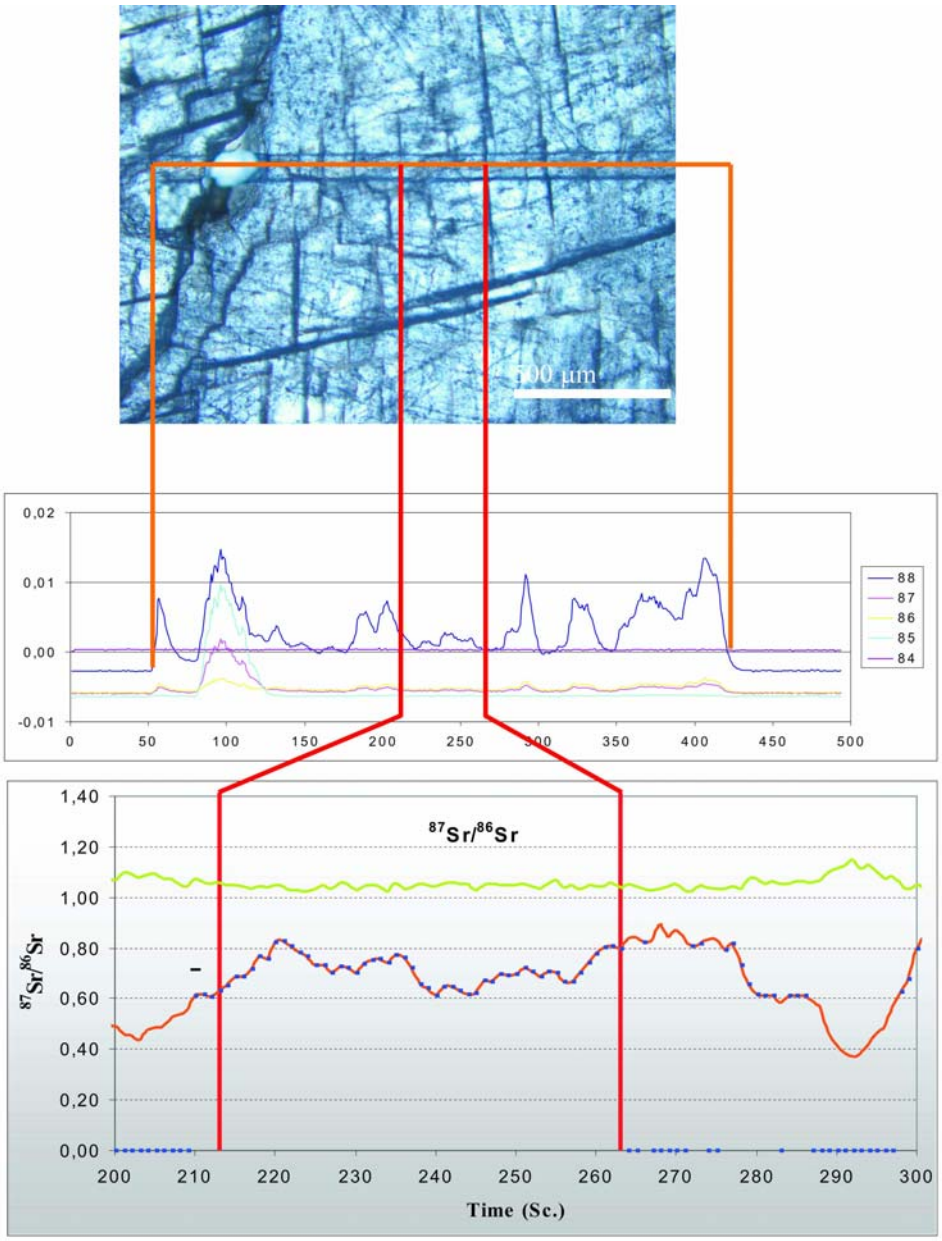

Fig. 4. 25 In situ Sr-isotope analysis by laser ablation MC-ICP-MS. a: A slit, approximately 1840 x 100 µm in size, is traversed (5 µm/Sec.) across the magnesite sample. b: Time (Sec.) - Intensity (CPS) plot represents distribution of different atomic masses along the profile. Scatter of Sr-isotopes and heterogeneity is indicated across a magnesite crystal. c: Recalculation of measured masses along a selected homogene segment of 250 µm shows a different $^{87}Sr/^{86}Sr$ ratio from the conventional solution-based analysis.*

** counts per second*

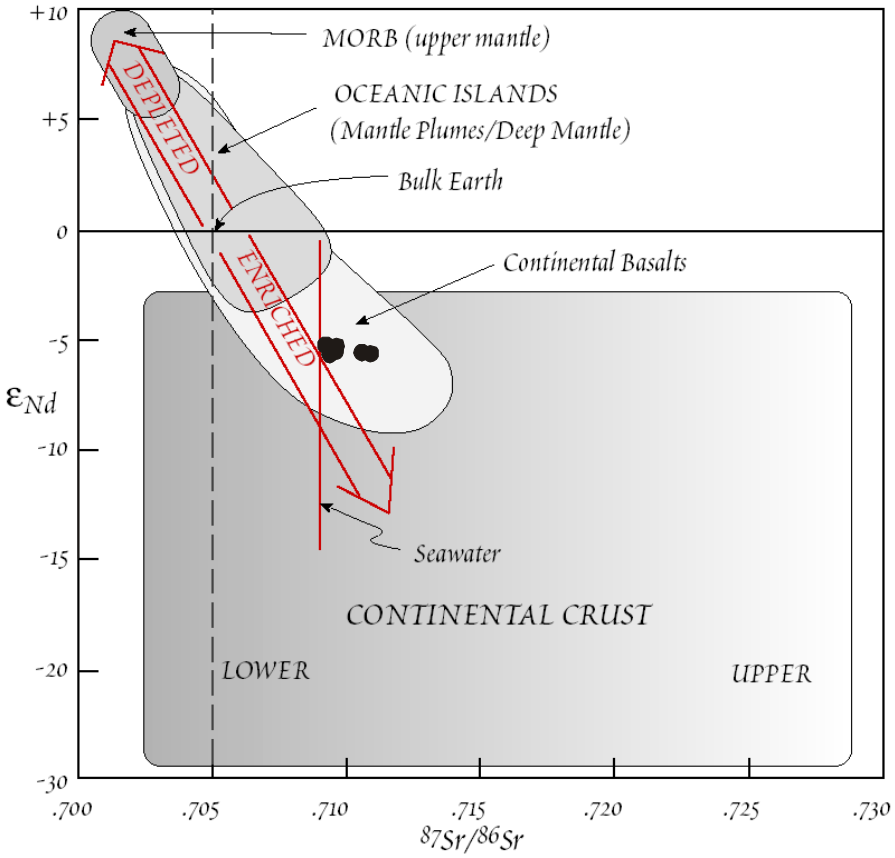

Fig. 4. 26 εNd versus $^{87}Sr/^{86}Sr$ correlation diagram showing a continental crust contamination of Mg rich fluids.

5. Isotope geochronology

5.1 Sr isotope stratigraphy

Sr isotope stratigraphy (SIS) is predominantly used for correlation and dating of marine sediments (Elderfeld 1986, McArture 1994, Veizer 1989) and the $^{87}Sr/^{86}Sr$ record can be also used to estimate the duration of stratigraphic gaps (Miller et al. 1988). When SIS is used for dating, the quality of its numeric date depends upon several factors, including (Howarth & McArthur 1997):

- the preservation quality of the original $^{87}Sr/^{86}Sr$ of a sample, whether artifacts are introduced during $^{87}Sr/^{86}Sr$ measurement,
- the slope of the curve of $^{87}Sr/^{86}Sr$ against numeric age,
- the accuracy of the age model used to assign a numerical calibration to the isotope curve,
- the way the best-fit curve and its associated uncertainty envelope are fitted to the Sr isotope data and used to derive a numeric age.

Howarth & McArthur (1997) compiled $^{87}Sr/^{86}Sr$ data and fitted to them a nonparametric LOWESS statistical regression function (LOcally WEighted Scatterplot Smoother). The resulting curve, with its 95% confidence intervals, was then converted into a simple table that gave numerical ages, and their 95% confidence limits, for any given $^{87}Sr/^{86}Sr$ value, the values being interpolated in steps of 0.000001. McArthur & Howarth (1998) and McArthur et al. (2001) updated the fit (V2:1/98 and V3:10/99) and added a second table for converting numerical ages to $^{87}Sr/^{86}Sr$ values. The last version that improves earlier releases (3:10/99 LOWESS model for the period 0-509 Ma) is used to date the limestone host rock of the magnesite ore body in Hohentauern/Sunk deposit.

The $^{87}Sr/^{86}Sr$ ratios of two limestone host rock samples [PM15-16-7 and PP-PO (K)], which were measured by solution-based analysis, yielded isotope ratios of 0.708256 and 0.708735, respectively. The Sr-isotope measurement by the laser ablation analysis along selected segments of the traversed slit (total length: 1280 μm), across the same limestone sample (PM15-16-7) yielded $^{87}Sr/^{86}Sr$ ratios of 0.70825 (first segment: 500 μm, Fig. 5. 1)

and 0.70808 (second segment: 100 µm, Fig. 5. 2). The concentration of Rb in the measured sample is 0.285 ppm, therefore recalculation is implemented using $^{87}Rb/^{85}Rb=0$.

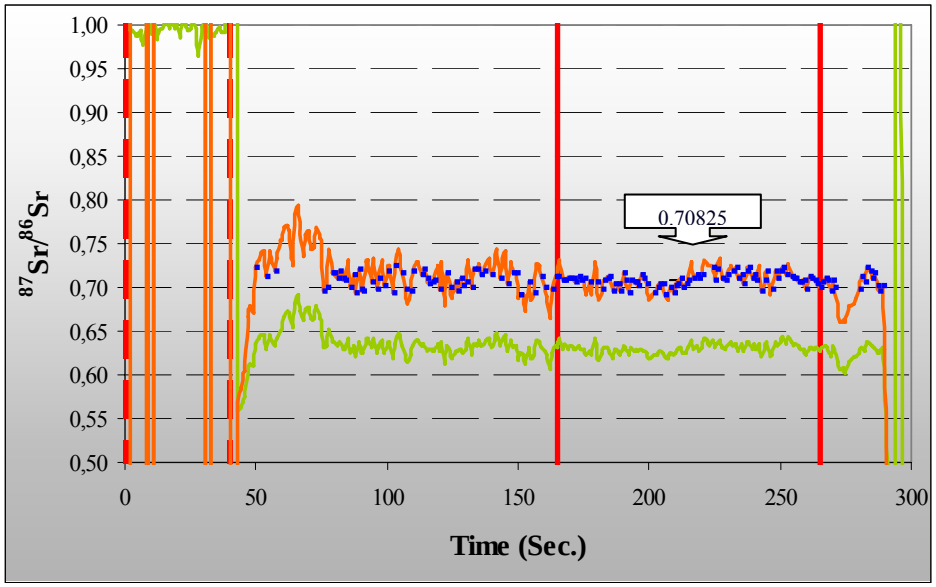

Fig. 5. 1 In situ Sr-isotope analysis by laser ablation MC-ICP-MS of limestone host rock (PM15-16-7) along a selected homogene segment of 500 µm lengt, (Green: raw data, Red: mass bias corrected data, Blue: data used for calculation).

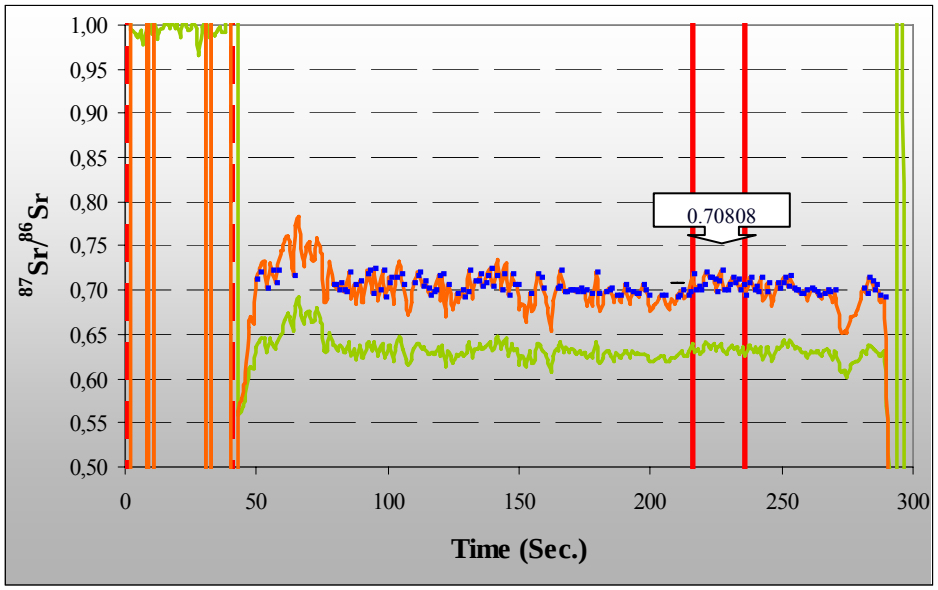

Fig. 5. 2 In situ Sr-isotope analysis by laser ablation MC-ICP-MS of limestone host rock (PM15-16-7) along a selected homogene segment of 100 µm length (Green: raw data, Red: mass bias corrected data, Blue: data used for calculation).

The solution-based HR-ICP-MS analysis of hand picked limestone host rock scatter between 0.708256 and 0.708735. They are increased in respect to Viséan sea water (Fig. 5. 3). The lower limit of $^{87}Sr/^{86}Sr$ ratios cuts the LOWESS model curve (McArthur et al.

2001) of the Carboniferous seawater (time period 299.0 – 359.2 Ma) at three positions: 304 Ma, 315 Ma, 358 Ma (Fig. 5. 3), the upper limit yielded a higher $^{87}Sr/^{86}Sr$ ratio in comparison with Carboniferous seawater. The values of laser ablation MC-ICP-MS measurement (0.70808 and 0.70825) along selected sections cross the Carboniferous seawater curve at three time intervals (299 - 304 Ma, 315 - 323 Ma, 351 - 358 Ma; Fig. 5. 3). These differ from the age of the mineralized carbonate country rocks which was determined biostratigraphically as late Viséan (D2-D3) by Felser (1977). As a result, the $^{87}Sr/^{86}Sr$ values of hand picked materials (solution-based HR-ICP-MS analysis) differ from LA-analysis along selected sections and the $^{87}Sr/^{86}Sr$ values of the biostratigraphically dated Viséan limestone host rocks are increased in relation to the Viséan Sr seawater curve.

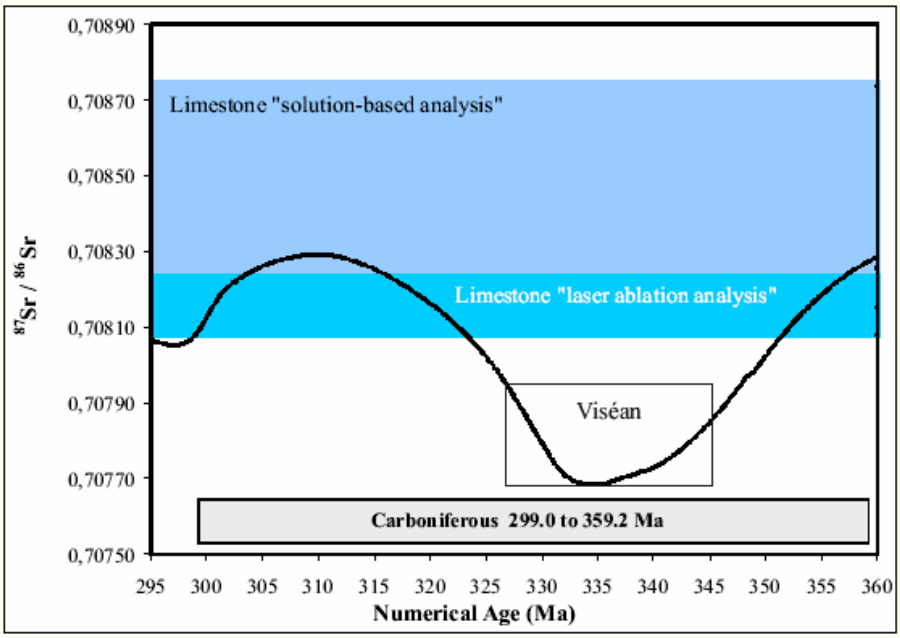

Fig. 5. 3 LOWESS best fit to the marine Sr-isotope curve for the Carboniferous (McArthur et al. 2001) and the position of the $^{87}Sr/^{86}Sr$ ratios of the limestone host rocks.

5.2 Samarium-Neodymium (Sm-Nd)

"Samarium (Sm, Z = 62) and neodymium (Nd, Z = 60) are rare-earth elements (REEs) that occur in many rock-forming silicate, phosphate, and carbonate minerals. One of the Sm isotopes (^{147}Sm) is radioactive and decays by α-emission to a stable isotpe of Nd (^{143}Nd) with a half-life of 1.53×10^{11} y and a decay constant of 6.54×10^{-12} y^{-1}. This decay scheme is useful for dating terrestrial rocks, stony meteorites, and lunar rocks." The decay of ^{147}Sm

to ^{143}Nd for dating rocks began in the mid-1970s and was widespread in the early 1980s (Faure & Mensing 2005).

"The isotope composition of Nd is expressed by the $^{143}Nd/^{144}Nd$ ratio, which increases as a function of time because of the decay of ^{147}Sm in accordance with equation $D = D_0 + N(e^{\lambda t}-1)$:

$$\frac{^{143}Nd}{^{144}Nd} = \left(\frac{^{143}Nd}{^{144}Nd}\right)_i + \frac{^{147}Sm}{^{144}Nd}(e^{\lambda t}-1) \qquad \textit{Equation 5. 1}$$

The $^{147}Sm/^{144}Nd$ ratios of rocks or minerals are calculated from the measured concentrations of Sm and Nd:

$$\frac{^{147}Sm}{^{144}Nd} = \left(\frac{Sm}{Nd}\right)_c + \frac{\text{at.wt. Nd x Ab}^{147}Sm}{\text{at.wt. Sm x Ab}^{144}Nd} \qquad \textit{Equation 5. 2}$$

at. wt.: Atomic weight; Ab: The present abundance.

The Sm-Nd method is most frequently used to date cogenetic mafic igneous rocks by the conventional isochrone method by equation 5. 1. The equation forms a straight line in coordinates of $^{147}Sm/^{144}Nd$ and $^{143}Nd/^{144}Nd$ in the slope-intercept form:

$$y = b + mx$$

such that the intercept $b = (^{143}Nd/^{144}Nd)_i$ and the slope $m = e^{\lambda t}-1$. Rocks or minerals that formed at the same time and had the same initial $^{143}Nd/^{144}Nd$ ratio are represented by points that define the straight line, which is called an isochron. The equation of the isochron is drived from the analytical data by least-squares cubic regression weighted by the reciprocals of the analytical errors. The date is calculated from the slope *m* of the isochron (Faure & Mensing 2005)": $m = e^{\lambda t}-1 \qquad t = 1/\lambda \ln(m+1)$

A most important aspect of isochron regression treatment is that it provides a realistic measure of the uncertainty in the age and initial ratios. A measure of the "goodness of fit" of an isochron is the Mean Squares of Weighted Deviates (MSWD). This is a measure of the fit of the line to the data within the limits of analytical error. Ideally an isochron should have an MSWD of 1.0 or less, anything greater than this is not strictly an isochrone because the scatter in the points cannot be explained solely by experimental error

(Rollinson 1996). However, the ideal of an MSWD of 1.0 or less is only applicable to isochron involving infinitly large numbers of samples and that for normal data-set the higer value of 2.5 is an acceptable cut-off for the definition of an isochron (Brooks et al. 1972). The origin of the scatter on an isochron is one of the most important interpretive aspects of geochronology (Rollinson 1996).

Sm and Nd concentrations and isotopic composition of the sparry magnesite samples are presented in Table 5. 1. The measured data are used on the first Sm-Nd dating of the sediment-hosted, stratiform Hohentauern/sunk sparry magnesite deposit.

Sample No.	Sm(ppm)	Nd(ppm)	$^{147}Sm/^{144}Nd$	error	$^{143}Nd/^{144}Nd$	error
M1(PI)	2.279	2.988	0.4611	0.0046	0.512846	0.000009
M2(PI)	2.264	2.747	0.4982	0.0050	0.512920	0.000011
PE16	3.034	7.168	0.2558	0.0026	0.512483	0.000012
PF24	1.136	2.750	0.2497	0.0025	0.512469	0.000007
PM15-16-1a	1.409	3.596	0.2369	0.0024	0.512430	0.000009
PP-PO(M)	2.594	9.135	0.1717	0.0017	0.512304	0.000007

Tab. 5. 1 Sm and Nd data for sparry magnesite samples from the Hohentauern/Sunk magnesite deposit.

Isotope dilution measurements on five sparry magnesite samples without signs of redolomitization and one sample with redolomitization [sample PP-PO(M)] show a Sm and Nd concentration of 1.136 – 3.034 ppm and 2.747 – 9.135, respectively (Tab. 5. 1). Six samples of mostly coarse-grained magnesite of the ore body yield a Sm-Nd isochron age of 285 ± 17Ma (Model 1, Solution on 6 points) with the initial isotope ratio: $^{143}Nd/^{144}Nd$ = 0.511991 ± 0.000033 (Fig. 5. 4), and 283 ± 15Ma (Model 3, Solution on 6 points) with the initial isotope ratio: $^{143}Nd/^{144}Nd$ = 0.511996 ± 0.000032 (Fig. 5. 5). MSWD values of both isochrons are 4.5. If the scatter results in an MSWD of 2.5 or less it is deemed analytical. If the MSWD is greater than 2.5 it is geological. Brooks et al. (1972) proposed the term "errorchron" for the situation where a stright line cannot be fitted to a suite of samples within the limits of analytical error. An errorchron implies that the scatter of the points is a consequence of geological error and indicates that one or more of the initial assumptions of the isochron has not been fulfilled. A Sm-Nd isochron age from same points using a robust, nonparametric regression is calculated (Fig. 5. 6). The Sm-Nd isochron age of 288 + 37/-16 Ma (298.5 ± 26.5 Ma) with the initial isotope ratio: $^{143}Nd/^{144}Nd$ = 0.51198 + 0.000036/-0.00021 is determined by robust regression algorithm. A Sm-Nd isochron age (using regression model 1 and model 3) from pinolit type magnesite indicate mainly an

early Permian age (268 to 302 Ma) which geological relevance is actually difficult to interpret. Nevertheless, it is ± contemporaneous with HT/LP metamorphism (peak around 270 ± 30 Ma), magmatism and extensional tectonics observed in other segments of the Austroalpine crystalline basement (Schuster et al. 2001). The Sm-Nd isochron age using robust regression model show an age range of 272 - 325 Ma. These ages are distinctly older than early Permian and partly correlated with the latest Carboniferous.

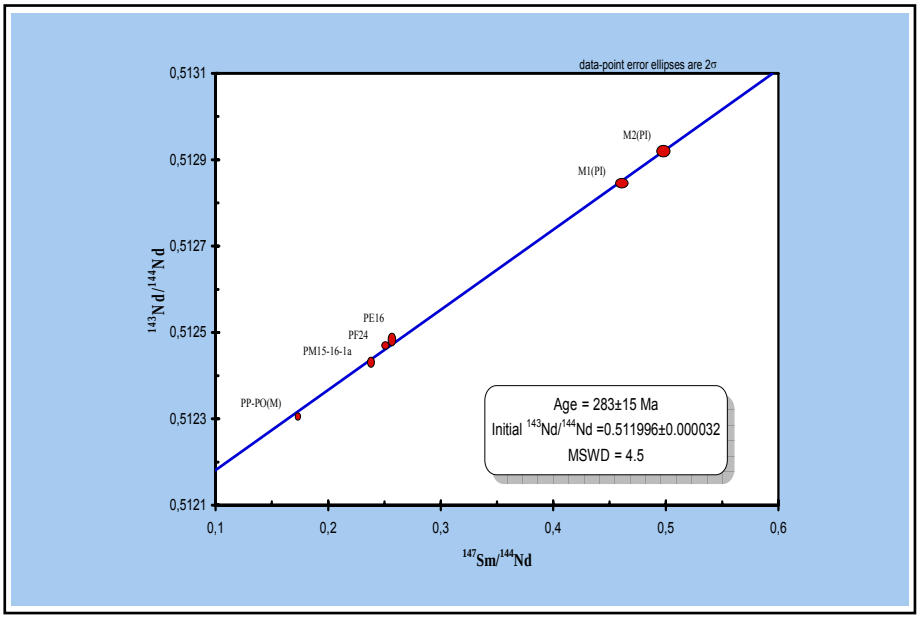

Fig. 5. 4 Sm-Nd isochron for hand picked sparry magnesite minerals (Model 1, solution on 6 points).

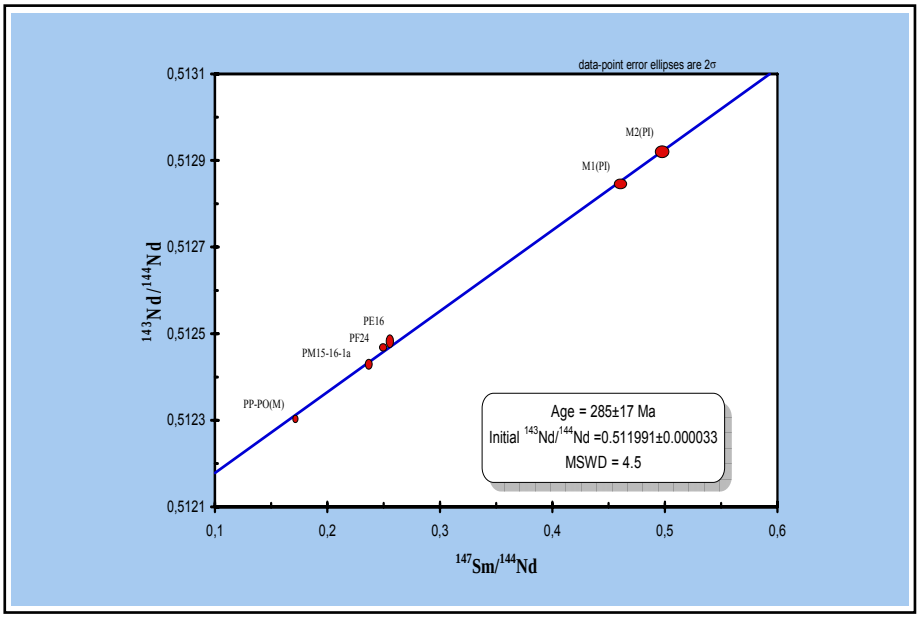

Fig. 5. 5 Sm-Nd isochron for hand picked sparry magnesite minerals (Model 3, solution on 6 points).

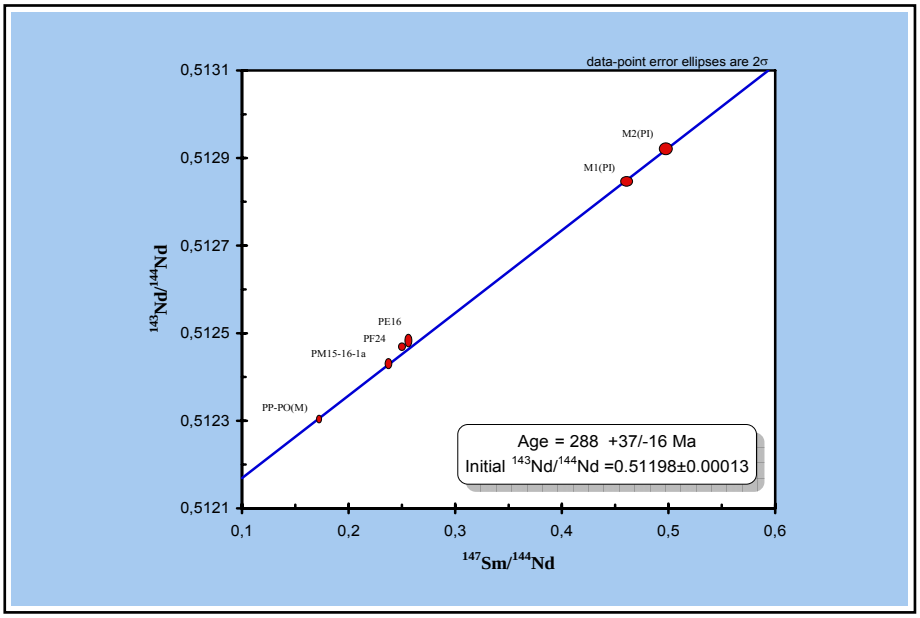

Fig. 5. 6 Sm-Nd isochron for hand picked sparry magnesite minerals (Robust regression model, solution on 6 points).

5.3 Sulfur isotope data

Sulfur is present in nearly all natural environments. It is an important constituent of the Earth's exogenic cycle. Most commonly it occurs in its oxidized form as dissolved sulfate in seawater or as evaporitic sulfate and in its reduced form as sedimentary pyrite. The isotopic compositions of both redox states are sensitive indicatores for changes of the geological, geochemical or biological environments in the past. The isotope record of marine sedimentary sulfate through time has been used successfully to determine global variation of the composition of seawater sulfate (Strauss 1997). "Sulfur occurrences cover the whole temperature range of geological interest. Thus, it is quite clear that sulfur is of special interest in stable isotope geochemistry (Hoefs 2004)". Sulfur has four stable isotopes with the following abundances (MacNamara & Thode 1950), ^{32}S: 95.02%, ^{33}S: 0.75%, ^{34}S: 4.21% and ^{36}S: 0.02%. The ratio of $^{34}S/^{32}S$ displays variations during a large number of inorganic and organic processes within the atmosphere, hydrosphere, geosphere, biosphere and is, thus, of interest to earth scientists (Strauss 1997). It is commonly expressed as $\delta^{34}S$, defined by the following equation:

$$\delta^{34}S\ (‰) = \left(\frac{\left(\frac{^{34}S}{^{32}S}\right)sa - \left(\frac{^{34}S}{^{32}S}\right)st}{\left(\frac{^{34}S}{^{32}S}\right)st} \right) \text{x } 1000 \qquad \textit{sa.: Sample, st.: Standard.}$$

and reported as per mil difference with respect to the internationally accepted Canyon Diablo Troilite (FeS) standard (CDT).

Some layers of gypsum and anhydrite intercalated within magnesite host sediments were found by underground drilling at two sites and along three exploration bore holes in the NW part of the deposit (Fig 5. 7).

Fig. 5. 7 Gypsum and anhydrite drill core which was intercalated within magnesite host sediments in NW underground parts of the deposit.

The $\delta^{34}S$ values of gypsum and anhydrite layers which were intercalated within the magnesite host rock sediments yield for anhydrite +17.2 ± 0.2 ‰ (CDT) and for gypsum + 17.6 ± 0.2 ‰ (CDT). They may be Carboniferous and identical with the stratigraphic age of the host rock (Petrascheck 1978, Fig 5. 8). These values are similar to the $\delta^{34}S$ values of two samples of evaporitic gypsum from Oberdorf-Laming/Styria magnesite deposit, which have been measured +17 ‰ (Schroll et al. 1989). One sample of pyrite from Hohentauern/sunk, near Trieben/Styria which occurs in a sparry magnesite of Late

Carboniferous age may have formed at a later stage of diagenesis or metamorphosis and shows $\delta^{34}S$ value of approximately zero (+0.6 ‰, Schroll et al. 1989).

The Phanerozoic evaporite-based sulfur isotope record (Fig. 5. 8) displays clearly discernible secular variations, on differing time scales, as already noted by earlier authors (e.g. Holser & Kaplan 1966, Claypool et al. 1980, Strauss 1993a). These include an isotopic maximum with $\delta^{34}S$ values around +30 to +35‰ in the Vendian and Cambrian, minimum values around +11‰ for the Permian and a value of +21‰ for modern seawater sulfate (Strauss 1999).

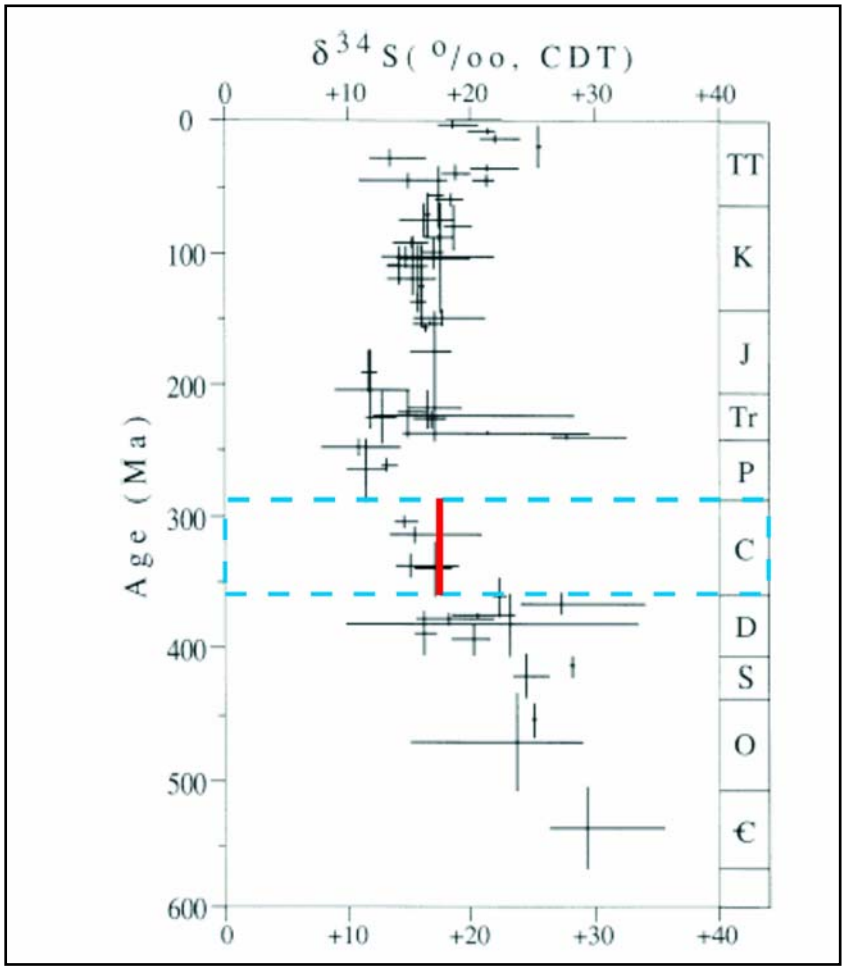

Fig. 5. 8 Sulfur isotopic composition of Phanerozoic evaporites (modified and updated after Strauss 1997; ages after Harland et al. 1990). Horizontal bars indicate ranges of sulfur isotopes, vertical bars, positioned at the average isotopic composition, represent the age uncertainty. The red line shows the $\delta^{34}S$ values of gypsum and anhydrite layers which may be identical with the Carboniferous age of the host rock as well as $\delta^{34}S$ values of gypsum from the Oberdorf-Laming magnesite deposit (Schroll et al. 1989).

6. Fluid characteristic

6.1 Fluid inclusions

"The study of fluid inclusions has become a routine method for solving a wide range of geoscientific problems, especially the genesis and exploration of mineral deposits. Fluid inclusions are small volume (from submicroscopic up to several hundred micrometers in diameter) of liquid, vapour, or mixtures of these phases, trapped as impurities within crystals. The fluid inclusions that formed during initial crystal growth are primary and pseudosecondary inclusions. These fluids can be trapped along growth zones, crystal edges and in any imperfection of a crystal during growth as primary inclusions. When a mineral fractured during growth syngenetic microcracks will be healed in the presence of a fluid which may be trapped as pseudosecondary inclusions. Fluid inclusions that formed some time after crystal growth are secondary inclusions. Any stress after crystal growth will lead to epigenetic fractures and secondary inclusions may be the result of their recrystallization. The main principle of the fluid inclusion study is to analyse the mineral forming fluid that remains conserved over millions of years. Primary and pseudosecondary inclusions will thus contain the fluid from which the host crystal has grown. Therefore they can provide information on the fluid composition of the corresponding environment. But also secondary inclusions may provide information on the later geological history of a crystal. By their composition the majority of fluid inclusions are water-salt-gas mixtures with NaCl being the most important salt and CO_2, CH_4 and N_2 as the most important gas species. In terms of thermodynamics a fluid inclusion represents a closed (isochoric) system which is defined by pressure (P), temperature (T), volume (V) and chemical composition (X). Two of these parameters (V, X) are fixed during formation of an inclusion while P and T remain variable after trapping. At room temperature most fluid inclusions contain two phases: a vapour bubble and an (aqueous) solution. But other phase combinations as two immiscible liquids (liquid CO_2 and water for example) with or without a vapour bubble are common as well. Additional solids may occur which are termed daughter crystals if they precipitated from the trapped solution. Halite is by far the most common solid phase observed. The aim of any fluid inclusion study is the reconstruction of the PTVX-properties (Wiesheu & Hein 1996)." Such inclusions can help to understand metamorphic processes, diagenetic systems, subsurface fluid evolution and porosity evolution. Inclusions can provide important insights into pressure-temperature conditions of crystallisation or mineral

precipitation and the composition of the fluid present when the host mineral grain formed. Also the later history of the rock can be traced by the continuous entrapment of pure fluids in newly grown inclusions.

In the present study fluid inclusions were observed and measured only in sparry magnesite samples. In the selected samples fluid inclusions were relatively abundant, but generally less than 5 μm in size (Fig. 6. 1). The number of inclusions in a given sample generally increases with decreasing inclusion size (Roedder 1984), and some milky quartz and calcite may contain as many as 10^9 fluid inclusions per cm^3 (Samson et al. 2003). Where possible, all inclusions were assigned a probable primary or secondary origin (Fig. 6. 2) according to the criteria of Roedder (1984).

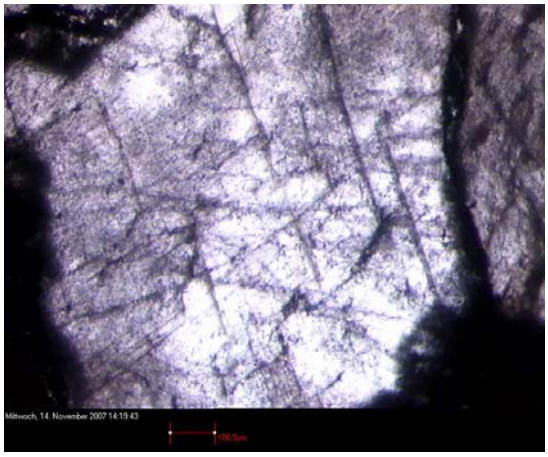

Fig. 6. 1 A cloud of small inclusions in magnesite. Crystals are divided in cloudy and clear zones because the fluid inclusions are distributed unevenly (sample No. M2-PI).

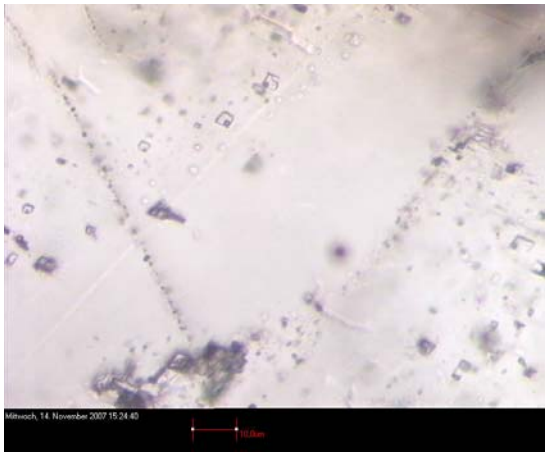

Fig. 6. 2 The secondary fluid inclusions are trapped along fractures (sample No. M2-PI).

Based on the phase composition at room temperature two types of fluid inclusions have been recognised (Fig. 6. 3 and Fig. 6. 4):

- Very common simple aqueous two-phase liquid-vapour (L-V) inclusions.
- Three phase aqueous liquid-vapour-solid (L+V+S) inclusions, containing a solid phase.

Two-phase aqueous inclusions (L+V), which are containing aqueous liquid and vapour are subdivided in two major groups: liquid-rich inclusions where liquid is the dominant phase with a small vapour or gas bubble (Fig. 6. 5) and gas-rich inclusions (Fig. 6. 6).

Fig. 6. 3 Primary two-phase aqueous inclusion with a vapour bubble and a liquid (sample No. M2-PI).

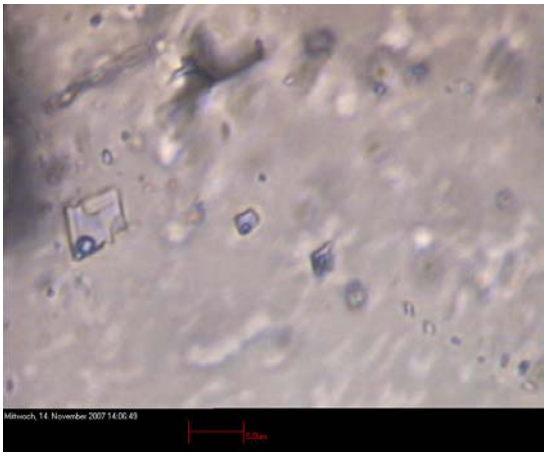

Fig. 6. 4 Three phase aqueous inclusions, containing a solid phase (sample No. M2-PI).

Fig. 6. 5 Liquid-rich inclusions (sample No. M2-PI).

Fig. 6. 6 Gas-rich inclusions (sample No. M2-PI).

Commonly fluid inclusions contain solid phases along with the fluid (Fig. 6. 4). These include aqueous inclusions containing crystals. Mineral identification of the solid phases in selected fluid inclusions are carried out by Raman spectroscopy. A different mineralogical composition of solid phase and the host crystal shows that the solid phase has not precipitated in optical continuity with the wall of the inclusion. The solid phases can be daughter crystals which actually precipitated from the inclusion fluid after entrapment as it cooled. Petrographically the ratio of fluid to solid phase in studied fluid inclusions is nearly constant. It is an evidence that the solid phases in the observed fluid inclusions are daughter crystals (Goldstein 2003). The daughter crystals differ from accidental solids which have settled on the surface of a growing crystal and then were incorporated as part of the fluid inclusion. Mineralogy of the daughter crystals in the aqueous fluid inclusions

of magnesite samples can provide an indication of the chemical composition of the ore forming fluid.

For describing the shape of the inclusions the definition model of Bakker & Diamond (2006) has been used (Fig. 6. 7). Using the program *ImageJ* the area, the perimeter and the major and minor axes of a best fit ellipse of the inclusions are measured. These values have been calculated with the Microsoft Excel to classification parameters.

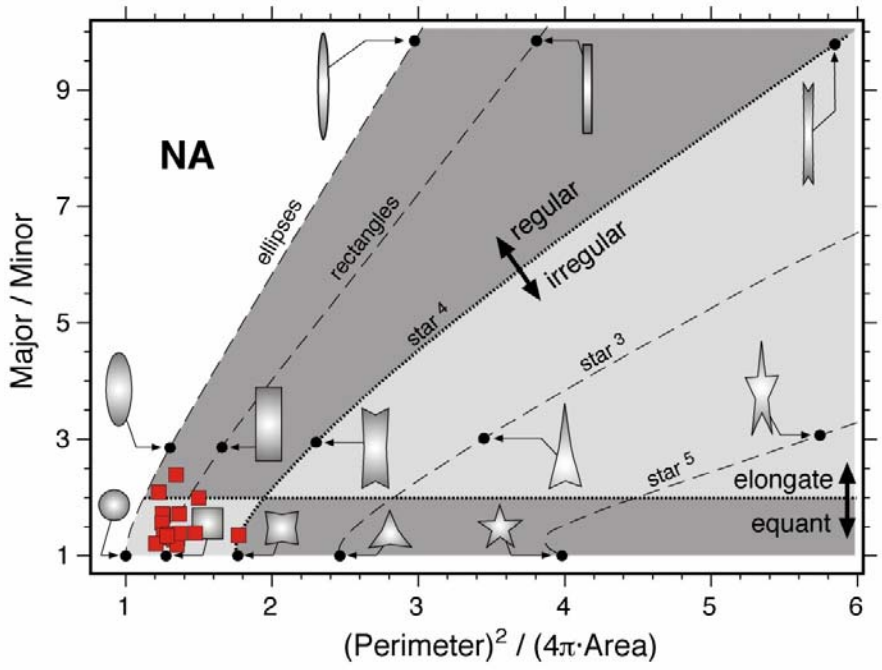

Fig. 6. 7 Definition of the shape of the inclusioins (Bakker & Diamond 2006).

Fluid inclusions in magnesite samples are regular in shape. Most of the measured fluid inclusions display the same or nearly the same diameter in all directions (equant forms). According to the inclusion shape definition (Bakker & Diamond 2006) the fluid inclusions in magnesite sample distributed in the rectangles area (Fig. 6. 7) and their shapes represent a negative crystal shape (Fig. 6. 3 to Fig. 6. 6). The negative crystal shapes are typical for many natural fluid inclusions and they are formed when the fluid inclusion cavity tends to form crystal phases by re-crystallization and/or dissolution–precipitation. By reducing the surface energy, regularly shaped inclusions represent the most stable state (Van den Kerkhof & Hein 2001). Using the negative crystal shape as one criterion for primary (early) entrapment (Roedder 1984) should be done with greatest care as re-equilibrated inclusions with the same characteristics have also been found in many cases.

6.2 Raman spectroscopy

Fluid inclusions in the magnesite sample are analyzed by Raman spectroscopy to identify the chemical composition of the liquid, gas and solid phases. Raman spectroscopy is an important analytical technique to characterize and distinguish the different types of fluid and gas inclusions and also to qualify solid phases in inclusions.

The liquid-rich fluid inclusions display a spectrum typical of H_2O in the range 3000 to 3700 cm^{-1} (Fig. 6. 8). The Raman signal of liquid H_2O is very broad and changes its shape depending on temperature and salinity of the solution.

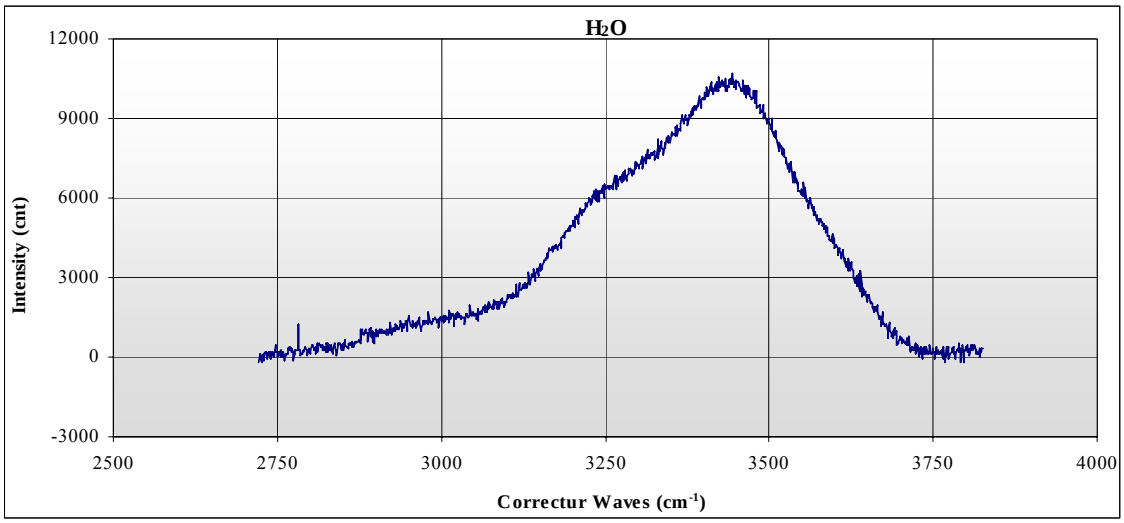

Fig. 6. 8 Raman spectrum of an aqueous solution (water) in liquid-rich fluid inclusions of magnesite samples at room temperature.

Some gas-rich fluid inclusions in the magnesite samples were measured by Raman spectroscopy. In some of the gas-rich fluid inclusions, the gas phase consists of CO_2. The Raman spectrum of CO_2 displays two main peaks at 1284 cm^{-1} and 1387 cm^{-1}. The spectrum of the gas phase measured in gas-rich fluid inclusions (Fig. 6. 9) has a similar peak position (1282 and 1386 cm^{-1}) which indicate CO_2. However, the intensity of the peaks depends on the depth of the inclusion below the surface of the slide and the CO_2 density. Those who are close to the surface give the highest intensity. The gas-rich fluid inclusions of magnesite samples contain mainly CO_2, and other gases were not observed. CO_2-bearing fluid inclusions can result from thermal decarboxylation of organic acids and from dissolution of rock-forming carbonate during progressive metamorphism and replacement reactions (Kodera & Radvanec 2002).

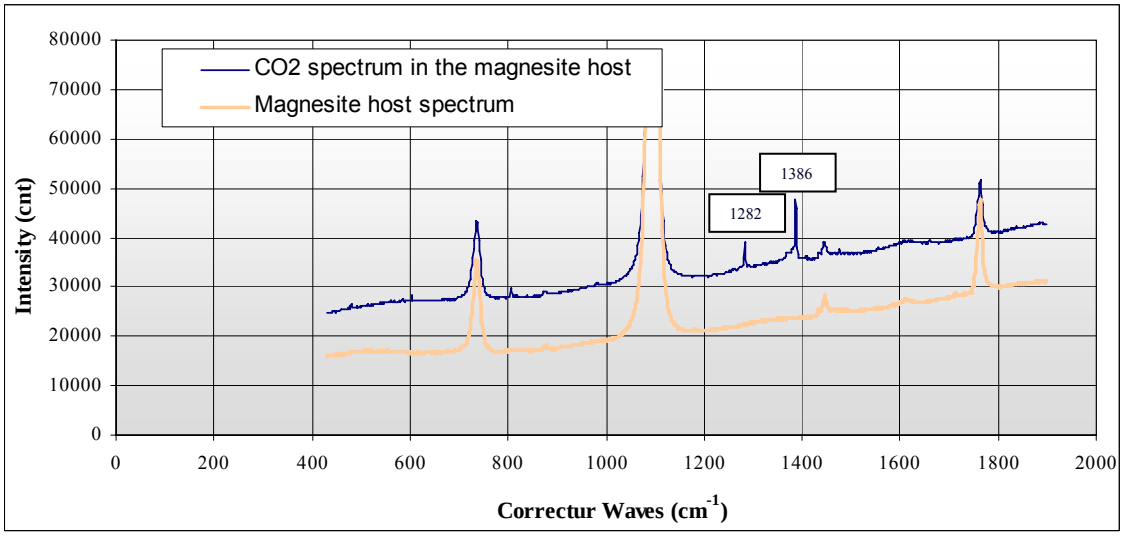

Fig. 6. 9 Fluid inclusion CO_2 spectrum with two main peaks in the magnesite host.

Some fluid inclusions from the magnesite samples contain solid phases as daughter crystals that are identified as dolomite based by their Raman spectrum (Fig. 6. 10). The Raman spectrum of the solid phase in the fluid inclusion displays some prominet peaks of dolomite in the magnesite host. The host mineral contains a main peak at 1095 cm^{-1}. The approximate position of this peak is characteristic for carbonates in general. The additional peaks at 211 cm^{-1}, 328 cm^{-1} and 738 cm^{-1} are specific for magnesite. However two prominet peaks at 175 cm^{-1} and 300 cm^{-1} are also observed which are specific for dolomite. The magnesite spectrum of the analyzed daughter crystal is clearly deriving from the host mineral and the additional prominet peaks at 175 cm^{-1} and 300 cm^{-1} represent dolomite as a daughter crystal within the inclusion.

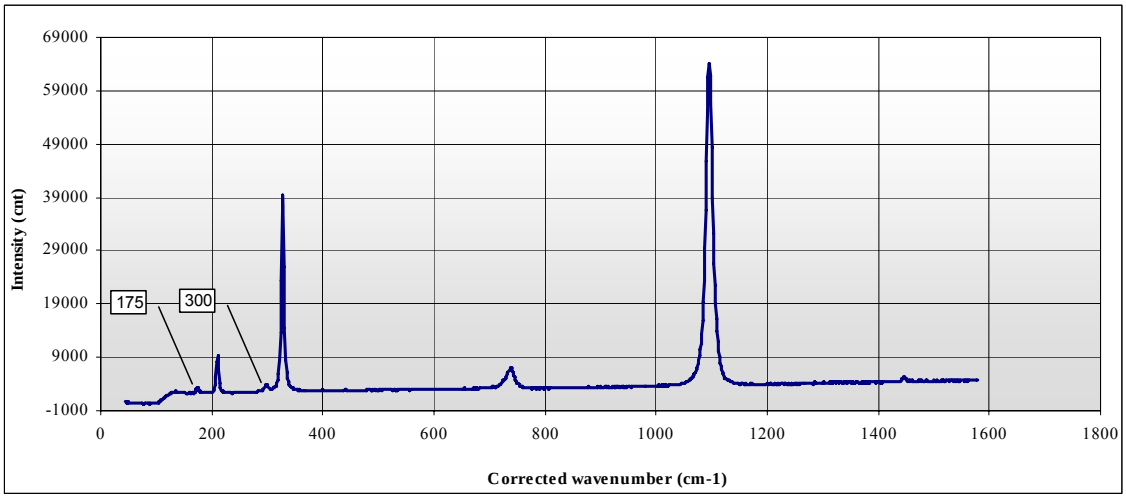

Fig. 6. 10 The Raman spectrum of a dolomite daughter crystal (peak positions at 175 cm^{-1} and 300 cm^{-1}) in a fluid inclusiontogether with the magnesite host Raman peaks.

6.3 Inclusion fluid chemistry

The characterization of extractable salts (TDS - Total Dissolved Solids) chemistry of inclusion fluids gives information on the source of solutes in the ore-forming brines and helps to explore genetic linkage among deposits. A general application of this technique is determination of Na/Br and Cl/Br ratios of inclusion fluids by crush-leach technique and ion chromatography analysis. In an initial stage of evaporation Na, Cl and Br are concentrated in the residual brine and their ratios (Na/Br, Cl/Br) do not change (Radvanec & Prochaska 2001). Nevertheless, Cl and Br have similar ionic radii (Cl = 1.81 Å, Br = 1.96 Å). Their fractional behaviour during evaporation is different. The fractional behaviour of Cl and Br during progressive evaporation is demonstrated in Fig. 6. 11.

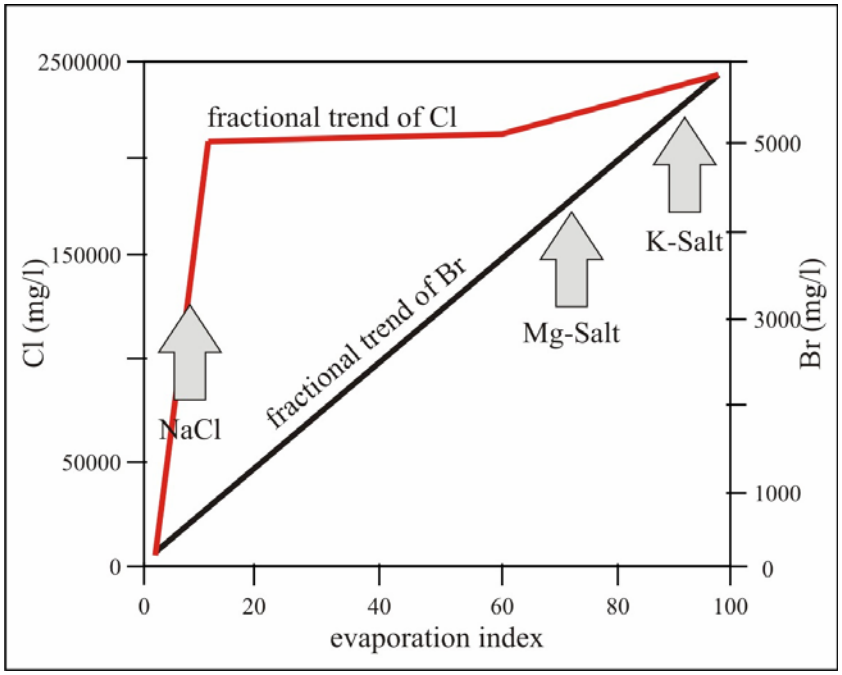

Fig. 6. 11 Fractional behaviour of Cl and Br during evaporation (data from McCaffrey et al. 1987).

During the beginning of evaporation Cl and Br are concentrated along the same path in a hypersaline environment that means their ratio at the start of evaporation remains constant. At an evaporation index (factor of concentration by evaporation of seawater) of >10, halite starts to precipitate. Br has a very conservative behavior (secondary integration into halite lattice) and is not incorporated into the halite lattice. Br is accumulated in residual solutions. Whereas Na and Cl are abstracted away from the system as halite, on an evaporation index of approx. 70, Mg-salts start to precipitate (Na/Br ~ 10, Cl/Br ~ 100)

and later K-salts (Fig. 6. 11). However Br is still concentrated in the residual brines. During precipitation Br indeed is integrated - but in secondary degree - so that fractionation can proceed. The cation systematics changed from an original Na preponderance to a Mg and K dominated system (McCafferey et al. 1987).

The molar ratios of Na/Br and Cl/Br are indicative for fluids, which were produced by evaporitic processes, because the Br shows subordinate emplacement in the halite lattice. The molar ratio of Na/Br and Cl/Br is very significant for fluids integrated in evaporitic processes and for fluids deriving their salinity from evaporation during migration through the crust. The evolution of the fluids by fractionation of halite from seawater is demonstrated on the ratio of Na/Br and Cl/Br (Fig. 6. 12) and two trends can be identified. Starting from the composition of seawater the “halite evaporation trend” and the “halite dissolution trend” above mentioned can be observed (Bottrell et al. 1988).

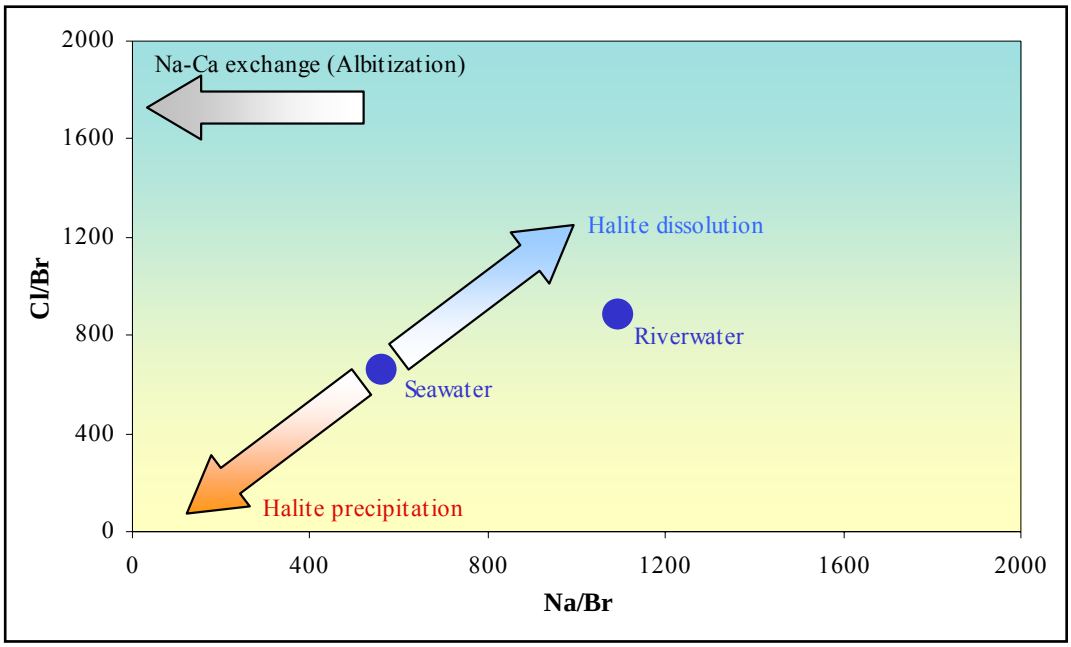

Fig. 6. 12 Na/Br and Cl/Br molar ratio diagram of extractable salts chemistry of fluid inclusions (Bottrell et al. 1988).

The “halite evaporation trend” can be observed when seawater starts to precipitate halite and Br concentrates in the residual fluid in comparison to Na and Cl (evaporation index of about 10). Accordingly the composition of evaporitic, bittern brine is shifting along the “halite evaporation trend”. Those salinar fluids differ from fluids which obtain their salinity by dissolving salt during migration. The Br concentration of the fluid is a very suitable indicator in this case. The absolute Br content in halite represents an indicator for

the evaporation index of seawater. The average ratio of Cl/Br of seawater (655 ± 4) decreases during evaporitic salt separation to 100. Fluids percolating through the crust acquiring salinity by dissolution of halite, are expected to change towards higher CL/Br and Na/Br molar ratios. The content of Br is diluted compared to Na and Cl by the dissolution of halite in the fluids migrating through the rock and dissolving halite and a "halite dissolution trend" can be observed. Concerning the "halite dissolution trend" exists the possibility of accumulation of Br in the fluid at very small ratio of the fluid to the country rock and on lower temperatures. That happens when halite layers are incongruently dissolved and recrystallized (Bottrell et al. 1988, Troby 2001, Hajizadeh 2000, Kaiser 2005).

The results of the chemical composition of the extracted fluid inclusion of the magnesite ore body and related mineral phases using crush-leach technique are illustrated in the Tab. 6. 1. It is supposed that mineralized fluids are preserved in fluid inclusions of sparry magnesite. It should be considered that these results represent bulk fluid analyses which do not allow an identification of separate types of fluids in individual crystals. The measurement of the standard inclusion-free calcite (Reßler 2007) show low Na/Br (312.60) and Cl/Br (408.88) ratios which is situated in the halite precipitation trend. The measured ratios are artifacts because the calcite is pure and inclusion-free. Therefore the calculated ratios according this bulk analytical technique should be taken with care and it must be concluded that this method is insufficient for the characterisation of fluids (Reßler 2007). However it is very important to know if several independent generations of inclusions are present, bulk analyses can lead on to non significant conclusions. Na/Br and Cl/Br ion ratios are used to interpret the signatures of the original fluid. The existence of different generations of fluid inclusions has been demonstrated in the previous sections.

The magnesite samples show very low Na/Br (22 to 77) and Cl/Br (60 to 119) ratios of the extracted fluids and their composition on the Na/Br and Cl/Br molar ratio diagram lie at the end of the evaporation trend (Fig. 6. 13). The position of the plots at the end of the evaporation trend and the extend of fractionation indicate that the highly saline fluids were the product of evaporitic concentration predominantly of seawater. No indications of halite dissolution whatsoever are observed with the fluid of the magnesite samples. The fluid composition of magnesite samples indicate evaporitic bittern brines to be the original fluid source.

Late dolomite occurring as orbicular dolomite and "Rosszähne" dolomite, quartz and talc veins exhibit different compositions in comparison to magnesite. Na/Br and Cl/Br molar ratios of late dolomite and non-carbonate mineral phases are higher than those of the magnesite (Tab. 6. 1, Fig. 6. 13). The higher value of Na/Br and Cl/Br molar ratios is due basically to depletion of Br concentration in fluid inclusions. Their orientation to seawater suggest that late stage surface waters and/or seawater migrated into the magnesite ore body and caused this late stage redolomitization (secondary dolomitization) and non-carbonate mineral phases (quartz and talc formation). Chemical composition of fluid inclusions in the late mineralization represent non evaporation events, probably formed late dolomite and non-carbonate mineral phases which crystallized in vugs or veins. The limestone as a host rock of sparry magnesite shows totally different fluid composition ratios in the diagram. They are significantly higher than the seawater ratio.

Samples	Li ppb	Na ppb	K ppb	Mg ppb	Ca ppb	Sum Cat.	F ppb	Cl ppb	Br ppb	J ppb	NO_3 ppb	SO_4 ppb	Sum An.	Na/Br	Cl/Br
Limestone															
PM 15-16-7	1	938	420	2528	8016	**11904**	35	2478	5	8.8	132	994	**3654**	652	1117
Magnesite															
M1(PI)	57	11252	1213	23495	2036	**38052**	29	37809	1255	28.6	-	241	**39363**	31	68
M2(PI)	76	14198	1464	20454	1422	**37615**	29	42786	1399	39.9	155	128	**44537**	35	69
M3(PI)	10	11492	1308	28851	1481	**43142**	33	48274	1787	21.3	-	71	**50178**	22	61
M4(PI)	38	10408	1244	20680	940	**33310**	26	25848	657	37.7	142	174	**26885**	55	89
PE16	89	10857	1486	25008	4632	**42070**	175	30105	773	22.6	1876	300	**33252**	49	88
PF24	50	10843	1201	21002	979	**34075**	30	31403	987	25.1	224	144	**32813**	38	72
XPH6(M)	58	15635	1560	23704	3301	**44257**	24	49009	1855	33.9	-	285	**51206**	29	60
PM15-16-1a	56	9241	825	22489	4286	**36896**	22	24119	736	27.2	126	202	**25233**	44	74
Magnesite (partly redolomitized)															
PN-U3	64	9229	1200	23055	5161	**38708**	70	23628	551	32.5	4094	365	**28742**	58	97
Orb. (M)	23	4104	359	21546	6380	**32412**	33	9780	185	29.3	-	353	**10380**	77	119
PQ (M)	19	7116	977	20068	4964	**33143**	59	26409	887	14.5	-	517	**27887**	28	67
PQ1	9	4722	441	29106	10453	**44731**	89	10580	228	34.2	-	743	**11674**	72	105
Late dolomite															
Orb. dolmite	26	12547	832	22046	11237	**46690**	18	27354	184	44.9	-	438	**28039**	238	336
Rosszähne	26	6866	804	16114	10908	**34718**	14	14672	66	10.3	-	174	**14936**	364	505
Dol. in joints	8	9807	824	37241	-	**47881**	-	23312	18	6.5	1522638	-	**1545975**	1878	2895
Non-carbonate minerals															
Qtz(PF-north)	6	6564	2993	1694	1275	**12531**	44	14459	108	14.7	341	179	**15146**	212	303
Talc (PE21)	3	1308	267	7778	3518	**12874**	622	2460	11	4.2	-	1347	**4444**	408	498
Gipsum	2	1164	2065	3687	-	**6917**	-	1953	-	-	-	-	**1953**	-	-

Tab. 6. 1 Chemical composition of extracted fluid inclusions of the Hohentauern/sunk magnesite deposit and related mineral phases.

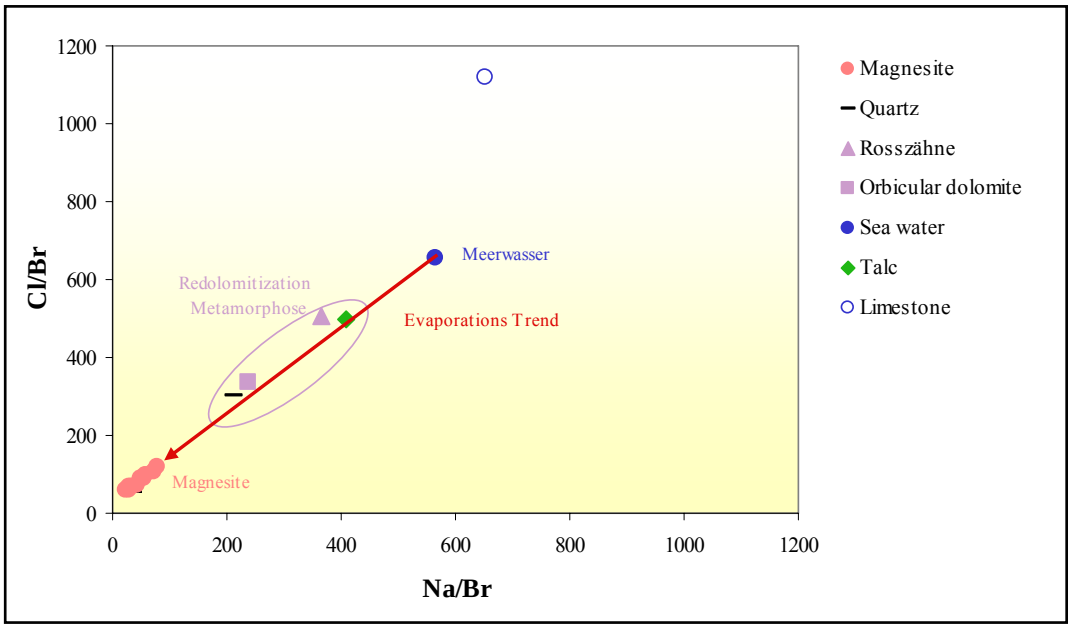

Fig. 6. 13 Na/Br and Cl/Br molar ratio diagram of the extracted fluid inclusions.

7. Thermometry and microthermometry

Estimation of temperature conditions during ore-forming processes could establish the origin of the ore carrying fluids. In samples of the study area several geothermometers were applied to carbonate minerals.

7.1 Carbonate (Calcite–Dolomite) geothermometry

This geothermometer relies on the analysis of Mg-calcite occurring in equilibrium with dolomite. The calcite-dolomite geothermometer requires reintegration of exsolved dolomite in calcite, and suffers from the same problems of retrograde exsolution and migration of exsolved dolomite to the grain boundaries. The calcite-dolomite geothermometer is best applied to rocks metamorphosed between 300 and 600°C in contact aureoles that cooled rapidly preserving peak metamorphic compositions (Bickle & Powell 1977, Powell et al. 1984).

The chemical compositions of calcite-dolomite mineral pairs are measured by the electron microprobe. However the analyzed data must be used carefully because using suitable standard and calibration for EPMA were not ordinary. Therefore the mean values of all chemical compositions have been used (Tab. 7. 1, sample No. PN-C). Representative analytical data of calcite-dolomite mineral pair are listed in Tab. 7. 2.

	CaO%	MgO%	FeO%	MnO%
		Calcite (n=6)		
Mean	55.30	1.80	0.03	0.05
Median	57.21	1.69	0.00	0.05
Standard deviation	5.69	0.76	0.06	0.03
		Dolomite (n=7)		
Mean	29.38	21.44	0.24	0.08
Median	30.17	21.42	0.06	0.05
Standard deviation	2.31	1.23	0.39	0.05

Tab. 7. 1 Statistical data of calcite and dolomite mineral pair electron microprobe analyses.

	CaO%	MgO%	FeO%	MnO%	CO_2%*	Total	Ca	Mg	Fe	Mn	Total
Calcite	55.30	1.80	0.03	0.05	45.40	102.58	0.986	0.045	0.000	0.001	1.032
Dolomite	29.38	21.44	0.24	0.08	46.67	97.81	0.966	0.981	0.006	0.001	1.954

*CO_2 is calculated from stoichiometry

Tab. 7. 2 Representative analytical data of carbonate.

With the chemical ratios of X_{Fe}=Fe/(Fe+Mg+Ca+Mn) in dolomite versus X_{Mg}=Fe/(Fe+Mg+Ca+Mn) in calcite, the temperature of the replacement was calculated using the carbonate geothermometry of Powell et al. (1984). The temperature was established at 489°C (Fig. 7. 1). The carbonate geothermometry of host rock carbonates showed a relatively wide range of temperature. This temperature corresponds to the Creatceous regional greenschist facies metamorphic overprint (Ratschbacher & Klima 1985).

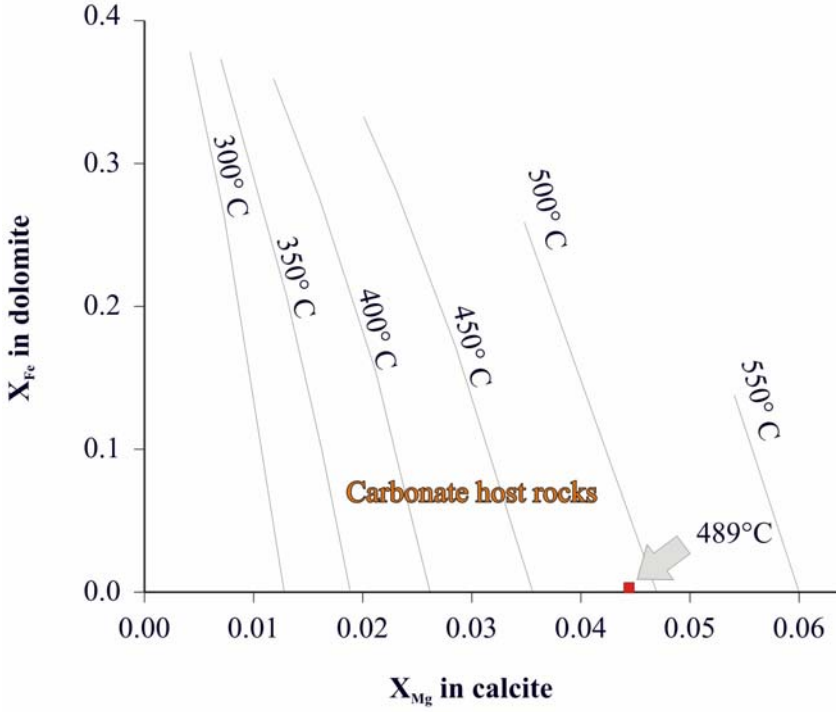

Fig. 7. 1 Diagram of X_{Fe} –dolomite versus X_{Mg} –calcite. The chemical ratios are calculated from EPMA analyses of dolomite microinclusions in limestone host rock (Fig. 3. 16b) using the carbonate geothermometry of Powell et al. (1984).

7.2 Chemical geothermometry

The concentrations of most dissolved elements in geothermal waters are functions of the water temperature and the weathered mineralogical assemblage (White 1965, Ellis 1970, Truesdell 1976, Arnórsson et al. 1983 and Fouillac 1983). Therefore, as concentrations can be controlled by temperature-dependent reactions, they could theoretically be used as geothermometers to estimate the temperature of the water at depth (Millot & Négrel 2007). The concentrations of silica and proportions of alkali (Na, K and Li) and alkaline earth (Ca, Mg) elements have been combined into 14 chemical geothermometers that are used successfully to estimate the subsurface temperatures of the reservoir rocks (Kharaka et al. 1985). The chemical geothermometers are developed in geothermal systems and based on

the temperature dependent chemical equilibrium between the water and the minerals at the deep reservoir conditions. The chemical geothermometers saved the temperature of the last chemical fluid-mineral equilibrium (White 1970, Truesdell 1976, Fournier 1977 and Ellis 1979).

The different types of chemical geothermometers include silica geothermometers and cation geothermometers (alkali geothermometers). A silica geothermometer is based on quartz, chalcedony, α or β cristobalite and amorphous silica solubility. The cation geothermometers (alkali geothermometers) are based on the partitioning of alkalies between solid and liquid phases. The geothermometers established on cationic exchange which are developed empirically include Na/K geothermometer (controlled by plagioclase and K-feldspar equilibrium) and the Na-K-Ca geothermometer (in the case of rich-Ca waters and that can include the Mg correction). Other cation geothermometers have been developed, in particular those using lithium (Fouillac & Michard 1981, Kharaka et al. 1982, Michard 1990). Modified versions of these Na-Li chemical geothermometers and an Mg-Li geothermometer have been developed for the estimation of sedimentary basin subsurface temperatures (from 30 to 200°C, Millot & Négrel 2007). Equations and parameters for different chemical thermometers are described as follows:

Na-K: $$t = \frac{1180}{\log(Na/K) + 1.31} - 273.15$$

Kharaka & Mariner (1989)

Na-K-Ca: $$t = \frac{1647}{\log(Na/K) + \beta\left[\log\left(\sqrt{Ca}/Na\right) + 2.06\right] + 2.47} - 273.15$$

*β = 1/3 for Ca/Na <1, T >100°C, β = 4/3 for Ca/Na >1, T <100°C

Fournier & Truesdell (1973)

Na-Li: $$t = \frac{1590}{\log(Na/Li) + 0.779} - 273.15$$

Kharaka & Mariner (1989)

Mg-Li: $$t = \frac{2200}{\log(\sqrt{Mg}/Li) + 5.47} - 273.15$$

Kharaka & Mariner (1989)

The combination of different processes and lack of thermodynamic equilibrium create difficulties for estimating temperatures under reservoir conditions by chemical geothermometers based on cationic concentrations (Giggenbach 1988). The best temperature estimation of deep fluid reservoirs with highly-saline waters can be obtained using geothermometers that do not include Mg in their equations, i.e. the Na-Li and Na-K geothermometers (Fouillac & Michard 1981, Giggenbach 1988, Kharaka & Mariner 1989, Prol-Ledesma et al. 2004). The Mg-Li geothermometer can be applied successfully to the low-temperature system (30°C to 200°C) and yield the most reliable temperatures in sedimentary basins (Meyer & McGee 1985, Kharaka & Mariner 1989). The empirical geothermometers based on Mg and Ca are improperly for calculations of temperatures of the Mg- and Ca-content of inclusion fluids, may be they are buffered by carbonate minerals and do not reflect the original signature of the fluids. The best and most reliable results from magnesite and siderite deposits in the southern Urals (Kaiser et al. 2003 & Kaiser 2005) and from sparry magnesite in the Eastern Alps (Prochaska & Henjes-Kunst 2007) were obtained by the Na-K and the Na-Li thermometer.

Na-K thermometer

The Na-K geothermometer has been progressively evolved from the initial observation that low Na/K ratios were indicative of high temperatures in the depth, to increasingly more precise calibration of the temperature-dependence of this ratio. The temperature-dependent variation of Na and K in high-temperature systems is due to iron exchange of these elements between co-existing alkali feldspars according to the reaction:

$$\text{Na-feldspar}_{(\text{albite})} + K^{+}_{(aq)} = \text{K-feldspar} + Na^{+}_{(aq)}$$

The different experimentally-derived geothermometry equations based on the Na/K ratio function is well for reservoirs with temperatures in the range of 180°C to 350°C, but they break down at lower temperatures, in particular at temperatures lower than 120°C.

Na-Li thermometer

A theoretical basis for the Na-Li geothermometer has not been established. As Li minerals are rare, it is improbable that the Li enters the aqueous phase following an equilibrium reaction with a Li mineral. Former observations by Ellis & Wilson (1960) and Koga (1970) had shown that the lowest Na/Li values corresponded to the hottest portions of the

geothermal field. Separate independent relationships between Li and Na concentration and temperature were also shown (Kharaka et al. 1982), with Li being more temperature dependent than Na. While these latter relationships could also be employed as geothermometers, they would be affected by dilution/mixing and boiling processes. The Na-Li geothermometer is used successfully in low to high temperature systems and when applied to both sedimentary- and vulcanic-hosted reservoirs. The temperatures calculated from the Na-K and Na-Li-ratios of the inclusion fluids and other solute chemistry data are listed in Tab. 7. 3.

Sample No.	Li ppb	Na ppb	K ppb	Ca ppb	Mg ppb	Na-K °C	Na-Li °C	Na-K-Ca °C	Mg-Li °C
					Limestone				
PM 15-16-7	1	938	420	8016	2528	438.30	140.84	247.20	29.83
					Magnesite				
PE16	89	10857	1486	4632	25008	269.68	281.30	228.04	111.33
PF24	50	10843	1201	979	21002	247.67	237.03	231.17	97.62
M4 (PI)	38	10408	1244	940	20680	255.37	221.00	235.85	90.54
M3 (PI)	10	11492	1308	1481	28851	250.45	138.81	229.71	54.22
M2 (PI)	76	14198	1464	1422	20454	240.65	248.38	228.26	109.93
M1 (PI)	57	11252	1213	2036	23495	244.95	243.51	222.15	99.56
PH6 (M)	58	15635	1560	3301	23704	237.44	222.16	219.06	100.09
PM 15-16-1a	56	9241	825	4286	22489	226.96	257.66	198.83	99.94
					Magnesite (partly redolomitized)				
PQ1	9	4722	441	10453	29106	231.24	182.88	180.41	53.48
Orb.(M)	23	4104	359	6380	21546	225.15	252.99	178.77	77.92
PN-U3	64	9229	1200	5161	23055	264.16	267.54	219.98	103.05
PQ (M)	19	7116	977	4964	20068	270.04	200.01	218.36	73.29
					Late dolomite				
Orbicular dol.	26	12547	832	11237	22046	201.09	187.08	178.85	80.61
Rosszähne	26	6866	804	10908	16114	253.29	224.01	199.83	84.22
Dol. in joints	8	9807	824	-	37241	221.53	137.52	-	47.71
					Non-carbonate minerals				
Qtz.(PF-north)	6	6564	2993	1275	1694	441.53	327.30	214.25	74.45
Talc (PE21)	3	1308	267	3518	7778	316.83	190.22	211.41	43.33
Gipsum	2	1164	2065	-	3687	839.04	184.15	-	46.36

Tab. 7. 3 Chemical geothermometry of the extracted fluid inclusions.

According to the geothermometric calculations the fluids in equilibrium with magnesite yielded mean value temperatures of 247°C for the Na-K geothermometer and 231°C for the Na-Li geothermometer. The average temperature calculated from the Na-K-Ca geothermometer of the inclusion fluids (224°C) is similar to the mean value from Na-K geothermometer. The Mg-Li geothermometer shows totally low mean value temperature

(95°C). This temperature is considerably lower than the temperatures obtained by any previous geothermometers.

7.3 Microthermometry

The study of fluid inclusions is proving to be the best method of determining temperatures of deposition (Guilbert & Park 1986). The technique of measuring the temperature of thermally-induced phase transitions in fluid inclusions (microthermometry) is the most important analytical technique for characterizing fluid inclusions. The measured homogenization (T_h) and melting (T_m) temperatures of the fluid inclusions microthermometry provide the inclusions formation temperature to be calculated. Additionally microthermometric measurements allow to estimate the bulk composition and density of the inclusions.

Fluid inclusions were selected for microthermometric measurement from are the representative pinolithic magnesite sample (M2-PI). In this sample 29 fluid inclusions were selected and inspected on temperature dependent phase changes which characterize the enclosed fluids. All of the fluid inclusions are primary and two-phase (liquid + vapour) inclusions at room temperature. No visible CO_2 was observed in any of the measured fluid inclusion. Dimensions of measured fluid inclusion range from 5 to 10 μm. The measured inclusions from sparry magnesite show different homogenization temperatures (T_h) of the vapour and liquid phases, but the main group of inclusions homogenized at around 150°C to 190°C. The measured inclusions have a well defined mode around 170 – 180°C and a broader range of T_h at 350°C (Fig. 7. 2).

Final ice melting temperatures (T_m) of the fluid inclusions from sparry magnesite were observed mainly between -30°C to -10°C with a clear peak centered on -20°C to -15°C (Fig. 7. 3), however they have a well defined mode around -20°C (Fig. 7. 3, Fig. 7. 4). This temperature indicates a substantial presence of NaCl in the fluids. Two inclusions have melting temperatures of -65°C and -54°C indicating CO_2-bearing inclusions.

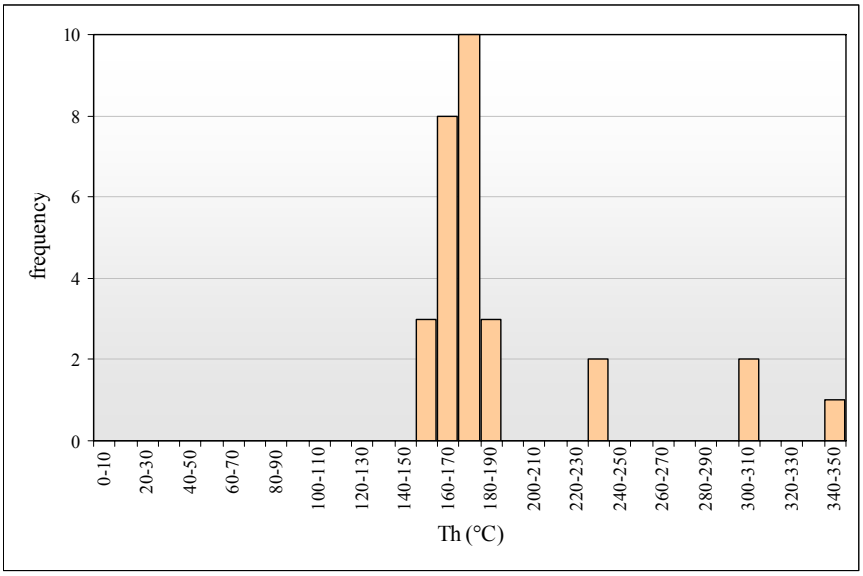

Fig. 7. 2 Histogram of total homogenization temperatures within sparry magnesite (M2-PI).

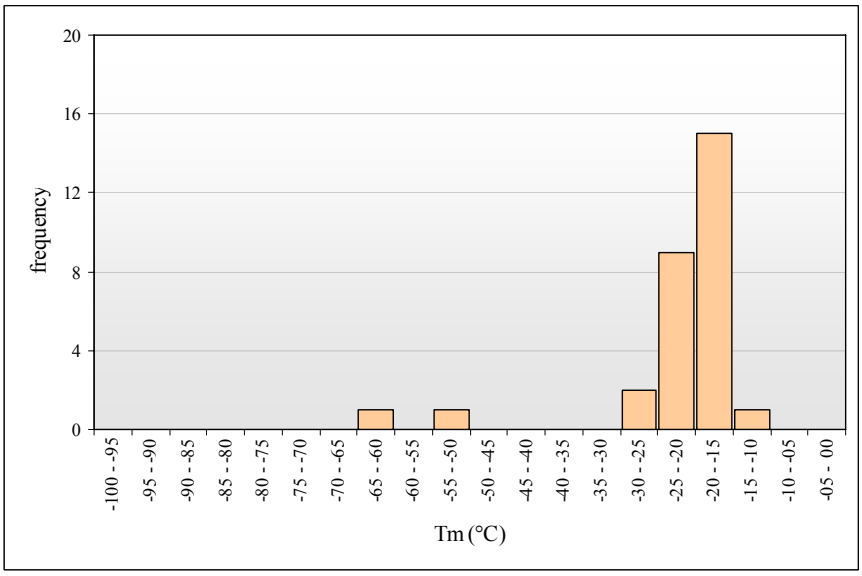

Fig. 7. 3 Histogram of melting temperatures in fluid inclusions in sparry magnesite (M2-PI).

The salinity of aqueous phase were calculated in the H_2O-NaCl system (Bodnar 1993) with the use of *BULK* software from the computer package *FLUIDS* (Bakker 2003). This program calculates bulk densities (and molar volumes) and bulk composition of fluid inclusions using information obtained from microthermometry, micro-Raman spectroscopy cation ratio and volume fraction estimates (Bakker & Brown 2003). Results of calculation using *BULK* software are listed in Box 7. 1. The salinity of the aqueous phase is 22.4 wt% NaCl equivalent.

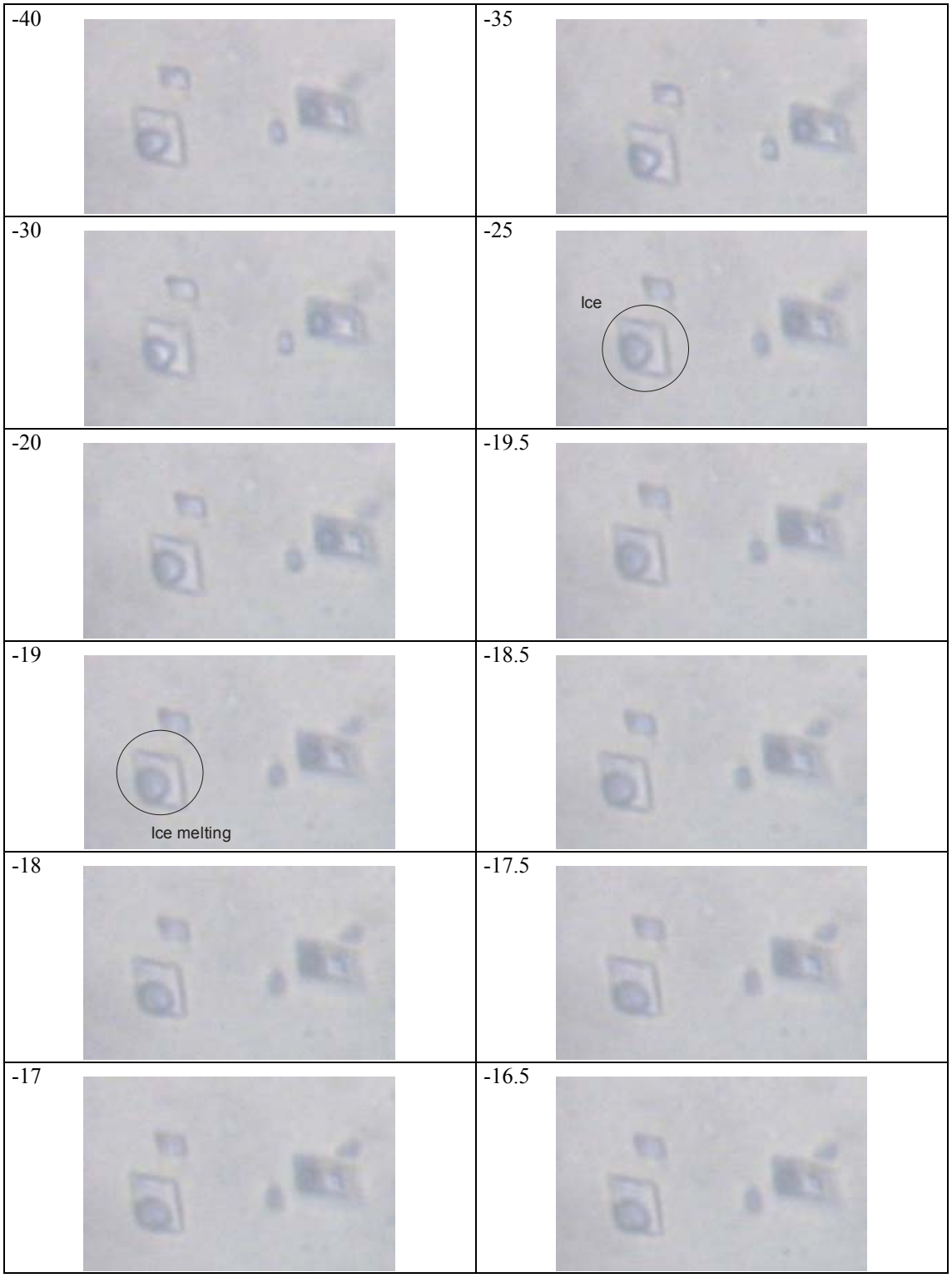

Fig. 7. 4 Typical change of a two-phase aqueous inclusion during heating within sparry magnesite (M2-PI).

FLUIDS, package of computer programs for fluid inclusion studies
Program 1: BULK, version 01/03
Product development Ronald J. Bakker
Filename: magnesite_1

BULK FLUID INCLUSION
Total homogenisation conditions:
Th (K) 443.150000 (170.000000 °C)
Ph (MPa) 0.662134 (6.621344 bar)
Equation of state: Zhang & Frantz (1987)
Vm (cc/mol) 20.162943
D (g/cc) 1.057138
amount-of-substance fractions
H_2O 0.849145
Na^+ 0.075428
Cl^- 0.075428

Fluid inclusion at room temperature (20 °C)
Internal pressure: 0.002339 MPa
Fluid phases present :
1. liquid rim aqueous solution 83.805347 vol.%
2. vapour-like gas mixture 16.194653 vol.%

VAPOUR-LIKE GAS MIXTURE (at 20 °C)
Equation of state: Wagner & Pruss (1993)
Vm (cc/mol) 1040596.392950
D (g/cc) 0.000017
amount-of-substance fractions
H_2O 1.000000

AQUEOUS SOLUTION (at 20 °C)
Equation of state for volumetric properties: Krumgalz et al. (1996)
Vm (cc/mol) 16.897678
D (g/cc) 1.166271
amount-of-substance fractions
H_2O 0.849144
Na^+ 0.075428
Cl^- 0.075428

ICE MELTING CONDITIONS
Purely empirical equation for salinity calculation: Bodnar (1993)
Tm (K) 253.150000 (-20.000000 °C)
Pm (MPa) 0.000008 (0.000075 bar)
Salinity Aqueous Phase (associated salt molecules)

	Molality	Mass%
NaCl	4.930708	22.376000

Box. 7. 1 Calculation of bulk densities, molar volumes and bulk composition of fluid inclusions using BULK software version 01/03 (Bakker 2003).

The formation temperature of inclusions in sparry magnesite is calculated by using the *ISOC* software from the computer package *FLUIDS* (Bakker 2003). The isochore was constructed in the system NaCl-H_2O for a selected fluid composition which is obtained from the *BULK* software. The calculated isochore is constructed in a *P-T* diagram with a geothermal gradient of 35°C/km and geobarometric gradient of 27.1 Mpa/km for lithostatic

conditions (Fig. 7. 5). The intersection point of calculated fluid inclusion isochore with the lithostatic thermobaric gradients indicate the *P-T* conditions of fluid trapping in measured sparry magnesite (Fig. 7. 5). The isochore crosses the lithostatic thermobaric gradients at 265°C and 190 Mpa, which corresponds to a depth of approximately 7 km. However a high heat flow could have increased the geothermal gradient in comparison to the selected gradient of the study area at the time of mineralization.

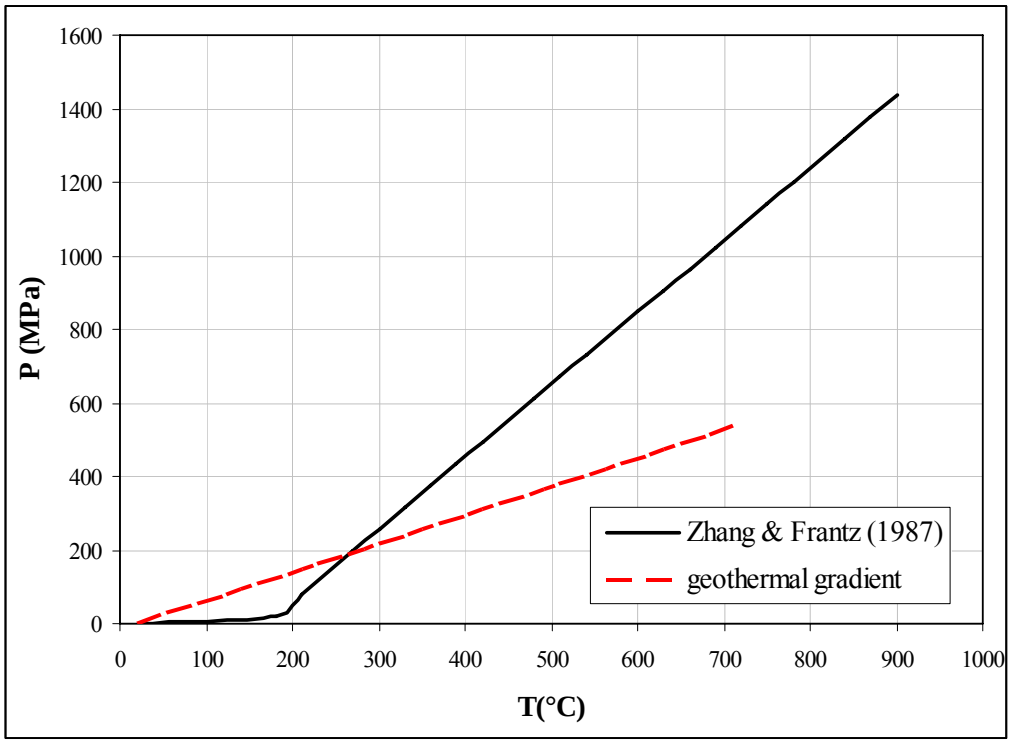

Fig. 7. 5 P-T plots showing the lithostatic thermobaric gradients and their intersection point with the isochore constructed from the inclusions formation temperature in sparry magnesite (Bakker 2003).

8. Succession and genesis of carbonate minerals

In the Hohentauern/Sunk deposit four associations of carbonate minerals have been recognized from geological, petrographical and geochemical criteria: limestone host rocks, dolostone precursor of magnesite, sparry magnesite and late dolomite. Studies of the carbonate rocks, which host the magnesite ore deposit, have importance to investigate the genetic aspects of sparry magnesite deposits. The limestone and dolostone comprise large parts of the stratigraphic record in the mining area and their study helps to understand the history of succession and condition of carbonate mineral formation.

8.1 Carbonate sedimentation

The Hohentauern/Sunk sparry magnesite deposit is hosted by the Steilbachgraben Fm. with a biostratigraphically dated age of Upper Viséan (Felser 1977). The Steilbachgraben formation is a clastic-carbonatic sequence (Fig. 8. 1) where the facies indicative parameters are as following.

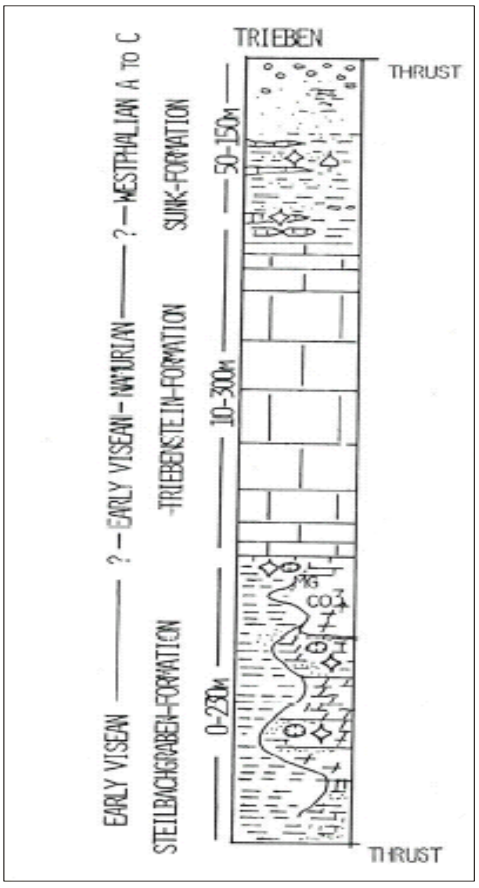

Fig. 8. 1 Schematic columnar section through the Veitsch nappe in the study area (Ratschbacher 1987a).

“Predominant fine-grained, laminated, clastic sediments are interbedded with sandstone beds with a high content of clastic feldspars (up to 50%, mean 14%). Most feldspars include hematite microlites. Shales and terrigeneous influenced limestones show synsedimentary precipitation of pyrite.” Mature sandstones well-sorted and well-rounded, lack contamination by organic material (graphite), which is otherwise widespread, and accompany dolomite lenses. “Basic, tuffogeneous rocks are intercalated locally into fine-grained clastic sediments. The lamination points to an episodic sedimentation below the range of wave action, interrupted by the deposition of the characteristic feldspar-rich silt (sand) stones (Ratschbacher 1987a).”

“A clastic littoral facies and hypersaline shelf lagoons (0-230 m), associated with the bioherms of the Triebenstein Fm. (10-300 m), have been suggested as being the depositional environment of the Steilbachgraben Fm.” They are generally continued by clastic sediments (50-150 m) of Sunk Fm. The sedimentary sequence and facies represent the evolution a shallow shelf, sometimes interfingering with hypersalinar lagoons in the Steilbachgrben-Fm to a subtidal, transgressive carbonate environment with lensoid bioherms in the Triebenstein-Fm, and finally to a regressive shoreline with distributary bay and river dominated delta deposits in the Sunk-Fm. (Ratschbacher 1984, 1987a).

The paleogeographic position in front of a metamorphic hinterland is constrained by the following major facts: The entire stratigraphic sequence of the Veitsch nappe in this paleogeographical model is a marine deposit without detectable stratigraphic breaks which is affected by acid plutonic source rocks from the hinterland (Fig. 8. 2). The depositional basin of the Steilbachgraben Fm. is interpreted as a shallow-marine shelf environment with hypersalinar lagoons which are attached to land masses. Shelves are relatively narrow depositional environments, characterized by a distinct break of slope at the shelf margin (Tucker 1985) and a gently slope of 1-3°. The truncated creep folds within the Steilbachgraben Fm. sediments suggest that material is crept (see chapter 3).

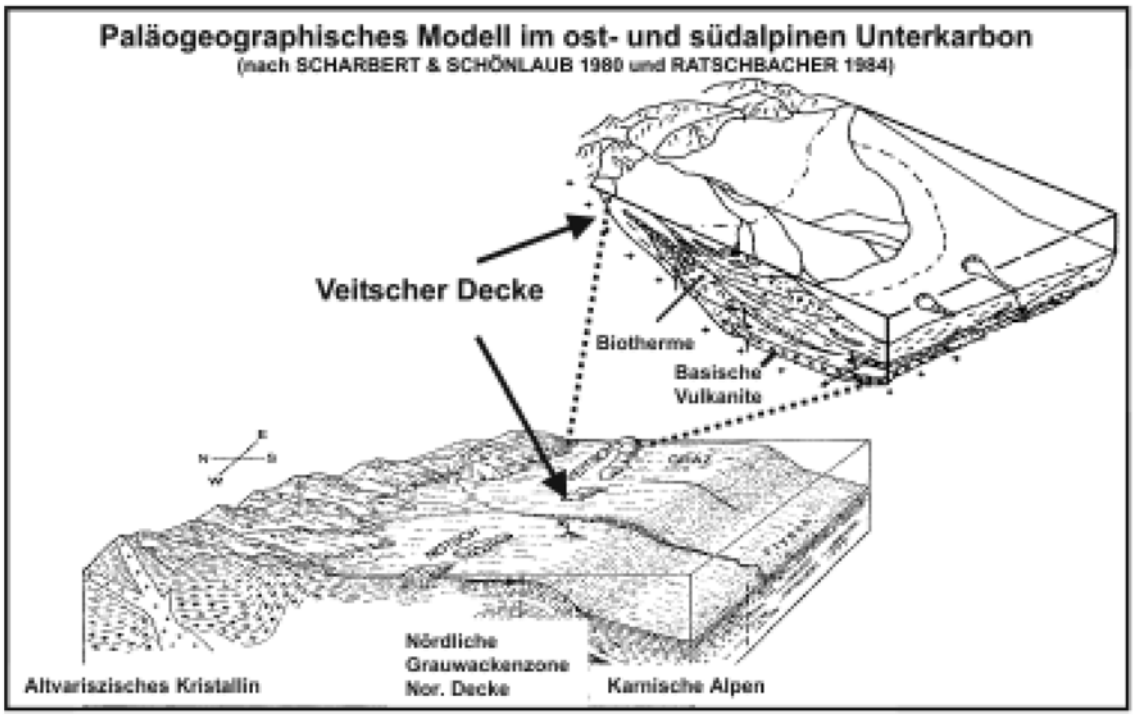

Fig. 8. 2 Paleogeographic model of the early Carboniferous in the Eastern and Southern Alps (Scharbert & Schönlaub 1980). The block model (Ratschbacher 1984) include: Carboniferous of the Veitsch nappe with basic volcanics in the Steilbachgraben Fm., Biohermes in the Triebenstein Fm. and a regressive shore line in the Sunk-Fm.

The tectonofacies in the Veitsch nappe is interpreted as a marine molasse after the first tectonothermal peak (Bretonic phase) of the Variscan orogeny (Flügel 1977, Ebner 1992). In terms of geodynamics it is interpreted as a post-orogenic molasse which started in the late Viséan in the forland of a deformed and metamorphosed zone, which is presently included in metamorphic complexes of the Eastern Alps (Ebner et al. 2007, 2008b).

The limestone of the Steilbachgraben Fm. is characterized by fine grained, banded and fossiliferous limestone with fine laminated microcrystalline dolomite. Mineralogically the bulk composition of limestone displays 7 to 12% of dolomite. The limestone has very low iron contents and high amount of Ti, Rb, Sr and Pb. The REE pattern of the limestone is typical for a marine environment with negative Ce and Eu anomalies. The $\delta^{18}O$ and $\delta^{13}C$ values of limestone are within the normal range of marine carbonate. The $^{87}Sr/^{86}Sr$ values of Steilbachgraben Fm. limestone (solution-based HR-ICP-MS and laser ablation MC-ICP-MS analysis) are defined in the Carboniferous seawater but differ to its biostratigraphically age (Viséan; see chapter 4).

8.2 Early dolomitization

The fossiliferous dense dolomite is the host of sparry magnesite and was formed during early dolomitization of the primary limestone of the Steilbachgraben Fm.. Early dolomitization is confirmed by geological, petrographical and geochemical data. The fine grained dolomite consistently occurs in stratiform beds and has a stratigraphic transition to limestone. Laminated microcrystalline dolomite, very fine grained/dense dolomite and dolomite relicts as microinclusions (<50 μm) within the sparry magnesite are the major petrographical features of the early dolomite.

Early dolomitization is characterized by a low Fe (about 0.7 % wt.), Mn and Al content. The small amount of Al_2O_3 in early dolomite is related to a low content of clay minerals. The early dolomite has low Li, Ti, Hf, Pb contents and the same REE pattern as limestone but with lower total REE absolute value and positive Eu anomaly. Stable isotopes data ($\delta^{18}O$ and $\delta^{13}C$ values) indicate that early fine-grained dolomite was formed by late diagenetic stages. The high Sr content of early dolomite especially in dolomite microinclusions within the sparry magnesite (up to 1500 ppm) can influence the $^{87}Sr/^{86}Sr$ ratios of magnesite (see chapter 4). However an enrichment of the $^{87}Sr/^{86}Sr$ ratios of early dolomite when compared to the contemporary Steilbachgraben Fm. limestone can be used to establish a model for dolomitization. Dolomite formation within the Veitsch nappe is reported (Lesko 1960, Briegleb 1971, Ratschbacher 1987a), however the model of dolomitization in the Veitsch nappe is not studied.

8.3 Magnesite mineralization

Sparry magnesite in the Hohentauern/Sunk deposit occurs in three magnesite bodies (see chapter 3, Fig. 3. 3): a thin magnesite layer at the footwall (magnesite I), 50 m thick bedded to massive sparry magnesite in the middle part (magnesite II) and some meters of magnesite at the hanging wall (magnesite III). Thin sulfate beds adjacent to the magnesite bodies have been drilled (Petraschek 1978). The magnesite bodies are stratiform and accompanied by sedimentary structures. However the field observations of the magnesite body display metasomatic structures at the contact of the host rocks. In addition, the XRF analyses reveal that most of the magnesite samples contain variable amounts of dolomite. Back-scattered electron images of all studied magnesites showed that these contain irregularly distributed dolomite microinclusions (<50 μm). Dolomite inclusions are

interpreted as relics of a dolostone precursor that has been replaced by Mg-rich fluids during sparry magnesite formation.

Petrographically the sparry magnesite is characterized by pinolite, rosettes and banded textures (Zebra banding) where the crystals are surrounded by black matrix. The matrix is composed of graphite, chlorite and carbonaceous materials. Frequently a zoning of magnesite crystals is visible under cathodoluminescence. The zoning of magnesite crystals correlate to Fe-rich and Fe-poor zones. Submicroscopic crystals of evaporite minerals (Sylvinite) are hosted in sparry magnesite (Fig. 3. 23b).

Geochemically the bulk composition of sparry magnesite from Hohentauern/Sunk deposit has lower MgO and higher CaO contents in comparison to single magnesite crystals. The sparry magnesite has also about 2 wt. % of SiO_2 and 1.90 wt. % (as well as EPMA analysis of individual magnesite crystal with 2.2 wt. %) of Fe_2O_3. The elevated CaO/MgO ratio of sparry magnesite derives from relics of dolomite microinclusions and various forms of late dolomite according to the redolomitization of magnesite. SiO_2 contents may derive from chlorite and talc mineralization and Fe_2O_3 contents are due to Fe substitution for Mg in the magnesite crystal lattice.

The concentrations of selected trace elements (Sr-Ba, Ti, Fe-Mn and Cr-Ni-Co) in sparry magnesite illustrate a marine/evaporitic and/or Mg^{2+}-metasomatism origin of magnesite mineralization. The REE pattern of sparry magnesite displays low LREE/HREE ratios and depletion of LREE. The sparry magnesite of Hohentauern/Sunk deposit is characterized by a negative Ce anomaly. The stable isotopes ($\delta^{18}O$ and $\delta^{13}C$) data of sparry magnesite overlap with those of magnesite formed by metasomatic dolomite replacement. The $^{87}Sr/^{86}Sr$ ratios indicate strong heterogeneity and are affected by a great deal of causes. Therefore they are not characteristic for the magnesite mineralization. However Nd-Sr isotopes chemistry show that the percolating Mg-rich fluid passed through crustal rocks (see chapter 4). The study of fluid inclusions of sparry magnesite indicates a high salinity of the Mg-rich solutions which transformed the dolomite protolites (see chapter 6). Isotope geochronology of sparry magnesite shows a range of Late Carboniferous to Early Permian (see chapter 5).

8.4 Late dolomite

The magnesite formation in the Hohentauern/Sunk deposit is followed by several generations of late dolomite which occur as five main types:

- Sparry dolomite at the contact to the magnesite and host rocks.
- Submicroscopic redolomitization of magnesite along cracks.
- Idiomorphic dolomite crystal ("Rosszähne" or "teeth of a horse") in veins and partially open spaces.
- Orbicular dolomite.
- Dolomite as joint filling.

The sparry dolomite at the contact of magnesite is formed by alteration phenomena and recrystallization of dolomite host rocks and does not depend on redolmitization processes of magnesite. The magnesite is invariably redolomitized along shear zones, faults and fractures and was partially replaced by late dolomite. Redolmitization of magnesite and formation of late dolomite are characterized by high iron content (up to wt. 2% of Fe_2O_3), low Ti content (below 0.3 ppm), high LREE/HREE ratio and negative Ce anomaly. Additionally this event resulted in $\delta^{18}O$ and $\delta^{13}C$ enrichment in comparison to sparry magnesite. The chemical composition of fluid inclusions indicates non evaporation events as late dolomite mineralization processes. Petrographical and geochemical properties of dolomite hosted by dolostone and filling the joints exhibit the formation of this type of late dolomite is different to the redolomitization of magnesite. Crystallization of dolomite occurred by dissolution and remobilization of early fine-grained dolomite at young geological events.

Redolmitization of magnesite is interpreted to have occurred through replacement of magnesite due to the action of more dilute solutions. The redolmitization of magnesite is well explained experimentally (Johannes 1966, 1970) according the reaction:

$$2MgCO_3 + CaCl_2 \leftarrow\rightarrow CaMg(CO_3)_2 + MgCl_2$$

9. Impacts of geological processes to the quality of magnesite

9.1 Introduction

The raw magnesite has limited markets as a source of magnesia. Magnesite ($MgCO_3$) is the component for the production for caustic calcined (caustic magnesia), dead burned (sintered magnesia) and electrofused magnesia. Magnesium metal can be produced from magnesite by electrolysis of magnesium chloride. The raw magnesite is also used as a filler in plastics and paints, and as an agricultural fertilizer (Harben 2002).

Pure magnesite contains theoretically 47.8 % MgO and 52.2 % CO_2. However, the refractory manufactures have indicated the following specifications of magnesite for use in the refractory industry (Tab. 9. 1). These are the general specifications. But, some manufactures allow silica up to 4%, CaO content up to 1.5% and iron content up to 5% (Ranawat 2009).

Physical specifications:	
Specific gravity	2.95 to 3.20
Hardness	3 to 4.5 on Mohs scale.
Chemical specifications:	
MgO	42.5% (min.)
SiO2	2.5% (max.)
Fe2O3	2% (max.)
Al2O3	2% (max.)
CaO	1% (max.)
L. O. I.	47.5 to 49.5%

Tab. 9. 1 Specifications of magnesite for use in the refractory industry (Ranawat 2009).

RHI is the leading refractory company in the world. The source material used in the extensive product range is raw magnesite that is extracted in different qualities at the RHI mines. The raw magnesite is used broadly for production of different type magnesia. The typical analysis for magnesia products of RHI refractories and chemical specifications of related raw magnesite components are listed in Tab. 9. 2.

		Animal Feed Industry	Building Materials	Sintered Magnesia
Magnesia	MgO	83.00 – 85.00	70.00 – 73.00	85.00 – 99.80
	CaO	4.00 – 5.00	4.00	0.10 – 3.50
	SiO_2	2.00 – 5.00	4.00 – 7.00	0.10 – 3.00
	Fe_2O_3	4.00 – 5.00	3.00	0.10 – 8.00
	Al_2O_3	0.70 – 1.00	1.00	–
	B_2O_3	–	–	< 0.30
	L. O. I.	1.00 – 4.00	14.00 – 15.00	–
Raw magnesite	MgO	41.66 – 43.62	38.99 – 39.56	43.46 – 47. 69
	CaO	2.10 – 2.45	2.14 – 2.26	0.06 – 1.52
	SiO_2	2.00 – 5.00	4.00 –7.00	0.10 – 3.00
	Fe_2O_3	2.10 – 2.45	1.60 – 1.70	0.06 – 3.48

Tab. 9. 2 Chemical analysis for magnesia products of RHI (www.RHI.at) and chemical specifications of related raw magnesite (stoichiometricallyy calculated).

An average of all magnesite chemical analysis had been documented during mining time in Hohentauern/Sunk magnesit mine (Tab. 9. 3). A SiO_2 content > 2 % was the limiting factor for mining. However, a general view of magnesite analysis of the Hohentauern/Sunk deposit shows a large geochemical variability (Tab. 1 App A). Different types of sparry magnesite have MgO values of 22.76% (strongly redolomitizied) to 45.26%, CaO: 0.28% to 26.57% (strongly redolomitizied), Fe_2O_3: 1.28% to 2.61% and SiO_2: 0.02% to 5.53%.

Average chemical composition of magnesite ore body during mining time:	
MgO	43.3%
CaO	2.5%
Fe_2O_3	2.4%
FeO	2.2%
SiO_2	2%
CaO/MgO	0.057
L. O. I.	49.8%

Tab. 9. 3 The average geochemistry of the mined Hohentauern/Sunk magnesite deposit (Ebner & Prochaska 2001).

9.2 Dolomite and talc mineralization as a reason of magnesite low quality

The magnesite bodies especially in the tectonized zones and at the contact of host rocks are increased in CaO contents and thus they don't have an ideal magnesite composition. Additionally, the MgO values are strongly scattered in comparison with the composition of ideal magnesite and average chemical composition of magnesite ore body. The lower MgO and higher CaO content is related to dolomite relicts in magnesite and late dolomite mineralization. The magnesite formation was partially replaced by late dolomite (redolomitization of magnesite) due to the action of more dilute solutions. Redolomitization of magnesite is achieved through intensive intergrowth with late dolomite mineralization in the macroscopic to submicroscopic scale (Azim-Zadeh et al. 2005). Although this event is documented by REE patterns, $\delta^{18}O$ and $\delta\ ^{13}C$ enrichment of the precursors were preserved. As a result, magnesite is followed by several generations of late dolomite and the pinolitic textures are destroyed in parts.

The magnesite ore body in some parts show relatively higher SiO_2 and Al_2O_3 contents. Higher SiO_2 content is depended on talc mineralization as an alteration product from magnesite and dolomite by the interaction with a SiO_2-rich fluid. Talc regularly forms along joints and shear zones in a very late orogenic stage. Higher SiO_2 content can be caused by chlorite mineralization in the matrix between magnesite crystals. The increased SiO_2 levels are set by the different proportions of dolomite crystals and fine-grained dark matrix. The matrix consists mainly of chlorite, magnesite and graphite. The geochemical limiting factor for refractories was primarily the SiO_2 content of 2%.

9.3 The orogenic fault tectonic and late mineralization

The sparry magnesite was formed by pre-orogenic metasomatic processes and affected by Cretaceous Alpine folding, low grade metamorphism and late-orogenic extensional and shear tectonics. CaO and SiO_2 contents are lowering the quality of the magnesite. These are the result of inclusions of dolomite as relics of dolostone precursor, redolomitization of magnesite and talc mineralization in the magnesite respectively along joints and shear zones. One of the basic structural elements of the late orogenic fault tectonic event is the Pöls-Lavanttal fault zone which is situated in the west part of the mining area (1500 m W of the open pit, Fig. 9.1).

9.4 The Pöls–Lavanttal fault system

The Idria-Lavanttal-Pöls fault system formed during the Miocene and is characterized by recent kinematics similar to the Miocene. The Pöls-Lavanttal strike slip fault zone is regarded as still active with a dextral sense of shear derived from focal plane solutions (Reinecker 2000, Reinecker & Lenhardt 1999).

The NNW trending, dextral Pöls–Lavanttal fault system crosses the Murtal-Mürztal fault system in a complex interference zone. Dextral offset as deduced from displaced lithological units amounts to ca. 8 km along the Pöls segment N and to ca. 10 km along the Lavanttal segment S of the Murtal–Mürztal fault. The Lavanttal fault formed pull apart basins at right-handed oversteps. In its southern part where it separates basement from Neogene strata of the Lavanttal basin, the fault displays a vertical throw of >2 km. The nature of the Lavanttal basin is probably an oblique graben structure formed in a transtensional regime (Frisch et al 2000). However new investigations indicate that the Lavanttal basin was formed as pull-apart basin (Reischenbacher 2009). Near its southern termination the Lavanttal fault cuts and offsets the Periadriatic lineament by about 20 km (Frisch et al 2000).

The compatible stress ellipsoid of dextral-strike slip Pöls fault in the study area and main tectonic structures (fold and fault systems) at the Hohentauern/Sunk mining area displays an effective function of Pöls fault on deformation features. The structural geology of the mining area illustrates that 38% of measured fault planes is distributed by similar trend of the Pöls fault (see chapter 3). Moreover redolomitization of magnesite and talc formation are occurred along joints and shear zones. Therefore main tectonic structures e.g. Pöls fault have major role in decreasing magnesite quality according dolomite and talc mineralization. A detailed study was carried out along a selected profile on the mining level XIV R at the open pit (Ebner & Azim-Zadeh 2007).

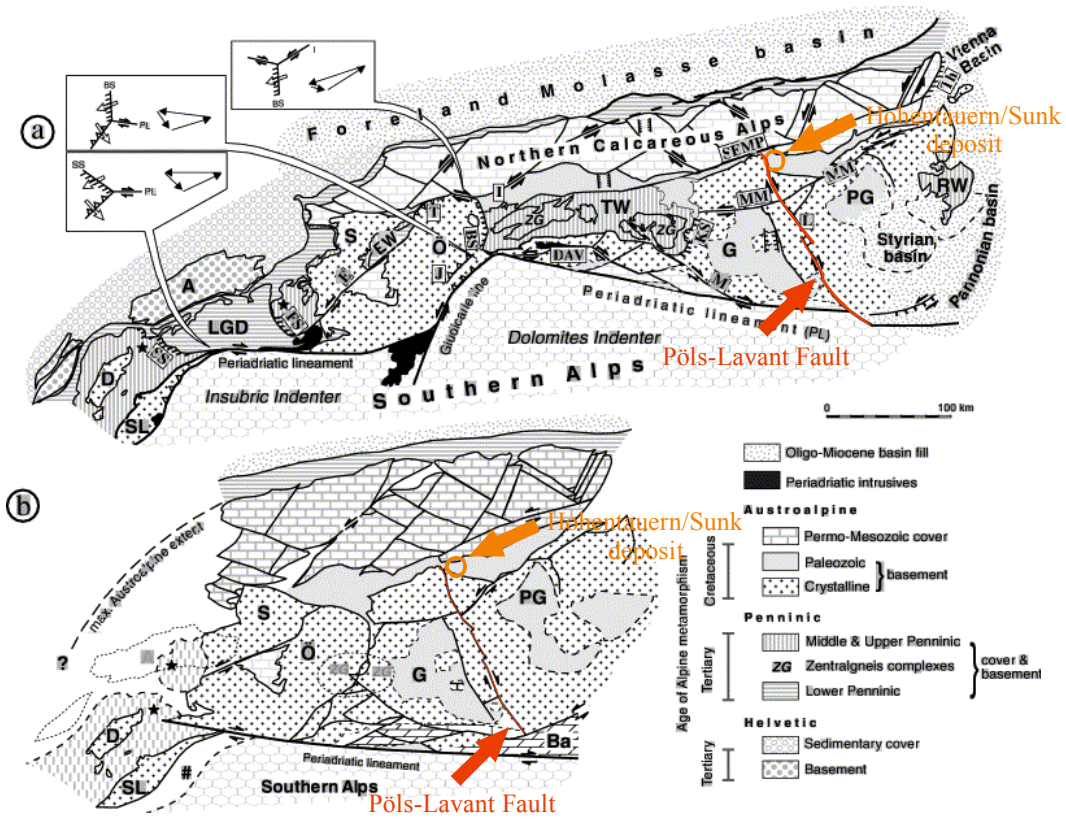

Fig. 9. 1 Pöls-Lavanttal fault system and the situation of the Hohentauern/Sunk deposit (Frisch et al 2000).

9.5 Investigation of a detailed profile

A NE to SW profile is studied along XIV R mining level. The lithological units, structural features and geochemical data of a detailed profile are shown in Fig. 9. 2 and Fig. 9. 3. The profile trend intersects the Cretaceous anticlinal-synklinal fold system. To assess the quality parameters of the magnesite ore body 20 samples of pinolite magnesite and dolomite in relation to tectonical structures (faults and joints) were investigated. The samples were analyzed by AAS (Tab. 9. 4). The geological - geochemical profile of the XIV R mining level illustrates that the quality of magnesite is decreasing along the faults and joints, near the shear zones and at the contact of the carbonate host rocks (Fig. 9. 2). In the tectonized zones the magnesite samples are increased in CaO/MgO ratios but there are no significant changes in the FeO contents. High values of CaO/MgO ratio clearly depend on the redolomitization of magnesite and existence of different types of late dolomite. The rate of redolomitization in the fault zones as well as shear zones is higher than redolomitization of magnesite along single faults or joints.

A detailed structural profile in combination with CaO/MgO and FeO ratios of analyzed magnesite samples is shown in Fig. 9. 3. According statistical distribution of tectonical structures and the direction of principal stresses of stress ellipsoid the fault and joint systems split into following directions:

1) NE-SW (ac-fractures perpendicular to the folds axis)
2) NW-SE (bc-fractures parallel to the folds axis)
3) ± N-S (parallel to Pöls fault)
4) ± E-W (Riedel plane of Pöls fault)

The average values of CaO/MgO and FeO of the magnesite ore body during mining time are 0.057 and 2.20 % respectively. The FeO content of all analyzed samples are below the average value but the values of CaO/MgO ratio range from under average value to 1.6. The samples with a higher value of the CaO/MgO ratio (up to 1) were identified as dolomite. The samples with 0.057 to 1 values of CaO/MgO ratio are partly to strongly redolomitized and are connected with the tectonized zones.

Sample No.	Ca %	Mg %	Fe %	Mn %	Sr %	CaO %	MgO %	CaO/MgO	FeO %
PB	4.85	22.59	1.04	0.07	0.02	6.79	37.46	1.18	1.34
PC1	15.11	18.75	1.16	0.11	0.05	21.15	31.10	0.68	1.49
PC5	9.06	21.11	1.10	0.08	0.04	12.68	35.00	0.36	1.42
PD1	1.84	25.98	0.96	0.08	0.00	2.58	43.07	0.06	1.24
PD8	0.68	22.50	0.82	0.07	0.00	0.95	37.31	0.03	1.06
PE3	0.73	23.60	0.86	0.07	0.00	1.02	39.14	0.03	1.11
PE4	25.88	13.73	1.13	0.10	0.06	36.24	22.76	1.59	1.45
PE7	21.10	15.03	0.99	0.07	0.08	29.54	24.92	1.19	1.28
PE10	6.12	20.96	0.89	0.08	0.01	8.57	34.75	0.25	1.15
PE14-g	1.71	23.64	0.78	0.06	0.00	2.40	39.19	0.06	1.00
PE14-f	0.62	20.97	0.70	0.05	0.00	0.87	34.77	0.03	0.91
PE16-g	1.17	21.56	0.72	0.06	0.00	1.64	35.74	0.05	0.92
PE16-f	0.59	24.76	0.98	0.07	0.00	0.83	41.06	0.02	1.27
PE21	0.77	21.44	0.66	0.05	0.00	1.08	35.54	0.03	0.86
PE24-g	0.92	24.28	0.89	0.07	0.00	1.28	40.26	0.03	1.14
PE24-m	1.09	24.80	0.89	0.07	0.00	1.52	41.11	0.04	1.15
PE28	0.89	20.22	0.74	0.06	0.00	1.24	33.53	0.04	0.95
PE33-g	1.93	24.95	1.23	0.09	0.00	2.71	41.37	0.07	1.59
PE33-f	19.21	16.34	0.76	0.05	0.03	26.90	27.10	0.99	0.98
PE33-Dark	23.65	14.05	0.60	0.05	0.04	33.11	23.30	1.42	0.77

Tab. 9. 4 Geochemical compositions of magnesite and dolomite samples from XIV R mining level (AAS analyses).

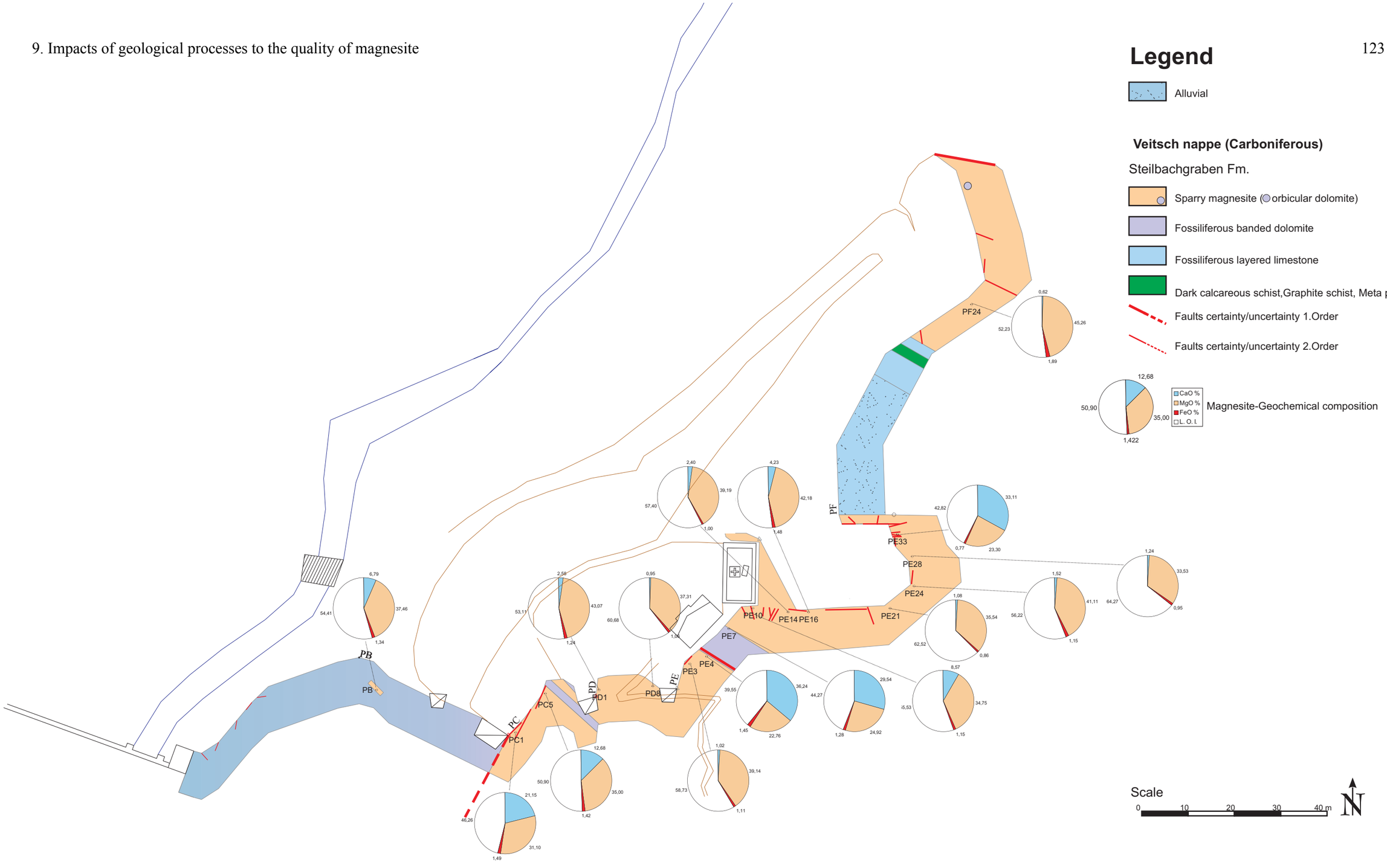

Fig. 9. 2 Geological-geochemical profile along XIV mining level.

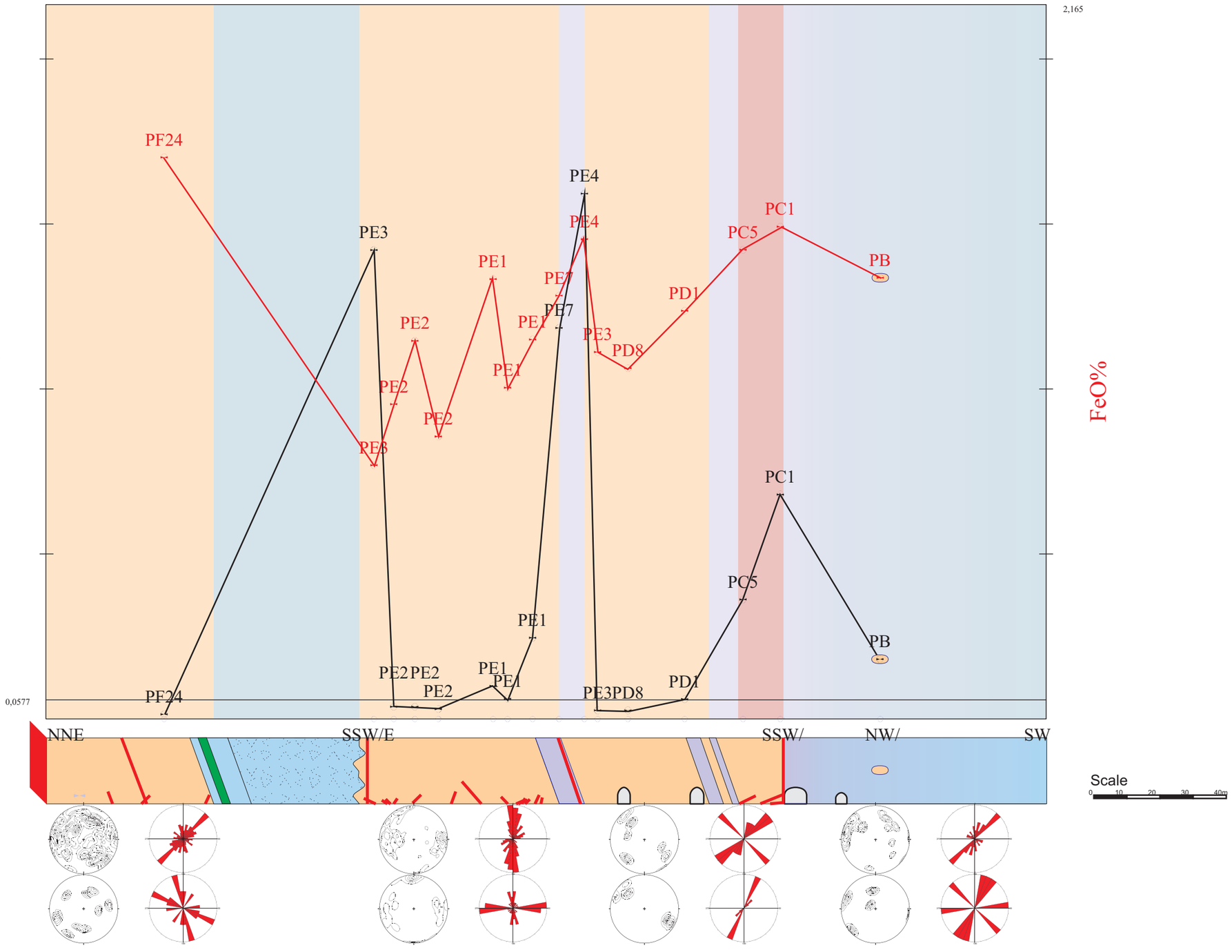

Fig. 9. 3 Structural-geochemical profile along XIV mining level.

10. Discussion

In carbonate rocks magnesite ore and dolomite forming processes due to replacement of Ca^{2+} by Mg^{2+} are controlled by the equation: $CaCO_3 + Mg^{2+} + aq \rightarrow MgCO_3 + Ca^{2+} + aq$ Generally this replacement happens 1) by accumulation crystallization within the soft sediment during the early diagenesis, 2) metasomatism by migrating Mg-rich crustal fluid deriving from evaporitic basins or seawater concentration and 3) metamorphogenic processes. The ore forming fluids are formation water, residual evaporitic brines, expelled basinal or metamorphogenic fluids. The Mg^{2+} source for the fluid is seawater or Mg-rich sediments/rocks. Mostly Mg^{2+} is transported by $MgCl_2$ solutions (Wilson & Ebner 2005).

The geological, petrographical and geochemical features shown by the Hohentauern/Sunk sparry magnesite deposit and related carbonates support a diagenetic dolomitization of carbonate host rocks and an epigenetic origin for the magnesite deposit via metasomatic replacement of a dolomitic protolith by high-salinity Mg-rich solutions. The particular appearances of evidence that were considered are outlined below.

- **Geological evidence**

The sparry magnesite in the Hohentauern/Sunk deposit occurs in three magnesite bodies. They are stratiform and intercalated with fossiliferous fine grained dolomite layers. However, the magnesite bodies display metasomatic textures at the contact of the dolomite host rocks. The magnesite bodies are accompanied also by sedimentary structures such as load casts, flame structures and creep folds at the bottom of the magnesite. This horizon is interpreted as creep horizon of an early dolomite precursor. Thick sulfate beds (gypsum and anhydrite) adjacent to the sequence of magnesite, calcareous schists and dark phyllites have been drilled. In accordance with the general strike (WWN-SEE) and steep dip of the host rock the layers of gypsum and anhydrite are considered as stratigraphic intercalations.

The magnesite bodies and their host rocks were deformed by Alpine folding and metamorphism which was followed in regional scale during the Tertiary by an E-directed lateral extrusion with intensive strike slip and fault tectonics. This suggests that the dolomitization and magnesite formation predate the main Alpine deformation. The major tectonic style at the Hohentauern/Sunk mining area, which also affected the magnesite, includes anticlinal and synclinal folding with the axis plunging to the NW. The huge

boudins are resulting from deformation of host rocks and magnesite with variable thickness and different competent-incompetent layers during folding and faulting.

- **Petrographical and mineralogical evidences**

All studied magnesite samples show irregularly distributed dolomite microinclusions under backscattered electron imaging. Dolomite microinclusions are interpreted as relics of an early dolomite precursor sediment that has been metasomatically replaced by Mg-rich fluids to form sparry magnesite. Coarse-grained magnesite crystals include more dolomite relicts than fine grained magnesite. It shows that the replacement rate of the dolomite precursor by the flow of metasomatizing fluids is related to the crystal size too. Throughout Mg-metasomatism fine grained dolomite was transformed completely to magnesite. Cathodoluminescence images of magnesite samples shows a visible zoning of Fe-poor and Fe-rich zones which indicate metsomatic growth.

One characteristic texture of the Hohentauern/Sunk magnesite is the arrangement of the magnesite crystals into a zebra structure. Zebra structures are generally bedding parallel and they consist of millimeter to centimeter scale rhythmic alteration of white and black bands. The detailed study of the magnesite rhythmites from Eugui magnesite deposit (Lugli et al. 2000) reveals that they derived during a complex replacement process of dolomite principally controlled by the structural and textural characteristics of the protholith. The process seems to have began with the flow of metasomatizing fluids along stylolites and bedding planes in the dolomite sequence (Lugli et al. 2000). As a result the zebra structure in magnesite has been interpreted as a replacement feature of magnesite after dolomite (Lugli et al. 2000, Kilias et al. 2006).

The magnesite bodies in the Hohentauern/Sunk deposit are partly replaced by dolomite. The redolomitization of magnesite is a characteristic feature of hydrothermal metasomatic magnesite deposits formed by replacement of dolomite such as Rum Jungle (Aharon 1988) and Eugui (Lugli et al. 2000). This feature has been attributed to a reversal of the order of dolomite by magnesite mineral replacement due to the increase of the release of substantial amount of Ca^{2+} into the fluid during the replacement of dolomite by magnesite (Aharon 1988).

- **Geochemical evidence**

Veitsch type magnesite is characterized by an elevated Fe-content of several percents, MnO is about to one tenth of FeO. Low Al_2O_3, SiO_2 and CaO are variable, depending on the quartz, chlorite, talc and dolomite contents (Pohl & Siegl 1986). In general, magnesite is remarkably poor in respect of trace elements. Locally they may contain trace elements, however, a high trace element content and even minor meatlliferous mineralization. In these latter instances it is discussed whether such mineralization is syngenetic or due to epigenetic introduction of elements by later hydrothermal or metamorphic processes (Pohl & Siegl 1986). Rare earth element distribution patterns and their contents in magnesite and enclosing dolomite were determined by Morteani et al. (1982). They are comparable and similar to marine carbonates in general. Magnesite and its host dolomite display the same REE patterns, although the dolomites have slightly higher total contents. Magnesite and dolomite contain less light REE in comparison to the limestone average.

In the Hohentauern/Sunk deposit the geochemistry of sparry magnesite is incompatible with its carbonate host rocks (limestones and early dolomites) from marine solutions. The bulk composition of sparry magnesite has lower MgO and higher CaO contents in comparison to single magnesite crystals. The sparry magnesite has also about 2 wt. % of SiO_2 and 1.90 wt. % of Fe_2O_3 (as well as an EPMA analysis of an individual magnesite crystal with 2.2 wt. %). The elevated CaO/MgO ratio of sparry magnesite derives from relics of dolomite microinclusions and various forms of late dolomite according to the redolomitization of magnesite. SiO_2 contents may derive from chlorite and talc mineralization and Fe_2O_3 contents are due to Fe substitution for Mg in the magnesite crystal lattice. All the investigated magnesite samples contain significant amounts of Ca and they are richer in Fe and Mn than their replaced dolomitic precursor. This suggests that magnesite was produced by permeant Mg-metasomatism of early dolomite by fluids carrying appreciable amounts of Fe and Mn. The final stage of such a metasomatic process would be the complete transformation of the original early dolomite into a massive sparry magnesite.

The concentrations of selected trace elements (Sr-Ba, Ti, Fe-Mn and Cr-Ni-Co) in sparry magnesite illustrate a marine/evaporitic and/or Mg^{2+}-metasomatism origin of magnesite mineralization (see chapter 4). The REE pattern of sparry magnesite displays low LREE/HREE ratios and depletion of LREE. Magnesite crystals typically grow

incorporating mainly HREE, whereas LREE are rejected (Bau & Möller 1992). Therefore, if magnesite shows detectable amounts of LREE, they may contain microinclusions of Ca-bearing minerals such as dolomite, suggesting replacement of a dolomite precursor (Möller 1989). In the studied magnesite samples without redolomitization the LREE content (∑LREE=8.6 ppm as an average value) may be inherited from impurities of the dolomite precursor, which were not displaced by magnesite growth. Additional fractionation and decrease of LREE is connected to metasomatic recrystallization (Möller 1989), because more quantity of fluids has passed through such zones (Krupenin 2002). The sparry magnesite of Hohentauern/Sunk deposit is characterized by a negative Ce anomaly. However, the REE patterns of the sparry magnesite cannot be explaned by interaction between the early dolomite host and marine or pore water in coastal sediments. Such processes would produce weakly fractionated REE patterns without positive Eu anomalies (Sholkovitz et al. 1989, Sholkovitz 1990). For those reasons the REE patterns of sparry magnesite are explained most probably by an inherited influence from a dolomite precursor and confirm that they are not a typical feature of sedimentary magnesite, but for metasomatic replacement.

The $\delta^{18}O$ and $\delta^{13}C$ values of limestone from the Steilbachgraben formation are within the normal range for marine carbonates. The Steilbachgraben limestone has $\delta^{18}O$ lower than typical marine limestone ($\delta^{18}O$: 25.2-28.6 SMOW ‰, Veizer & Hofes 1976) and also marine shallow deposits (30.4-32.5 ‰ SMOW, Veizer 1983). The $\delta^{18}O$ depletion may be due to: isotope exchange between the carbonates and fluids with an external source of light O influences of more depleted seawater (Tucker & Wright 1990), reequilibration with solutions that were more depleted in $\delta^{18}O$ than marine waters, most likely during diagenesis (Fernandez-Nieto et al. 2003) or isotope exchange with ^{16}O-rich pelitic rocks (Valley 1986). The $\delta^{13}C$ values overlap with average $\delta^{13}C$ values of Phanerozoic marine limestone (-2.0 to +6.0 PDB ‰, Veizer et al. 1999) suggesting that C derived from marine carbonate. The $\delta^{18}O$ value of the early dolomite is about 4 ‰ heavier than those of the limestone. It can be interpreted as a result of dolomite-calcite fractionation $\Delta\ ^{18}O_{dol\text{-}cal}$ during diagenesis. The $\delta^{13}C$ values of the early dolomite are situated within the field of marine $CaCO_3$. This suggests that the $\delta^{13}C$ has been inherited from the $CaCO_3$ replaced by the dolomite or derived from the dolomitizing fluids (modified seawater) which had a $\delta^{13}C$ value similar to the seawater from which the $CaCO_3$ grains were precipitated (Tucker &

Wright 1990). The $\delta^{18}O$ and $\delta^{13}C$ values of the early dolomite indicate that dolomite formed during late diagenetic stages. The O and C isotope values of the Hohentauern/Sunk sparry magnesite deposit are depleted relative to the carbonate host rocks and overlap partly or wholly with those reported for metasomatic sparry magnesite formed by dolomite replacement (Aharon 1988, Kralik et al. 1989, Lugli et al. 2002, Schroll 2002). But they differ from those of magnesite from recent playas and sabkhas, which have heavier O and C isotope compositions (Melezhik et al. 2001). The lighter $\delta^{18}O$ values of magnesite samples can be referred to as results of increasing temperature during diagenetic and metamorphic processes. The $\delta^{13}C$ values of magnesite tend toward lighter and negative contents. This would be expected if the sedimentary C was mixed with the lighter C from the organic material oxidized during metamorphic processes (Velasco 1987). Increasing metamorphism changes the $\delta^{13}C$ into lighter C (Schroll 2002). Furthermore, comparing with sparry dolomite, the lighter values of $\delta^{13}C$ in magnesite samples with similar $\delta^{18}O$ values could result from high fluid/rock ratios, whereas those of dolomite require moderate to low fluid/rock ratios (Fernandez-Nieto et al. 2003). The isotope composition of the magnesite-forming fluid (Fig. 10. 1) is consistent with formation waters (Hofes 2004).

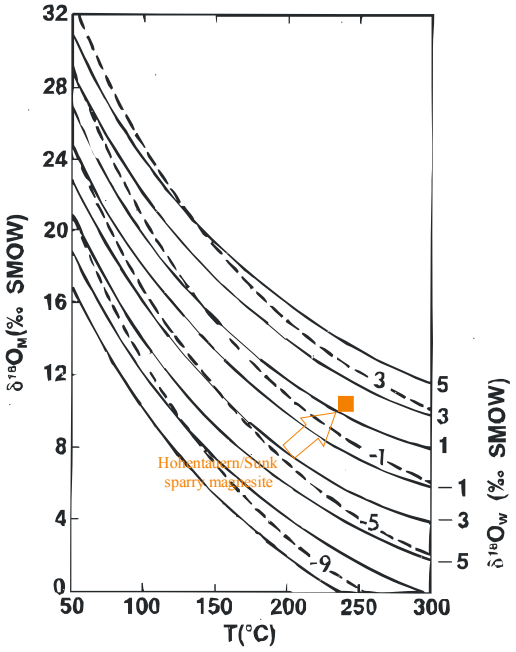

Fig. 10. 1 The $\delta^{18}O$ composition of mineralization fluid in equilibrium with magnesite at fluid inclusions trapping temperature. Iso-δ lines (full line and dashed line are from Aharon 1988).

The $^{87}Sr/^{86}Sr$ ratios, which were measured in magnesite by HR-ICP-MS range from 0.70918 to 0.710881. The higher $^{87}Sr/^{86}Sr$ ratios of the magnesite in comparison to limestone host rocks are affected by a great deal of causes such as high $^{87}Sr/^{86}Sr$ ratios of dolomite microinclusions and ^{87}Sr-enriched solutions (interaction with Rb bearing minerals). The electron microprobe analyses of Sr in sparry magnesite and their dolomite microinclusions show that magnesite has lower Sr contents than dolomite. The high Sr content of dolomite microinclusions can change the $^{87}Sr/^{86}Sr$ ratios of magnesite, respectively. In situ Sr-isotopes (laser ablation MC-ICP-MS analysis) of the magnesite samples along the selected profiles differ from the conventional solution-based analysis of selected crystals. The $^{87}Sr/^{86}Sr$ ratios indicate strong heterogeneity between matrix materials, individual crystals and even inside the crystals. The scatter of Sr-isotopes is not clearly known, it can depend on different mineral phases, specially dolomite relicts or redolomitization, compositional heterogeneity between individual crystals and distributions of fluid inclusions. Sr-isotope values along measured sections which have a low compositional heterogeneity indicated an average $^{87}Sr/^{86}Sr$ ratio of 0.70815 which is similar to the limestone host rocks. However, the scatter of Sr-isotopes along the profile displays a variable change in the $^{87}Sr/^{86}Sr$ ratios. As a result the $^{87}Sr/^{86}Sr$ ratios indicate strong heterogeneity, therefore they are not characteristic for the magnesite mineralization.

The correlation between εNd and $^{87}Sr/^{86}Sr$ ratios has been used to define a thoroughfare for the Mg-rich solutions. The magnesite samples with Sr isotopic ratios of 0.709167 to 0.710821 and εNd of –5.6087 to –5.1793 concentrate in the continental crust domain, suggesting that continental crust contamination played a major role in the genesis of the magnesite mineralization. The Nd-Sr isotopes chemistry show that the percolating Mg-rich fluid passed through crustal rocks (see chapter 4).

- **Age of the magnesite mineralization**

The age of the mineralized carbonate host rocks of the magnesite ore body was determined biostratigraphically by corals as Upper Viséan Dibonuphyllum zones 2–3 (Felser 1977). Sr isotope stratigraphy (SIS) using $^{87}Sr/^{86}Sr$ values (solution-based HR-ICP-MS and laser ablation MC-ICP-MS analysis) of the limestone host rock differ from the biostratigraphically dated Viséan limestone host rocks. The $^{87}Sr/^{86}Sr$ values of the Viséan limestone host rocks are increased in relation to the Viséan Sr seawater curve. S isotopic composition of gypsum and anhydrite layers which are intercalated within the magnesite

host rocks show a Carboniferous age and are identical with the stratigraphic age of the host rock. The Sm-Nd isochron age using different regression models (model 1, model 3 and robust) of sparry magnesite show a range of Late Carboniferous to Early Permian (see chapter 5).

- **Fluid inclusion evidence**

Fluid inclusions in the magnesite samples are relatively abundant, but generally less than 5 μm in size. Two types of fluid inclusions have been recognized at room temperature: Two phase (L-V) inclusions and three phase (L+V+S) inclusions. The liquid-rich fluid inclusions display a Raman spectrum typical of H_2O and in some of the gas-rich fluid inclusions, the gas phase consists of CO_2. CO_2-bearing fluid inclusions can result from thermal decarboxylation of organic acids and from dissolution of rock-forming carbonate during progressive metamorphism and replacement reactions (Kodera & Radvanec 2002). Commonly, fluid inclusions contain solid phases as daughter crystals along with the fluid. They are identified as dolomite based by their Raman spectrum. The mineralogy of the daughter crystals in the aqueous fluid inclusions of magnesite samples can provide an indication of the chemical composition of the ore forming fluid. The results of the chemical composition of the extracted inclusion fluid of the magnesite samples using crush-leach technique show very low Na/Br (22 to 77) and Cl/Br (60 to 119) ratios. Their compositions lie at the end of the evaporation trend on the Na/Br and Cl/Br molar ratio diagram (see chapter 6). The position of the plots at the end of the evaporation trend and the extent of fractionation indicate that the highly saline fluids were the product of evaporitic concentration predominantly of seawater. The fluid compositions of magnesite samples indicate evaporitic bittern brines to be the original fluid source. Microthermometric data indicate that fluids trapped in primary fluid inclusions in Hohentauern/Sunk magnesite are brines characterized by high and variable bulk total salinities (22.4 wt% NaCl equivalent) belonging to the H_2O-NaCl system. The observed variation in homogenization temperatures (T_h) and final ice melting temperatures (T_m) of the fluid inclusions from sparry magnesite may be interpreted as the result of local mixing of two fluids with different salinities. As a result, the study of fluid inclusions of sparry magnesite indicates a high salinity of the Mg-rich solutions which transformed the dolomite protolites.

The possible *P-T* conditions of fluid trapping at Hohentauern/Sunk magnesite deposit are estimated using the intersection point of isochores with the lithostatic thermobaric gradients. Considering that the timing for magnesite mineralization coincides with HT/LP metamorphism (peak around 270 ± 30 Ma), magmatism and extensional tectonics which are observed in other segments of the Austroalpine crystalline basement (Schuster et al. 2001). A geothermal field gradient of 45 C°/km (HT/LP metamorphism with a peak around 270 ± 30 Ma; Schuster et al. 2001) and geobarometric gradients of 27.1 Mpa are supposed to have existed at the time of fluid trapping. The isochore crosses the lithostatic gradient at the magnesite mineralization time at 245°C and 135.6 Mpa. These correspond to a depth of approximately 5 km (Fig. 10. 2). The calculated temperature is the maximum achievable temperature for the fluids. Therefore the real trapping temperature of the Hohentauern/Sunk magnesite is most probably between the measured T_h with a mode at 170°C and a temperature of 275°C for lithostatic pressure with a geothermal field gradient of 45 C°/km. The trapping temperature calculated based on this method is similar to the temperature which is calculated by the Na-K geothermometer (see chapter 7). According to the geothermometric calculations, the fluids in equilibrium with magnesite yielded a mean value of temperatures of 247°C for the Na-K geothermometer.

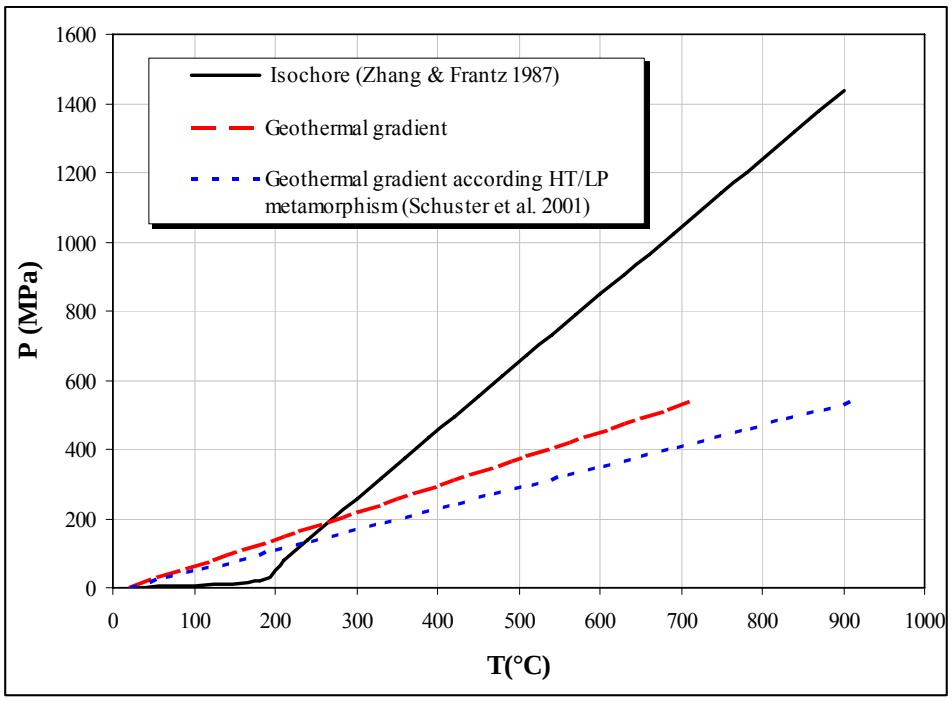

Fig. 10. 2 P-T plots showing the lithostatic thermobaric gradients (35°C/km, 27.1 Mpa/km), lithostatic thermobaric gradients of HT/LP metamporphism (45°C/km, 27.1 Mpa/km) and their intersection point with the isochore (Zhang & Frantz 1987) constructed from the inclusions formation temperature in sparry magnesite (Bakker 2003).

- **Redolomitization of magnesite**

Redolomizization of magnesite and formation of late dolomite are observed in a large number of samples. The magnesite formation in the Hohentauern/Sunk deposit is followed by several generations of late dolomite. The replacement of magnesite by dolomite is interpreted to have occurred in two different stages. Redolomitization of magnesite along cleavage planes, crystal rims and internal microfractures of magnesite crystals has occurred during formation of magnesite. The replacement process through Mg-metasomatism of dolomite (Johannes 1970) releases significant amounts of Ca^{2+} into the fluids. The released Ca^{2+} was responsible for the late dolomite. The REE pattern of late dolomite supports early redolomitization. It seems that the dolomite with the relatively high concentration of LREE crystallized from LREE-enriched solution which were rejected by the magnesite mineral phase. The magnesite also is invariably redolomitized along shear zones, faults and fractures and was partially replaced by late dolomite. In the tectonized zones the magnesite samples show increased CaO/MgO ratios. High values of the CaO/MgO ratio clearly depend on the redolomitization of magnesite and existence of different types of late dolomite. The rate of redolomitization in the fault zones as well as shear zones is higher than the rate of redolomitization of magnesite along single faults or joints. The second stage of redolomizitation occurred during Alpine orogeny and especially late-orogenic extensional and shear tectonics (Ebner & Azim Zadeh 2007). Redolomitization of magnesite requires high initial Ca^{2+}/Mg^{2+} ratio in the rededolomitizing solution. Possible sources of Ca-rich fluid for redolomitization include calcite in limestone units and the dissolution of Ca-rich salts such as gypsum and anhydrite which have been observed in drill-cores from NW of the mining area.

11. Conclusions

In the Veitsch nappe of the Graywacke zone sparry magnesite is always hosted by Carboniferous carbonatic shallow marine sediments. The magnesite is forming irregular bodies which are often discordant to the regional strike and lithological boundaries. Generally the magnesite is surrounded by dolomite. Formation of sparry magnesite is still the subject of intensive discussions. During the past the published genetic models included a wide range of syn- and epigenetic (diagenetic, metasomatic, metamorphogenic) concepts (e. g. Leitmeier & Siegl 1954, Niedermayr et al. 1989, Morteani et al. 1982, Prohaska 2000a, b). In summary all geological, mineralogical, geochemical and fluid inclusion characteristics of the Hohentauern/Sunk deposit are consistent with a concept of metasomatic magnesite formation by replacement of an early diagenetic dolomite precursor. This model includes and explains the following constraints which are documented in the previous chapters:

- Position of the Veitsch nappe within the Alpine nappe structure.
- The sedimentary, paleogeographic and geodynamic evolution of the sedimentary sequence of the Veitsch nappe.
- Lithology and sedimentary facies of the host rocks.
- Tectonic structure of the deposit and the exclusively Alpine (Cretaceous) deformation/metamorphism of the host rocks and the magnesite.
- Succession, petrography, geochemistry and texture of all observed carbonate mineral phases and the occurrence of dolomite microinclusions in the sparry magnesite.
- Geochemistry (major, trace and RE elements; Sr, Sm/Nd, O, C isotopes) of host rock and magensite.
- Biostratigraphic and radiometric (Sm/Nd) age constraints.
- Fluid inclusions and fluid geochemistry.
- *P-T* conditions for magnesite/dolomite formation.
- Pre- and postmagnesite dolomite formation.
- Position of evaporite domains.
- Origin of the mineralizing fluid.
- Scenarios for fluid migration.

The sedimentary schelf facies of the Steilbachgraben Fm. is dominarted by shallow marine fossiliferous limestones laterally interfgingering with clastic sediments and hypersalinar lagoons. The evaporites form thick layers of gypsum and anhydrite explored by underground drillings in the NW part of the deposit. Basis volcanics are also known outside the Hohentauern area (Petrascheck 1978, Felser 1977, Ratschacher 1987, Prochaska & Ebner 1997).

Dolomitization of the primary Steilbachgraben limestone as the first phase of magnesite formation seems to be a regional feature (Fig. 11. 1a). This dolomitization has occurred during early diagenetic stages, but the process of converting Steilbachgraben fossiliferous limestone to dolomite is not known in detail. It seems that early dolomite has interbasinally creeped to deeper positions (Fig. 11. 1b). Generally soft deformation depositional fabrics including debris flows, turbidites, slumping and creeped beds are common in the shallow-marine shelf and ramp environments (Sherman et al. 2001). Creep scars at the bottom of the magnesite show an initial creeping in the shallow-water facies and imply gravitationally unstable and slightly differentiated morphological conditions.

The sparry magnesite in the Hohentauern/Sunk deposit occurs in three stratiform magnesite bodies associated with fossiliferous fine grained early diagenetic dolomite. Magnesite clearly postdates the early diagenetic dolomitization of the calcareous host rock. All field observations fit best to magnesite metasomatism of the dolomite precursor before the Alpine (Cretaceous) deformation. Low Fe microinclusions of early digenetic dolomite in magnesite and zebra bandings are the characteristic features for metasomatic replacement. Additionally major, trace, RE-elements geochemistry and O/C isotope signatures confirm metasomatism. The age of magnesite formation is indicated by Sm-Nd geochronology within Late Carboniferous to Early Permian. However, the age of mineralization is still the subject of intensive discussion and recent investigations by Prochaska & Henjes-Kunst. The fluid compositions of the magnesite indicate high-salinity Mg-rich solutions to be the original fluid source. Submicrocopic evaporite minerals (sylvite) within the magnesite are further indications for high salinar solutions. The solutions are characterized by evaporitic bittern brines which could be related to evaporate environments in the following positions:

(1) Permotriassic evaporites far distributed in the basement of the Calcareous Alps and only proposed hypothetically for the Veitsch nappe (Prochaska 2000 a, b). Due to the

Alpine tectonic architecture and pre-Alpine paleogeographic arrangement (Neubauer et al. 1994) the evaporites at the basement of the Calcareous Alps can be eliminated as the source.

(2) Carboniferous evaporites within the Steilbachgraben Fm.

Scenario (1) related to Permotriassic evaporites requires extensional tectonics during Permoscthian rifting to open channelways for fluid infiltration from the surface to the depth (Prochaska 2000a, b; Fig. 11. 1c). However such structures which may have played a key role for fluid circulation to reach permeable carbonate horizons are not observed in the study area and no indications of dolomite formation and magnesite mineralization in the carbonatic Triebenstein Fm. above the Steilbachgrabe Fm. is reported.

Scenario (2) requires increased burial to reach temperature to shift the mineral stability from dolomite to magnesit and leaching Fe from the country rocks during the indicated mineralilzation age (Late Carboniferous - Early Permian). The continuation of sedimentation and deposition of Triebenstein Fm., Sunk Fm. and Graschnitz Fm. may have provided depth to reach enough temperature. This and HT/LP metamorphism with a peak around 270 ± 30 Ma observed in other segments of the Eastern Alps (Schuster et al. 2001) are the probably driving mechanisms that increased the geothermal gradient to produce enough energy. This scenario (Fig. 11. 1d) proposes formation waters with the bittern brines signature after deposition of the Steilbachgraben Fm. which could have migrate into permeable carbonates. High permeability zones between different lithological units as well as the creeping surface could have let percolate mineralizing fluids into permeable carbonates, although this idea has not been tested. However, the flow of metasomatizing fluids along stylolites and bedding planes in the dolomite sequence is proposed (Lugli et al. 2000). Clastic sediments with intercalation of basic and tuffogeneous rocks are the probable source of the Fe and Mn. High-salinity Mg-rich solutions during downward flow can be leached Fe. The element transfer from the Fe-enriched fluid results in the formation of Fe-rich dolomite (dolomite at the contact of magnesite) and Fe-rich magnesites. The replacement process releases into the fluid a considerable amount of Ca^{2+} which was partly used for late dolomite during redolomitization of magnesite. The late stage of redolomizitation occurred during Alpine orogeny and especially late-orogenic extensional and shear tectonics.

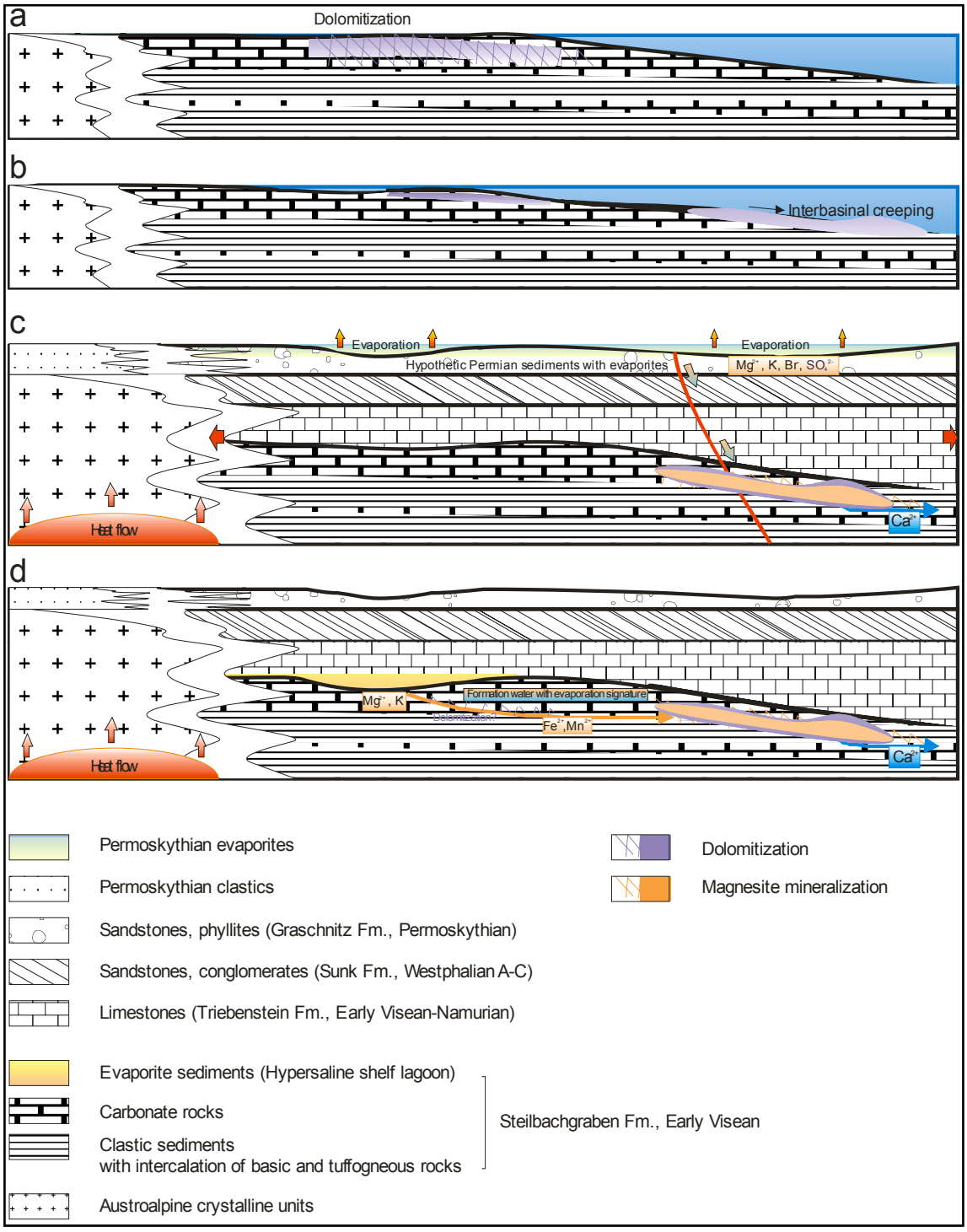

Fig. 11. 1 Schematic representation of magnesite formation with a metasomatic origin by replacement of a early dolomite precursor through influx of high-salinity Mg-rich solutions.

The Hohentauern/Sunk sparry magnesite deposit has many similarities to other Alpine-type strata-bound sparry magnesite deposits in the Paleozoic basement of the Eastern Alps, the western Carpathians, the Pyrenees as well as the Mississipi Vally-type Zn-Pb and Fe deposits in the Basque-Cantabrian basin, which have been interpreted as hydrothermal metasomatic deposits formed by dolomite replacement (Morteani et al. 1983, Pohl & Siegl

1986, Velasco et al. 1987-1994, Prochaska 2000a,b, Lugli et al. 2000-2002, Fernandez-Nieto et al. 2003, Kilias et al. 2006). Some aspects still need to be clarified, such as the dolomitization model of early dolomite, the channelling mechanism of the mineralizing fluids, the exact timing of replacement and the heat flow driven mechanism as well as additional heat to shift the mineral stability from dolomite to magnesite.

References:

Abonyi A. & Abonyiova M. (1981) Magnezitove loziska slovenska (Deposits of crystalline magnesite in Slovakia). Miner. Slovaca, 1: 125 (English summary).

Aharon P. (1988) A stable isotope study of magnesites from the Rum Jungle uranium field, Australia: Implications for the origin of strata-bound massive magnesite. Chem. Geol. 69:127-145.

Angel F. & Trojer F. (1953) Der Ablauf der Spatmagnesit-Metasomatose. - Radex-Rdsch., 7/8: 315-334.

Angel F. & Trojer F. (1955) Zur Frage des Alters und der Genesis alpiner Spatmagnesite. Radex Rundschau, 374-392.

Angel F. (1939) Unser Erzberg. Mitt. Naturwiss. Ver. Steiermark, 75.

Angelier J. & Goguel J. (1979) Sur une méthode simple de détermination des axes principaux des contraintes pour une population de failles. - C. R. Acad. Sci. Paris, 288: 307-310.

Arnorsson S., Gunnlaugsson E. & Svavarsson H. (1983) The chemistry of geothermal waters in Iceland. II. Mineral equilibria and independent variables controlling water compositions. Geochim. Cosmochim. Acta, 47: 547-566.

Azim Zadeh A. M., Ebner F. & W. Prochaska (2004) The Sunk/Hohentauern magnesite deposit (Austrian/Eastern Alps): Geological situation and genetic aspects, 32. international geological congress, Florence-Italy.

Azim Zadeh A. M., Ebner F., Prochaska W. & Jiang, S. Y. (2005) Tektonische Struktur und Geochemie der Magnesitlagerstätte Hohentauern. – Mitt. Österr. Geol. Ges., 151: 23, Wien.

Azim Zadeh A. M., Ebner F. & Jiang S.-Y (2007) Stable Isotope ($\delta^{18}O$ and $\delta^{13}C$) pattern of the Hohentauern/Sunk sparry magnesite deposit (Austria/Eastern Alps). The 8th Austrian Stable Isotope User Group Meeting, Isotopes in Ecology and Earth Sciences (Stable Isotope Network Austria), Vienna/Austria.

Azim Zadeh A. M., Ebner F., Jiang S.-Y & Klötzli U. (2008) Mineralisationsphasen in der Spatmagnesitlagerstätte Sunk/Hohentauern-Stmk./Ostalpen. Journal of Alpine Geology, 49: P. 5, Pangeo 2008, Wien/Österreich.

Bakker R. J. (2003) Package FLUIDS 1. New computer programs for the analysis of fluid inclusion data and for modelling bulk fluid properties. Chemical Geology, 194: 3-23.

Bakker R. J. & Brown P. (2003) Computer modelling in fluid inclusion research. In: Samson I., Anderson A. & Marshall D. (Eds.) Fluid inclusions: Analysis and Interpretation. Mineralogical Association of Canada, Short Course 32.

Bakker R. J. & Diamond L. W. (2006) Estimation of volume fractions of liquid and vapour phases in fluid inclusions and definition of inclusion shapes.-American Mineralogist, 91: 635-657.

Banks D. A. & Yardley B. W. D. (1992) Crush-leach analysis of fluid inclusions in small natural and synthetic samples. Geochim. Cosmochim. Acta. 56: 245-248.

Bau M. & Möller P. (1992) Rare earth elements fractionation in metamorphic hydrothermal calcxite, magnesite and siderite. Mineral. Petrol. 45: 231-246.

Bickle M. J. & Powell R. (1977) Calcite-dolomite geothermometry for iron-bearing carbonates. Contrib. Mineral. Petrol. 59: 281–292.

Bodnar R. J. (1993) Revised equation and table for determining the freezing point depression of H_2O-NaCl solutions, Geochim. Cosmochim. Acta 57: 683–684.

Botrell S. H., Yardley B. W. D. & Buckley F. (1988) A modified crush-leach method for the analysis of fluid inclusion electrolytes. Bulletin Minéralogie, 111: 279-290.

Briegleb D. (1971) Geologie der Magnesitlagerstätte am Sattlerkogel in der Veitsch (Stmk.). – BHM, 116/10: 359-375.

Brooks C., Hart S. R. & Wendt T. (1972) Realistic use of two-error regression treatments as applied to rubidium-strontium data. Rev. Geophys. Space Phys., 10: 551-577.

Canterford J. H. (1985) Magnesia-An important industrial mineral: A review of processing options and uses. Miner. Process. Extract. Metall. Rev., 2: 57-104.

Clar E. (1954) Über die Herkunft der Ostalpinen Vererzung. - Geol. Rundschau, 42: 107-127.

Clark I. & Fritz P. (1997) Environmental isotopes in Hydrogeology. Lewis Publishers. New York.

Clauer N. (1976) $^{87}Sr/^{86}Sr$ composition of eveporitic carbonates and sulphates from Miocene sediment cores in the Mediterranean Sea (D.S.D.P., Leg 13), Sedimentology, 23: 133-140.

Clauer N. & Tardy Y. (1971) Distinction, par la composition isotopique du strontium contenu dans les carbonates, entre le milieu continental des vieux socles cristallins et le nilieu marin. C.R.hebd. séance. Acad. Sci. Paris, 273: 2191-2194.

Cong-Xi C., Shao-Yong J., Ke-Qin C. & Bing M. (2003) Geology and geochemistry of Magnesite and Talc Deposits in the Early Proterozoic Mg-rich Carbonate Formations, Eastern Liaoning Province, China. International conference of mineralization in precamberian terranes & Unesco/IUGS IGCP 443 Annual meeting and field correlation, 47-53, Nanjing-China.

Dallmeyer R. D., Handler R., Neubauer F. & Fritz H. (1998) Sequence of trusting within a thick-skinned tectonic wedge: Evidence from $^{40}Ar/^{39}Ar$ ages from the Austroalpine nappe complex of the Eastern Alps.-J. Geol., 106: 71-86.

De Llarena J.G. (1953) Über die sedimentäre Entstehung des ostalpinen Magnesits "Typus Veitsch". – Montan-Zeitung, 69: 55–62, Wien.

Dickin A. P. (2005) Radiogenic Isotope Geology. Cambridge University Press.

Dünkel I. (2002) The genesis of east Elba iron ore deposits and their interrelation with Messinian tectonics. Diss. Institut für Geowissenschaften, Universität Tübingen.

Ebner F. (1992) Correlation of marine Carboniferous sedimentary units of Slovakia, Hungary and Austria.- Spec. Vol. IGCP Project No. 276: 37-47, Dionyz Stur Inst., Bratislava.

Ebner F. (1997) Die geologischen Einheiten Österreichs und ihre Rohstoffe.- In: L. Weber (Ed.): Metallogenetische Karte von Österreich (1: 500.000) und Handbuch der Lagerstätten

der Erze, Industrieminerale und Energierohstoffe Österreichs.- Arch. Lagerst. forsch. Geol. B.-A., 19:49-229, Wien.

Ebner F. & Azim Zadeh A. M. (2007) Beeinflussung der Magnesitlagerstätte Sunk/Hohentauern durch die Pölsstörung, Im Rahmen des Schwerpunktprojektes, „Lagerstätten und Mineralisationsprozesse in spätorogenen Scherzonensystemen von Kollisionsorogenen“. Kommission für Grundlagen der Mineralrohstoffforschung der Österreichischen Akademie der Wissenschaften.

Ebner F. & Prochaska W. (2001) Die Magnesitlagerstätte Sunk/Hohentauern und ihr geologischer Rahmen.- Joannea, Geol. Paläont., 3: 63–103.

Ebner F. & Wilson I. (2006) Magnesit-globales Potenzial und geologische Lagerstättencharakteristik, Berg- und hüttenmännische Monatshefte: BHM 151/4: 164-174.

Ebner F., Cerny I., Eichhorn R., Götzinger M., Paar W. H., Prochaska W. & Weber L. (2000) Mineral Resources in the Eastern Alps and Adjoining Areas.-Mitt. Österr. Geol. Gesell., 92: 157-184.

Ebner F., Mali H. & Prochaska W. (2003a) Excursion to iron, magnesite and talk deposits in SE-Austria.

Ebner F., Prochaska W. & Azim Zadeh A. M. (2003b) The type region of „Veitsch type“ sparry magnesite (Austrian/Eastern Alps), International conference of mineralization in precamberian terranes & Unesco/IUGS IGCP 443 Annual meeting and field correlation, 11-18, Nanjing-China.

Ebner F., Prochaska W., Troby J. & Azim Zadeh A. M. (2004a) Carbonate hosted sparry magnesite of the Greywacke zone, Austria/Eastern Alps. -Acta Petrol. Sinica., 20/4: 791-802, Peking.

Ebner F., H. Mali, W. Prochaska & Azim Zadeh A. M. (2004b) Guide of Excursion to Magnesite, Siderite and Talk Deposits in Austria, Final Fieldmeeting 2004 IGCP 443, University of Leoben, Austria.

Ebner F., Vozarova A. & Kovacs S. (2007) Die variszische Orogenese im Circum-Pannonischen Raum – reflektiert an Devon-Karbon-Sedimenten.- Jb. Geol. B.-A., 147: 315–329.

Ebner F., Azim Zadeh A. M. & Jiang S.-Y (2008a) Isotope characteristics of Veitsch type sparry magnesite. MRB-01 General contributions to industrial mineral deposits, The 33rd International Geologiical Congress, Oslo/Norwegen.

Ebner F., Vozarova A., Kovacs S., Kräutner H.-G., Krstic B., Szederkenyi T., Jamicic D., Balen D., Belak M. & Trajanova, M. (2008b) Devonaian-Carboniferous pre-flysch and flysch environments in the Circum Pannonian Region.- Geologica Crapathica, 59:159-195.

Elderfeld H. (1986) Strontium isotope stratigraphy. Palaeogeog. Palaeoclimatol. Palaeoecol., 57: 71–90.

Ellis A. J. (1970) Quantitative interpretations of chemical characteristics of hydrothermal systems. Geothermics Special Issue 2: 516–528.

Ellis A. J. (1979) Chemical geothermometry in geothermal systems. Geothermics, 25: 219-226.

Ellies A. J. & Wilson S. H. (1960) The geochemistry of alkali metal ions in the Wairakei hydrothermal system. N. Z. J. Geol. Geophys., 3: 593-617.

Faure G. & Barrett P. J. (1973) Strontium isotope compositions of non-marine carbonate rocks from the Beacon Supergroup of the Transantarctic Mountains. J. Sediment. Petrol. 43: 447-457.

Faure G. & Mensing T. M. (2005) Isotopes: Principles and Applications. Third Edition, John Wiley & Sons, Inc.

Faure G. & Powell J. L. (1972) Strontium Isotope Geology. Monograph Series of Theoretical and Experimental Studies, Spriger-Verlag.

Felser K.O. (1977) Die stratigraphische Stellung der Magnesitvorkommen in der östlichen Grauwackenzone (Steiermark, Österreich). Berg- u. Hüttenmänn. Mh., 122: 17–23, Wien.

Fernandez-Nieto C., Torres-Ruiz J., Subias Perez I., Fanlo Gonzalez I. & Gonzalez Lopez J. M. (2003) Genesis of Mg-Fe Carbonates from the Sierra Menera Magnesite-Siderite Deposits, Northeast Spain: Evidence from Fluid Inclusions, Trace Elements, Rare Earth Elements, and Stable Isotope Data. Economic Geology, 98: 1413-1426.

Fleuty M. J. (1964) Tectonic slides. Geol. Mag. 101: 452-456.

Flügel H. W. (1977) Paläogeographie und Tektonik des alpinen Variszikums.- N. Jb. Geol. Paläont. Mh., 659–674, Stuttgart.

Fouillac C. (1983) Chemical geothermometry in CO_2-rich thermal waters. Example of the French Massif Central. Geothermics, 12: 149–160.

Foulliac C. & Michard G. (1981) Sodium/lithium ratio in water applied to geothermometry of geothermal reservoirs. Geothermics 10: 55-70.

Fournier R. O. (1977) Chemical Geothermometers and mixing models for geothermal systems. Geothermics, 5: 41-50.

Fournier R. O. & Truesdell A. H. (1973) An empirical Na-K-Ca geothermometer for natural waters. Geochim. Cosmochim. Acta, 37: 1255-1275.

Frank W. (1987) Evolution of Austroalpine Elements in the Cretaceous.- In: Flügel H.W. & Faupl P. (Eds.): Geodynamics of the Eastern Alps, 379–407, Vienna (Deuticke).

Friedrich O. M. (1969) Beiträge über das Gefüge von Spatlagerstätten, IV Teil. - Radex-Rdsch., 3: 550-562.

Frimmel H. (1988) Strontium isotopic evidence for the origin of siderite, ankerite and magnesite mineralizations in the Eastern Alps. Mineral. Deposita, 23: 268-275.

Frisch W. & Neubauer F. (1989) Pre-Alpine terrane and tectonic zoning in the rastern Alps. –Geol. Soc. Amer. Spec. Pap., 230:91-100.

Frisch W., Dunkl I. & Kuhlemann J. (2000) Post-collisional orogen-parallel large-scale extension in the Eastern Alps. Tectonophysics 327/3-4: 239-265.

Giggenbach W. F. (1988) Geothermal solute equilibria. Derivation of Na-K-Mg-Ca geoindicators. Geochem. Cosmochim. Acta, 52: 2749-2765.

Gleeson S.A. (2003) Bulk analyses of electrolytes in fluid inclusions. In: Samson I., Anderson A. & Marshall D. (Eds.) Fluid inclusions: Analysis and Interpretation. Mineralogical Association of Canada, Short Course 32: 233–247.

Goldstein R. H. (2003) Petrographic analysis of fluid inclusions. In: Samson I., Anderson A. & Marshall D. (Eds.) Fluid inclusions: Analysis and Interpretation. Mineralogical Association of Canada, Short Course 32: 9-53.

Guilbert J. M. & Park C. F. Jr. (1986) The geology of ore deposits. New York, Freeman, 985 p.

Guillong M. (2004) Laser Ablation Inductively Coupled Plasma Mass Spectrometry: Laser ablation system developments and investigations on elemental fractionation. Diss. ETH Zürich, pp. 190.

Guillou J. J. (1970) Les magnesites cambriennes de Pacios (province de Lugo, Espagne), Leur environnement paleogeographique. Bull. BRGM, 2eme Ser., IV/3: 5-20.

Haditsch J. G. (1968) Beiträge über das Gefüge von Spatlagerstätten (Bemerkungen zur Genese des Kokardendolomites der Magnesitlagerstätte Sunk bei Trieben). - Radex-Rundschau, 1968/3:188–193, Radenthein.

Haditsch J. G. & Mostler H. (1979) Genese und Altersstellung der Magnesitlagerstätten in den Ostalpen.- Verh. Geol. B.-A., 1979:357-367, Wien.

Hajizadeh F. (2000) Genetische Untersuchungen an hydrothermalen und sedimentären Karbonatgesteinen der Ostalpen. Diss. Montanuiniversitätt Leoben, 202 S.

Harben P. W. (2002) The Industrial Minerals Handybook. A Guide to Markets, Specifications & Prices. Industrial Mineral Information, London, pp. 412.

Hoefs J. (2004) Stable Isotope Geochemistry. Fifth revised and updated edition, Springer-Verlag, pp. 244.

Hoeppener R. (1955) Tektonik im Schiefergebirge. – Geol. Rdsch., 44: 26-58, Stuttgart.

Hoinkes G., Koller F., Rantitisch G., Dachs E., Höck V., Neubauer F. & Schuster R. (1999) Alpine metamorphism in the Eastern Alps. – Schweiz. Mineral. Petrogr. Mitt., 79/1: 155-181.

Hope G. A., Woods R., & Mand C. G. (2001) Raman microprobe mineral identification. - Minerals Engineering, 14/12:1565-1577.

Howarth R. J. & McArthur J. M. (1997) Statistic for Strontium Isotope Stratigraphy: A Robust LOWESS Fit to the Marine Sr-Isotope Curve for 0 to 206 Ma, with Look-up Table for Derivation of Numeric Age. The Journal of Geology, 105: 441-456.

Hudson J. D (1977) Stable isotopes and limestone lithification. J. Geol. Soc. Lond. 133:637-660.

Ilic M. (1968) Problems of the Genesis and Genetic Classification of Magnesite Deposits. - Geologica Carpathica, 19/1: 149-160, Bratislava.

Jiang S.-Y., Slack J. F. & Palmer M. R. (2000) Sm-Nd dating of the giant Sullivan Pb-Zn-Ag deposite, British Columbia. Geology, 28/8: 751-754.

Johannes W. (1966) Experimentelle Magnesitbildung aus Dolomit+$MgCI_2$. Contr. Mineral. and. Petrol. 13: 51-58.

Johannes W. (1970) Zur Entstehung von Magnesitvorkommen. - N. Jb. Min., Abh. 113: 274-325.

Kaiser C. (2005) Evidence of inclusion fluid chemistry for the formation of magnesite and siderite deposits in the Southern Urals. Dipl. Arb. Montanuiniversitätt Leoben, 118 S.

Kaiser C., Prochaska W. & Krupenin M. (2003) Chemistry of paleofl uids forming the magnesite and siderite deposits in the Soutern Urals. In: Eliopoulos et al. (Eds.) Mineral Exploration and Sustainable Development, 2: 887-890, Millpress, Rotterdam.

Kharaka Y. K. & Mariner R. H. (1989) Chemical Geothermometers and Their Application to Formation Waters from Sedimentary Basins. In: Naeser, N. D., McCulloh, T. H.. Thermal history of Sedimentary Basins. Springer, New York, 101-117.

Kharaka Y. K., Lico M. S. & Law L. M. (1982) Chemical geothermometers applied to formation waters, Gulf of Mexico and California basins. Am. Assoc. Petrol. Geol. Bull, 66: 588.

Kharaka Y. K., Specht B. J. & Carothers W. W. (1985) Low-tointermediate subsurface temperatures calculated by chemical geothermometers. The American Association of Petroleum Geologists. Annual Convention, Book of Abstracts, New Orleans, 24–27.

Kiesl W., Koeberl C., & Körner W. (1990) Geochemistry of magnesites and dolomites at the Oberdorf/Laming (Austria) deposit and implications for their origin. Geologische Rundschau 79/2: 327-335.

Kilias S. P., Pozo M. & Bustillo M. (2006) Origin of the Rubian carbonate-hosted magnesite deposit, Galicia, NW Spain: mineralogical, REE, fluid inclusion and isotope evidence. Miner Deposita, 41: 713-733.

Klement C. (1895) Über die Bildung des Dolomites. Tscherm. Min. Petr. Mitt., 14:. 526-544.

Koch M. (1893) Mittheilung über einen Fundpunkt von Untercarbon-Fauna in der Grau-wackenzone der Nordalpen. – Z. Dtsch. Geol. Ges. 45:294 - 298.

Kodera P. & Radvanec M. (2002) Comparative mineralogical and fluid inclusion study of the Hnúšt'a-Mútnik talc-magnesite and Miková-Jedl'ovec magnesite deposit (Western Carpathians, Slovakia), Boletim Paranaense de Geociências, 50: 131-150, Editora UFPR.

Koga A. (1970) Geochemistry of waters discharged from drillholes in Otake and Hatchobaru areas (Japan). Geothermics, Special Issue 2: 1422-1425.

Krainer K. (1992) Fazies, Sedimentationsprozesse und Paläogeographie im Karbon der Ost – und Südalpen.- Jb. Geol. B.-A., 135:99-193, Wien.

Kralik C. & Kiesl W. (1992) Geochemische Untersuchungen an Kugeldolomiten der Magnesitlagerstätte Sunk-Hohentauern (Steiermark/Österreich). - Mitt. Ges. Geol. Bergbaustud. Österr., 38:31-39, Wien.

Kralik M. (1989) Strontium isotope in magnesite. In: Möller P. (Eds.) Monograph Series on Mineral deposites, 28: 225-231.

Kralik M., Aharon P., Schroll E. & Zachmann D. (1989) Carbon and oxygen isotope systematics of magnesites: a review. In: Möller P. (Eds.) Monograph Series on Mineral Deposits 28: 197-223.

Krisch K. (2001) Die Geschichte vom Bruch im Sunk. - Joannea, Geol. Paläont., 3: 5–43.

Krupenin M. T. (2002) Comparison of Lower and Middle Riphean sparry magnesite deposits of the Southern Urals province. IGCP 443 Newsletter No.2 -2002, a Special Issue of the Boletim Paranaense de Geociencias, 50. EditoraUFPR. Curitiba, Brasil: 43-50.

Lein R. (1987) Evolution of the Northern Calcareous Alps during Triassic times.-In: Flügel H. W. & Faupl P. (Eds.): Geodynamics of the Eastern Alps, 85-102, Deuticke, Wien.

Leitmeier H. (1917a) Die Genese des kristallinen Magnesites. –Centralbl. Mineral. Geol. Paläontol., 446-454.

Leitmeier H. (1917b) Einige Bemerkungen über die Entstehung von Magnesit- und Sideritlagerstätten. – Mitt. Geol. Ges. Wien, 9: 159-166.

Leitmeier H. & Siegl W. (1954) Untersuchungen an Magnesiten am Nordrande der Grauwackenzone Salzburgs und ihre Bedeutung für die Entstehung der Spatmagnesite der Ostalpen. – BHM 99: 201-208 and 221-235.

Leitner A. (2003) Der Magnesitbergbau Hohentauern. Diss. Institut für Volkskunde, Univ. Graz.

Lesko I. (1960) Geologische und lagerstättenkundliche Untersuchungen im Raume Oberdorf a. d. Laming. Mitt. Ges. Geol. Bergb. Stud. 11: 3-65.

Lugli S., Torres-Ruiz J., Garuti G. & Olmedo F. (2000) Petrography and Geochemistry of the Eugui Magnesite Deposit (Western Pyrenees, Spain): Evidence for the Development of a Peculiar Zebra Banding by Dolomite Replacement Economic Geology, 95/8: 1775-1791.

MacNamara J. & Thode H G. (1950) Comparison of the Isotopic Constitution of Terrestrial and Meteoritic Sulfur. Phys. Rev., 78: 307–308.

Martiny E. & Rojkovic I. (1977) Trace elements in magnesites of Slovakia (Central west Carphatians). – Geol. Zbor. Geol. Carpath., 28: 311-322.

Maxwell J. (1968) Rock and mineral analysis. Interscience publishers (Chemical analysis, 27).

McArthur J. M. (1994) Recent trends in strontium isotope stratigraphy. Terra Nova, 6: 331–358.

McArthur J. M. & Howarth R. J. (1998) Strontium Isotope Stratigraphy: LOWESS Version 2: A revised best-fit to the Marine Sr-Isotope Curve for 0 to 206 Ma, with a revised look-up table for derivation of numeric age. Am. Assoc. of Petrol. Geologists Annual Meeting (Salt Lack City, Utah, May 17-20, 1988), Tulsa, Okla., AAPG.

McArthur J. M., Howarth R. J. & Bailey T. R. (2001) Strontium Isotope Stratigraphy: LOWESS Version 3: Best Fit to the Marine Sr-Isotope Curve for 0 to 509 Ma and Accompanying Look-up Table for Derivation of Numeric Age. The Journal of Geology, 109: 155-170.

McCafferey M. A., Lazar B. & Holland H. D. (1987) The Evaporation Path of Seawater and the Coprecipitation of Br^- and K^+ with Halite. Journal of Sedimentary Research, 57.

McLaughlin R. (1977) Atomic absorption spectroscopy 2. In Zussman J. (Hg.), Physical methods in determinative mineralogy. Academic Press, 371–389, London.

Melezhik V. A., Fallick A. E., Medvedev P. V. & Makarikhin V. V. (2001) Palaeoproterozoic magnesite: lithological and isotopic evidence for playa/sabkha environments. Sedimentology 48:379-397.

Meyer H. J. & McGee H. W. (1985) Oil and gas fields accompanied by geothermal anomalies in Rocky Mountain region. Amerian Association of Petroleum Geologists Bulletin 69: 933-945.

Michard G. (1990) Behaviour of major elements and some trace elements (Li, Rb, Cs, Sr, Fe, Mn, W, F) in deep hot waters from granitic areas. Chem. Geol. 89: 117–134.

Miller K. G., Feigenson M. D., Kent D. V. & Olson R. K. (1988) Upper Eocene to Oligocene isotope ($^{87}Sr/^{86}Sr$, $\delta^{18}O$, $\delta^{13}C$) standard section, Deep Sea Drilling Project site 522. Paleoceanography, 3: 223–233.

Millot R. & Négrel P. (2007) Multi-isotopic tracing (δ^7Li, δ^{11}B, ^{87}Sr/^{86}Sr) and chemical geothermometry: evidence from hydro-geothermal systems in France, Chemical Geology 244: 664–678.

Möller P. (1989) Magnesite-Geology, Mineralogy, Geochemistry, Formation of Mg-Carbonates. - Monograph Series on Mineral Deposits, 300 S., Borntraeger, Berlin–Stuttgart.

Möller P. (1989) Minor and trace elements in magnesite. In: Möller P. (Eds.) Monograph Series on Mineral Deposits 28: 173-195.

Morteani G. (1989) Mg-metasomatic type sparry magnesites of Entachen Alm, Hochfilzen/Bürglkopf and Spiessnägle (Austria). In: Möller P. (Eds.) Monograph Series on Mineral Deposits 28: 105-113.

Morteani G., Möller P. & Schley F. (1982) The Rare Earth Element Contents and the Origin of the Sparry Magnesite Mineralizations of Tux-Lanersbach, Entachen Alm, Spiessnägel and Hochfilzen, Austria and the Lacustrine Magnesite Deposits of Diani-Kozani, Greece and Bela Stena, Yugoslavia.-Econ. Geol. 77: 617-631.

Morteani G., Schley F. & Möller P. (1983) On the formation of magnesite. In: Schneider H. J. (Eds.) Mineral deposit of the Alps and of the Alpine Epoch in Europe. Springer, Berlin, Heidelberg, New York, 106-116.

Mostler H. (1973) Alter und Genese ostalpiner Spatmagnesite unter besonderer Berücksichtigung der Magnesitlagerstätten im Westabschnitt der Nördlichen Grauwackenzone (Tirol, Salzburg). - Ver- . öff. Univ. Innsbruck, 86: 237-266.

Neubauer F. R. (1983) Bericht 1982 über geologische Aufnahmen im Renfeld- und Gleinalmkristallin und in der Grauwackenzone auf Blatt 134 Passail.- Jb. Geol. B.-A., 126: 315-316, Wien.

Neubauer F. & Frisch W. (1993) The Austro-Alpine Metamorphic Basement E of the Tauern Window. - In: Raumer J. F. & Neubauer F. (Eds.): Pre-Mesozoic Geology in the Alps, 515-536, Springer, Berlin.

Neubauer F. & Handler R. (2000) Variscan orogeny in the eastern Alps and Bohemian Massif: How do these units correlate. - Mitt. Österr. Geol. Ges., 92:3 5-59, Wien.

Neubauer F. & Höck V. (2000) Aspects of Geology in Austria and Adjoining Areas: Introduction. - Mitt. Österr. Geol. Ges., 92: 7-14, Wien.

Neubauer F. & Vozarova A. (1990) The Nötsch-Veitsch North Generic Zone of the Alps and Carpathians; Correlation, paleogeography and significance for Variscan orogeny.- Festive Volume: Thirty years of geol. Cooperation between Austria and Czechoslovakia, Ústr. Ústav geologický, Praha, 167-170, Praha.

Neubauer F., Handler R., Hermann S. & Paulus G. (1994) Revised Lithostratiraphy and Structure of the Eastern Graywacke Zone (Eastern Alps). - Mitt. Österr. Geol. Ges., 86: 61-74.

Neubauer F., Genser J. & Handler R. (2000) The Eastern Alps: Result of a two-stage collision process. - Mitt. Österr. Geol. Ges., 92: 117-134.

Niedermayer G., Beran A. & Brandstätter F. (1989) Diagenetic type magnesites in the Permo-Scythian rocks of the Eastern Alps, Austria. In: Möller P. (Eds.) Monograph Series on Mineral Deposits 28: 35-60.

Nievoll J. (1983) Stratigraphische und strukturgeologische Untersuchungen in der Grauwackenzone bei Veitsch (Steiermark). - Unveröff. Diss. Univ. Graz, 150 S., Graz.

Parekh P. P., Möller P., Dulski P. & Bausch W. M. (1977) Distribution of trace elements between carbonate and non-carbonate phases of limestone. – Earth Planet. Sci. Lett., 34: 39-50.

Petrascheck W. E. (1932) Die Magnesite und Siderite der Alpen.- Sitz.-Ber. Akad. Wiss., math.-naturwiss. Kl. Abt. 1, 141: 195-242, Wien.

Petrascheck W. E. (1978) Zur Altersbestimmung einiger ostalpiner Erzlagerstätten. – Mitt. Österr. Geol. Ges., 68: 79–87, Wien.

Pohl W. (1989) Comparative Geology of Magnesite Deposits and Occurrences. Monograph Series on Mineral Deposits 28: 1-13, Gebrüder Borntraeger, Berlin-Stuttgart.

Pohl W. (1990) Genesis of magnesite deposits - models and trends. - Geol. Rdsch., 79: 291–299.

Pohl W. & Siegl W. (1986) Sediment-hosted magnesite deposits. -In: Wolf K. H. (Eds.): Handbook of strata-bound and stratiform ore deposits. 14: 223–310, Elsevier V., Amsterdam.

Powell R. J., Condliffe D. M. & Condliffe E. (1984) Calcite-dolomite geothermometry in the system $CaCO_3$-$MgCO_3$-$FeCO_3$: An experimental study. J.metamorphic Geol., 2: 33-41.

Price N. J. & Cosgrove J. W. (2005) Analysis of Geological Structures. Cambridge University Press.

Prochaska W. (2000a) Siderite and magnesite mineralizations formed during initial rifting of the Alpine cycle. - In: F. Ebner et al. (2000): Mineral Resources in the Eastern Alps and Adjoining Areas. - Mitt. Österr. Geol. Ges., 92: 157–184.

Prochaska W. (2000b) Magnesite and talc deposits in Austria. - Mineralia Slovaca, 32: 543–548.

Prochaska W. & Ebner F. (1989) Geochemische Untersuchungen an Metavulkaniten der Veitscher-Decke/Grauwackenzone.- Sitz. Ber., 197: 191-205, Wien.

Prochaska W. & Henjes-Kunst F. (2007) The origin of sparry magnesite in the Eastern Alps (Austria): evidence from inclusion fluid and Sr-Nd istotope chemistry. – In: Proceedings of the 9th Biennial Meeting of the Society for Geology Applied to Mineral Deposits, Dublin, Ireland, 20th–23rd Aug. 2007 (Eds. C. J. Andrew et al.), II: 823–826, IAEG 2007.

Prol-Ledesma R. M., Canet C., Torres-Vera M. A., Forrest, M. J. & Armienta M. A. (2004) Vent fluid chemistry in Baia Concepcion coastal submarine hydrothermal system, Baja California Sur, Mexico. J. Volcanol. Geoth. Res., 137: 311-328.

Radvanec M. & Prochaska W. (2001) Successive replacement of Upper Carboniferous calcite to dolomite and magnesite in Dúbrava magnesite deposit (Western Carpathians, Slovakia), Mineralia Slovaca, 33: 517-525.

Ramsay J. G. & Huber M. I. (1987) The techniques of modern structural geology. Volume 2: Folds and fractures. Academic Press, London.

Ranawat P. S. (2009) http://www.psranawat.org/non_mettalic/magnesite.htm

Rantitsch G., Grogger W., Teichert Ch., Ebner F., Hofer Ch., Maurer E.-M., Schaffer B. & Toth M. (2004) Conversion of carbonaceous material to graphite within the Greywacke Zone of the Eastern Alps. Int. J. Earth Sci., 93: 959–973.

Ratschbacher L. & Klima K. (1985) Übersicht über Gesteinsbestand und Metamorphose in einem Querprofil vom Altkristalin zur kalkalpenbasis (Obersteirmark-Österreich).-Jb. Geol. B.-A.,128: 151-173, Wien.

Ratschbacher L. (1984) Beitrag zur Neugliederung der Veitscher Decke (Grauwackenzone) in ihrem Westabschnitt (Obersteiermark, Österreich). - Jb. Geol. B.-A., 127: 423-453.

Ratschbacher L. (1986) Kinematics of Austro-Alpine cover nappes: changing translation path due to transpression. – Tectonophysics, 125: 335-356.

Ratschbacher L. (1987a) Stratigraphy, tectonics and paleogeography of the Veitsch nappe /Graywacke zone, Eastern Alps, Austria): A rearrangement. -Mineralia Slovaca, Monogr., 407-414, Bratislava.

Ratschbacher L. (1987b) Strain, rotation and translation of Austroalpine nappes.- In. Flügel, H.W. & Faupl, P. (Eds.): Geodynamics of the Eastern Alps, 236-243, Deuticke, Wien.

Ratschbacher L., Frisch W. & Linzer H. -G. (1991) Lateral extrusion in the eastern Alps, part II: structural analysis. - Tectonics, 10: 257-271.

Ratschbacher L. & Nievoll, J. (1984) Die Aussagekraft von Schwermineraldaten aus der Veitscher Decke (Steiermark, Österreich). - Jb. Geol. B.-A., 127: 455–469, Wien.

Redlich K. A. (1907) Die Genesis der Pinolitmagnesite, Siderite und Ankerite der Ostalpen. - Tscherm. Min. Petr. Mitt., 26: 499-505.

Redlich K. A. (1909) Die Typen der Magnesitlagerstätten. - Z. prakt. Geologie, 17: 300-310. Berlin.

Redlich K. A. (1911) Entstehung und Vorkommen des Magnesit. – In: Doelter C. (Eds.) Handbuch der Mineralchemie, 243-253, Enke Verlag Dresden.

Redlich K. A. (1913) Der Karbinzug der Veitsch (Steiermark). – Z. prakt. Geol. 21.

Reinecker J. (2000) Stress and Deformation: Miocene to present-day tectonics in the eastern Alps. Tübinger Geowissenschaftliche Arbeiten, A (55): 128.

Reinecker J. & Lenhardt W. A. (1999) Present-day stress field and deformation in eastern Austria. International Journal of Earth Sciences, 88/3: 532-550.

Reischenbacher D. (2009) Beckenentwicklung und Bildung von Kohleflözen und organischreichen Sedimenten am Beispiel des neogenen Lavanttaller Beckens. Diss. Montanuiniversitätt Leoben, 233 S.

Reiter F. & Acs P. (2000) TectonicsFP. Computer Software for Structural Geology. Innsbruck. Austria.

Reßler A. (2007) Investigation of fluid inclusions in marbles. Dipl.-Arb. Montanuiniversitätt Leoben, 100 S.

RHI (2009) www.RHI.at

Roedder E. (1958) Technique for the extraction and partial chemical analysis of fluid filled inclusions from minerals. Economic Geology, 53: 235-69.

Roedder E. (1984) Fluid inclusions, Min. Soc. Am. Rev. in Min. 12: 644.

Roedder E., Ingram B. & Hall W. E. (1963) Studies of fluid inclusions, III. Extraction and quantitative analysis of inclusions in the milligram range. Economic Geology, 58: 353–374.

Rollinson H. (1996) Using Geochemical Data: Evaluation, Presentation, Interpretation, Longman.

Rosza M. (1925) Mechanismus und physikalisch-chemische Bedingungen der Differenzierung sedimentärer Carbonatgesteine. Zentralbl. Miner. Geol. Paläontol., Jg., 357-361.

Rüger L. (1939) Die Bodenschätze Großdeutschlands. Beck'sche Verlagsbuchhandlung, München, 360.

Rumpf J. (1873) Über krystallisierte Magnesite aus den nordöstlichen Alpen. - Min. Petr. Mitt., 1873: 263–272.

Samson I., Anderson A. & Marshall D. (2003) Fluid Inclusions- Analysis and Interpretation, Volume 32.- Mineralogical Association of Canada, Canada, 374.

Scharbert S. & Schönlaub H. P. (1980) Das Paläozoikum und Variszikum.- In. Oberhauser, R. (Eds.) Der geologische Aufbau Österreichs.- 4-20, Springer, Wien–New York.

Schmid S., Fugenschuh B., Kissling E. & Schuster R. (2004) Tectonic map and overall architecture of the Alpine orogen, Eclogae Geologicae Helvetiae, 97: 93–117.

Schönlaub H. P. (1979) Das Paläozoikum in Österreich. – Abh. Geol. B.-A. 33: 124, Wien.

Schönlaub H. P. (1982) Die Grauwackenzone in den Eisenerzer Alpen (Österreich). Jb. Geol. B. –A. 124: 361-423.

Schönlaub H. P. & Heinisch H. (1993) The Classic Fossiliferous Units of the Eastern and Southern Alps. –In: Raumer J. F. & Neubauer F. (Eds.): Pre-Mesozoic Geology in the Alps, 395-422, Springer, Berlin.

Schroll E. (2002) Genesis of magnesite deposits in the view of isotope geochemistry, Boletim Paranaense de Geociências, 50: 59-68, Editora UFPR.

Schroll E., Siegl W. & Papesch W. (1986) Kohlenstoff- und Sauerstoffisotopenverteilung in einigen Magnesiten. – Anz. Österr. Akad. Wiss., math. Naturew. Kl. 1-4.

Schroll E., Siegl W. & Pak E. (1989) Sulphur isotopes of minerals of Austrian magnesite occurrences. In: Möller P. (Eds.) Monograph Series on Mineral Deposits, 28: 233-236.

Schuster R., Scharbert S., Abart R., & Frank W. (2001) Permo-Triassic extension and related HT/LP metamorphism in the Austroalpine- Southalpine realm: Mitteilungen der Geologie und Bergbau Studenten Österreichs, 44: 111–141.

Schweigl J. & Neubauer F. (1997) Structural development of the central Northern Calcareous Alps: Significance for the Jurassic to Tertiary geodynamics in the Alps. – Ecl. Geol. Helv., 60/2: 303-323.

Shannon R. D. (1976) Revised effective Ionic Radii and Systematic Studies of Interatomie Distances in Halides and Chaleogenides. -Acta cryst., Ser. A, 32: 751-767.

Sherman A. G., Narbonne G. M. & James N. P. (2001) Anatomy of a cyclically packaged Mesoproterozoic carbonate ramp in northern Canada. Sedimentary Geology 139:171-203.

Sholkovitz E. R. (1990) Rare-earth elements in marine sediments and geochemical standards. Chemical Geology 88: 333–347.

Sholkovitz E. R., Piepgras D. J. & Jacobsen, S. B. (1989) The pore water chemistry of rare earth elements in Buzzards Bay sediments. Geochim. Cosmochim. Acta 53: 2847–2856.

Siegl W. & Felser K. O. (1973) Der Kokardendolomit und seine Stellung im Magnesit von Hohentauern (Sunk bei Trieben). – BMH 118: 251-256.

Strauss H. (1997) The isotopic composition of sedimentary sulfur through time. Palaeogeography, Palaeoclimatology, Palaeoecology, 132: 97-118.

Strauss H. (1999) Geological evolution from isotope proxy signals—sulfur. Chemical Geology, 161: 89–101.

Tenchov Y. (1980) Die paläozoische Megaflora von Österreich. Eine Übersicht. - Verh. Geol. B.-A., 1980: 161-174, Wien.

Tollmann A. (1977) Die Geologie von Österreich, Bd. 1, Die Zentralalpen, 1-765, Deuticke, Wien.

Troby J. (2001) Die Magnesitlagerstätte Oberdorf a. d. Laming (Steirmark, Österreich). Dipl.-Arb. Montanuniversitätt Leoben, 209 S.

Truesdell A. H. (1976) Summary of Section III. Geochemical techniques in exploration. Proceedings 2nd UN Symposium on the development and use of geothermal resources, San Francisco 1975, 1, Liii-lxxix.

Tucker M. E. (1985) Shallow-marine carbonate facies and facies models. Geological Society, London, Special Publications, 18: 147-169.

Tucker M. E. & Wright V. P. (1990) Carbonate Sedimentology, pp. 482, Blackwells, Oxford.

Turner F. J. (1953) Nature and dynamic interpretation of deformation lamellae in calcite of three marbles. - Am. J. Sci., 251: 276-298; New Haven, CT.

Vacek M. (1886) Über die geologischen Verhältnisse des Flußgebietes der unteren Mürz. Verh. Geol. Reichsanst., 455-464.

Valley J. W. (1986) stable isotope geochemistry of metamorphic rocks. Rev Miner 16: 445-486.

Van den Kerkhof A. M. & Hein U. F. (2001) Fluid inclusion petrography. Lithos 55: 27–47.

Veizer J. (1983) Trace elements and isotopes in sedimentary carbonates. In: R. J. Reeder, Editor, Carbonates: Mineralogy and Chemistry, Mineralogical Society of America, Washington D. C., 265–299.

Veizer J. (1989) Strontium isotopes in seawater through time. Ann. Rev. Earth Planet. Sci., 17: 141–167.

Veizer J. (2003) isotopic evolution of seawater on geological time scales: sedimentological perspective. In: Lentz D. R. (Eds.) Geochemistry of Sediments and Sedimentary Rocks: Evolutionary considerations to Mineral Deposit-forming Environment: Geological Association of Canada, GeoText 4: 53-68.

Veizer J. & Hofes J. (1976) The nature of O^{18}/O^{16} and C^{13}/C^{12} secular trends in sedimentary carbonate rocks. Geochim Cosmochim Acta, 40: 1387-1395.

Veizer J., Ala D., Azmy K., Bruckschen P., Buhl D., Bruhn F., Carden G. A. F., Diener A., Ebneth S., Godderis Y., Jasper T., Korte G., Pawellek F., Podlaha O. G. & Strauss H. (1999) Sr-87/Sr-86, delta C-13 and delta O-18 evolution of Phanerozoic seawater. Chemical Geology, 161/1-3: 59-88.

Velasco F., Pesquera A., Arce R. & Olmedo F. (1987) A contribution to the ore genesis of the magnesite deposit of Eugui, Navarra (Spain), Mineral. Deposita 22: 33-41.

Walter S. H. G. (2001) 3D-Modellierung der Magnesitlagerstätte Hohentauern.– Diplomarbeit, FU Berlin, Inst. Geologie, Geophysik und Geoinformatik, 57 S., Berlin.

Weber L. Eds. (1997) Metallogenetische Karte von Österreich (1: 500.000) und Handbuch der Lagerstätten der Erze, Industrieminerale und Energierohstoffe Österreichs. - Arch. Lagerst. forsch. Geol. B.-A., 19: 1-607.

Weber L. & Schroll E. (1997) Magnesit-(Talk-)Bezirk Vietscher Decke, 339-341. In: Weber L. (Eds.): Metallogenetische Karte von Österreich (1: 500.000) und Handbuch der Lagerstätten der Erze, Industrieminerale und Energierohstoffe Österreichs.- Arch. Lagerst. forsch. Geol. B.-A., 19: 49-229, Wien.

Weiss V. & Horn G. (1989) A RADEX innovation-Biomag. A magnesite product for biological application. Radex Rundsch., Yearbook, 167-171.

Welz B. & Sperling M. (1997) Atomabsorptions-spektrometrie, Wiley-VCH.

White D. E. (1965) Saline waters of sedimentary rocks. In: Fluids in subsurface environments – A symposium. Americ. Assoc. Petrol. Geol. Mem., 4: 342-366.

White D. E. (1970) Geochemistry applied to the discovery, evaluation and exploitation of geothermal energy resources. Geothermics, Special Issue 2/1: 58-80.

Wiesheu R. & Hein U. (1996) The history of fluid inclusion studies. In: Fritscher B. & Henderson F. (1996) Toward A History Of Mineralogy, Petrology, And Geochemistry Proceedings of the International Symposium on the History of Mineralogy, Petrology and Geochemistry, Munich.

Wilson I. & Ebner F. (2005) A review of the world's current and potential magnesite resources. Industrial Minerals MagMin, Vienna-Austria.

Woodhead J., Swearer S., Hergt J. & Maas R. (2005) In situ Sr-isotope analysis of carbonates by LA-MC-ICP-MS: interference corrections, high spatial resolution and an example from otolith studies. Journal of Analytical Atomic Spectrometry 20: 22-27.

Zhang Y. G. & Frantz J. D. (1987) Determination of homogenization temperatures and densities of supercritical fluids in the system NaCl-KCl-$CaCl_2$-H_2O using synthetic fluid inclusions. Chemical Geology, 64: 335－350.

Appendix A. (Tables):

- Tab. A. 1 Major element oxides of whole-rock samples by XRF.
- Tab. A. 2 Major elements of whole-rock samples by AAS.
- Tab. A. 3 Major elements of separated mineral samples by AAS.
- Tab. A. 4 Trace elements of separated mineral samples (state key laboratory of mineral deposit research, University of Nanjing, China).
- Tab. A. 5 Rare earth elements of separated mineral samples (state key laboratory of mineral deposit research, University of Nanjing, China).
- Tab. A. 6 Stable and radiogenic isotopes of separated mineral samples (state key laboratory of mineral deposit research, University of Nanjing, China).
- Tab. A. 7 Chemical compositions of the extracted fluid inclusions by IC (crush and leach technique).
- Tab. A. 8 Major element oxides of selected points by EPMA.
- Tab. A. 9 Sedimentary bedding planes.
- Tab. A. 10 Joint planes.
- Tab. A. 11 Fault planes.

Sample No.	SiO_2%	CaO%	Fe_2O_3%	Al_2O_3%	Cr_2O_3%	MnO%	MgO%	K_2O%	Na_2O%	TiO_2%	SO_3%	P_2O_5%	V_2O_5%	NiO%	ZrO_2%	BaO%	HfO_2%	LOI%	Total%
Limestone																			
PM15-16-3	2.23	53.08	0.34	0.79	0.00	0.05	1.08	-	-	-	-	-	-	-	-	-	-	42.64	100.21
PM15-16-4	1.48	53.76	0.24	0.51	0.00	0.04	1.24	-	-	-	-	-	-	-	-	-	-	43.01	100.29
PM15-16-5	1.55	53.49	0.26	0.65	0.00	0.03	1.13	-	-	-	-	-	-	-	-	-	-	42.86	99.97
PM15-16-6	2.45	52.86	0.29	0.81	0.00	0.04	1.22	-	-	-	-	-	-	-	-	-	-	42.43	100.09
PM15-16-7	2.56	53.22	0.25	0.57	0.00	0.03	1.09	-	-	-	-	-	-	-	-	-	-	42.64	100.37
PO14a	4.46	52.48	0.25	0.67	0.01	0.04	0.91	-	-	-	-	-	-	-	-	-	-	41.60	100.42
PO14c	4.43	52.20	0.36	0.88	0.00	0.05	0.84	-	-	-	-	-	-	-	-	-	-	41.47	100.22
PP-POc	1.73	52.56	0.27	0.57	0.00	0.05	2.21	-	-	-	-	-	-	-	-	-	-	43.16	100.55
Dolomite																			
PL4-1	4.65	28.92	1.86	1.42	0.00	0.13	18.62	-	-	-	-	-	-	-	-	-	-	43.61	99.21
PL4-2	3.91	31.72	0.62	0.59	0.00	0.06	18.03	-	-	-	-	-	-	-	-	-	-	44.91	99.83
PL4-3	3.98	31.89	0.61	0.63	0.00	0.06	18.23	-	-	-	-	-	-	-	-	-	-	44.52	99.91
PL4-4	2.85	31.54	0.66	0.85	0.00	0.08	18.56	-	-	-	-	-	-	-	-	-	-	45.40	99.93
PL4-5	5.28	30.16	0.97	1.21	0.00	0.10	18.11	-	-	-	-	-	-	-	-	-	-	43.94	99.76
PL4-6	2.03	30.58	1.69	0.56	0.00	0.15	19.39	-	-	-	-	-	-	-	-	-	-	45.74	100.14
PL4-7	3.60	29.88	1.89	1.00	0.00	0.16	18.77	-	-	-	-	-	-	-	-	-	-	44.56	99.87
PL4-8	2.42	29.27	1.19	0.80	0.00	0.13	20.96	-	-	-	-	-	-	-	-	-	-	45.36	100.13
PM15-16-2	0.99	30.02	1.26	0.53	0.00	0.13	20.53	-	-	-	-	-	-	-	-	-	-	46.58	100.04
PM15-16-8	3.16	32.50	0.63	0.84	0.00	0.08	17.95	-	-	-	-	-	-	-	-	-	-	44.97	100.12
PM15-16-9	1.27	30.20	1.22	0.64	0.00	0.12	20.74	-	-	-	-	-	-	-	-	-	-	45.97	100.15
PN-U1	2.86	32.71	0.61	0.52	0.00	0.10	17.85	-	-	-	-	-	-	-	-	-	-	45.44	100.10
PN-U2	2.83	31.08	2.41	0.85	0.00	0.51	17.54	-	-	-	-	-	-	-	-	-	-	44.66	99.88
PN-U4	0.85	32.09	1.70	0.51	0.00	0.20	20.50	-	-	-	-	-	-	-	-	-	-	44.36	100.21
PN-U5	1.59	30.20	1.76	0.90	0.00	0.18	19.30	-	-	-	-	-	-	-	-	-	-	45.74	99.66
PN-U6a	1.27	30.24	2.17	0.90	0.00	0.29	18.91	-	-	-	-	-	-	-	-	-	-	45.57	99.36
PN-U6b	3.43	30.30	3.31	0.94	0.00	0.65	17.24	-	-	-	-	-	-	-	-	-	-	43.49	99.37
PN-U7	3.38	30.00	3.27	0.88	0.00	0.62	17.25	-	-	-	-	-	-	-	-	-	-	43.89	99.29
PN-U8	2.23	29.57	0.91	1.39	0.00	0.10	19.64	-	-	-	-	-	-	-	-	-	-	45.41	99.25
PO14b	1.84	30.47	2.74	0.73	0.00	0.22	18.65	-	-	-	-	-	-	-	-	-	-	45.45	100.09
PP-POb	1.64	33.01	1.38	0.65	0.00	0.10	17.85	-	-	-	-	-	-	-	-	-	-	45.22	99.84

Tab. A. 1 Major element oxides of whole-rock samples by XRF.

Sample No.	SiO_2%	CaO%	Fe_2O_3%	Al_2O_3%	Cr_2O_3%	MnO%	MgO%	K_2O%	Na_2O%	TiO_2%	SO_3%	P_2O_5%	V_2O_5%	NiO%	ZrO_2%	BaO%	HfO_2%	LOI%	Total%
PQ(D)	0.01	30.86	1.31	0.02	0.01	0.13	19.93	0.0052	0.0418	0.0052	0.0052	0.0052	0.0052	0.0052	0.0052	0.0052	0.0052	47.70	100.05
PQ(K)	0.06	30.53	1.61	0.03	0.01	0.10	20.51	0.0053	0.0265	0.0053	0.1643	0.0053	0.0053	0.0053	0.0053	0.0053	0.0053	47.00	100.09
XPH2	1.10	30.12	1.23	0.43	0.01	0.10	20.29	0.0854	0.0374	0.0160	0.0053	0.0053	0.0053	0.0053	0.0053	0.0053	0.0053	46.60	100.05
XPH3	0.74	30.37	1.72	0.22	0.01	0.15	19.68	0.0053	0.0265	0.0106	0.0053	0.0053	0.0053	0.0053	0.0053	0.0053	0.0053	47.10	100.06
XPH4	6.68	30.74	0.59	0.39	0.01	0.07	17.50	0.0617	0.0281	0.0112	0.0056	0.0056	0.0056	0.0056	0.0056	0.0056	0.0056	43.90	100.01
XPH4a	2.47	32.47	0.49	0.41	0.01	0.06	18.25	0.0706	0.0326	0.0109	0.0054	0.0054	0.0054	0.0054	0.0054	0.0109	0.0054	45.70	100.01
XPH5	1.49	29.64	1.54	0.51	0.01	0.12	20.35	0.0107	0.0269	0.0107	0.0054	0.0054	0.0054	0.0054	0.0054	0.0107	0.0054	46.30	100.04
Magnesite																			
M1(PI)	0.02	5.26	2.61	0.03	0.01	0.14	41.13	0.0049	0.0246	0.0049	0.0049	0.0049	0.0049	0.0049	0.0049	0.0098	0.0049	50.80	100.07
M2(PI)	0.27	0.28	2.44	0.14	0.01	0.12	44.64	0.0048	0.0240	0.0048	0.0048	0.0048	0.0048	0.0048	0.0048	0.0048	0.0048	52.10	100.06
M4(PI)f	1.90	7.38	2.00	0.74	0.01	0.10	38.74	0.0051	0.0255	0.0153	0.0051	0.0051	0.0051	0.0051	0.0051	0.0051	0.0051	49.10	100.04
M4(PI)g	0.08	0.67	2.59	0.02	0.01	0.14	44.59	0.0048	0.0241	0.0048	0.0048	0.0096	0.0048	0.0048	0.0048	0.0048	0.0048	51.90	100.06
PE16	1.96	4.23	1.48	0.11	0.01	0.11	42.18	0.0050	0.0301	0.0050	0.0050	0.0050	0.0050	0.0050	0.0050	0.0100	0.0050	49.90	100.06
PF24	0.08	0.62	1.89	0.02	0.01	0.11	45.26	0.0048	0.0240	0.0048	0.0048	0.0192	0.0048	0.0048	0.0048	0.0048	0.0048	52.00	100.07
XPH1	1.71	2.95	1.71	0.16	0.01	0.11	43.13	0.0050	0.0349	0.0050	0.0050	0.0050	0.0050	0.0050	0.0050	0.0050	0.0050	50.20	100.05
XPH6	5.53	1.89	1.74	0.73	0.01	0.10	43.09	0.0160	0.0319	0.0213	0.0053	0.0053	0.0053	0.0106	0.0053	0.0053	0.0053	46.80	100.01
Magnesite (partly redolomitized)																			
PL4-9	4.13	9.81	1.53	1.24	0.00	0.11	36.99	-	-	-	-	-	-	-	-	-	-	46.29	100.10
PM15-16-10	5.43	26.57	1.31	0.53	0.00	0.10	22.76	-	-	-	-	-	-	-	-	-	-	43.53	100.23
PM15-16-1a	2.60	6.81	1.60	0.61	0.00	0.12	39.84	-	-	-	-	-	-	-	-	-	-	48.65	100.23
PM15-16-1b	4.61	24.66	1.29	0.91	0.00	0.11	24.46	-	-	-	-	-	-	-	-	-	-	44.14	100.18
PN-U3	3.19	20.90	1.44	0.67	0.00	0.15	27.75	-	-	-	-	-	-	-	-	-	-	46.12	100.03
PP-POa	3.91	19.78	1.46	0.43	0.00	0.11	28.70	-	-	-	-	-	-	-	-	-	-	45.76	100.15
PQ(M)	0.12	10.65	1.79	0.02	0.01	0.11	37.20	0.0050	0.0250	0.0050	0.1000	0.0050	0.0050	0.0050	0.0050	0.0050	0.0050	50.00	100.05

Tab. A. 1 Major element oxides of whole-rock samples by XRF.

Sample No.	Ca%	Mg%	Fe%	Mn%	Sr%	CaO%	MgO%	CaO/MgC	FeO%	Fe_2O_3%	MnO%	SrO%
PB	4.85	22.59	1.04	0.07	0.02	6.79	37.46	0.18	1.34	1.48	0.092	0.020
PC1	15.11	18.75	1.16	0.11	0.05	21.15	31.10	0.68	1.49	1.65	0.146	0.059
PC5	9.06	21.11	1.10	0.08	0.04	12.68	35.00	0.36	1.42	1.58	0.107	0.052
PD1	1.84	25.98	0.96	0.08	0.00	2.58	43.07	0.06	1.24	1.37	0.103	0.003
PD8	0.68	22.50	0.82	0.07	0.00	0.95	37.31	0.03	1.06	1.18	0.086	0.001
PE10	6.12	20.96	0.89	0.08	0.01	8.57	34.75	0.25	1.15	1.28	0.099	0.016
PE14-f	0.62	20.97	0.70	0.05	0.00	0.87	34.77	0.03	0.91	1.01	0.062	0.001
PE14-g	1.71	23.64	0.78	0.06	0.00	2.40	39.19	0.06	1.00	1.11	0.077	0.003
PE16-f	0.59	24.76	0.98	0.07	0.00	0.83	41.06	0.02	1.27	1.40	0.095	0.001
PE16-g	1.17	21.56	0.72	0.06	0.00	1.64	35.74	0.05	0.92	1.03	0.076	0.001
PE21	0.77	21.44	0.66	0.05	0.00	1.08	35.54	0.03	0.86	0.95	0.060	0.001
PE24-g	0.92	24.28	0.89	0.07	0.00	1.28	40.26	0.03	1.14	1.27	0.084	0.001
PE24-m-Polierte	1.09	24.80	0.89	0.07	0.00	1.52	41.11	0.04	1.15	1.27	0.085	0.001
PE28	0.89	20.22	0.74	0.06	0.00	1.24	33.53	0.04	0.95	1.06	0.078	0.000
PE3	0.73	23.60	0.86	0.07	0.00	1.02	39.14	0.03	1.11	1.23	0.087	0.001
PE33-Dunkel	23.65	14.05	0.60	0.05	0.04	33.11	23.30	1.42	0.77	0.85	0.062	0.043
PE33-f	19.21	16.34	0.76	0.05	0.03	26.90	27.10	0.99	0.98	1.09	0.065	0.038
PE33-g	1.93	24.95	1.23	0.09	0.00	2.71	41.37	0.07	1.59	1.76	0.113	0.002
PE4	25.88	13.73	1.13	0.10	0.06	36.24	22.76	1.59	1.45	1.61	0.126	0.068
PE7	21.10	15.03	0.99	0.07	0.08	29.54	24.92	1.19	1.28	1.42	0.095	0.090

Tab. A. 2 Major elements of whole-rock samples by AAS.

Sample No.	Ca%	Mg%	Fe%	Mn%	Pb%	Zn%	Sr%	K%	Na%	CaO%	MgO%	CaO/MgO	FeO%	Fe_2O_3%	MnO%	PbO%	ZnO%	SrO%	K_2O%	Na_2O%
												Limestone								
PM15-16-7	38.65	0.83	0.17	0.02	0.0000	0.0023	0.0888	0.0453	0.0127	54.11	1.38	39.22	0.22	0.24	0.023	0.000	0.003	0.105	0.055	0.017
												Magnesite								
M1(PI)	0.34	26.71	1.75	0.12	0.0021	0.0014	0.0021	0.0043	0.0197	0.48	44.29	0.01	2.26	2.50	0.149	0.002	0.002	0.002	0.005	0.027
M2(PI)	0.02	20.77	1.63	0.11	0.0025	0.0014	0.0005	0.0034	0.0185	0.03	34.43	0.00	2.11	2.33	0.138	0.003	0.002	0.001	0.004	0.025
M3(PI)	0.31	24.98	1.21	0.09	0.0000	0.0015	0.0002	0.0015	0.0104	0.43	41.41	0.01	1.56	1.72	0.120	0.000	0.002	0.000	0.002	0.014
M4(PI)	0.14	26.95	1.53	0.11	0.0000	0.0017	0.0005	0.0014	0.0107	0.20	44.68	0.00	1.98	2.19	0.137	0.000	0.002	0.001	0.002	0.014
PE16	1.73	25.35	0.90	0.08	0.0000	0.0020	0.0066	0.0032	0.0195	2.42	42.04	0.06	1.16	1.29	0.097	0.000	0.002	0.008	0.004	0.026
PF24	0.40	27.06	1.17	0.08	0.0000	0.0019	0.0000	0.0014	0.0136	0.56	44.87	0.01	1.51	1.67	0.109	0.000	0.002	0.000	0.002	0.018
PM15-16-1a	1.31	25.13	1.11	0.08	0.0000	0.0018	0.0051	0.0029	0.0151	1.84	41.67	0.04	1.43	1.58	0.097	0.000	0.002	0.006	0.003	0.020
XPH6(Mg)	0.73	26.92	1.06	0.09	0.0000	0.0013	0.0020	0.0020	0.0163	1.02	44.64	0.02	1.37	1.52	0.119	0.000	0.002	0.002	0.002	0.022
												Magnesite (redol.)								
PN-U3	2.51	19.41	1.08	0.08	0.0000	0.0023	0.0121	0.0013	0.0109	3.51	32.19	0.11	1.39	1.54	0.104	0.000	0.003	0.014	0.002	0.015
PQ1	14.32	16.89	1.03	0.09	0.0000	0.0021	0.1485	0.0013	0.0095	20.05	28.00	0.72	1.32	1.47	0.121	0.000	0.003	0.175	0.002	0.013
Orb. dol. (Mag)	6.38	21.75	1.16	0.08	0.0000	0.0107	0.0400	0.0012	0.0093	8.93	36.06	0.25	1.49	1.65	0.105	0.000	0.013	0.047	0.001	0.013
												Dolomite								
Dol. in joints	23.50	10.99	0.83	0.16	0.0000	0.0052	0.0543	0.0014	0.0167	32.90	18.21	1.81	1.07	1.18	0.203	0.000	0.006	0.064	0.002	0.022
Orbicular dol.	20.97	12.35	0.48	0.05	0.0000	0.0034	0.0702	0.0023	0.0194	29.36	20.47	1.43	0.62	0.69	0.066	0.000	0.004	0.083	0.003	0.026
Rosszähne	20.41	12.70	0.48	0.05	0.0000	0.0015	0.1129	0.0013	0.0088	28.57	21.06	1.36	0.62	0.69	0.064	0.000	0.002	0.133	0.002	0.012
												Non-carbonate								
Qtz.(PF-north)	0.00	0.10	0.01	0.00	0.0000	0.0019	0.0000	0.0039	0.0082	0.00	0.16	0.00	0.02	0.02	0.000	0.000	0.002	0.000	0.005	0.011
Gipsum	24.58	0.14	0.04	0.00	0.0000	0.0019	0.1210	0.0070	0.0079	34.41	0.23	148.05	0.05	0.05	0.001	0.000	0.002	0.143	0.008	0.011
Anhydrite	33.16	0.20	0.04	0.00	0.0000	0.0024	0.1607	0.0100	0.0120	46.42	0.33	139.79	0.05	0.05	0.002	0.000	0.003	0.190	0.012	0.016
Talc (PE21)	0.00	18.55	0.36	0.00	0.0000	0.0112	0.0000	0.0007	0.0176	0.00	30.76	0.00	0.47	0.52	0.002	0.000	0.014	0.000	0.001	0.024

Tab. A. 3 Major elements of separated mineral samples by AAS.

Sample No.	Li (ppm)	Rb (ppm)	Sr (ppm)	Cs (ppm)	Ba (ppm)	Zr (ppm)	Nb (ppm)	Hf (ppm)	Ta (ppm)	Pb (ppm)	Th (ppm)	U (ppm)
PM15-16–7	0.411	0.285	609.0	0.095	2.7	0.565	0.014	0.015	0.000	4.704	0.108	0.369
PP-PO(K)	0.531	1.900	727.0	0.085	10.9	1.478	0.006	0.050	0.000	30.846	0.676	0.499
PQ(K)	0.141	0.047	413.0	0.012	1.8	0.359	0.001	0.007	0.001	0.065	0.030	0.560
M1(PI)	1.989	0.126	24.6	0.049	2.6	0.293	0.007	0.011	0.000	2.964	0.111	0.020
M2(PI)	1.648	0.077	6.1	0.055	2.5	0.213	0.000	0.017	0.000	2.516	0.208	0.055
M4(PI)	0.874	0.019	2.0	0.045	1.6	0.026	0.003	0.002	0.000	0.308	0.005	0.003
PE16	3.379	0.025	22.8	0.076	3.2	0.026	0.002	0.009	0.001	2.340	0.068	0.107
PF24	2.711	0.011	5.1	0.066	1.8	0.074	0.003	0.006	0.000	1.000	0.108	0.005
XPH6(Mag)	1.358	0.005	24.4	0.082	2.4	0.077	0.004	0.003	0.001	0.470	0.072	0.018
XPH6(Mat)	1.995	0.037	10.4	0.050	0.4	2.875	0.004	0.073	0.001	2.668	0.233	0.175
PM15-16-1a	2.168	0.020	62.7	0.094	1.5	0.289	0.004	0.013	0.001	1.935	0.179	0.054
PN-U3	2.219	0.243	358.4	0.033	1.1	0.897	0.002	0.023	0.001	2.107	0.198	0.255
PQ1	2.437	0.055	526.2	0.037	4.0	0.051	0.004	0.006	0.001	1.137	0.007	0.175
PQ(M)	1.132	0.032	60.9	0.020	1.3	0.190	0.005	0.003	0.000	14.425	0.003	0.102
PP-PO(M)	2.429	0.019	125.5	0.132	1.8	0.113	0.003	0.008	0.000	1.266	0.059	0.064
Orbicular dolomite (Mag)	1.296	0.042	260.1	0.048	2.2	0.060	0.004	0.002	0.001	0.584	0.156	0.029
PQ(D)	1.932	0.018	45.1	0.022	1.8	0.081	0.001	0.002	0.001	3.874	0.013	0.288
PM15-16–2(D)	2.795	0.088	99.4	0.109	2.6	0.308	0.004	0.013	0.000	1.050	0.209	0.103
PM15-16–2(Mat)	6.526	0.585	88.6	0.125	3.3	4.076	0.006	0.113	0.001	0.571	0.738	0.251
Orbicular dolomite	1.552	0.006	381.3	0.079	1.3	0.061	0.004	0.002	0.000	1.186	0.040	0.101
Orbicular dolomite (Mat)	3.183	0.016	137.7	0.110	1.9	0.028	0.002	0.013	0.001	3.188	0.084	0.060
Rosszähne	0.199	0.046	572.3	0.036	0.9	0.020	0.003	0.004	0.000	0.305	0.001	0.008
Dol. in joints	0.360	0.073	221.9	0.010	5.1	0.092	0.005	0.014	0.001	1.049	0.014	0.607

Tab. A. 4 Trace elements of separated mineral samples (state key laboratory of mineral deposit research, University of Nanjing, China).

Sample No.	Sc (ppm)	Ti (ppm)	V (ppm)	Cr (ppm)	Mn (ppm)	Co (ppm)	Ni (ppm)	Zn (ppm)	Ga (ppm)	Mo (ppm)	Cd (ppm)	Sn (ppm)	W (ppm)	Bi (ppm)
PM15-16–7	0.231	17.123	1.032	0.493	184.998	0.678	7.147	4.065	0.093	0.028	0.904	0.015	0.040	0.023
PP-PO(K)	1.387	8.709	2.591	2.223	283.286	2.202	9.228	9.605	0.391	0.128	0.300	0.102	0.123	0.069
PQ(K)	0.130	0.075	2.656	3.535	236.911	0.545	6.589	4.158	0.033	0.214	0.021	0.075	0.031	0.010
M1(PI)	0.568	4.214	3.522	3.006	728.541	0.233	2.639	9.840	0.096	0.007	0.016	0.014	0.057	0.000
M2(PI)	0.998	6.414	7.423	13.553	626.349	0.237	1.996	12.325	0.115	0.003	0.018	0.003	0.029	0.004
M4(PI)	0.115	0.229	3.090	4.012	608.466	0.172	4.039	4.382	0.063	0.009	0.004	0.003	0.036	0.002
PE16	0.068	2.414	2.836	3.077	567.657	0.208	3.515	11.480	0.110	0.008	0.005	0.021	0.015	0.001
PF24	1.094	3.879	6.263	16.735	599.601	0.137	3.306	5.357	0.088	0.007	0.002	0.001	0.028	0.005
XH6(Mag)	1.068	1.170	2.150	1.601	585.026	0.250	4.959	3.290	0.116	0.001	0.007	0.009	0.001	0.003
XH6(Mat)	0.564	8.361	9.755	4.934	443.837	0.225	8.823	2.997	1.788	0.036	0.002	0.286	0.021	0.008
PM15-16-1a	1.541	0.976	2.859	1.672	529.952	0.255	4.031	2.389	0.064	0.005	0.008	0.015	0.007	0.003
PN-U3	0.445	1.421	4.463	2.808	517.184	0.435	7.475	3.364	0.269	0.095	0.196	0.115	0.143	0.009
PQ1	0.225	0.814	2.546	3.838	613.851	0.436	4.397	9.903	0.055	0.004	0.242	0.022	0.020	0.006
PQ(M)	0.096	0.176	11.039	11.875	668.173	0.457	5.535	0.645	0.091	0.033	0.003	0.067	0.011	0.008
PP-PO(M)	1.010	0.319	2.489	1.228	296.888	0.424	3.537	1.119	0.115	0.009	0.067	0.008	0.062	0.001
Orbicular dolomite (Mag)	0.773	5.547	5.571	4.896	589.128	0.217	2.131	3.765	0.099	0.001	0.081	0.043	0.016	0.002
PQ(D)	0.008	0.034	9.853	14.404	880.193	0.401	4.481	4.173	0.058	0.079	0.017	0.198	0.100	0.019
PM15-16–2(D)	0.425	0.526	1.930	2.120	714.201	0.727	5.963	6.876	0.144	0.005	0.056	0.012	0.021	0.021
PM15-16–2(Mat)	1.506	15.268	15.809	12.328	809.345	0.837	11.653	8.357	2.609	0.044	0.014	0.044	0.024	0.038
Orbicular dolomite	0.147	0.260	4.581	0.486	361.782	0.348	4.948	1.413	0.048	0.001	0.189	0.019	0.016	0.001
Orbicular dolomite (Mat)	1.324	1.144	2.734	2.530	626.625	0.362	3.478	6.610	0.105	0.007	0.009	0.012	0.041	0.000
Rosszähne	0.372	0.155	5.774	2.125	288.157	0.289	4.745	2.682	0.105	0.001	0.049	0.003	0.061	0.002
Dol. in joints	0.016	0.125	3.608	2.148	787.738	11.056	32.175	8.910	0.154	0.015	0.319	0.031	0.007	0.003

Tab. A. 4 Trace elements of separated mineral samples (state key laboratory of mineral deposit research, University of Nanjing, China).

Sample No.	La (ppm)	Ce (ppm)	Pr (ppm)	Nd (ppm)	Sm (ppm)	Eu (ppm)	Gd (ppm)	Tb (ppm)	Dy (ppm)	Ho (ppm)	Er (ppm)	Tm (ppm)	Yb (ppm)	Lu (ppm)	Y (ppm)
PM15-16-7	3.994	5.353	0.843	3.578	0.776	0.172	0.806	0.142	0.708	0.159	0.419	0.059	0.269	0.046	6.493
PP-PO(K)	5.379	7.951	1.314	5.839	1.580	0.322	1.787	0.325	1.858	0.416	1.204	0.206	1.154	0.172	15.788
PQ(K)	0.675	0.619	0.109	0.466	0.089	0.047	0.156	0.025	0.162	0.042	0.123	0.020	0.105	0.018	2.314
M1(PI)	0.379	1.424	0.403	2.988	2.279	1.098	2.870	0.380	1.325	0.213	0.487	0.070	0.329	0.043	7.419
M2(PI)	0.373	1.337	0.358	2.747	2.264	1.016	2.866	0.408	1.395	0.241	0.559	0.082	0.422	0.063	7.700
M4(PI)	0.016	0.081	0.017	0.123	0.120	0.055	0.350	0.117	0.817	0.207	0.597	0.100	0.512	0.074	6.638
PE16	2.904	7.113	1.347	7.168	3.034	0.533	3.340	0.515	1.844	0.307	0.655	0.069	0.301	0.041	10.034
PF24	0.615	1.825	0.412	2.750	1.136	0.380	1.157	0.153	0.814	0.176	0.514	0.086	0.432	0.062	6.805
XPH6(Mag)	0.937	2.837	0.557	3.161	0.850	0.295	0.814	0.126	0.624	0.135	0.376	0.056	0.290	0.043	5.321
XPH6(Mat)	0.096	0.517	0.102	0.728	0.312	0.110	0.389	0.076	0.400	0.090	0.269	0.038	0.227	0.035	3.115
PM15-16-1a	0.693	2.213	0.572	3.596	1.409	0.404	1.249	0.183	0.805	0.192	0.485	0.075	0.406	0.068	6.425
PN-U3	3.542	4.566	0.746	3.463	0.894	0.250	0.924	0.150	0.708	0.145	0.416	0.059	0.276	0.039	5.625
PQ1	1.098	2.637	0.556	3.409	1.754	0.378	2.198	0.423	2.266	0.468	1.169	0.184	0.951	0.134	13.023
PQ(M)	1.119	4.174	0.855	4.756	1.158	0.314	0.962	0.129	0.591	0.115	0.322	0.052	0.254	0.040	4.785
PP-PO(M)	2.909	7.678	1.742	9.135	2.594	0.633	2.438	0.422	2.194	0.488	1.276	0.180	0.941	0.142	17.766
Orbicular dolomite (Mag)	0.847	1.990	0.445	2.555	1.340	0.565	1.455	0.189	0.811	0.154	0.392	0.057	0.330	0.048	6.044
PQ(D)	0.931	1.194	0.162	0.726	0.122	0.072	0.107	0.022	0.118	0.036	0.111	0.014	0.088	0.015	1.435
PM15-16-2(D)	3.237	4.983	0.782	3.698	0.720	0.231	0.715	0.115	0.526	0.111	0.322	0.043	0.244	0.034	3.953
PM15-16-2(Mat)	3.957	6.706	1.246	5.534	1.302	0.234	1.088	0.171	0.769	0.159	0.453	0.073	0.338	0.051	5.903
Orbicular dolomite	2.400	3.134	0.462	2.159	0.633	0.194	0.706	0.123	0.590	0.133	0.337	0.053	0.257	0.035	5.163
Orbicular dolomite (Mat)	0.566	1.861	0.443	3.237	2.153	0.414	2.932	0.590	2.928	0.610	1.618	0.231	1.129	0.170	18.927
Rosszähne	4.638	7.690	1.357	6.851	2.824	1.068	3.059	0.424	1.671	0.307	0.753	0.101	0.438	0.059	12.087
Dol. in joints	17.099	9.239	2.374	9.957	2.066	0.569	3.808	0.740	3.569	0.705	1.533	0.157	0.541	0.059	22.534

Tab. A. 5 Rare earth elements of separated mineral samples (state key laboratory of mineral deposit research, University of Nanjing, China).

Sample No.	$\delta^{13}C$ (PDB)	error	$\delta^{18}O$ (PDB)	error	$\delta^{18}O$ SMOW	$^{87}Sr/^{86}Sr$	error	$^{147}Sm/^{144}Nd$	error	$^{143}Nd/^{144}Nd$	error
PM15-16–7	3.13	0.04	-15.88	0.04	14.54	0.708256	0.000013	-	-	-	-
PM15-16–7	3.27	0.03	-15.93	0.07	14.49	-	-	-	-	-	-
PP-PO(K)	1.59	0.14	-15.58	0.21	14.85	0.708735	0.000019	-	-	-	-
PQ(K)	1.11	0.06	-11.46	0.09	19.10	0.709338	0.000004	-	-	-	-
PQ(K)	1.10	0.08	-11.60	0.14	18.95	-	-	-	-	-	-
PQ(K)	1.09	0.08	-11.45	0.14	19.11	-	-	-	-	-	-
M1(PI)	-2.05	0.09	-19.34	0.06	10.97	0.710881	0.000003	0.4611	0.0046	0.512846	0.000009
M1(PI)	-1.95	0.10	-19.45	0.15	10.86	-	-	-	-	-	-
M1(PI)	-1.83	0.05	-19.44	0.06	10.87	-	-	-	-	-	-
M2(PI)	-2.23	0.08	-20.55	0.12	9.72	0.709668	0.000004	0.4982	0.0050	0.512920	0.000011
M4(PI)	-2.01	0.13	-18.03	0.05	12.32	0.710026	0.000011	-	-	-	-
PE16	-1.20	0.04	-20.68	0.05	9.59	0.709180	0.000003	0.2558	0.0026	0.512483	0.000012
PF24	-1.82	0.11	-20.67	0.03	9.60	0.709591	0.000009	0.2497	0.0025	0.512469	0.000007
XH6(Mag)	-0.02	0.08	-20.24	0.12	10.05	0.709662	0.000004	-	-	-	-
XH6(Mat)	-1.33	0.02	-16.63	0.15	13.77	0.709924	0.000012	-	-	-	-
PM15-16-1a	-0.61	0.03	-18.33	0.07	12.01	0.710506	0.000006	0.2369	0.0024	0.512430	0.000009
PN-U3	-0.76	0.06	-15.87	0.09	14.55	0.709872	0.000002	-	-	-	-
PQ1	-0.83	0.04	-14.24	0.05	16.23	0.709940	0.000012	-	-	-	-
PQ(M)	-0.34	0.07	-20.08	0.14	10.21	0.710003	0.000002	-	-	-	-
PP-PO(M)	-0.71	0.05	-19.91	0.10	10.38	0.709315	0.000008	0.1717	0.0017	0.512304	0.000007
PP-PO(M)	-0.69	0.04	-19.76	0.04	10.54	-	-	-	-	-	-
Orbicular dolomite (Mag)	-1.12	0.12	-15.99	0.11	14.43	0.708457	0.000004	-	-	-	-
PQ(D)	0.79	0.53	-19.43	0.58	10.88	0.709128	0.000015	-	-	-	-
PM15-16–2(D)	0.34	0.09	-19.18	0.10	11.14	0.708976	0.000005	-	-	-	-
PM15-16–2(D)	0.33	0.05	-18.98	0.04	11.34	-	-	-	-	-	-
PM15-16–2(Mat)	0.26	0.19	-14.89	0.18	15.56	0.709158	0.000002	-	-	-	-
Orbicular dolomite	-0.54	0.11	-16.57	0.18	13.83	0.708392	0.000018	-	-	-	-
Orbicular dolomite (Mat)	-0.27	0.08	-16.34	0.11	14.06	0.708374	0.000028	-	-	-	-
Rosszähne	-1.31	0.08	-16.51	0.13	13.89	0.709790	0.000009	-	-	-	-
Dol. in joints	1.74	0.13	-11.47	0.17	19.08	0.710513	0.000009	-	-	-	-

Tab. A. 6 Stable and radiogenic isotopes of separated mineral samples (state key laboratory of mineral deposit research, University of Nanjing, China).

Sample No.	Li (ppb)	Na (ppb)	K (ppb)	Mg (ppb)	Ca (ppb)	F (ppb)	Cl (ppb)	Br (ppb)	J (ppb)	NO_3 (ppb)	SO_4 (ppb)
						Limestone					
PM15-16-7	1	938	420	2528	8016	35	2478	5	8.8	-	994
						Magnesite					
M1(PI)	57	11252	1213	23495	2036	29	37809	1255	28.6	-	241
M2(PI)	76	14198	1464	20454	1422	29	42786	1399	39.9	-	128
M3(PI)	10	11492	1308	28851	1481	33	48274	1787	21.3	-	71
M4(PI)	38	10408	1244	20680	940	26	25848	657	37.7	142	174
PE16	89	10857	1486	25008	4632	175	30105	773	22.6	1876	300
PF24	50	10843	1201	21002	979	30	31403	987	25.1	224	144
PM15-16-1a	56	9241	825	22489	4286	22	24119	736	27.2	126	202
XPH6(Mag)	58	15635	1560	23704	3301	24	49009	1855	33.9	-	285
						Magnesite (partly redolomitized)					
PN-U3	64	9229	1200	23055	5161	70	23628	551	32.5	4094	365
PQ(Mag)	19	7116	977	20068	4964	59	26409	887	14.5	-	517
PQ1	9	4722	441	29106	10453	89	10580	228	34.2	-	743
Orbicular dol. (Mag)	23	4104	359	21546	6380	33	9780	185	29.3	-	353
						Late dolomite					
Rosszähne	26	6866	804	16114	10908	14	14672	66	10.3	-	174
Dol. in joints	8	9807	824	37241	-	-	23312	18	6.5	-	-
Orbicular dolomite	26	12547	832	22046	11237	18	27354	184	44.9	-	438
						Non-carbonate minerals					
Talc (PE21)	3	1308	267	7778	3518	622	2460	11	4.2	-	-
Qtz. (PF-north)	6	6564	2993	1694	1275	44	14459	108	14.7	341	179
Gipsum	2	1164	2065	3687	-	175	30105	773	22.6	1876	-

Tab. A. 7 Chemical compositions of the extracted fluid inclusions by IC (crush and leach technique).

Sample No.	Point No.	MnO%	FeO%	*Fe_2O_3	SiO_2%	K_2O%	CaO%	Na_2O%	MgO%	Al_2O_3%	SrO%	TiO_2%	ZnO%	PbO%	Total
							Magnesite								
PF24	3	0.17	2.11	2.34	0.00	0.01	0.11	0.12	48.15	0.00	0.00	-	-	-	50.67
PF24	11	0.13	1.76	1.95	-	-	0.44	-	51.73	-	0.00	-	0.11	0.00	54.17
PF24	13	0.16	1.89	2.10	-	-	0.20	-	48.67	-	0.00	-	0.00	0.00	50.92
PF24	9	0.05	1.71	1.90	-	-	1.15	-	46.91	-	0.00	-	0.07	0.00	49.89
PM15-16-a	3	0.10	1.48	1.64	-	-	0.43	-	49.10	-	0.09	-	0.04	0.00	51.24
PM15-16-a	6	0.15	1.79	1.99	0.00	0.00	0.36	0.12	49.54	0.00	0.00	-	-	-	51.96
PM15-16-a	7	0.11	1.54	1.71	0.05	0.00	0.11	0.00	48.05	0.56	0.00	-	-	-	50.42
PP-PO	3	0.15	1.87	2.08	0.04	0.01	0.09	0.00	46.65	0.00	0.00	0.00	-	-	
PP-PO	4	0.12	1.66	1.84	0.00	0.00	2.10	0.00	41.22	0.05	0.00	0.02	-	-	45.17
PE16	1	0.15	1.23	1.37	-	-	1.16	-	45.27	-	0.00	-	0.00	0.00	47.81
PE16	3	0.12	1.17	1.30	-	-	0.28	-	45.68	-	0.08	-	0.00	0.00	47.33
PE16	5	0.09	1.16	1.29	0.04	0.00	0.33	0.00	45.86	0.00	0.00	0.02	-	-	47.50
PE16	10	0.22	1.55	1.72	-	-	1.32	-	47.27	-	0.00	-	0.01	0.00	50.37
M1	3	0.21	2.51	2.79	0.00	0.00	0.17	0.00	50.28	0.08	0.00	0.00	-	-	53.25
M1	4	0.15	2.42	2.69	0.00	0.02	0.20	0.00	45.75	0.00	0.01	0.00	-	-	48.55
M1	6	0.16	2.72	3.02	-	-	0.15	-	47.19	-	0.07	-	0.00	0.00	50.29
M2	2	0.21	2.51	2.79	0.06	0.00	0.69	0.00	51.28	0.00	0.01	0.01			54.77
M2	5	0.12	2.62	2.91	-	-	0.52	-	50.96	-	0.00	-	0.00	0.00	54.22
M2	6	0.19	2.66	2.95	-	-	0.64	-	50.84	-	0.00	-	0.01	0.00	54.34
M2	8	0.16	2.62	2.91	-	-	0.26	-	47.05	-	0.00	-	0.00	0.00	50.09
M2	9	0.16	2.80	3.11	-	-	0.24	-	53.68	-	0.00	-	0.00	0.03	56.91
M2	10	0.22	2.29	2.54	-	-	0.02	-	47.19	-	0.08	-	0.00	0.04	49.84
M2	13	-	2.42	2.69	-	-	0.54	-	46.35	-	0.00	-	0.03	0.05	49.39
M2	14	0.15	2.13	2.36	-	-	0.01	-	46.77	-	0.00	-	0.00	0.08	49.14
M2	15	0.22	2.45	2.72	-	:-	0.33	-	47.38	-	0.00	-	0.00	0.04	50.42
M2	16	0.19	2.34	2.60	-	-	0.87	-	47.95	-	0.08	-	0.00	0.00	51.43
M2	17	0.07	1.03	1.14	-	-	0.06	-	40.12	-	0.00	-	0.00	0.00	41.28
M2	18	0.12	1.96	2.18	-	-	0.15	-	50.00	-	0.06	-	0.00	0.00	52.29
M2	19	0.19	1.96	2.18	-	-	0.28	-	49.35	-	0.00	-	0.01	0.04	51.83

Tab. A. 8 Major element oxides of selected points by EPMA.

Sample No.	Point No.	MnO%	FeO%	*Fe_2O_3	SiO_2%	K_2O%	CaO%	Na_2O%	MgO%	Al_2O_3%	SrO%	TiO_2%	ZnO%	PbO%	Total
Dolomite relics															
PF24	4	0.13	0.58	0.64	0.00	0.00	15.91	0.00	27.82	0.00	0.01	-	-	-	44.45
PF24	5	0.06	0.97	1.08	0.04	0.00	16.53	0.00	27.79	0.00	0.02	-	-	-	45.41
PF24	10	0.05	0.57	0.63	-	-	26.07	-	27.25	-	0.30	-	0.00	0.00	54.24
PF24	12	0.05	0.59	0.65	-	-	32.38	-	23.83	-	0.00	-	0.00	0.00	56.85
PF24	15	0.05	0.46	0.51	-	-	31.27	-	23.70	-	0.00	-	0.00	0.06	55.54
PM15-16-a	1	0.08	0.49	0.54	-	-	30.94	-	24.09	-	0.07	-	0.00	0.03	55.70
PP-PO	5	0.06	1.10	1.22	0.00	0.01	13.63	0.00	32.35	0.00	0.00	0.03	-	-	47.18
PE16	2	0.13	0.41	0.46	-	-	34.31	-	24.69	-	0.00	-	0.00	0.00	59.54
PE16	7	0.06	0.45	0.50	0.08	0.00	6.78	0.00	31.55	0.18	0.00	0.00	-	-	39.10
PE16	8	0.09	0.54	0.60	0.00	0.02	30.84	0.00	25.46	0.04	0.02	0.03	-	-	57.04
M1	5	0.06	0.45	0.50	0.00	0.01	24.19	0.00	21.13	0.10	0.00	0.02	-	-	45.96
M1	7	0.15	0.41	0.46	-	-	35.26	-	19.14	-	0.17	-	0.00	0.00	55.13
M2	3	0.15	0.67	0.74	0.00	0.01	21.52	0.00	24.37	0.00	0.00	0.00	-	-	46.72
M2	7	0.00	0.65	0.72	-	-	31.71	-	23.29	-	0.00	-	0.10	0.00	55.66
M2	11	0.13	0.62	0.69	-	-	33.68	-	20.43	-	0.00	-	0.00	0.04	54.90
M2	12	0.12	0.53	0.59	0.03	0.00	33.48	0.06	22.70	0.04	0.04	0.00	-	-	57.00
Late dolomite															
PF24	14	0.03	0.62	0.69	-	-	31.19	-	21.76		0.07	-	0.04	0.09	53.80
PM15-16-a	2	0.08	1.19	1.32	-	-	31.09	-	22.14	-	0.00	-	0.00	0.03	54.53
PM15-16-a	5	0.15	2.68	2.97	0.12	0.01	24.08	0.00	22.81	0.06	0.00	-	-	-	49.91
PM15-16-a	8	0.10	1.86	2.06	0.04	0.01	32.79	0.00	23.97	0.00	0.00	-	-	-	58.77
PP-PO	2	0.18	1.72	1.91	0.04	0.00	27.84	0.00	21.34	0.04	0.00	0.00	-	-	51.16
PP-PO	6	0.22	1.89	2.10	-	-	26.34	-	21.50	-	0.06	-	0.00	0.07	50.08
PE16	6	0.06	0.39	0.43	0.00	0.00	29.73	0.06	18.43	0.00	0.01	0.00	-	-	48.68
M1	2	0.03	0.80	0.89	0.00	0.00	35.44	0.00	26.08	0.00	0.02	0.00	-	-	62.37

Tab. A. 8 Major element oxides of selected points by EPMA.

Sample No.	Point No.	MnO%	FeO%	*Fe_2O_3	SiO_2%	K_2O%	CaO%	Na_2O%	MgO%	Al_2O_3%	SrO%	TiO_2%	ZnO%	PbO%	Total
Chlorite															
PF24	2	0.00	1.62	1.80	30.41	0.01	0.01	0.00	32.10	21.18	0.00	-	-	-	85.33
PF24	6	0.08	1.69	1.88	32.77	0.01	0.05	0.12	35.62	20.02	0.00	-	-	-	90.36
PF24	7	0.02	1.03	1.14	34.89	0.00	0.00	0.00	33.06	19.17	0.00	-	-	-	88.17
PM15-16-a	4	0.06	1.96	2.18	36.54	0.00	0.07	0.13	31.04	23.52	0.00	-	-	-	93.32
PM15-16-a	9	0.00	1.76	1.95	25.76	0.01	0.04	0.00	32.64	22.57	0.00	-	-	-	82.78
PP-PO	1	0.00	1.87	2.08	32.23	0.01	0.15	0.00	33.78	19.76	0.00	0.03	-	-	87.83
PE16	9	0.00	1.01	1.12	38.43	0.00	0.04	0.05	35.84	15.68	0.00	0.04	-	-	91.09
M1	1	0.00	1.96	2.18	33.56	0.02	0.02	0.00	40.46	24.87	0.00	0.05	-	-	100.94
M2	1	0.00	1.78	1.98	37.43	0.01	0.10	0.05	38.88	20.73	0.00	0.00	-	-	98.98
M2	4	0.03	1.74	1.93	34.22	0.00	0.04	0.00	30.39	19.38	0.00	0.01	-	-	85.81
Talc															
PF24	1	0.04	0.64	0.71	63.17	0.08	0.04	0.13	30.50	0.37	0.00	-	-	-	94.97
PF24	8	0.00	0.74	0.82	65.48	0.00	0.04	0.00	34.22	0.13	0.00	-	-	-	100.61
PE16	4	0.00	0.51	0.57	67.30	0.02	0.02	0.05	29.37	0.10	0.00	0.01	-	-	97.38

Tab. A. 8 Major element oxides of selected points by EPMA.

Dip Dir/Dip	Dip Dir/Dip	Dip Dir/Dip	Dip Dir/Dip	Dip Dir/Dip	Dip Dir/Dip	Dip Dir/Dip	Dip Dir/Dip
PA:	**PB:**	**PF:**	020/84	002/85	056/65		
044/71	018/56	024/63	358/85	190/75	074/75		
070/66	358/55	030/71	**PI:**	178/80	067/72		
088/70	338/49	030/70	013/85	178/70	068/78		
042/76	346/32	030/67	**PJ:**	000/85	056/65		
042/80	004/36	025/50	014/62	**PN:**	**Schacht:**		
036/58	014/70	355/41	002/55	166/80	023/86		
030/53	010/65	000/24	342/35	335/85	014/50		
024/51	354/36	356/45	338/56	337/80	024/77		
040/65	356/66	**PG:**	**PK:**	350/87	023/86		
034/48	358/64	028/72	016/64	174/78	014/50		
036/56	350/38	002/70	004/56	000/82	014/50		
010/34	352/40	012/89	020/73	347/87	346/87		
052/20	358/47	014/89	354/66	162/55	002/75		
024/16	008/52	002/65	350/60	157/70	002/75		
246/11	**PC:**	357/72	346/60	170/66	346/75		
022/31	032/60	015/85	**PL:**	002/45	346/87		
342/10	042/49	017/50	345/70	002/30	346/86		
044/66	048/64	028/82	358/74	002/85	350/64		
032/50	**PD:**	010/81	350/85	**PO:**	342/56		
298/05	030/70	030/65	342/85	020/89	021/52		
000/34	015/57	**PH:**	330/76	000/89	007/70		
042/55	030/67	020/83	010/60	**PP:**	198/87		
020/31	**PE:**	000/73	020/70	067/72			
024/32	028/75	000/60	**PM:**	074/75			
288/16	030/75	020/72	180/75	164/80			
314/26	038/68	020/73	277/85	230/78			
358/35	212/85	036/57	344/84	225/64			
334/50	212/85	343/65	036/85	067/72			
012/50	022/58	356/89	042/76	074/75			
002/54	028/56	356/88	200/80	068/78			

Tab. A. 9 Sedimentary bedding planes.

Dip Dir/Dip	Dip Dir/Dip	Dip Dir/Dip	Dip Dir/Dip	Dip Dir/Dip	Dip Dir/Dip	Dip Dir/Dip	Dip Dir/Dip
PA-PB:	132/40	066/57	098/80	069/64	218/58	134/57	350/27
124/55	138/48	095/50	067/73	272/70	105/37	079/40	098/64
132/47	**PC-PD-PE:**	102/70	282/33	096/69	202/55	136/40	258/44
204/60	040/65	096/77	169/79	264/73	106/70	314/73	137/47
194/71	046/70	088/79	082/82	165/75	218/56	193/50	330/42
132/68	146/56	082/60	300/52	265/76	120/48	128/70	111/84
128/85	138/54	284/75	096/40	263/75	148/35	312/60	330/48
136/83	148/86	276/75	122/82	295/77	314/73	075/67	188/57
136/74	105/45	108/42	175/89	105/86	152/60	070/77	064/70
112/81	307/70	100/38	112/52	294/89	353/35	355/52	092/52
124/88	294/50	280/80	122/80	201/22	144/35	128/56	113/80
280/42	135/80	087/30	344/83	310/82	172/60	123/47	055/64
312/59	040/66	077/33	268/63	125/74	348/15	314/80	125/88
228/42	108/77	266/74	144/80	150/40	003/43	198/52	250/35
204/62	105/77	296/62	096/65	130/77	135/30	080/65	280/88
210/62	028/60	076/36	105/43	008/35	162/70	296/55	045/62
238/60	040/75	270/70	340/45	197/60	100/70	180/55	312/80
120/72	**PE:**	055/64	138/57	024/87	310/37	346/45	262/20
104/80	264/77	095/60	070/47	134/85	120/60	282/12	080/48
238/62	300/60	280/57	105/72	220/57	142/46	194/40	328/62
108/76	268/83	122/27	159/78	078/89	112/73	340/45	318/50
110/75	264/83	305/74	292/89	212/58	294/38	208/53	217/59
012/76	110/72	282/80	062/73	120/55	150/55	345/41	336/65
100/70	078/40	168/88	171/88	210/68	269/40	200/40	254/68
090/75	105/60	268/83	334/75	130/70	322/86	340/60	104/60
080/76	265/75	270/72	145/87	190/54	316/55	310/75	307/83
088/86	090/65	150/64	**PF:**	250/85	110/70	107/65	180/70
092/75	045/65	130/76	082/83	210/53	318/65	085/40	055/55
084/89	162/84	070/75	228/42	156/65	316/60	077/60	330/61
078/83	264/89	156/75	268/72	278/74	140/55	108/80	066/26
130/56	172/85	154/76	072/70	262/85	250/85	088/60	205/57

Tab. A. 10 Joint planes.

Dip Dir/Dip	Dip Dir/Dip	Dip Dir/Dip	Dip Dir/Dip	Dip Dir/Dip	Dip Dir/Dip	Dip Dir/Dip	Dip Dir/Dip
302/47	022/57	025/65	132/46	093/32	060/89	047/20	142/56
270/89	098/65	098/65	132/60	294/63	348/75	213/16	**PK:**
258/60	120/80	123/64	134/54	092/24	320/70	142/50	097/73
180/62	092/55	328/75	080/46	147/81	280/85	028/77	185/85
217/66	352/25	120/80	125/65	260/40	260/60	007/60	061/76
320/40	074/48	148/89	318/82	077/57	348/89	136/56	160/82
142/32	084/44	316/72	314/76	260/50	268/50	116/56	176/78
272/88	218/47	306/84	**PI:**	334/85	144/37	276/89	146/89
312/31	305/75	284/30	136/39	112/35	115/29	144/75	265/55
052/52	262/45	290/50	135/53	046/26	216/68	120/76	154/86
100/54	257/40	138/55	062/66	152/87	053/62	142/54	225/64
266/63	180/85	070/25	325/85	332/80	050/58	346/65	130/50
120/25	004/80	122/78	112/51	280/65	162/72	140/74	120/86
160/50	275/42	130/85	194/75	304/70	024/45	002/72	130/54
242/75	081/71	298/40	071/72	320/83	069/54	087/84	182/45
155/40	108/65	084/47	311/50	052/30	184/77	128/68	110/50
150/35	098/85	113/60	311/50	310/85	042/76	140/69	200/35
240/85	280/88	138/60	048/85	110/30	157/53	141/69	220/80
132/50	348/82	112/50	082/60	124/75	184/84	160/84	227/65
315/48	080/44	280/30	114/74	054/40	104/65	070/60	180/30
PG:	066/45	162/38	107/30	054/78	098/43	203/63	240/89
314/77	060/50	**PH:**	073/59	330/57	083/63	138/82	236/50
014/67	125/83	252/22	073/50	343/10	148/45	220/70	090/45
321/85	185/40	130/85	078/45	282/57	093/75	137/65	**PL:**
103/58	118/85	113/53	072/50	080/35	318/82	280/85	270/77
036/21	323/85	224/45	106/80	260/67	116/81	132/50	320/75
327/70	202/44	228/83	097/40	128/85	068/56	294/85	060/77
332/82	314/80	150/60	055/67	236/45	122/54	228/66	122/60
125/85	002/85	252/25	**PJ:**	266/66	056/27	282/85	163/70
328/78	004/75	129/47	283/37	084/42	280/80	265/64	074/45
095/60	318/76	127/38	192/74	090/54	007/67	268/89	044/63

Tab. A. 10 Joint planes.

Dip Dir/Dip	Dip Dir/Dip	Dip Dir/Dip	Dip Dir/Dip	Dip Dir/Dip	Dip Dir/Dip	Dip Dir/Dip	Dip Dir/Dip
066/66	108/60	287/80	105/85	242/75	174/68	354/30	
060/50	068/62	210/72	162/85	292/87	170/60	066/65	
062/30	115/30	088/89	066/60	316/80	256/50	074/72	
356/72	100/80	066/83	076/37	140/84	172/62	255/89	
126/50	139/69	112/85	071/39	100/85	090/36	016/85	
158/67	096/73	112/45	220/85	130/65	**PO:**	216/65	
116/70	259/62	275/47	270/75	336/89	220/80	274/88	
265/80	120/58	095/85	182/43	080/60	160/89	220/65	
267/87	220/75	235/50	194/85	152/65	070/72	130/35	
198/78	**PM:**	050/62	278/86	148/85	064/86	112/60	
090/60	240/89	080/85	268/80	056/75	104/25	104/70	
142/60	162/72	045/30	062/89	280/84	047/82	088/56	
110/40	166/66	063/75	322/85	174/65	072/47	145/76	
112/67	176/75	102/78	050/48	142/70	128/35	218/80	
287/45	074/76	028/60	072/35	090/85	205/77	074/55	
350/73	097/55	182/82	065/30	256/75	026/89	232/78	
100/65	350/35	340/89	158/65	108/85	218/85	235/65	
120/30	088/75	138/50	024/84	280/82	217/70	226/85	
090/45	105/47	110/70	182/77	102/75	055/25	059/89	
260/80	099/40	070/84	065/25	258/85	152/84	335/65	
248/85	124/85	123/80	112/77	096/70	134/52		
120/30	168/54	070/85	120/38	052/78	138/76		
090/45	162/48	190/82	170/89	300/88	132/47		
105/25	170/50	073/67	020/89	252/84	134/80		
128/48	150/45	098/86	190/80	310/50	292/86		
045/77	155/45	030/45	178/70	250/60	**PP:**		
102/84	115/80	038/35	130/75	140/60	067/72		
090/25	018/50	074/48	348/60	254/60	255/40		
164/65	085/65	306/70	280/46	006/55	230/87		
090/21	248/85	**PN:**	355/89	242/54	220/63		
100/68	277/68	070/85	087/32	160/45	216/25		

Tab. A. 10 Joint planes.

Dip Dir/Dip	Dip Dir/Dip	Dip Dir/Dip	Dip Dir/Dip	Dip Dir/Dip	Dip Dir/Dip	Dip Dir/Dip	Dip Dir/Dip
PA-PB:	179/89	098/48	080/80	**PM:**	154/85	170/80	
033/57	180/86	016/70	084/89	172/72	020/63	020/80	
048/83	070/67	017/80	326/83	004/80	048/52	075/78	
112/79	255/60	318/85	170/85	340/85	238/60	255/40	
100/89	276/70	096/50	245/88	090/50	102/70	050/89	
128/19	264/88	142/70	223/88	173/76	022/47	092/89	
172/47	180/74	141/66	166/86	**PN:**	172/85		
PC-PD:	188/87	140/58	166/86	075/89	263/85		
132/57	174/78	094/46	223/88	168/80	269/78		
292/63	166/87	**PH:**	085/86	154/89	190/88		
135/57	180/84	020/83	072/72	354/85	176/80		
298/63	178/79	135/88	040/46	160/64	048/80		
142/80	172/75	120/67	016/77	152/54	168/75		
118/89	100/47	315/80	108/60	178/60	**PO:**		
300/76	178/85	264/33	007/86	032/88	002/75		
296/64	177/84	132/72	116/52	160/89	160/64		
298/74	044/65	144/80	148/45	230/83	**PP:**		
114/78	**PF:**	144/80	088/78	335/85	174/70		
PE:	262/66	154/68	116/65	244/78	243/79		
132/88	032/78	010/87	100/75	326/86	244/60		
120/85	020/50	136/65	124/56	305/70	017/80		
063/80	276/40	**PI:**	096/74	344/84	060/75		
255/63	075/67	187/86	160/80	060/65	125/80		
276/64	070/77	074/45	160/88	350/87	048/75		
262/58	355/52	106/30	**PK:**	354/78	070/89		
296/75	128/56	**PJ:**	016/64	230/76	174/70		
120/89	194/40	020/70	170/89	250/70	074/89		
282/63	208/53	152/87	126/42	174/65	062/80		
186/86	354/50	004/74	188/55	142/70	200/78		
146/89	**PG:**	002/70	**PL:**	090/85	174/89		
092/70	078/47	008/77	045/77	098/80	174/70		

Tab. A. 11 Fault planes.

Appendix B. (Maps):

- Fig. B. 1 Geological map of study area (Ebner & Prochaska 2001).
- Tab. B. 1 List of the samples.
- Fig. B. 2 Location of traversed profiles.
- Fig. B. 3. Geological map of the Hohentauern/Sunk deposit in the open pit (Ebner & Azim Zadeh 2007).

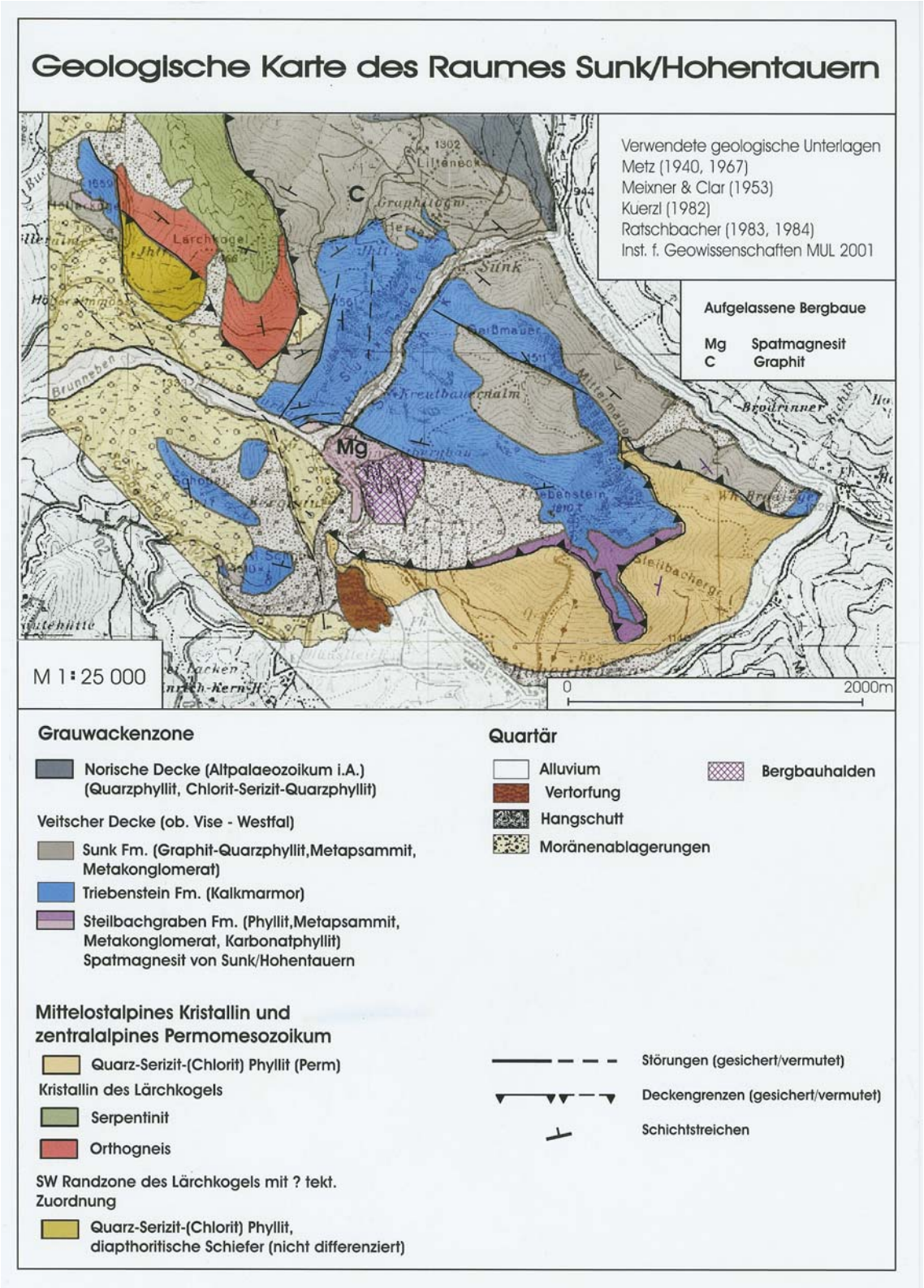

Fig. 1 Geological map of study area (Ebner & Prochaska 2001)

Profile	Sample	Profile	Sample	Profile	Sample
PA:	PA1		XPH3		PM15b
	PA11		XPH4		PM15-16(1)
			XPH4a		PM15-16(1a)
PB:	PB(Boudin)		XPH5		PM15-16(2)
	PB13		XPH6		PM15-16(2-D)
	PB14		XPH6(Mag)		PM15-16(2-Mat)
			XPH6(Mat)		PM15-16(3)
PC:	PC1				PM15-16(4)
	PC5	**PI:**	M1(PI)		PM15-16(5)
	PC6		M2(PI)		PM15-16(6)
	PC7		M3(PI)		PM15-16(7)
			M4(PI)		PM15-16(8)
PD:	PD1				PM15-16(9)
	PD8	**PJ:**	PJ1		PM15-16(10)a-b-c
			PJ16a		
PE:	PE3		PJ16b	**PN:**	PN(U1)
	PE4		PJ24		PN(U2)
	PE7		PJ*		PN(U3)
	PE10				PN(U4)
	PE14	**PK:**	PK2 up		PN(U5)
	PE16		PK2 down		PN(U6)
	PE21		PK4a		PN(U7)
	PE24a		PK4b		PN(U8)
	PE24b		PK5a		PN*a
	PE24x		PK5b		PN*b
	PE28		PK7		PN*c
	PE33a				PN wega
	PE33b	**PL:**	PL3		PN wegb
	PE33c		PL4		PN wegc
	PE33d		PL4-1		PN wegd
	PE35		PL4-2		
	PE37		PL4-3	**PO:**	PO8
			PL4-4		PO11a
PF:	PF14		PL4-5		PO11b
	PF15		PL4-6		PO12a
	PF16		PL4-7		PO12b
	PF17a		PL4-8		PO14a
	PF17b		PL4-9		PO14b
	PF17c		PL7		PO14c
	PF17d		PL15a		
	PF17e		PL15b	**PP-PO:**	PP-PO a
	PF17f		PL18a		PP-PO b
	PF17g		PL18b		PP-PO c
	PF24		PL18c		
	PF36		PL21	**PP:**	PP6
	PF(Nord)		PL23		PP kalk
					PP*
PG:		**PM:**	PM4a		
			PM4b	**PQ:**	PQ(M)
PH:	PH2		PM6 kalk		PQ(D)
	PH3a		PM7		PQ(K)
	PH3b		PM8 kalk		PQ1
	PH4		PM8 dolomit		PQ2
	PH13		PM11a		PQ3
	PH14a		PM11b		PQ4
	PH14b		PM11c		
	PH14c		PM14a		
	XPH1		PM14b		
	XPH2		PM15a		

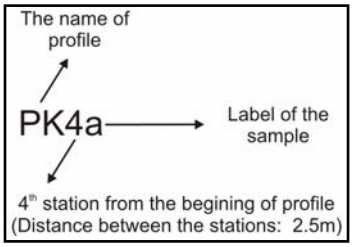

Tab. B. 1 List of the samples.

Location of profiles

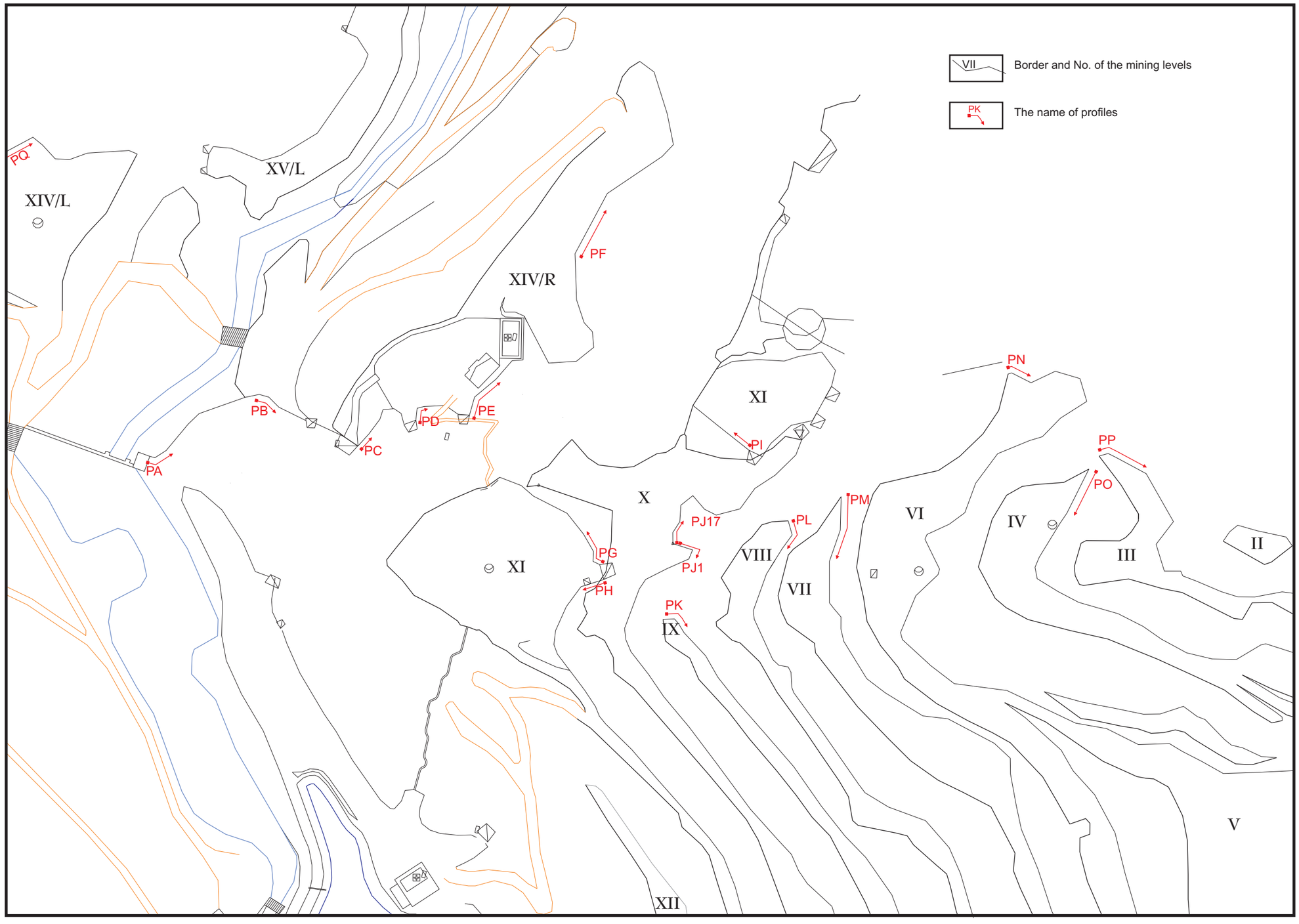

Fig. B. 2 Location of traversed profiles.

Geological map of the Hohentauern/Sunk deposit in the open pit

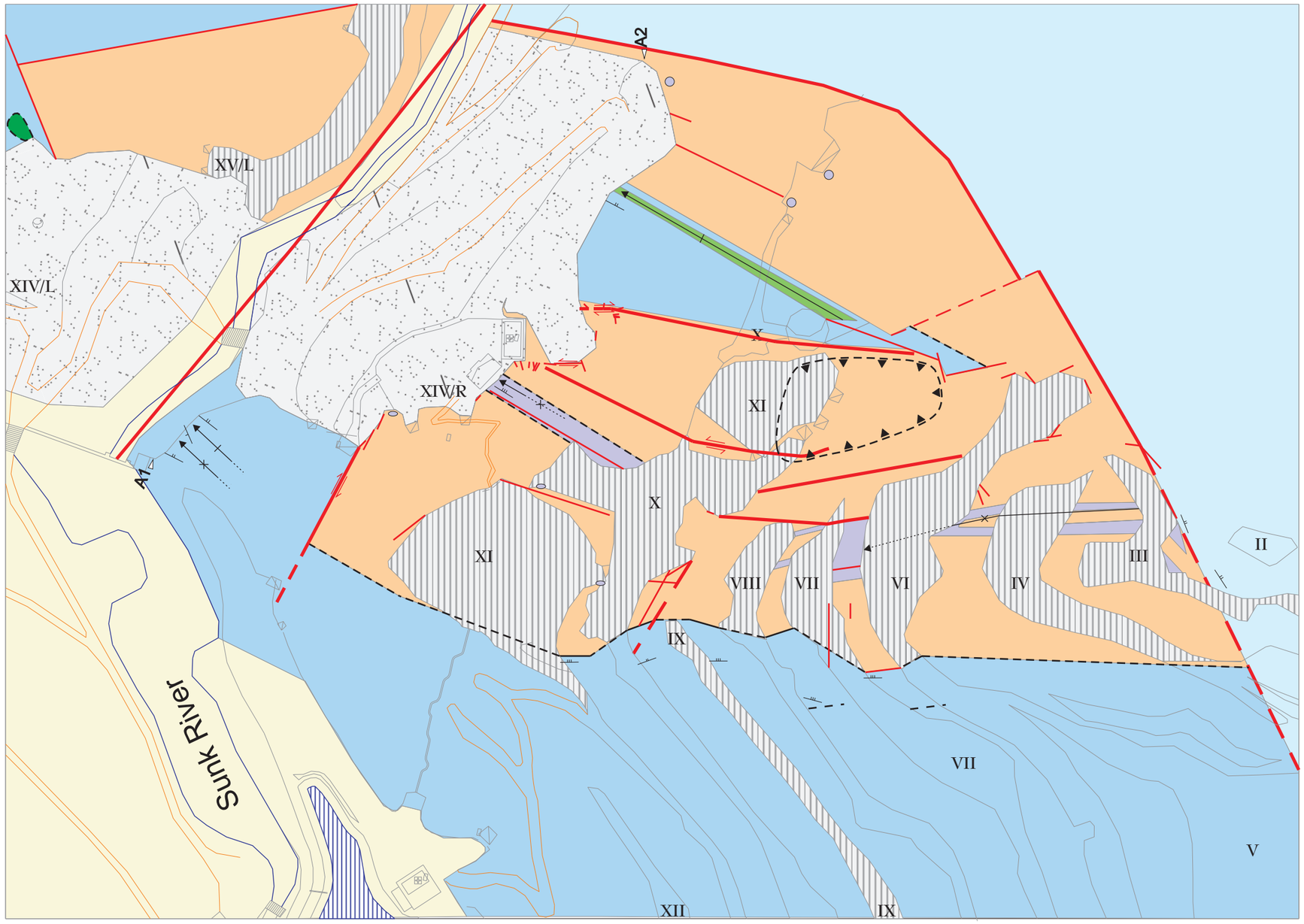

Legend

- Mine waste
- Landslide
- Cover of the levels (indicated in the open pit only)
- Quaternary, alluvial and talus
- VII Border and No. of the levels

Carboniferous of the Veitsch Nappe (Viséan - Namurian)

Triebenstein Fm.

- Bedded calcite marble

Steilbachgraben Fm.

- Sparry magnesite (orbicular dolomite)
- Fossiliferous bedded dolomite
- Fossililferous bedded limestone
- Dark grey calcareous, graphitic, metapelitic, psammitic schists
- Strike and dip (0-30 / 30-60 / 60-90)
- Fold axis with inclination — Anticline / Syncline
- 1st order fault (indicated, assumed)
- 2st order fault (indicated, assumed)
- A1 A2 Detailprofil

Scale 0 10 20 30 40 50m

N

Fig. B. 3. Geological map of the Hohentauern/Sunk deposit in the open pit (Ebner & Azim Zadeh 2007).